The black arbon in european atmosphere : identification, transfert, deposition and impacts

Marco Zanatta

Communauté
UNIVERSITÉ Grenoble Alpes

THÈSE

Pour obtenir le grade de

DOCTEUR DE L'UNIVERSITÉ GRENOBLE ALPES

Spécialité : **Science de la terre, univers, environnement**

Arrêté ministériel : 7 août 2006

Présentée par

Marco Zanatta

Thèse dirigée par **« Paolo Laj »** et
codirigée par **« Urs Baltensperger »** et **« Martin Gysel »**

préparée au sein du **Laboratoire de Glaciologie et Géophysique de l'Environnement (LGGE, UMR 5183, CNRS - UJF)**
dans **Terre Univers Environnement**

Le carbone-suie dans l'atmosphère Européenne: identification, transfert, dépôts et impacts

Thèse soutenue publiquement le **« 04 Avril 2016 »**,
devant le jury composé de :

Mme. Paola FORMENTI
Directrice de Recherche CNRS, (Rapporteur)
M. Christian GEORGE
Directeur de Recherche CNRS, (Rapporteur)
M. Andreas PETZOLD
Head of Group/Senior scientist, Jülich (Examinateur)
M. Jean-Luc JAFFREZO
Directeur de Recherche CNRS, LGGE (Examinateur-President)
M. Martin GYSEL
Head of Group,PSI (Co-Directeur de thèse)
M. Paolo LAJ
Physicien, LGGE (Directeur de thèse)

Summary

Black carbon (BC) induces a warming effect (RF_{BC} = +1.1 W m^{-2} ± 90%) through two main pathways: aerosol-radiation interaction (RF_{ari}) and aerosol-cloud interaction (RF_{aci}). Both BC-radiation and BC-cloud interaction are affected by the mixing of black carbon with other non-refractory and non-absorbing matter present in the atmosphere. An estimation of the global radiative forcing of BC rarely accounts for internal mixing of BC while the net global cloud radiative forcing is sensitive to assumptions in the initiation of cloud glaciation, which is mostly unknown for black carbon particles. Within this thesis we investigated the variability of the light absorbing properties of black carbon, the mixing of black carbon, and the impact of mixing on light absorption and ice activation.

In the first part of this thesis we investigated the spatial and seasonal variability of the mass absorption cross section (MAC) over Europe. MAC values were determined from ambient observations of elemental carbon mass concentrations (m_{EC}) and absorption coefficients (σ_{ap}). The data had been acquired during several years at different background ACTRIS supersites spread over Europe. Site specific MAC values were found to be spatially homogeneous, suggesting that the overall MAC average 9.5 ± 1.9 m^2 g^{-1} at a wavelength of 637 nm might be representative of BC at European background locations. The MAC values showed a distinct seasonal cycle at every station. This seasonality might be related to chemical composition and aging. We observed that the MAC value has a linear and positive proportionality with the relative mass amount of non-absorbing matter.

The second part of the work focuses on the coating acquisition of BC and the induced absorption enhancement after long-range transport. Within the CLIMSLIP (climate impact of short-lived pollutants and methane in the Arctic) project field experiments were conducted at the Zeppelin research site in Svalbard, Norway, during the Arctic spring. SP2 data were used to characterize the BC size distribution and mixing. BC containing particles having a core diameter between 170 and 280 nm were found to have a median coating thickness of 47 nm. The relationship between coating thickness and BC absorption was simulated. The observed coating thickness enhanced the mass absorption cross section by 46%, which led to a decrease of less than 1% in the single scattering albedo.

In the final part of this work, the role of black carbon as ice nuclei in mixed phase clouds was investigated at the high elevation measuring site Jungfraujoch, Switzerland, during the cloud and aerosol characterization experiment (CLACE) held in 2013. The ice-CVI inlet and a single particle soot photometer were used to select and quantify the ice activated BC particles. According to the observations, BC containing particles were depleted in the ice residuals. The activation efficiency showed a size dependency, with larger BC containing particles being activated more efficiently compared to smaller ones. Activated BC cores having a diameter between 170 and 240 nm showed a larger coating thickness (median = 53 nm) compared to the total aerosol (median = 16 nm).

The results obtained in this thesis shed new light on the effect of the mixing state on the optical properties and cloud activation of black carbon particles. Absorbing properties of BC showed a distinct seasonal pattern, while aging was found to consistently increase its absorption behavior. However, black carbon was found not to act as ice nuclei in low tropospheric mixed-phase clouds, where the coating thickness might play a role in the activation efficiency. This work provides freshly

determined physical properties derived from ambient observations that will improve the accuracy of future aerosol and cloud radiative forcing estimations.

Résume

Le carbone-suie, ou “black carbon” (BC), contribue de manière significative au réchauffement climatique avec un forçage positif de l’ordre de +1.1 W m^{-2} mais dont l’incertitude reste très significative (de l’ordre de 90% autour de cette valeur). Ce forçage s’effectue à travers deux mécanismes : l’interaction aérosol-radiation (RFari) et l’interaction aérosols-nuage (RFaci). Ces deux mécanismes sont affectés par le degré de mélange des particules contenant du BC avec divers matériaux non-réfractaires et non-absorbants présents dans l’atmosphère. Cependant, les estimations du forçage radiatif considèrent rarement les effets du mélange interne compte tenu de sa complexité. Par ailleurs le rôle du BC comme noyau glaçogène qui influence fortement l’interaction aérosol-nuage est largement inconnu. L’objectif de ce travail de thèse est de contribuer à mieux comprendre la variabilité spatiale et temporelle des propriétés optiques du BC, de déterminer les mécanismes par lesquels le degré de mélange interne du BC influence cette variabilité et son impact sur les propriétés d’activation des *noyaux glaçogènes* contenant du BC.

Cette thèse se base en grande partie sur l’utilisation de la technique SP2 (Single Particle Soot Photometer) qui permet, dans des conditions d’utilisation décrites dans la première partie du travail, la mesure directe de la distribution de taille du BC mais aussi l’évaluation du degré de mélange à partir détermination de paramètres optiques des particules. Le travail se base également sur la disponibilité de longues séries temporelles de certaines propriétés des particules, comme le coefficient d’absorption et les concentrations en carbone élémentaire obtenues dans le cadre du projet ACTRIS (Aerosol, Cloud and Trace gases Research InfraStructure).

Dans le premier chapitre de cette thèse, nous avons exploré la variabilité spatiale et *saisonnière* du coefficient d’absorption massique -mass absorption cross-section (MAC)- dans l’atmosphère en Europe. Les valeurs de MAC sont déterminées à partir des observations environnementales de concentrations de carbone élémentaire (mEC) et de coefficients d’absorption (σ_{ap}). Les données acquises proviennent de différentes stations d’observation européenne du réseau ACTRIS et offrent une représentation statistique pluri-annuelle robuste de la variabilité. Les résultats montrent une faible variabilité spatiale du MAC avec une moyenne de 9.5 ± 1.9 m^2 g^{-1} à 637 nm de longueur d’onde qui peut être considérée comme représentative du BC en Europe. Le cycle saisonnier marqué du MAC est probablement lié à la composition chimique de l’aérosol et son état de mélange. Nous avons observé une augmentation du MAC avec lien avec la présence de matériel non-absorbant. Cet article, soumis à la revue *Atmospheric Chemistry and Physics*, permettra de mieux évaluer le forçage radiatif dû à la présence de BC de manière plus fiable.

Les résultats précédents nous ont amenés à nous intéresser au lien entre l’absorption spécifique du BC et son état de mélange dans le cadre d’un processus de transport longue-distance dans l’atmosphère. Le second chapitre se base sur des mesures effectuées dans le cadre du projet CLIMSLIP (CLimate IMpact of Short-Lived Pollutants and methane in the Arctic). Une campagne de mesure intensive a été conduite sur la station de recherche Zeppelin au Svalbard, Norvège en Avril 2012. Les données acquises avec un single particle soot photmeter nous ont permis de caractériser la distribution en taille du BC et son état de mélange. Nous avons observé que le BC est généralement

présent en mélange interne dont l'épaisseur moyenne de la couche superficielle de matériel non-absorbant est de 47 nm pour des particules de BC de diamètre compris entre 170 et 280 nm. Ce mélange interne conduit à une augmentation d'absorption de 46%. Elle entraîne cependant une diminution relativement faible de l'albédo de simple diffusion, de l'ordre de 1%.

Enfin, dans le dernier chapitre, la capacité du BC à agir comme noyaux glaçogène pour la formation de cristaux de glace a été étudiée sur site de haute altitude du Jungfraujoch (Suisse) dans le cadre du "cloud and aerosol characterization experiment" (CLACE) en 2013. Nous avons utilisé la technique de séparation des différents éléments du nuage à partir d'une prise d'entrée type *ice-CVI* connectée au single particle soot photometer. Ce dispositif permet de sélectionner uniquement les cristaux de glace et quantifier la fraction de carbone suie activée à partir de la connaissance de l'aérosol présent en phase interstitielle du nuage. Une réduction de la présence de carbone suie dans les résidus de glace a été observée. Des mesures de l'épaisseur de la couche de mélange interne des particules contentant du BC ont montré des différences considérables entre la population d'aérosols totale et les résidus de cristaux de glace seuls, les premiers étant entourés d'une couche de taille moyenne, tandis que les seconds présentaient des enrobages bien plus épais. Ces travaux ont également permis de mettre en évidence certaines limitations du SP2 à différencier le BC de certaines particules terrigènes.

Les résultats obtenus au cours de ce travail de thèse ont permis de mieux comprendre l'impact du degré de mélange interne sur les propriétés optiques du BC et sur son rôle dans la formation de cristaux de glace. Les propriétés optiques du BC évoluent en fonction de la saison, tandis que la formation d'une couche superficielle amplifie sa capacité d'absorption du rayonnement solaire. De plus, cette étude permet de souligner l'importance du vieillissement atmosphérique du BC sur sa capacité à servir de noyau de nucléation de la glace. Enfin, il fournit une avancée au sujet des propriétés sensibles mesurées dans l'atmosphère avec des techniques innovantes qui permettront la simulation plus précise du forçage radiatif.

Acknowledgments

It's 2 AM and I can finally take care of the acknowledgments.
First I want to thank my French-Italian supervisor Paolo. Despite he will never admit so, he has a more pronounced Italian temper, that's why I like him. I'm pretty bad in this kind of things, but I'm proud to consider you as my scientific father.
Now, there is my full Swiss supervisor Urs. Mondays will never be the same without "*It doesn't seem to be the case, I wish you a good week*". Anyway, thanks to guide me with passion, enthusiasm and a lot of patience.
Martin, you are the last in this "boss list" but not the least. I will remember for a while when you approved and supported my decision to stay in science, in my mind I was thinking "If Martin thinks that I'm good, it means that I'm good for real ! ". However, thanks a lot for the discussions, the shared ideas and your inextinguishable love for statistics, which I never shared too much. It wouldn't be possible to do all this work without you.
A special mention for JLJ and his CERMO crew.
The entire lab knows the next two person, they cheered me up during the difficult periods, mainly with good food. Un bacione a Giorgio e Giuliana, aka mamma e papà.
A lot of love to all PSI people
Manu: Boninsegna, Burgnich, Riva, Rivera; Grosso, Del Piero; Balotelli, Balotelli. Giancarlo: A A BEN WAREM A BEN BEN; WAREM BEN BEN BEN; WAREM A WA TWO BEN BEN. Manolis: everybody has a crazy friend, you are mine; Jasmin: he is our last hope. Ugo: amici tutti in bici. No Bianchi no party. Imad: my lovely falafel; Nassia: ahh, greeck girls; Miriam: "Gurda che ti faccio male". Kaspar: I'm not allowed here, but you know. Bobby: china is waiting for you; Saehee: old rock. And Giulia: baghini. Thanks a lot guys, I'll miss all of you.

When young…

Table of contents

1 Introduction

Warming of the climate system is unequivocal, and since the 1950ies, many of the changes observed in the atmosphere, in the oceans and in the cryosphere are unprecedented over decades and centuries. In terms of observations, atmospheric global temperatures have been increasing by 0.85 °C over the period 1880 to 2012 (Hartmann, et al., 2013). Similarly the ocean has warmed by 0.11 °C per decade over the period 1971 to 2010 (Rhein et al., 2013). The combined effect of ocean and atmosphere warming induced a retreat of the perennial sea ice of 9-14% per decade between 1979 and 2012 (Vaughan et al., 2013).

But, what the human responsibility in such processes is? Human influence on the climate system is now clear, as reported in the Intergovernmental Panel for Climate Change (IPCC) report of 2013: "*It is extremely likely the human influence has been the dominant cause of the observed warming since the mid-20th century*". Temperature anomalies reflect a perturbation of the Earth's radiative budged. The latter is regulated by different substances and processes, the drivers. Such perturbation is called radiative forcing (RF) and is defined as the difference in energy fluxes caused by the change of the drivers between 2011 and 1750 (IPCC, 2013). Some of the drivers are directly related to human activity, which has been constantly intensifying since the demographic explosion of the 1950s (World Population Prospect, 2015) and has been leading to a constant increase of energy consumption. The latter is expected to increase substantially in the next decades, leading to an increase of liquid fuels consumption of 40% by 2040 (International Energy Outlook, 2014) and emission of climate change drivers as greenhouse gasses and aerosols.

In order to confine the impact of climate change, mitigation and adaptation strategies are now under development. These strategies are meant to stabilize the concentration of greenhouse gases and aerosols at a level that would prevent dangerous anthropogenic interference with the climate system within a time frame sufficient to allow ecosystems to adapt naturally to climate change, to ensure that food production is not threatened and to enable economic development to proceed in a sustainable manner. Mitigation and adaptation need to account for climate processes and socio-economic system and their targets are based on future economic, climate change and air quality projections.

Aerosols influence several atmospheric processes regulating the Earth's radiative budged and have undeniable effects on human health. In order to establish effective adaptation/mitigation strategies a deep knowledge of aerosol properties and accurate prediction of future aerosol concentrations is needed. Better understanding of aerosol properties and related atmospheric processes will reduce the highest source of uncertainty associated to anthropogenic RF, which is quantified between 1.13 and 3.33 W m^{-2} and leads to a net warming (IPCC, 2013). Otherwise, the net warming might increase frequency and intensity of extreme pollution events, making difficult to accurately estimate future aerosol concentrations and air quality (IPCC, 2013).

To make it a bit more clear, the aerosol plays a role in atmospheric processes directly related to climate change, which has feedbacks on atmospheric processes that regulate the abundance of

aerosol in the atmosphere. How to deal with such complexity? In this thesis we have done a small step forward in understanding some specific properties of a specific aerosol with the aim to increase the level of confidence in aerosol RF estimation, which is considered to be the greatest contributor of total radiative forcing uncertainty.

1.1 The atmospheric aerosol

1.1.1 Definition, classification and sources

An aerosol is defined as a suspension of liquid or solid particles in a gas (Seinfeld and Pandis, 2006). Aerosol particles have different origins, properties, sizes and lifetimes, thus different roles in climate and ecosystem processes. One of the nomenclature systems for aerosol is based on their size, which is influenced by sources and atmospheric processes (Figure 1.1). The aerosol population is generally log-normally distributed as a function of particle size with four distinct modes defined as the nucleation mode (particle diameter D_p < 10 nm), the Aitken mode (10 nm < D_p < 0.1 µm), the accumulation mode (0.1 µm < D_p < 2.5 µm) and the coarse mode (D_p > 2.5 µm). Two complementary classification systems of the aerosol are based on the type of source. One classifies the particles as a function of their origin, which can be anthropogenic or natural; while a second one distinguishes primary and secondary aerosols as a function of their formation mechanism.

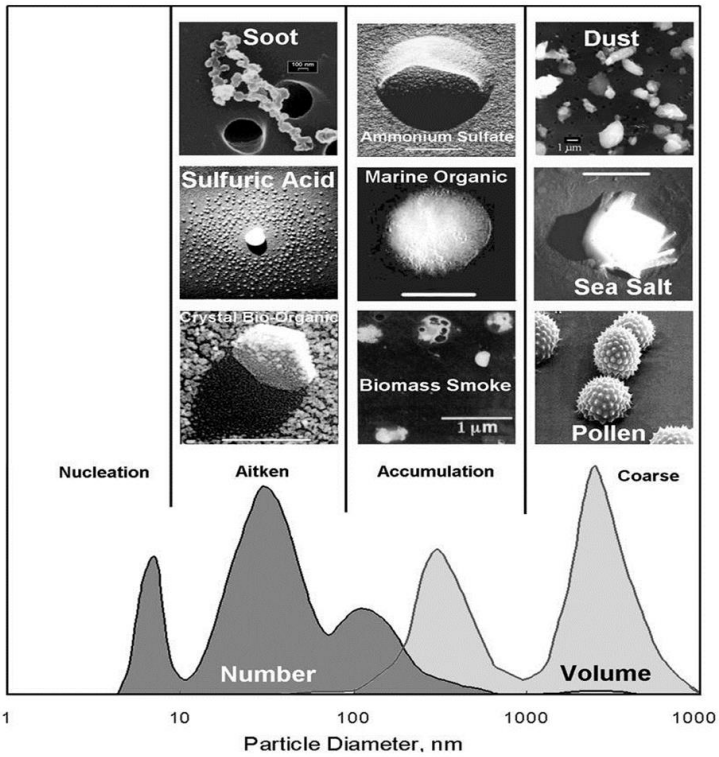

Figure 1.1 Size classification in number and volume of aerosol as function of different modes (Dahl et al.; 2005).

Primary aerosols are directly emitted into the atmosphere; the main natural primary aerosols are mineral dust, sea salt, biogenic material, volcanic ashes, and soot from forest fires. Further, the main primary particles emitted during human activity are carbonaceous matter, including soot, organic material and mineral dust. Differently from primary, secondary particles are formed in the atmosphere trough different pathways resumed as following. The new particle formation, based on gas-particle conversion leads to the formation of small particles (nanometer size). The most common involved gases are sulfuric acid, ammonia or oxidized organic species (Smith 2005; Laaksonen 2008; Holmess 2007). Furthermore, Brownian motion leads to coagulation of aerosol particles, while gaseous compounds with a low vapor pressure may condense on preexisting particles. Together, coagulation between particles and condensation on particles drive the growth process. Coagulation and condensation mechanisms control the mixing of primary particles as soot with other atmospheric materials (Section 1.4.4). Most strong natural sources for secondary particulate are the biosphere, volcanos and oceans. On a global scale, the natural emissions account for 80-90% of the total aerosol burden (Seinfeld and Pandis 1998). This dominance is due to the emission strength of primary aerosols dominated by sea salt (Erickson and Duce, 1988; Tegen et al., 1997) and mineral dust (Duce, 1995) (Figure 1.2). Still concerning primary particles, carbonaceous aerosol such as organic matter and black carbon, and industrial dust (mineral particles emitted during human activity) are a minor component in mass (Penner et al., 1993 and 1995; Liousse et al., 1996; Wolf and Hidy, 1997; Cook et al., 1999; Gong et al., 1998; Scholes and Andreae, 2000).

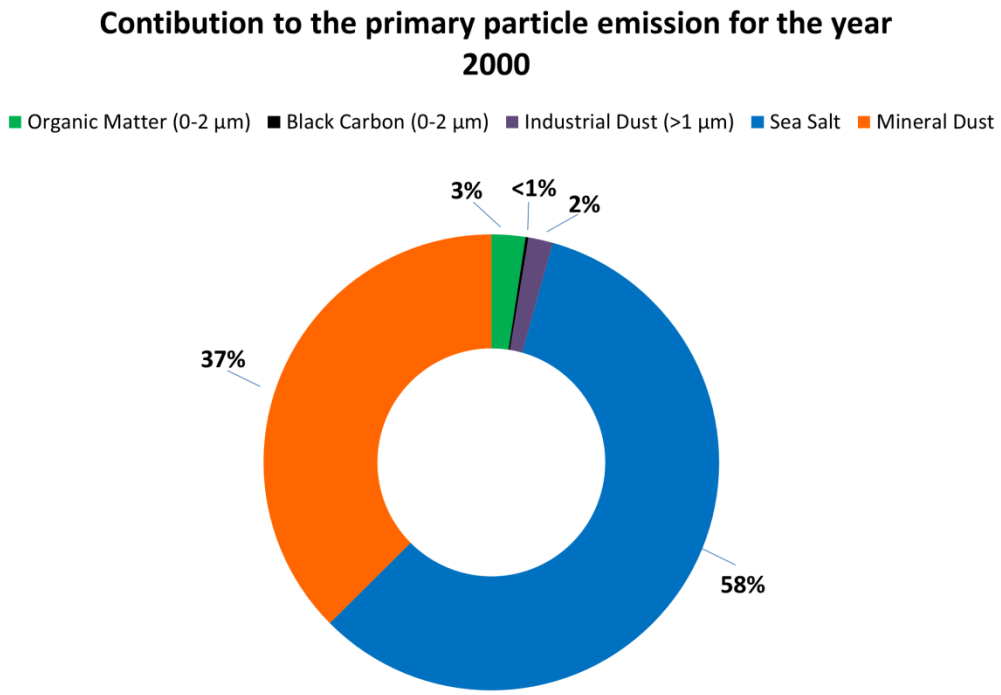

Figure 1.2 Mass fraction contribution of primary particle emission for the year 2000. Adapted from IPCC (2007).

A last alternative classification will be often used in this work and is based on the optical properties. Particles can interact with light in two different ways: scattering or absorption. Along the entire thesis we will discuss the optical properties of aerosol particles only in the visible spectrum. Thus, all particles constituted by a material with predominant scattering behavior in the visible spectrum such as sulfate, nitrate and organic matter are addressed as "non-absorbing". Aerosol particles with absorbing behavior in the visible spectrum such as black carbon are called "absorbing".

1.1.2 Aerosol impact on climate system

As shown by historical pattern-matching studies, the aerosol loading in the atmosphere is critical to explain the historical spatial and temporal patterns of temperature changes (Santer et al., 1995; IPCC, 2013). In addition to radiative forcing, the effective radiative forcing (ERF) is nowadays considered to be a better indicator of the global mean surface temperature and thus climate warming (Boucher et al., 2013). The ERF allows for rapid adjustments to perturbations, for all variables except for global mean surface temperature or ocean temperature and sea ice cover. The ERF and RF values are significantly different for the anthropogenic aerosols, owing to their influence on clouds and on snow or ice cover. The resulting cooling effect is triggered by the aerosols interacting with the solar radiation and playing a role in the formation and dissipation of clouds. The corresponding RFs are then defined as aerosol-radiation interaction (RFari) and aerosol-cloud interaction (RFaci) (Boucher et al., 2013). The total ERF due to aerosols (ERFari+aci, excluding the effect of absorbing aerosol on snow and ice) is assessed to be –0.9 (–1.9 to –0.1) W m^{-2} (Myhre et al., 2013). The ERFari+aci estimate includes rapid adjustments, such as changes in the cloud lifetime and aerosol microphysical effects on mixed-phase, ice and convective clouds. Individual contributions of ERFari and ERFaci to ERF are difficult to separate; this might be achieved assuming linearity of both interactions, without accounting for mutual feedbacks. Within this approach ERFari and ERFaci are both quantified at -0.45 W m^{-2}, but there is no a priori reason why the ERFs should be additive because by definition they occur in a system that is constantly readjusting to multiple nonlinear forcings (George and Wood, 2010; Lohmann et al., 2010; Mauger and Norris, 2010; Painemal and Zuidema, 2010).

Aerosol particles interact with solar radiation through absorption and scattering and, to a lesser extent with terrestrial radiation through absorption, scattering and emission (

Figure 1.3). The RFari is defined as the change in radiative flux caused by scattering and absorption by aerosol at the top of the atmosphere. Although radiative effects due to aerosol-radiation interaction are well understood, the knowledge of the real aerosol behavior in the atmospheric system remains incomplete (Anderson et al., 2005; Satheesh and Moorthy, 2005; Jaegle et al., 2011). The RFari needs deep knowledge of spectrally dependent scattering and absorption coefficients as well as the single scattering albedo and the phase function. These properties are not homogeneous and depend on the size of the aerosol particles, as well as on composition and on mixing state (Boucher et al., 2013). Environmental conditions such as surface albedo and cloud cover also influence the effects of RFari,

making it extremely spatial heterogeneous. Under clear sky conditions the RFari is usually negative at the top of the atmosphere, but can become positive depending on the fraction of absorbing particles, the forward scattered light fraction or the surface albedo (Yu et al., 2006; Bergamo et al., 2008; Di Biagio et al., 2010; Bauer et al., 2011, Flanner et al., 2010). Rapid adjustments concerning the aerosol-radiation interaction are particularly pronounced for aerosols having an absorbing behavior, which modify the atmospheric stability (e.g., Wendisch et al., 2008; Babu et al., 2011) influencing the cloud cover (e.g., Yoshimori and Broccoli, 2008; Allen and Sherwood, 2010; Koch and Del Genio, 2010; Persad et al., 2012).

Clouds play an important role in regulating the Earth's radiative budged, they almost double the albedo of the Earth, reflecting the incoming shortwave solar radiation and re-emitting the longwave terrestrial radiation (Ramanathan et al., 1989). The microphysical properties on which the cloud radiative properties are based might be potentially modified by the presence of atmospheric aerosols. Indeed, aerosols can serve as cloud condensation nuclei (CCN) and ice nuclei (IN) upon which cloud droplets and ice crystals form. The idea is that particulate matter plays a role in cloud formation and modifies the cloud properties

Figure 1.3). Increasing the number of CCN induces an enhancement in the number of cloud droplets and a decrease of their size (Twomey, 1977). The radiative consequence is an increase in the cloud albedo. Additionally, the decrease of droplet size leads to an increase of cloud lifetime (Albrecht, 1989) and cloud vertical extent (Pincus and Baker, 1994). Hence, absorbing aerosol imbedded in the cloud might lead to a burn-off of the cloud (Tosca et al., 2015). However is difficult to isolate all the possible aerosol-cloud interactions, the radiative consequence of the interaction are grouped together into the ERFaci

Figure 1.3). The latter accounts for microphysical modification to the cloud albedo, and any additional effect that results from cloud adjusting to their environment (lifetime and vertical extent).

In addition to the aerosol-cloud interaction uncertainty, different clouds have different effects on the Earth's radiative budget. Compared to liquid clouds, glaciated and mixed-phase clouds have different radiative properties. Clouds with a higher fraction of ice generally have fewer, but larger, ice crystals, as compared to more numerous, smaller droplets in a liquid cloud. As direct consequence, glaciated clouds have a lower extinction coefficient than liquid clouds at the same water content. While liquid clouds have a higher reflectivity than ice clouds, which have a higher absorptivity across most solar zenith angles (Sun and Shine, 1994a). Meanwhile, assuming an identical optical thickness, ice clouds have a higher albedo than liquid clouds (Mishchenko et al., 1996). Ice formation also enhances the development of precipitation, due to the rapid diffusional growth of ice crystals (Rogers and Yau, 1989), and thus leads to a decrease in the lifetime of a glaciated cloud relative to a liquid cloud. DeMott et al. (2010) showed how the climate simulations are sensitive to assumption on the initiation of cloud glaciation. It was found that the global net cloud radiative forcing increases by $\sim$1 W m^{-2} for each order of magnitude increase in ice nuclei concentrations. At temperatures above −38 °C ice in the atmosphere forms via heterogeneous nucleation (Seinfeld and Pandis, 2006). In this process, a foreign substance, known as an ice nucleus, lowers the Gibbs free energy barrier, thus

allowing nucleation to take place at lower supersaturations. Mineral dust has been shown to be efficient ice nucleus in numerous laboratory and ambient studies (Cziczo et al., 2004; Hoose and Möhler, 2012). Differently, the ice nucleating activity of black carbon is a matter of some controversy. Quantification of the ERFaci forcing is, although, fraught with uncertainties (Haywood and Boucher, 2000; Lohmann and Feichter, 2005) making the uncertainty associated to ERFaci the most important contributor to the total anthropogenic RF (Forster et al., 2007; Haywood and Schulz, 2007).

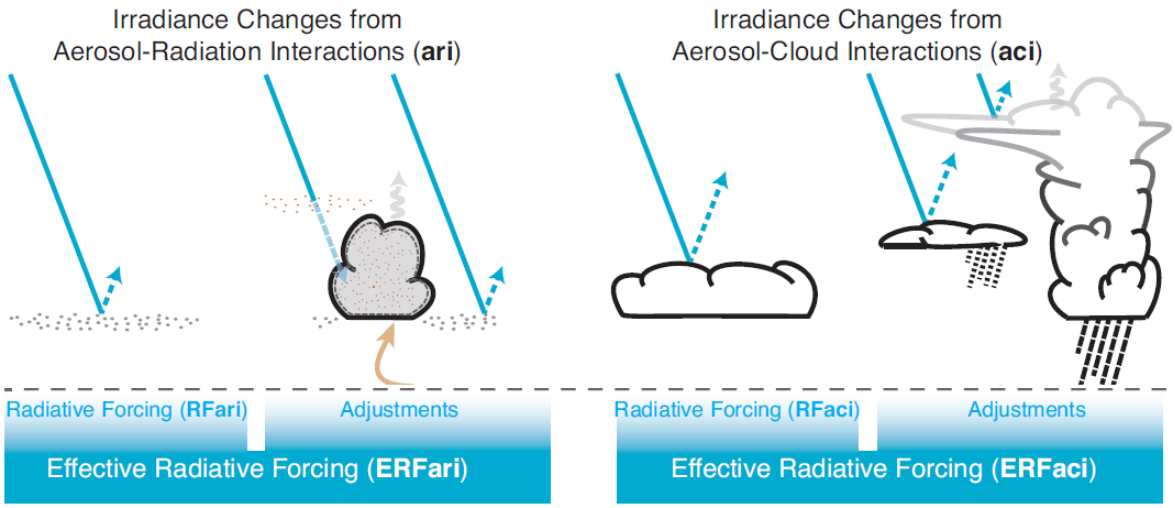

Figure 1.3 A schematic of the mechanisms through which aerosols affect atmospheric radiative transfer via aerosol-radiation interaction (left) and aerosol-cloud interaction (right). The blue arrows depict solar radiation, the grey arrows terrestrial radiation and the brown arrow symbolizes the couplings between the surface and the cloud layer for rapid adjustments. Black dotted lines with different thickness represent precipitation intensity. Adapted from IPCC (2013).

1.1.3 Aerosol impact on human health

In addition to its climate impact, particulate air pollution impacts on human health and has been associated with cardiovascular morbidity and mortality in numerous epidemiological studies (Brook, 2008; Huang et al., 2009; Fang et al., 2013). In the human body, the coarse fraction of the particulate matter (PM) is stopped in the upper respiratory system; while the PM2.5 penetrates to the lower respiratory tract, furthermore the ultra-fine aerosols reach the bronchioles. However, the impact of size and chemical composition on health impact is not clearly established (Pope et al., 2006); epidemiological studies demonstrated that an increased PM2.5 increases the possibility of contracting lung cancer and cardiovascular diseases (e. g. Pekkanen et al., 2002). BC itself has been linked to several pathologies such as cardiac and ventricular arrhythmias (Rich et al., 2005), lowered heart rate variability (Schwartz et al., 2005), and more generally increased cardiovascular mortality (Maynard et al., 2007). The World Health Organization reviewed the current knowledge on BC health impact (Janssen et al., 2011) and concluded that BC may act as a carrier for a wide variety of chemical constituents of different toxicities (e.g., polycyclic aromatic hydrocarbons; McCreanor et al., 2007;

Harrison and Yin, 2000) due to its small size; thus, the measurement of the size and the mixing state of BC is of interest for development of new health-related policies.

1.2 Trend, composition and properties of the European aerosol

Substantial change in the anthropogenic aerosol concentration over Europe has been observed over the recent decades. The discovery and assessment of transboundary transport of aerosols and precursor gasses in 1970s (Eliassen and Saltbones, 1983; Menz and Seip, 2004; Grennfelt and Hov, 2005) triggered an international collaboration in order to reduce the emissions of sulfur dioxide, oxides of nitrogen, ammonia and organic compounds. Since the 1980ies most of the precursor gasses have been substantially decreasing. Sulfur dioxide emissions have been constantly decreasing from 1990 to 2004, resulting in a final reduction of 54% in sulfur emissions (Vestreng et al., 2007). Over the period 1990-2009 the nitrogen oxides emission have been cut by 41% (European Environment Agency). Otherwise, the total suspended matter concentrations in Europe have decreased by 42% over the period 1978-1998, e.g., PM10 by 9% between 1997 and 2009 (Turnock et al., 2015) while atmospheric visibility has increased over the last 30 years (Vautard et al., 2009; Tørseth et al., 2012). Such processes are the results of policies born to reduce acidic rain and improve the European air quality. However, what is the impact on the European climate system and radiative budget? Observations of surface radiation revealed that surface solar radiation declined from 1950 to the mid-1980ies, this process is called “dimming” and documented by Stanhill and Cohen (2001). Simultaneously to the reduction of aerosol burden the solar radiation began to recover (Figure 1.4c). This event is now called “brightening” and takes place under cloud-free conditions (Ruckstuhl et al., 2008); in Europe it suggests a relationship with the aerosol depletion (Streets et al. 2006). Observations and simulations over Europe, shown in Figure 1.4a and Figure 1.4b, confirmed that PM10 and aerosol optical depth have been decreasing simultaneously since the 1980s inducing a positive surface solar radiation anomaly (Ruckstuhl and Norris, 2009; Chiacchio et al., 2011; Turnock et al., 2015). This anomaly is the cause of the transition from negative to positive aerosol radiative forcing over Europe around the mid-1980s (Turnock et al., 2015), contributing to the observed 0.5 K decade^{-1} European warming (Cherian et al., 2014). As parametrized by Smith and Bond (2014), the current air quality policies, without a discrimination between absorbing or scattering aerosol, will leave to the greenhouse gases the role of dominant radiative forcers. Seen from a pure climate aspect, reduction of aerosol emissions should be selective and focused to decrease the burden of positive forcers. In order to help in the implementation of the current policies and future scenarios, the European aerosol chemical composition and its properties have been widely investigated.

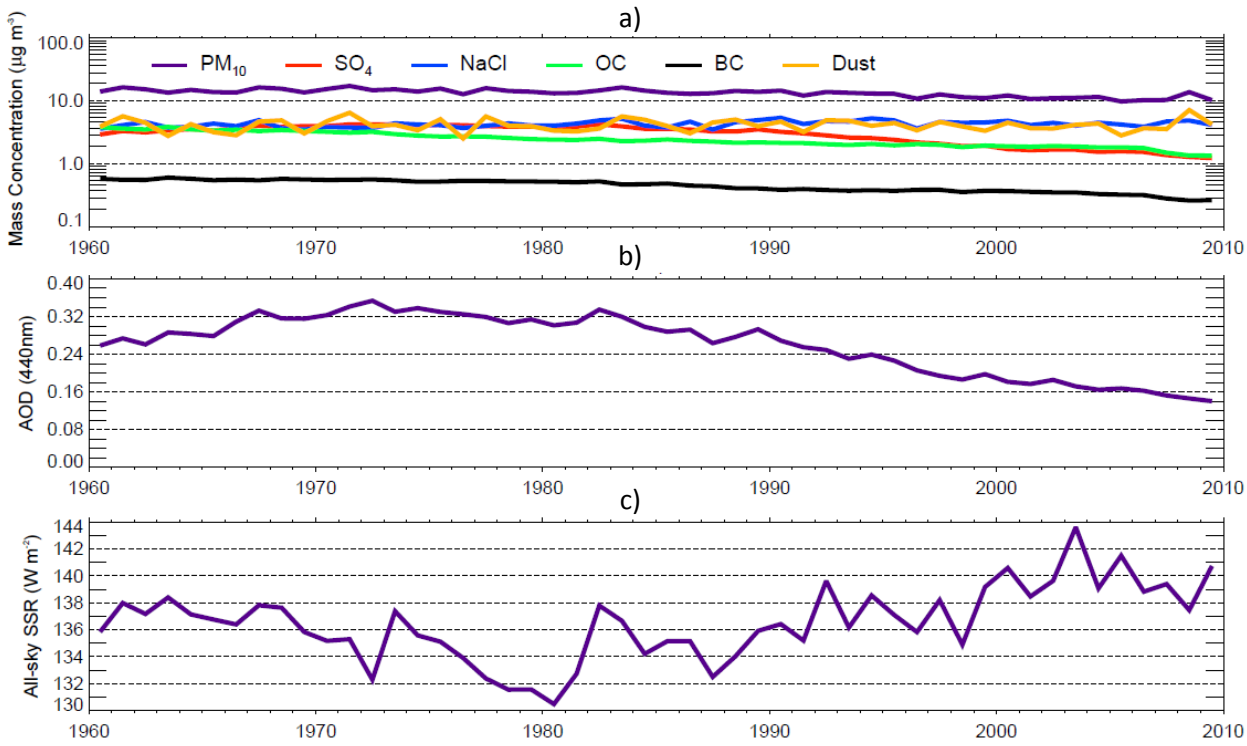

Figure 1.4 Simulated annual mean: a) PM10 and composition resolved mass concentration; b) Aerosol optical depth (AOD); c) Surface solar radiation (SSR) between 1960 and 2009 over Europe. Adapted from Turnock et al. (2015).

At present, the PM10 and PM2.5 averaged background concentrations over Europe are quantified at 7 ± 4.1 µg m^{-3} and 4.8 ± 2.4 µg m^{-3}, respectively (Van Dingenen et al., 2004). The same authors reported that the absolute concentration of the suspended matter is highly variable as a function of the sampling location, with low PM10 mass concentrations (less than 20 µg m^{-3}) at free tropospheric such as the Jungfraujoch (Switzerland) and natural background sites in Scandinavia. Higher values (between 20 and 40 µg m^{-3}) were observed at locations representing rural background, near city and urban background conditions such as Harwell (England), Melpitz (Germany) and Ispra (Italy). The highest aerosol concentrations are reported at kerbside sites. Maximum concentrations are reported to occur during the cold season due to domestic heating and contraction of the planetary boundary layer (Putaud et al., 2003).These works suggested that the European aerosol is extremely variable, and its variability depends mainly on the sampling location.

Asmi et al. (2011) found a dependence of the aerosol particle size distribution and number concentration with geographic location (Figure 1.5). Central Europe is characterized by a uniform aerosol, with high concentration, weak seasonal cycle and a single mode median size distribution. Western Europe is characterized by heterogeneous air masses and high seasonal variability. Aerosol particle concentrations in Scandinavia showed pronounced seasonal variability, with lower concentrations compared to central Europe and dominated by heterogeneous air masses. Aerosol properties in the European Arctic showed a strong seasonal variability, with a higher concentration of the accumulation mode during winter and smaller particles (Aitken mode) during summer indicating new particle formation. Aerosol in the Mediterranean region exhibits large seasonal variability due, in

part, to sea salt and Saharan dust intrusions (Querol et al., 2003; Rodriguez et al., 2002, 2003). Aerosol in the free troposphere observed from Mountain top sites showed a strong seasonal cycle in aerosol number concentrations, high variability, and very low number concentrations (Venzac et al., 2009; Herrmann et al., 2015).

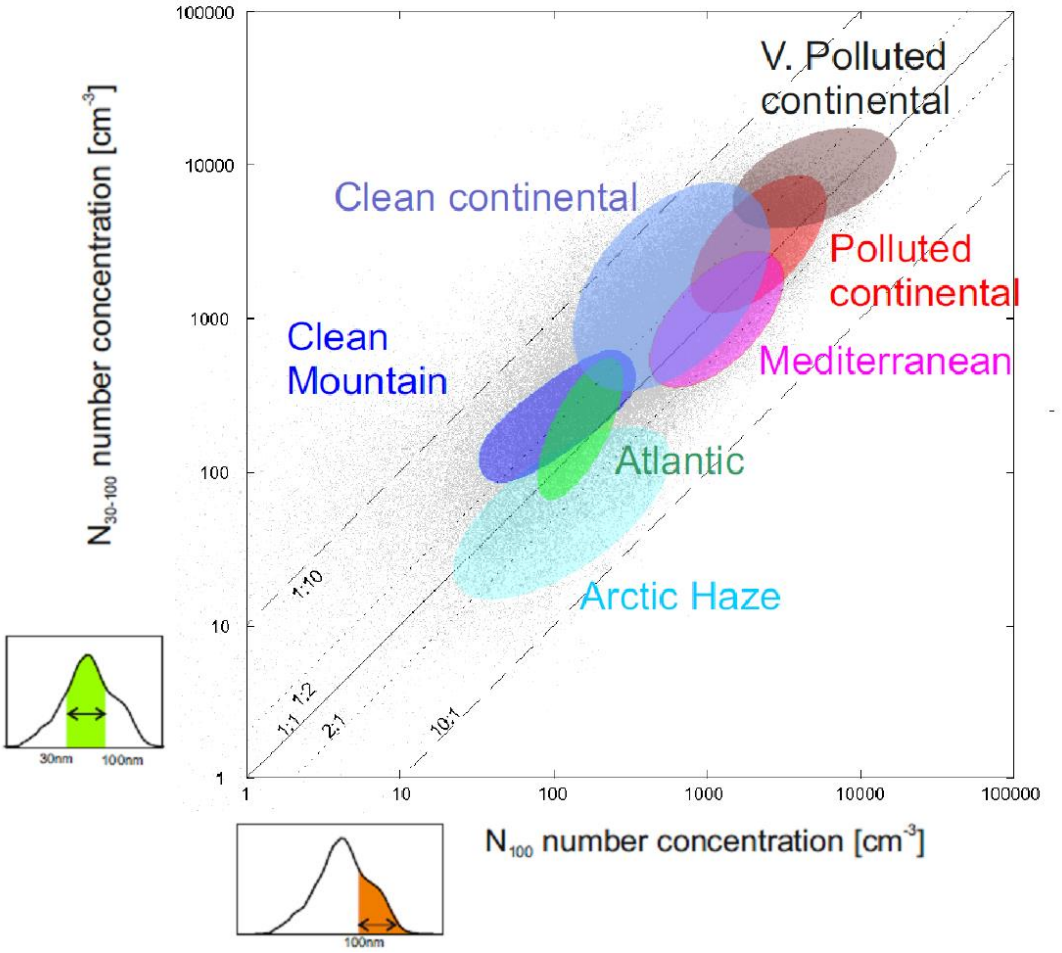

Figure 1.5 Scatter plot of particle number concentration between 30 and 100 nm as a function of particle number concentrations above 100 nm (grey points). The station groupings are shown with different colours, with the contours showing the areas with greatest density of each station grouping. The contours are drawn to include 83% of the each group data points. The insert shows an interpretation of the approximate aerosol types in the same. Adapted from Asmi et al. (2011).

If we consider the aerosol chemical composition, at natural, rural background, near urban and urban city locations the dominant components of both PM10 and PM2.5 are the organic matter and sulfate, followed by nitrate, while black carbon contributes between 5 and 10% (Putaud et al., 2004). It is important to note that sulfate, nitrate and organic particles have a dominant scattering behavior in the visible spectrum, while black carbon is a strong light absorber. Hence absorbing species are a minor component of the European aerosol population. Summarizing, the European background aerosol experiences great variability in number and mass concentration and size distribution as a

function of geographic region. Furthermore the concentration decreases moving away from central Europe. Additionally, the aerosol population is dominated by scattering material as sulfate and organic matter, while absorbing aerosol, as black carbon, is only a minor component.

1.3 Soot particles

1.3.1 From emission to deposition

Black carbon (BC) is a particular type of carbonaceous matter which is directly emitted into the atmosphere through anthropogenic and natural combustion processes. The exact formation mechanism of black carbon is not fully understood yet, but involves several steps resumed as follows (Masiello, 2004; Moosmüller et al., 2009; Bond et al., 2013): i) pyrolysis of fuel and thermal degradation; ii) formation of polycyclic aromatic hydrocarbons; iii) growth of polycyclic aromatic hydrocarbon structures; iv) gas to particles conversion; v) surface growth and coagulation to form the new particles. These processes lead to a formation of a conglomerate of spherules, which is insoluble in water, hydrophobic (Weingartner et al., 1997). BC is characterized by a pronounced stability at high temperature, reaching the vaporization point around 4000 K (Moteki et al., 2010), and by a strong light absorption in the visible spectrum. While our interest in black carbon has been rising in the last decades due to its light absorption and radiative forcing, our attitude to produce it is almost as old as humanity. Technically, black carbon emission started with the first handled fire in human history; even though heavily disputed, extensive use of fire by human population is dated to 0.2-1.7 million years ago (Bird, 1995; Bird and Cali, 1998; Weiner et al., 1998; Brown et al., 2009; John Webb, 2009; Roebroeks and Villa, 2011; Bowman et al., 2011; Berna et al., 2012). Coming to more recent eras, the global black carbon emissions have been increasing constantly over the period 1850-2000 (Lamarque et al., 2010) with a change in the type of sources. In the preindustrial time, BC emissions accounted for 20% of the 2000 emissions and were dominated by biomass burning for heating and cooking (Bond et al., 2007). Starting in 1850 the global emission of BC have shown a general increase due to coal and biomass consumption in the residential sector (Smith and Bond, 2014). Within the 1950ies the emission rate of BC accelerated under the input of transportation, industrial sectors and forest fires intensity (Smith and Bond, 2014). The increase in emissions and the evolution of sources is displayed in Figure 1.6.

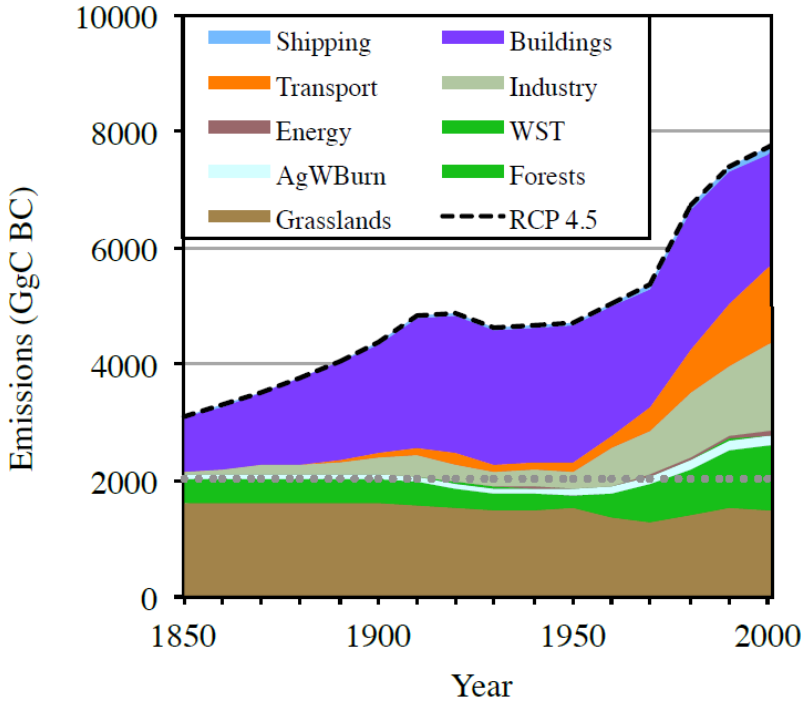

Figure 1.6 Historical black carbon emissions under the global climate atmospheric model and climate policy scenarios (RCP 4.5). The grey dotted line shows the assumed preindustrial BC open burning emissions. Adapted from Smith and Bond (2014).

Globally, total BC emission in the year 2000 was about 7500 Gg yr^{-1}, with a high uncertainty range of 2000 to 29000 Gg yr^{-1}. Compared to the past, the total emission in the year 2000 was around 5 times higher due to greater energy consumption than in 1750 background, which was 1400 Gg yr^{-1}. Nowadays (2000) BC is mainly produced by two sources, biomass burning and energy-related activities. Energy related emissions include combustion processes such as diesel burning, coal burning for industry activities, residential fuel burning and other sources like shipping and biofuel burning. The open biomass burning class includes grassland and woodland fires, forest fires and agricultural fires. Energy related emissions accounted for 59% of global emission in 2000, while biomass burning contributed with 41% (Bond et al., 2013). Despite the significant uncertainty, the three major contributors to BC emissions are open burning, diesel engines and residential solid fuel burning (Figure 1.7).

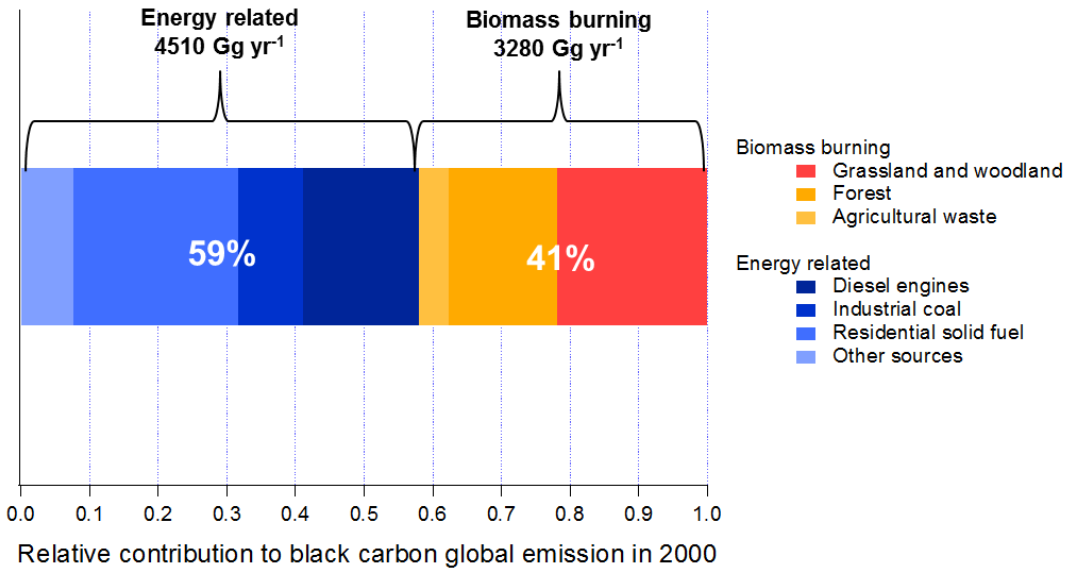

Figure 1.7. Relative contribution, in fraction, to the global emissions of BC during 2000. Source are estimated using the bottom-up speciated pollutant emissions wizard model (Bond et al., 2004, 2007; Lamarque et al., 2010). Adapted from Bond et al. (2013).

But what happens to black carbon after emission? It undergoes different processes taking place during its atmospheric lifetime. The latter is defined as the suspension time of particles in the atmosphere before removal and can last between hours and days before wet or dry deposition occurs (Ogren and Charlson, 1983). Due to its small size (submicron diameters) BC has the longest residence time among the atmospheric particles, this allows great horizontal and vertical transport from the emission point to high altitude mountains (Lavanchy et al., 1999; Ming et al., 2009), and polar regions (McConnell et al., 2007; Bourgeois and Bey, 2011; Bisiaux et al., 2012a, 2012b). Therefore, BC is ubiquitous in the atmosphere, but the spatial distribution, usually simulated using global chemistry and transport models, shows certain heterogeneity. Due to geographic distribution of continents, and highly industrialized and densely populated countries, the atmospheric concentration of BC in the northern Hemisphere is 10 times higher than the southern Hemisphere (Chung and Seinfeld, 2002; Ramanathan & Carmichael, 2008). Additionally, regional hotspots of atmospheric BC burden include the Indo-Gangetic plains in South Asia, Eastern China, most of Southeast Asia and regions of Africa between sub-Sahara and South Africa. Other weaker hotspots are found over Europe, urban North and South America (Chung and Seinfeld, 2005; Ramanathan and Carmichael, 2008) as shown in Figure 1.8.

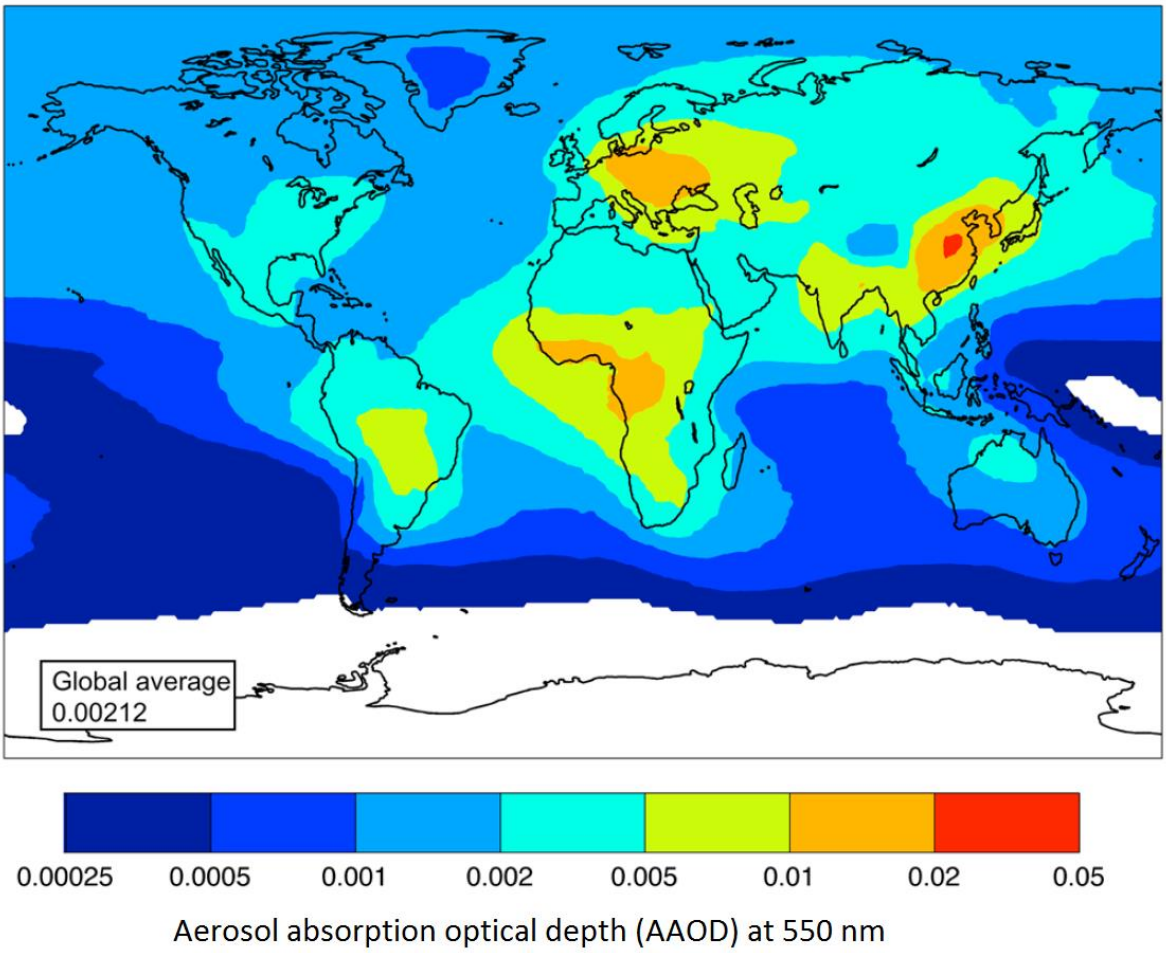

Figure 1.8 Aerosol absorption optical depth associated to black carbon from AeroCom simulations (Schulz et al., 2006). Adapted from Bond et al. (2013).

During its suspension time and transport, BC particles undergo chemical and physical transformations; such processing is called atmospheric aging and includes the interaction between BC and other atmospheric particles or gases. Condensation and coagulation of organic matter and inorganic salts on BC cores leads to internal mixing within a few hours and several days from emission (Jacobson, 2001; Fierce et al., 2015). Internal mixture describes a population of heterogeneous agglomerates, in which black carbon and other materials are mix together in the particles. Nowadays it is commonly accepted that internal mixing of BC takes place; nevertheless a debate on the geometry of the BC-containing particles is still going on. It is often assumed that non-BC material surrounds the BC completely and symmetrically, such configuration is called core-shell geometry. Mixing geometries with partial and non-concentric shell may also exist (Sedlacek et al., 2012; Adachi et al., 2010; Dahlkötter et al., 2014) as well as BC cores attached to other non-BC particles (Moteki et al., 2014).

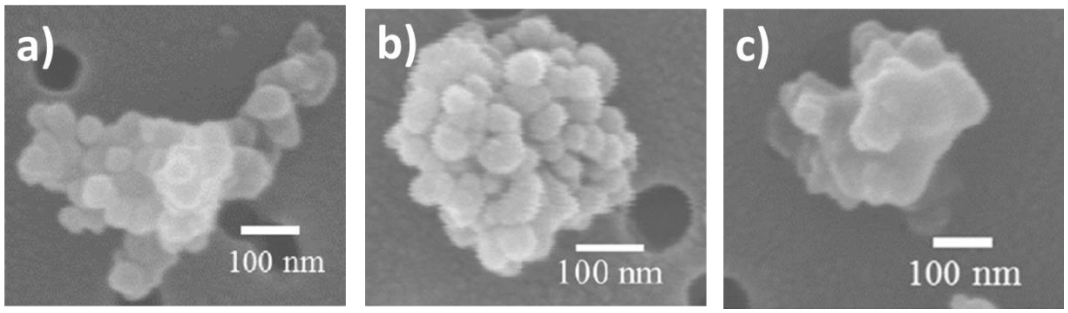

Figure 1.9 Scanning electron microscopy images show the typical morphology of partly coated (a), thinly coated BC (b) and embedded (c) BC particles. Adapted from China et al. (2015).

The ageing processes modify BC hygroscopic properties. Freshly emitted BC is mainly hydrophobic with a ramified structure (Figure 1.9a) (Weingartner et al., 1997), but its hygroscopicity increases during ageing mostly by condensation of hygroscopic sulfates or organics (Chung, 2002; Dusek et al., 2006; Wex et al., 2010). It is considered that BC can acquire hydrophilic properties within 1 to 2 days in the atmosphere and can serve as cloud condensation nuclei (Koch et al., 2009). During the ageing, BC aggregates may collapse to form less fractal, more compact particles (Tritscher et al., 2011; China et al., 2015) as shown in panels (b) and (c) of Figure 1.9. Morphology modification, together with uptake of a coating, modifies also the optical properties of BC. Such modification will be fully discussed in detail in Section 1.4.4.

Such processes take place during the suspension time of BC in the atmosphere, which is defined as the elapsed time between emission and deposition. There exist two dominant removal mechanisms of BC: wet deposition and dry deposition. The former contributes to 66 % to the total removal of BC (Chung and Seinfeld, 2002) and is more efficient for large BC particles (Moteki et al., 2012). In this way, the size distribution of the BC population will gradually change during transport and aging. In BC chemistry models, wet removal is 3 times more efficient in removing BC from the atmosphere compared to dry deposition processes (Bauer et al., 2013). BC particles deposited on the surfaces can finally be preserved in soils, snow and ice, water and sediments (Bisiaux et al., 2011; Lavanchy et al., 1999; Schmidt & Noack, 2000).

1.4 Impact of black carbon on climate

Despite its relatively low particle mass concentration, it has been argued that BC is the second most important atmospheric positive forcer after CO_2 (Jacobson, 2001; Bond et al., 2013), but a controversy around this notion exists (Feichter et al., 2003). The net effective BC radiative forcing was estimated to be around +1.1 W m^{-1} (Bond et al., 2013) and includes aerosol-radiation-clouds interactions with rapid adjustments. This value is, however, affected by an uncertainty of 90%, resulting in an ERF range between 0.17 and 2.1 W m^{-1} (Myhre et al., 2013). As introduced in Section 1.1.2, aerosols might influence climate in different ways. In the specific case of black carbon, it

directly interacts with the solar radiation, plays a role in the cloud formation and modifies the snow albedo; all these mechanism are addressed in detail in the following.

1.4.1 Black carbon-radiation interaction

On a local scale, absorbing aerosols decrease the downward solar radiation flux, resulting in a heating of the aerosol layer and a cooling of the lower atmospheric levels. At a larger scale, the atmospheric circulation redistributes the thermal energy, leading to a net warming effect (IPCC, 2013). An accurate quantification of RFari of BC requires knowledge of its mass concentration and size distribution, as well as its optical properties, which define its effective interaction with the solar radiation. A detailed description and formulation of all optical properties used and investigated in this work will be given in Section 2.1; here we report the most significant ones for the understanding of this section. The degree of light absorption by BC is measured as absorption coefficient; the latter is then influenced by other non-optical properties such as size, morphology, density and mixing state (Bond et al., 2013 and references therein). Generally, the degree of light absorption by BC is normalized by its mass concentration in order to derive an intensive property called mass absorption cross section (MAC), which is widely used during radiative calculations. High MAC values involve, considering the same mass concentration of absorbing material, a higher absorption and more positive RFari. The RFari of BC was estimated by two different studies, and quantified at +0.23 W m^{-2} (Myhre et al., 2013) and +0.51 W m^{-2} (Bond et al., 2013). Model estimates of RFari might suffer from some biases such as underestimation of the BC burden near the sources and overestimation in remote locations, as well as underestimation of the MAC (IPCC; 2013) due to inaccuracies in the emission database, removal mechanisms and mixing state. Such biases might lead to a significant underestimation of RFari. An additional uncertainty is added by the rapid adjustment of the aerosol-radiation interactions, which us more pronounced for absorbing aerosols compared to gases or non-absorbing aerosols. As a function of the height of BC relative to the altitude of cloud cover, BC modifies the atmospheric stability (Babu et al., 2011) and reduces the downward solar radiation reaching the surface. Assuming constant optical properties, size distribution and concentration of BC, RF varies as a function of the surface albedo; in fact the over a bright surface, such as snow-covered soils in the Arctic, deserts or clouds the positive forcing is enhanced (Zarzycki and Bond, 2010).

1.4.2 Black carbon-cloud interaction

The ability of BC to act as a cloud condensation nucleus depends on its size and mixing state. Smaller particles have a higher critical supersaturation meaning that larger diameters promote activation. Moteki et al. (2012) confirmed, from aircraft observations, that larger BC containing particles are more efficiently removed by wet deposition mechanisms. The mixing state also plays an important role, fresh and externally mixed BC was observed to be hardly activated due to their non-hygroscopic

behavior (Weingartner et al., 1997; Dusek et al., 2006). Condensation of hydrophilic/water soluble organic matter and inorganic salts on BC cores as well as coagulation increases the ability of BC to act as a CCN, thanks to a change in hygroscopicity (Dusek et al., 2006; Kuwata et al., 2009). From ambient observations, the activated fraction of BC in liquid clouds was found to be around 60% (Cozic et al., 2007). Despite quite homogeneous literature results, closure studies have insufficient robustness (number of ambient observations, metrics differences etc..) to confirm the contribution of coated BC to CCN (Bond et al., 2013). While BC might enhance the formation of clouds, it could also dissipate them. In fact, an absorbing aerosol component such as BC can lead to cloud dissipation (burn-off) and to a decrease in cloud cover (semi-direct effect; Koren et al., 2004; Tosca et al., 2015). Tosca et al. (2015) showed that cloud dynamics over western Africa are partly driven by aerosol. More specifically, biomass burning aerosol inhibits regional convection, limiting upward vertical motion reducing the upward moisture movement, thus inhibiting cumulus cloud formation. As a result, the convective suppression will lead to a rapid adjustment contributing to a positive effective radiative forcing.

Laboratory studies showed a wide spread of results in terms of the nucleation onset condition, with some of them failing to detect any ice nucleation under certain condition (Hoose and Möhler, 2012). Similarly, field measurements of ice nucleating particles have given contradicting results with regard to the role of BC under atmospheric conditions. For example, a study by Cozic et al. (2008b) found enrichment of black carbon in ice residuals measured at the high alpine research station Jungfraujoch, while another study by Kamphus et al. (2010) failed to find any enrichment and a third study by Chou et al. (2011) found no correlation of IN concentrations and black carbon mass at the same measurement site (Jungfraujoch). Furthermore, aerosol processing in the atmosphere can influence a particle's ice nucleating properties. The effect of the coating process on BC particles was never investigated in the atmosphere. However, smog chamber experiments showed a complete suppression of the ice nucleating activity of flame soot coated with organic carbon (Möhler, 2007). In contrast, Friedman et al. (2011) did not observe a substantial difference in the nucleating activity between coated and bare BC cores. Without adequate characterization of BC size and mixing, field measurements may infer correlations between IN components and heterogeneous ice nucleation but cannot distinguish the processes by which certain BC-containing particles partition in glaciated and mixed-phase clouds.

1.4.3 Snow darkening

Recent studies highlighted the role of black carbon in cryosphere perturbation. Fresh and pristine snow efficiently scatters the visible light; this high reflectivity might be reduced significantly by the deposition of light-absorbing material (Warren and Wiscombe, 1980; Warren, 1982; Chylek et al., 1983b). Due to multiple scattering, the enhanced optical path of light in the snowpack amplifies the absorption of impurities and the decrease of snow albedo. The climate effect induced by absorbing material, such as BC, in snow is not due to the initial albedo decrease but due to following rapid adjustment. The initial albedo decrease triggers a chain reaction involving the acceleration of aging

process of snow (Clarke and Noone, 1985; Hansen and Nazarenko, 2004; Warren, 1984). Increased solar heating fastens the growth of snow crystals, which leads to a further albedo reduction and consequent melting (Warren and Wiscombe, 1980). Additionally, during melting the hydrophobic BC is left at the surface (Conway et al., 1996; Doherty et al., 2010), increasing the surface burden and promoting the snow melting (Flanner et al., 2007). On longer time scale, months to years, this effect might lead to an earlier exposure of underling low-albedo surfaces such as tundra or ice. Simulations confirmed that deposited BC darkens snow and ice surface and can modify the local radiative balance with potential consequences on climate at a larger scale (Doherty et al., 2010; Flanner et al., 2007a; Painter et al., 2013). At high altitude locations such as the Himalaya and Tibetan Plateau, BC deposited on snow surfaces is identified as one significant potential contributing factor that may lead to increased snow melt (Flanner et al., 2007b; Xu et al., 2009a; Yasunari et al., 2010; Ginot et al., 2014). Although this impact still remains to be quantified with precision high concentrations of BC and brown carbon have been shown to be correlated with surface darkening and temperature increase in the Himalayan region (Ramanathan et al., 2007; Ming et al., 2008). In the Arctic, the albedo reduction and the related fast aging (Flanner et al., 2009), leads to a perturbation of the summertime surface energy budget of 3 W m^{-2} (McConnell et al., 2007). The best estimate of climate forcing from black carbon deposition on snow and sea ice in the industrial era is +0.13 W m^2, with 90% uncertainty (Bond et al., 2013). Estimates of present-day global-mean radiative forcing from BC in snow suggest that this mechanism has greater efficacy than any other anthropogenic agent (Hansen et al., 2005; Flanner et al., 2007b). The role of black carbon in the melting of glaciers is still highly uncertain. Few measurements of glacial black carbon content exist, and studies of the impact on glacial snow melt have not sufficiently accounted for natural impurities such as soil dust and algae or for the difficulty in modeling regions of mountainous terrain.

1.4.4 Effects of mixing on optical properties of black carbon

As shortly described in section 1.3.1, coagulation and condensation of organic and inorganic material on black carbon particles occur during its atmospheric lifetime. Such processes lead to internal mixing of BC with other atmospheric material. During daytime, the dominant mixing process is condensation, while during nighttime coagulation becomes dominant (Riemer et al., 2010). Organic matter such as hydrocarbon-like organic aerosol and sulfate material are associated with BC and represent the main components constituting the coating matter (Hara et al., 2003; Okada et al., 2005; Adachi and Buseck, 2008; Massoli et al., 2015). Due to its insolubility, BC is always distinctly separated from other material in an internally mixed cluster. Typically, freshly emitted BC particles have a lacy ramified structure, where acquisition of coating induces a shrinking of the core into a compact nearly spherical shape (China et al., 2015). Although sulfate does not absorb light and organic matter, e.g., brown carbon, slightly absorbs visible light (Ackerman and Toon, 1981), the presence of a coating on BC cores can change dramatically the radiative properties of internally mixed particles compared to freshly emitted BC (Bond and Bergstrom, 2006). Soot compaction alters as well the scattering and absorption cross section of BC-containing particles (Liu et al., 2008; Scarnato et al., 2013). Aging

mainly affects the intensive BC optical properties and thus the mass absorption-cross section. A MAC's variation may introduce a significant change in the single scattering albedo (SSA), which is used to qualify the warming or cooling effect of an aerosol. The influence of aging on MAC is still widely investigated because the SSA is the aerosol property most relevant to the balance between negative and positive forcing. A wide variety of MAC values determined from measurements is available in the literature. It was found that freshly generated and uncoated BC has a MAC of 7.5 ± 1.2 g^{-1} m^2 at 550 nm (Bond and Bergstrom, 2006). MAC values from atmospheric measurements have a range spanning between 4 and 23 m^2 g^{-1} at 637 nm , depending on emission type (Liousse et al., 1993a; Schwarz et al., 2008b; Reche et al., 2011; Genberg et al., 2013), distance from source (Cozic et al., 2008b; Liu et al., 2010; Laborde et al., 2013; Pandolfi et al., 2014) and instrumental approach (Slowik et al., 2007a; Knox et al., 2009). MAC enhancement values from atmospheric measurements show high variability and need to be measured before and after thermal removal of the coating. Laboratory experiment showed that the enhancement is proportional to the coating thickness (Slowik et al., 2007a) and can reach values up to 2 (Shiraiwa et al., 2010). A MAC enhancement, with respect to a bare BC core, between 1.2 and 1.6 was observed close to emission (Knox et al., 2009) and 1.4 for biomass burning plumes (Lack et al., 2012). However, not all field observations agree on the enhancement amplitude; for urban plumes a weak absorption enhancement of 6% was observed (Cappa et al., 2012). Cappa et al. (2012) hypothesized that the low values of enhancement are caused by BC inclusions at the edge of the sampled particles. The MAC of BC can also be simulated using optical models. For BC containing particles the geometry of the mixing is a fundamental parameter to account for. Usually, a core-shell configuration is assumed. Some frequently used mixing rules are: i) volume mixing, in which refractive indices are mixed proportional to the substance volume, ii) Bruggeman or Maxwell-Garnet effective medium approximations (Heller, 1965), or iii) the dynamic effective medium approximation (Chylek et al., 1996).

Table 1.1. Simulated mass absorption cross-section (MAC) at 550 nm and radiative forcing (RF) of BC assuming different mixing rules. Enhancement is defined as the ratio of MAC or RF of the selected mixing geometry to the uncoated sphere case. MAC values are calculated using the following refractive indexes 1.85–0.71i for soot (Bond and Bergstrom, 2006), 1.49 for organic matter (Moffet and Prather, 2009), and 1.43 for sulfate (Hess et al., 1998). Adapted from Adachi et al. (2010).

Mixing rules						
	Uncoated sphere	Uncoated aggregate	Maxwell-Garnett effective medium	Volume mixing	Core-shell	3D tomography
						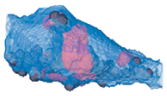
MAC [m^2 g^{-1}]	6.44	6.14	13.3	13.6	12.0	9.90
MAC enhancement	1.00	0.95	2.06	2.11	1.86	1.54
RF [W m^{-2}]	0.35	0.36	0.63	0.63	0.53	0.5
RF enhancement	1.00	1.03	1.80	1.80	1.51	1.43

The assumption of different mixing rules leads to a different absorption and absorption enhancement: Adachi et al. (2010) calculated a MAC at 550 nm for uncoated BC spheres of 6.4 m^2g^{-1}, where the MAC increases for volume mixing, core shell and Maxwell-Garnet effective medium approximation up to 13.6 m^2g^{-1}. A MAC of 9.9 m^2 g^{-1} was attributed to a more realistic BC particle (Table 1.1). The absorption enhancement is also sensitive to the chosen geometric configuration; compared to a bare spherical BC the enhancement might vary between 1.5 and 2.1. Radiative transfer models require the scattering and absorption coefficient. Atmospheric models convert modeled mass concentrations of BC into optical coefficients using the MAC and the mass scattering cross-section (MSC). An accurate estimation of these intensive properties is crucial in order to estimate a proper radiative forcing of aerosol, including BC. This approach make the radiative forcing estimation quite sensitive to MAC values and thus to the assumed mixing geometry. The assumption of externally mixed BC would lead to a global radiative forcing of 0.35 W m^{-2}, while internal mixing leads to a doubling of the RF.

1.5 Variability of BC concentration in the European atmosphere

Due to the fact that this thesis investigates some life aspects of black carbon in Europe, a brief overview of emissions, concentrations and variability of European BC is given as following. According to Lamarque et al. (2010) and Bond et al. (2013), European BC is mostly emitted during combustion processes related to traffic. A second important contributor to European black carbon emissions is

found to be residential sources. Excluding traffic emission, residential and biomass burning emissions follow a well-defined seasonal trend. In fact, residential emissions contribute substantially to European BC emissions during winter and spring (Lukács et al., 2007). Otherwise, wildfires and agricultural fires emissions became more important in summer (Amiridis et al., 2009, 2010; Bovchaliuk et al., 2013). European anthropogenic emissions are characterized by a longitudinal trend, with higher emission rates in Western Europe compared to Eastern Europe. On the other hand, the biomass burning contribution to total BC emissions is definitely higher in Eastern Europe than in Western Europe, where traffic emissions largely dominate (Lamarque et al., 2010).

Besides emission inventories, the spatial variability of BC atmospheric concentration over European is constantly monitored and it has been investigated in several studies (Putaud et al., 2004; Yttri et al., 2007; Lanz et al., 2010; McMeeking et al., 2010; Reddington et al., 2013). European BC concentrations vary from high values recorded in Continental Europe (>1 μg m^{-3}) to lower values (<0.5 μg m^{-3}) in Nordic locations (Yttri et al., 2007). Long-range transport allows BC to be transported to remote European regions such as the Azores, the Finnish Arctic and Svalbard where averaged concentrations of less than 0.1 μg m^{-3} are usually observed (Pio et al., 2007; Eleftheriadis et al., 2009; Raatikainen et al., 2015a). The spatial variability of BC mass concentration over Europe is well represented in Figure 1.10.

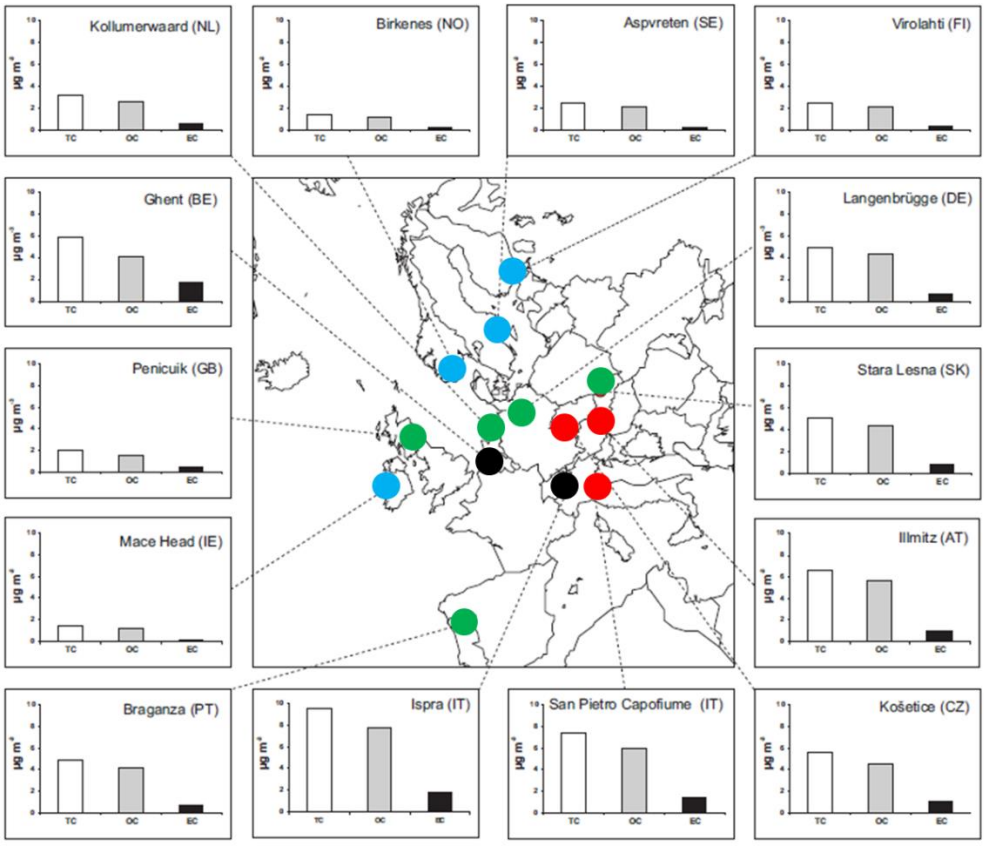

Figure 1.10 Annual mean total carbon (TC), organic carbon (OC) and elemental carbon (EC) concentrations (μg m^{-3}) at different European sites for the period July 2002-July 2003 (modified from Yttri et al., 2007). This one-year sampling campaign conducted within the European Monitoring and Evaluation Program (EMEP) included 12 European rural background sites and two urban background sites. Blue dots: BC concentration <0.5 μg m^{-3}; green dots: BC concentration between 0.5-1.0 μg m^{-3}; red dots: BC between 1.0-1.5 μg m^{-3}; black dots: BC concentration >1.5 μg m^{-3}.

Additionally to the spatial distribution, the BC concentrations in Europe often show a seasonal pattern. Generally, atmospheric BC is around twice more abundant in wintertime than in summertime at ground-level sites (Pio et al., 2007; Yttri et al., 2007) reflecting higher energy consumption and unfavorable meteorological conditions. A similar trend, but driven by efficient transport and scarce removal, is also observed for European Arctic locations such as Mount Zeppelin and Pallas, with maximum values in the late winter and minima during summer (Eleftheriadis et al., 2009; AMAP, 2015). In contrast, BC levels are two to ten times higher during summertime than during wintertime at mountain sites, reflecting the efficient upward transport from the polluted boundary layer during summertime (Lavanchy et al., 1999; Pio et al., 2007; Freney et al., 2011; Ripoll et al., 2014). Thus, BC and in general aerosol concentrations are quite variable over Europe. Knowledge of BC atmospheric concentration and its variability is of crucial importance to quantify the radiative forcing, but how well do models derive the BC concentrations and properties over Europe? The answer is: pretty badly. Reddington et al. (2013) compared black carbon mass and number concentrations and size distributions over Europe between global model and aircraft measurements. A substantial mismatch between observed and simulated BC size distribution was noted. Number concentrations predicted by the model were higher by a factor of 3.5-5.7 with a size mode diameter smaller of 40- 65 nm than observed. However this is only one example and many model-observation cross checks need to be done, it gives us an order of magnitude in quantifying the gap between measurements and simulations. Having precise and accurate measurements of the black carbon burden in Europe, and all over the globe, is a crucial step to correctly assess emission inventories and effects on climate.

1.6 Soot measuring techniques and nomenclature

In this section the nomenclature of soot is discussed, including a brief introduction of various BC-measuring techniques. The ones used in this study will be discussed in detail in the methodology chapters 2.2, 2.3 and 2.4.

One of the current limitations to a proper investigation of black carbon is the absence of a universally recognized technique to quantify BC in the atmosphere. BC measuring techniques are based on different physical and chemical BC properties. Therefore, the related nomenclature, specific for each measuring method, refers to a particular property of BC under certain conditions. The diversity of soot measuring technique generates ambiguity in the scientific literature. In this work we follow the terminology recommended by Petzold et al. (2013), shown in Figure 1.11 and summarized as following :

- *Soot is a useful qualitative description when referring to carbonaceous particles formed from incomplete combustion.*

- *Black carbon (BC) is a useful qualitative description when referring to light-absorbing carbonaceous substances in atmospheric aerosol; however, for quantitative applications the term requires clarification of the underlying determination.*
- *Mixed particles containing a BC fraction should be termed BC-containing particles.*
- *Elemental carbon (EC) should be used for data derived from methods that are specific to the carbon content of carbonaceous matter.*
- *Equivalent black carbon (eBC) should be used for data derived from optical absorption methods.*
- *Refractory black carbon (rBC) should be used for measurements derived from incandescence methods.*

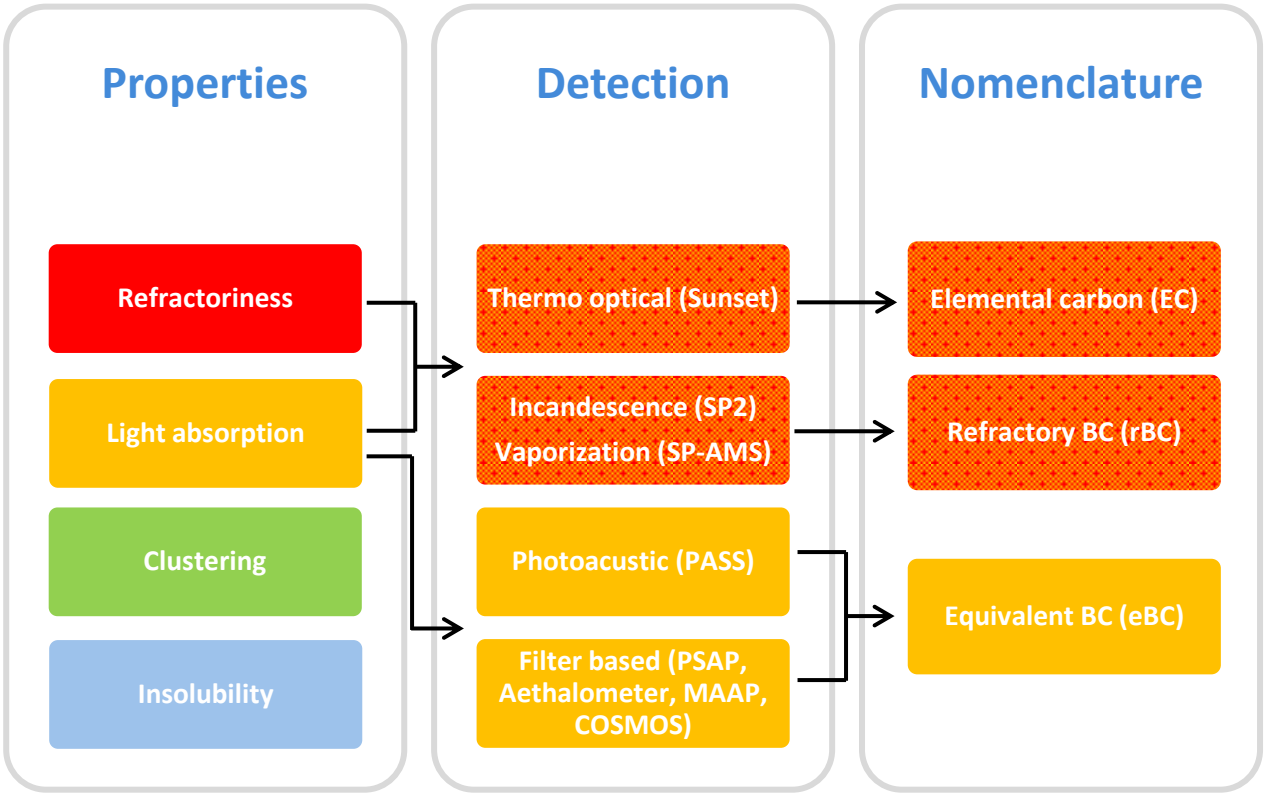

Figure 1.11. Schematic of black carbon nomenclature. Left column: the four main physical and chemical properties of black carbon; middle column: different detection techniques; right column: the recommended terminology used in this work.

1.6.1.1 Elemental carbon

Elemental carbon (EC) describes the carbonaceous fraction of particulate matter that is thermally stable in an inert atmosphere to temperatures near 4000 K and can only be gasified by oxidation starting at temperatures above 340 °C. It is assumed to be inert and nonvolatile under atmospheric conditions and insoluble in any solvent (Ogren and Charlson, 1983). The thermo-optical method

measures particulate matter having the properties described above. The particles are deposited on a filter, later analyzed under controlled temperature, RH and gaseous composition (Birch and Cary, 1996; Schmid et al., 2001). The method is based on the idea that OC and EC can be separated by heating to the point where OC has evaporated away and only EC remains. In reality, various artefacts (e.g. charring of OC, although corrected by optical measurement) exist and the research is still on-going (Schmid et al., 2001; Cavalli et al., 2010).

1.6.1.2 Equivalent black carbon

Mainly two methods are used to measure the BC light absorption: the filter based light transmission method and the photoacoustic method. Filter based photometers are relatively cheap, robust and plug and play instruments; for these reasons they are widely used for long-term measurements. Particles are continuously deposited onto a filter tape while a light beam is focused on the collecting spot. Along aerosol loading the light transmitted through the filter decreases due to increase in the optical path (Hansen et al., 1984). The absorption and thus the light-absorbing aerosol mass are assumed to be proportional to the light transmission decrease. A wide range of filter-based photometers are commercially available; despite some differences they are all based on this principle. More details about operating principles of filter based photometers will be discussed in Section 2.2. The second method available for the measurement of eBC is the photoacoustic method. The aerosol, heated up through the absorption of a pulsing laser light, heats the surrounding air and creates a sound wave that is measured by one or several microphones (Petzold and Niessner, 1996). The intensity of the sound wave is proportional to the amount of black carbon. The main advantage of the photoacoustic method is the independence of the measurement to the mixing state of BC (Lack et al., 2009). It is therefore commonly accepted as a benchmark for measuring aerosol absorption. However, its use and maintenance is rather demanding and it cannot really be used in long-term measurements. Both approaches yield an absorption coefficient, which is then converted to a black carbon mass concentration using a conversion factor called mass absorption cross-section (MAC). The MAC is an intensive optical property of BC, which describes its light absorption efficiency per mass. Thus, since this method does not allow measuring directly the mass concentration of BC, the derived mass concentration of BC is so called equivalent BC (eBC). Characterization and comparability of different absorption photometers and data treatments are under continuous development (Bond et al., 1999; Slowik et al., 2007; Collaud Coen et al., 2010; Ogren, 2010; Müller et al., 2011; Baumgardner et al., 2012; Kanaya et al., 2013).

1.6.1.3 Refractory black carbon

A third technique based on laser induced incandescence has been developed to measure the carbonaceous fraction of particulate matter that is insoluble and vaporizes only at temperatures near

4000 K (Moteki and Kondo, 2010). This carbonaceous fraction is called refractory black carbon (rBC). rBC is nowadays measured with the single particle soot photometer (SP2; Stephens et al., 2003) and the soot particles aerosol mass spectrometer (SP-AMS; Onasch et al., 2012). The mass of refractory black carbon is indirectly measured, in every single particle, from the amount of light emitted at the vaporization point of rBC, independently of the amount of non-refractory, internally mixed matter. In addition, the amount of non- and less refractory matter coating the rBC core can also be retrieved (Gao et al., 2007). All technical details and theoretic principles are described in Section 2.4.

1.7 Objectives of the present study

Black carbon represents a small fraction of the total aerosol, however, it considerably contributes to the total positive radiative forcing, playing a consistent role in climate warming. Due to its short lifetime in the atmosphere, an effective limitation of emissions would reduce the positive forcing after a relatively short period compared to the greenhouse gases. Unfortunately, a consistent number of uncertainties in its quantification and properties still exist: metrology, time-limited dataset, uncertainties on removal mechanisms and radiative forcing pathways. This work aims to contribute to a better understanding of black carbon cycle, contributing to some of the major questions:

- What is the spatial and seasonal variability of light absorption properties of black carbon in the European regions?
- How does aging during long-range transport modify light absorption by BC particles?
- Is black carbon an active seed for formation of glaciated clouds?

Chapter 3 focuses on the investigation of BC mass absorption cross-section over Europe, considering its spatial and seasonal variability. The work is based on data collected from observation platforms being part of the Aerosol, Clouds and Trace Gases Research InfraStructure (ACTRIS) over the last 10 years. Overall, the dataset reports more than 34 years of measurements from the different stations, spread around Europe, and allows to investigate the study of the seasonal cycle of MAC and its spatial variability.

Chapter 4 addresses the issue of optical properties of BC but further away from emission sources. Despite is short lifetime, BC can be transported over long distances and, as explained in the previous sections, undergo changes of its optical properties through coating by non-absorbing material on its surface. The climate impact of short-lived pollutants and methane in the Arctic (CLIMSLIP) project aims to investigate the presence and the effects of BC during the Arctic haze in the late winter. We wanted to answer to three main challenges raised by the Summary for Policy-makers of the Arctic Climate Issues 2015 report: qualify the BC measuring techniques in the Arctic, understand the physical properties of BC after the long-range transport and provide the optical parameters needed for an accurate RF assessment in the Arctic.

Finally, in chapter 5, we treat the largely unknown processes of BC-clouds interaction and address the uncertainties and contradictions found in the scientific literature concerning the role of BC as ice nuclei. During the cloud and aerosol characterization experiment (CLACE) at the high altitude site Jungfraujoch in winter 2013, we investigated the role of BC in glaciated clouds formation using the

SP2 technique, which allowed for the first time to selectively investigating the activated fraction of BC as a function of its diameter and coating thickness.
Within all the projects, filter based photometers were used to quantify the absorption coefficient of BC. Even though these instruments are affected by several instrumental artifacts, they are suitable for long-term measurements as in the case of the ACTRIS network. The use of the freshly developed single particle soot photometer allows us to investigate more in detail the microphysical properties of BC such as the size distribution and mixing state. Thanks to its features, it is possible to investigate, without major interferences, the size distribution and coating thickness of rBC containing particles. Such properties are fundamental to derive the optical properties required for radiative forcing estimates.

2 Methodology

In this chapter the main BC-measuring techniques adopted in this work are discussed. Before, a brief description of the main optical properties of the aerosol and how they are determined is given as following.

2.1 Parametrization of the aerosol optical properties

Atmospheric aerosols can both absorb and diffuse light. Light and aerosol interaction is simulated using Mie theory, this is due to aerosol size and light wavelength. The combination makes geometric optics and Rayleigh scattering not suitable for investigation of optical properties in the visible spectrum of aerosol having a submicron dimeter (<1µm). Mie (1908) based on Maxwell's equations, parametrized the relationship between microphysical properties of a particle and the absorbed and scattered light. The differential scattering cross section of a particle with a diameter D_p is defined as the amount of scattered light per unit of time into a unit solid angle for unit of incident light. The scattering cross section (C_{sp}) is then calculated integrating over the whole surface of a unit sphere. This feature is used in most part of instruments for determination of optical size of particles including the SP2. Practically, the scattering cross section quantifies the energy scattered ($\tilde{F}_{sp}$) in all direction relative to the amount of the incident intensity of light (F_0):

$$C_{sp} = \frac{\tilde{F}_{sp}}{F_0} \tag{2.1}$$

The absorption cross section (C_{ap}) quantifies the energy absorbed ($\tilde{F}_{ap}$) from all direction relative to F_0:

$$C_{ap} = \frac{\tilde{F}_{ap}}{F_0} \tag{2.2}$$

where the intensity is measured in unit of W m^{-2} and cross section in unit of m^2. According to the conservation of energy, the combined effect of scattering in all direction and absorption of light is referred as extinction; extinction cross section (C_{ep}) is defined as:

$$C_{ep} = C_{sp} + C_{ap} \tag{2.3}$$

Scattering and absorption are governed by a few key parameters as wavelength of incident radiation (λ) and diameter of the particle (D_p), assuming its sphericity. Particle size and light wavelength are parametrized with a dimensionless parameter called the size parameter (χ):

$$\chi = \frac{\pi D_p}{\lambda} \tag{2.4}$$

The size parameter is used to define the optical domains; the Mie domain is defined by χ values close to unity, when the wavelength of incident light is similar to the size of the particle.
An additional key factor is the refractive index (*RI*), which describes the optical properties of the particles relative to the surrounding medium as function of λ. RI is a complex number composed by a real part (n) describing scattering and an imaginary part (k) related to absorption. In atmospheric science, RI is normalized on the refractive index of air, which is for instance equal to unit

$$RI(\lambda) = n + ik \tag{2.5}$$

RI is used in this work for SP2 measurements as will be described in Section 2.4.1 and in optical simulation (see Section 4). Literature values of n and k for flame produced carbon have a large variability and vary between 1.2-2 and 0.3-1, but a RI = 1.95 + i0.79 at 550 nm is representative of amorphous absorbing carbon heated at 750°C and having little to no void fraction (Bond and Bergstrom, 2006 and references therein). For comparison, always at 550 nm, the RI of organic carbon mixed with sulfate is 1.55 + i0.001 (Bond et al., 2006a). All photometers used in this work are based on Mie theory, but properties that are more often used in atmospheric science are the scattering (σ_{sp}), absorption (σ_{ap}) and extinction (σ_{ep}) coefficients quantified in invers meters (m^{-1}). They are functions of the particle size, refractive index, the wavelength of the incident light and are defined as

$$\sigma_{sp}(\lambda) = \int_0^{D_p^{max}} \frac{3}{2\rho_p D_p} Q_{sp}(RI, \chi) n_M(D_p) dD_p \tag{2.6}$$

$$\sigma_{ap}(\lambda) = \int_0^{D_p^{max}} \frac{3}{2\rho_p D_p} Q_{ap}(RI, \chi) n_M(D_p) dD_p \tag{2.7}$$

$$\sigma_{ep}(\lambda) = \int_0^{D_p^{max}} \frac{3}{2\rho_p D_p} Q_{ep}(RI, \chi) n_M(D_p) dD_p \tag{2.8}$$

where n_M defines the aerosol mass distribution, ρ_p is the density of the particle. Q represents the scattering, absorption or extinction efficiencies. The latter are defined as the ratio of the scattering, absorption or extinction cross section over the geometric cross section area (C_G) of the particle.

$$Q_{sp} = \frac{C_{sp}}{C_G} = 4\,\frac{C_{sp}}{\pi D_p^2} \tag{2.9}$$

$$Q_{ap} = \frac{C_{ap}}{C_G} = 4\,\frac{C_{ap}}{\pi\, D_p^2} \tag{2.10}$$

$$Q_{ep} = \frac{C_{ep}}{C_G} = 4\,\frac{C_{ep}}{\pi\, D_p^2} \tag{2.11}$$

Equation 2.6 might be rewritten as

$$\sigma_{sp}(\lambda) = \int_0^{D_p^{max}} \mathrm{E}_{sp}\left(D_p RI, RI\right) n_M\left(D_p\right) dD_p \tag{2.12}$$

where E_{sp} is the mass scattering efficiency:

$$E_{sp}\left(D_p, \lambda, RI\right) = \frac{3}{2\rho_p D_p} Q_{sp}(RI, \chi) \tag{2.13}$$

Mass absorption and extinction efficiency are then defined as

$$E_{ap}\left(D_p, \lambda, RI\right) = \frac{3}{2\rho_p D_p} Q_{ap}(RI, \chi) \tag{2.14}$$

$$E_{sp}\left(D_p, \lambda, RI\right) = \frac{3}{2\rho_p D_p} Q_{ap}(RI, \chi) \tag{2.15}$$

More practically, the scattering coefficient describes a medium containing many scattering particles at a concertation described as a volume density (ρ) quantified in inverse cubic meters. σ_{sp} is essentially the cross-sectional area per unit of volume of the medium. Absorption and extinction coefficients are defined in the same way.

$$\sigma_{sp}(\lambda)\,[m^{-1}] = \rho\,[m^{-3}] * C_{sp}[m^2] \tag{2.16}$$

$$\sigma_{ap}(\lambda)[m^{-1}] = \rho\,[m^{-3}] * C_{ap}\,[m^2] \tag{2.17}$$

$$\sigma_{ep}(\lambda)[m^{-1}] = \rho\,[m^{-3}] * C_{ep}\,[m^2] \tag{2.18}$$

These optical coefficients are extensive properties meaning that are proportional to the amount of aerosol, and can be instrumentally measured. E_{sp}, E_{ap} and E_{ep}, can also be calculated from observations and are commonly called mass scattering cross-section (*MSC*), mass absorption cross-section (*MAC*) and mass extinction cross-section (*MEC*) respectively. They represent the amount of scattered, absorbed or attenuated light for unit of mass of non-absorbing, absorbing or total aerosol matter:

$$\boldsymbol{MSC}\ (\lambda)\ [\boldsymbol{m^2/g}] = \frac{\boldsymbol{\sigma_{sp}}\ (\lambda)[\boldsymbol{Mm^{-1}}]}{\boldsymbol{m_{sp}}\ [\mu\boldsymbol{g/m^3}]} \tag{2.19}$$

$$\boldsymbol{MAC}\ (\lambda)\ [\boldsymbol{m^2/g}] = \frac{\boldsymbol{\sigma_{ap}}\ (\lambda)[\boldsymbol{Mm^{-1}}]}{\boldsymbol{m_{ap}}\ [\mu\boldsymbol{g/m^3}]} \tag{2.20}$$

$$\boldsymbol{MEC}\ (\lambda)\ [\boldsymbol{m^2/g}] = \frac{\boldsymbol{\sigma_{ep}}\ (\lambda)[\boldsymbol{Mm^{-1}}]}{\boldsymbol{m_{tot}}\ [\mu\boldsymbol{g/m^3}]} \tag{2.21}$$

m_{sp} designates the mass concertation of non-absorbing matter, m_{ap} the mass concertation of absorbing matter and m_{tot} the total mass of the aerosol. Despite all these formulas seem far from reality, they are the base on which all the filter based photometers and other instruments relay on. Filter based photometers measure absorption coefficients, which is then converted into equivalent black carbon mass concertation (m_{eBC}) adapting Equation 2.20 using a proper MAC value.

$$\boldsymbol{m_{eBC}}\ [\mu\boldsymbol{g/m^3}] = \frac{\boldsymbol{\sigma_{ap}}\ (\lambda)[\boldsymbol{Mm^{-1}}]}{\boldsymbol{MAC}\ (\lambda)\ [\boldsymbol{m^2/g}]} \tag{2.22}$$

The MAC quantifies the absorption-mass behavior of every material showing absorption. In the visible spectrum, MAC values of BC containing particles range between 5-20 $m^2\ g^{-1}$ (Liousse et al., 1993b), while MAC values of organic matter and mineral dust are typically smaller than unity (Hoffer et al., 2006; Utry et al., 2014). Other intensive properties, not influenced by the aerosol quantity, may be calculated merging σ_{sp} and σ_{ap}. The single scattering albedo (*SSA*) defines the dominant light-aerosol interaction, and is defined as:

$$\boldsymbol{SSA}\ (\lambda) = \frac{\boldsymbol{\sigma_{sp}}(\lambda)}{\boldsymbol{\sigma_{ext}}(\lambda)} = \frac{\boldsymbol{\sigma_{sp}}(\lambda)}{\boldsymbol{\sigma_{sp}}(\lambda) + \boldsymbol{\sigma_{ap}}(\lambda)} \tag{2.23}$$

SSA is a key property to define, in climate science, the scattering and absorbing behavior of and aerosol, and its cooling or warming role in the atmosphere. Air masses with high fraction of black carbon will be characterized by a low single scattering albedo and warming behavior (Seinfeld and Pandis, 2006). Otherwise, values close to unity are specific of an air masses composed by non-absorbing matter that would lead to a cooling. *SSA* can be derived from measurements as

nephelometers and filter based photometers or calculated from Mie theory knowing the refractive index of the aerosol material. Together with *SSA*, the asymmetry parameter (*g*) is used during radiative forcing estimation to express the distribution of scattered intensity. It is calculated from the scattering phase function (*P*), which gives the angular distribution of light intensity scattered at a certain λ.

$$g\ (\lambda) = \frac{1}{2}\int_0^{\pi} cos\ \theta\ P(\theta)\ sin\theta\ d\theta \tag{2.24}$$

The ½ factor ensures that g = 1 for light completely scattered in the forward direction while for light totally scattered in the backward direction g = -1. For sub-micrometric particles, the Henyey-Greenstain approximation (Wiscombe and Grams, 1976) might be used to calculate g from the hemispheric back scattering ratio (b), which is defined as:

$$b\ (\lambda) = \frac{\int_{\pi/2}^{\pi} P(\theta)\ sin\theta\ d\theta}{\int_0^{\pi} P(\theta)\ sin\theta\ d\theta} = \frac{\sigma_{sp}\ (\lambda)}{\sigma_{bsp}\ (\lambda)} \tag{2.25}$$

Where σ_{bsp} is the back scattering coefficient and can be calculated or instrumentally observed with the nephelometer. Thus, following Wiscombe and Grams (1976) and from measured σ_{sp} and σ_{bsp}

$$g\ (\lambda) = -7.1438989 * b^3 + 7.464439 * b^2 - 3.9656 * b + 0.9893 \tag{2.26}$$

Another intensive optical property widely used in atmospheric science is the aerosol optical depth (*AOD*). AOD parameterizes the extinction of the radiation traversing a path length, in this case the atmosphere, as function of the amount of aerosol matter along the path. The path thickness is defined by the altitude (z), thus AOD can be expressed as

$$AOD\ (z,\lambda) = \int_{z_0}^{z_{TOA}} \sigma_{ep}\ (z,\lambda)dz \tag{2.27}$$

Commonly, extinction coefficient is integrated between the altitude bounding the top of the atmosphere (z_{TOA}) and any altitude between z_{TOA} and the ground. AOD is dimensionless and can vary between 1 for extremely polluted events and smaller than 0.1 for remote and clean environment (Hoffmann et al., 2009) and it's measured with remote sensing as ground and satellite based radiometers (Seinfeld and Pandis, 2006). All the previous described optical properties vary as function as the wavelength of radiation; this wavelength dependence is described by the Ångström exponent (α; Ångström, 1929). Concerning extinction, α is calculated as:

$$\alpha_{\lambda 1,\lambda 2} = -\frac{log\left(\sigma_{ep}^{\lambda 1}/\sigma_{ep}^{\lambda 2}\right)}{log(\lambda_1/\lambda_2)} \tag{2.28}$$

Because scattering, absorption, and extinction depend on wavelength and on the diameter of particles, the Ångström exponent, calculated between two different wavelengths (λ_1, λ_2), depends also on the size distribution of the aerosol population. Generally, low values indicate a large mode, while small values are found for smaller sizes (Kaufman, 1993; Gobbi et al., 2007 and reference therein). Absorption Ångström exponent depends also on the composition of the particles, and is used to identify different sources of black carbon emissions(Sandradewi et al., 2008; Lack and Langridge, 2013).

2.2 Attenuation photometry

The most adopted filter based photometers for online long-term measurements of eBC are the aethalometer (Hansen et al., 1984), the multi angle absorption photometer (MAAP; Petzold and Schönlinner, 2004), the particle soot absorption photometer (PSAP; Bond et al., 1999) and the continuous soot monitoring system (COSMOS; Miyazaki et al., 2008). All these instruments have been used during this work. A short resume of theory and operating principles of these instruments is given here while a more detailed description of data treatment will be given in Section 3. Despite some conceptual building differences, all the photometers measure the change in transmittance of the incoming radiation through a filter as particles are deposited on the loading spot. The amount of aerosol is thus inversely proportional to transmittance or, directly proportional to attenuation. Attenuation (*ATN*) is defined as

$$ATN\ (\lambda) = ln\left(\frac{I_0}{I}\right) \tag{2.29}$$

where I_0 is the intensity of light trespassing a pristine portion of the filter, while I is the intensity of light passing through the loaded filter. As consequence, absorption coefficient at certain wavelength is proportional to the variation of attenuation measured at different time

$$\sigma_{ap}(\lambda) \propto \frac{ATN\ (\lambda, t + \Delta t) - ATN\ (\lambda, t + \Delta t)}{\Delta t} \tag{2.30}$$

Despite the fact that the technique is widely used, the use of a filter is not an ideal method and introduces consistent biases in the absorption coefficient quantification. According to theory, positive variation in attenuation (ΔATN) should be proportional to the amount of absorbing matter imbedded into the filter (Figure 2.1a). In reality, the optical properties of the filter, the presence of non-absorbing particles and the loading of absorbing particles influence the ATN measurements. The filter matrix has its characteristic optical depth, multiple scattering occurs within the filter fibers, so that the intensity of light is consistently attenuated after passing through the pristine filter layer (Figure 2.1b). The light intensity used as reference is not then the intensity of the source (I_{source}), but the already attenuated signal due to filter presence (I_0). Moreover, the loading of non-absorbing material

leads to an increase of the backscattered light, which induces an apparent greater reflectance of the filter (Figure 2.1c). The percentage of scattering that is interpreted as absorption is anyway negligible and quantified as less than 5% (Bond et al., 1999; Weingartner et al., 2003). This effect depends on the asymmetry parameter of the deposited particles which is function of particle diameter and wavelength of incident light. Presence of non-absorbing particles became important when absorbing matter is also loaded on the filter and is parametrized in function of the single scattering albedo (Collaud Coen et al., 2010).

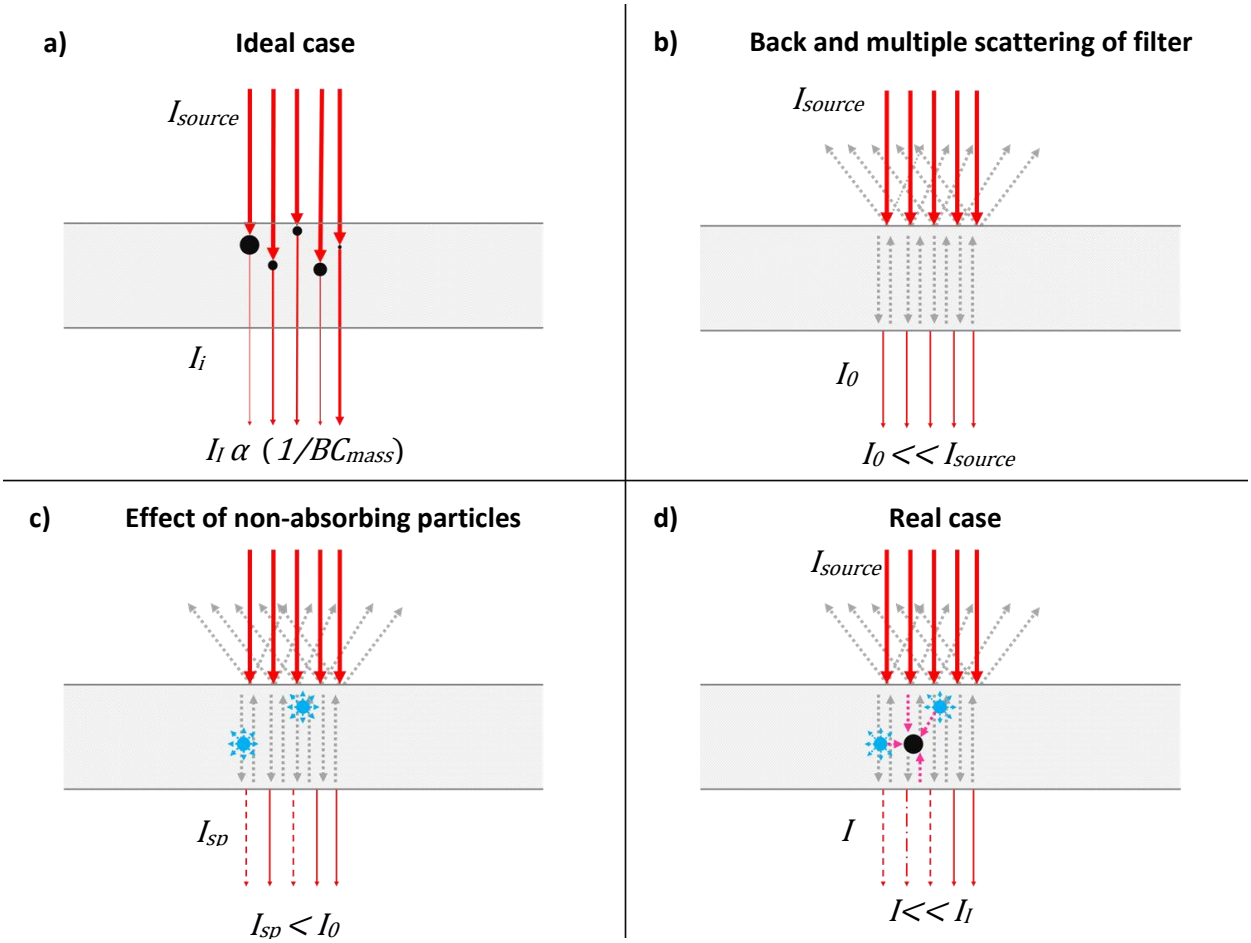

Figure 2.1. Schematic of optical processes occurring in a filter matrix. a) Ideal case where the variation of ATN is proportional only to the amount of absorbing material loaded on the filter. b) Effective back scattering and multiple scattering (grey dotted lines) of the filter matrix in absence of loaded aerosol. c) Presence of non-absorbing particles (blue spheres), induce additional scattering (dotted blue lines). Back scattering can be misunderstood as absorption and lead to a decrease in transmitted light. d) Filter loaded with absorbing and scattering aerosol. Multiple scattering induced by filter matrix and non-absorbing particles increases the optical path of light enhancing the probability of light absorption (pink dotted line) by absorbing particles (black spheres).

Scattering due to particles increases the optical path of light leading to higher probability of encountering and embedded absorbing particle (Figure 2.1d). Multiple scattering of the filter matrix leads to similar effect. The increase of optical path leads to overestimation of absorption. This absorption enhancement can be partially compensated by the “shadowing” effect, which is induced

by the loading of absorbing aerosol on the filter. The lately loaded particles will absorb light, reducing the optical path for a loaded filter, decreasing the probability of absorption by previously loaded particles. Particle size determines the vertical distribution of particles in the filter; large particles have smaller mobility and are more likely to be embedded in the superficial layer of the filter (Nakayama et al., 2010). Under this condition back scattering and absorption is dominated by superficial non-absorbing and absorbing particles.

The optical effects just described take place in almost every filter based photometers, inducing a non-linearity in the attenuation-BC relationship. Several correction procedures have been developed for the Aethalometer (Weingartner et al., 2003; Collaud Coen et al., 2010), the PSAP (Bond et al., 1999; Ogren, 2010), the MAAP (Petzold and Schönlinner, 2004; Petzold et al., 2005) and the COSMOS (Miyazaki et al., 2008; Nakayama et al., 2010). All of them are described in more detail in Section 3.2.3.2 and 4.2.2.2. After correction, absorption coefficient might be converted in equivalent black carbon mass concentration as in Equation 2.22 using an adequate mass absorption cross-section. Investigation of mass absorption cross-section variability is presented in this work in Section 3.

2.2.1 Uncertainties

The variability of the absorption coefficient derived by seven MAAPs, four Aethalometers (7-wavelengths model) and six PSAPs (3- wavelength model) was investigated by (Müller et al., 2011). The so called unit-to-unit variability is defined by the coefficient of variation, which is the ratio of the standard deviation and the average absorption coefficient. It was calculated as the slope of the fitting line in the scatter plots showed in Figure 2.2.

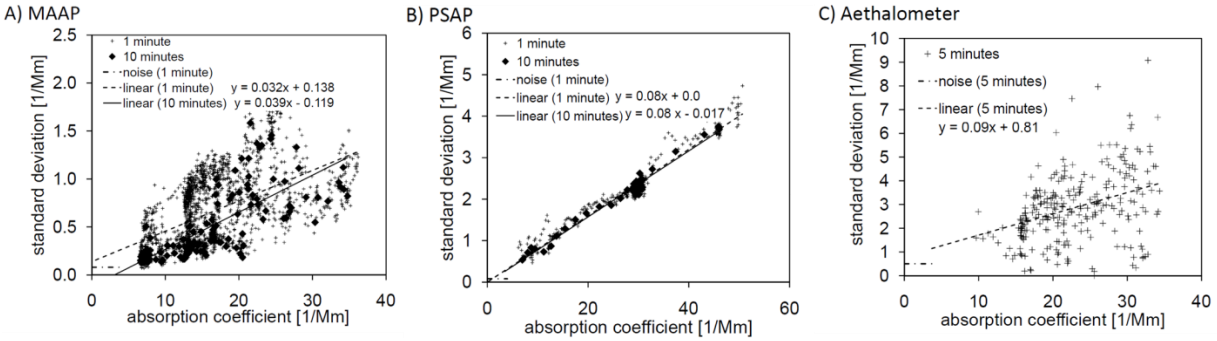

Figure 2.2 Unit-to-unit variability (standard deviation of several instruments) versus absorption coefficient for (a) MAAP at 637 nm; (b) PSAP at 530 nm; (c) Aethalometer at 660 nm. PSAP and MAAP data are shown for the highest time resolution of one minute and for an averaging time of ten minutes. Aethalometer data are shown for an averaging time of 5 min. The noise level is indicated as horizontal line. From Müller et al. (2011).

Considering only simultaneous measurements performed with a set of identical instruments, the most common causes of unit-to-unit variability are systematic errors as inaccuracy in sample flow and in the loading spot area. The unit-to-unit variability of MAAP was of 3% while variability among PSAP was quantified in 8%. Despite the fact that the Aethalometer showed a coefficient of variation of 9%,

its spread (Figure 2.2C) was considerably larger than PSAP. The high instrumental noise of the aethalometer partly explains the spread. Noise in the aethalometer was quantified in 0.3-0.8 Mm^{-1}, while MAAP and PSAP showed noise of 0.22 and 0.08 Mm^{-1} respectively. The two values reported for aethalometer refer to instruments having a small spot area, high sensitivity for clean environments, and a large area, extended range for polluted environments. Systematic errors, with same origin affect COSMOS results by 12% (Miyazaki et al., 2008). The same author found that absorption coefficients measured at 590 nm by two COSMOS perfectly agree (difference <1%). Due to the scarcities of instruments used in his study, this variability might not reflect the real unit-to-unit variability.

2.3 Thermal optical technique

The thermal-optical technique allows determining the total carbonaceous matter concertation, more simply called total carbon (TC). Thanks to the different thermal stability of organic and elemental carbon, these two fractions may be separated using a thermal sequence. This technique requires thus an instrument (OC/EC analyzer) and a thermal protocol. Nowadays all the OC/EC analyzer are able to operate different thermal protocols. In this section of the thesis the principle of OC/EC analyzer and the thermal protocol adopted in the European Supersites for Atmospheric Aerosol Research (EUSAAR) project will be described.

2.3.1 The OC/EC analyzer

A large variety of OC/EC analyzers are commercially available and are all based on the thermal differentiation between EC and OC. A general schematic of the Sunset OC/EC analyzer (Birch and Cary, 1996; Sunset Laboratories Inc.) is given in Figure 2.3 .

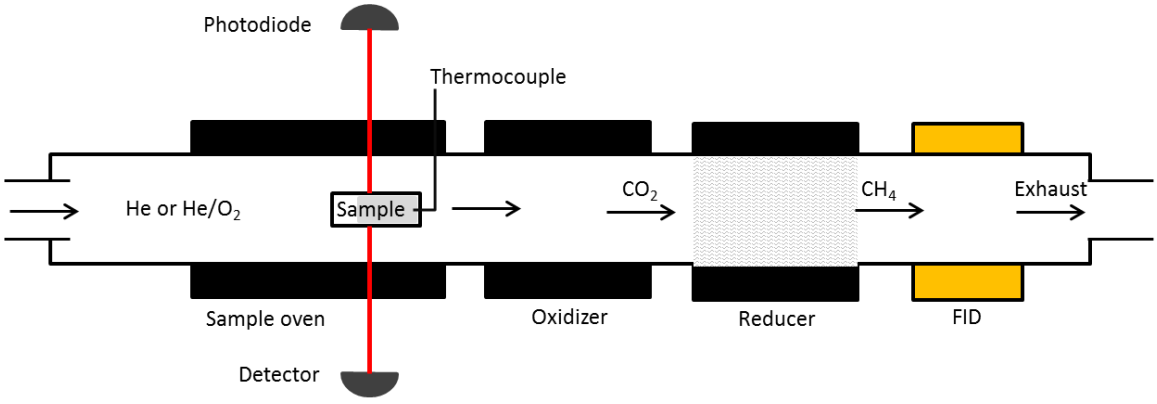

Figure 2.3 Schematic of the thermal-optical OC/EC analyser.

The instrument is composed by three different ovens, in each of them a different chemical reaction and vaporization of carbonaceous fraction take place. The sample, quartz filter, is placed in the first hoven, where undergoes an increase of temperature by regular steps. The temperature ramp and the helium atmosphere induce a selective vaporization of the organic carbon. The resultants vapors are oxidized to CO_2 in a second oven (oxidizer) and then reduced to methane (CH_4) in a third Nickel hoven (reducer). The quantity of produced methane is monitored by a flame ionization detector (FID). The concentration of detected CH_4 is proportional to the OC mass deposited on the sample filter. The second step take place in an oxidant atmosphere (He-O_2), with generally higher temperatures compared to the OC analysis. EC is burned and volatilized to CO_2 and then methane, which is then quantified in the FID. The sum of OC and EC is defined as TC. Usually, different OC/EC analyzers agree on the measured TC, while consistent discrepancies might be observed during OC and EC mass speciation (e.g. Schmid et al., 2001; Park et al., 2002; ten Brink et al., 2004; Park et al., 2005). During the thermal analysis, a fraction of OC pyrolyses under the inert atmosphere phase in pyrolytic carbon (PC), which is thermally refractory and might be erroneously identify as elemental carbon. In order to correct the charring/pyrolysis effect aforementioned, the reflectance or the transmittance of the filter is monitored; such techniques are respectively called thermal-optical reflectance (TOR) and thermal-optical transmittance (TOT) methods (Dod et al., 1978; Johnson and Huntzicker, 1979). Both optical correction methods, TOT and TOR, are based on the thermal stability of EC, which does not volatilize up to very high temperature without oxygen presence. During charring, reflectance or transmittance of filter decreases, indicating the formation of pyrolysed absorbing carbon. When PC evolves, the sample reflectance or transmittance increases to reach its original value, as the charred OC has been removed. The OC:EC split point is usually defined in the aforementioned manner (Karanasiou et al., 2015).

2.3.2 Existing thermal procedures and discrepancies

The correct quantification of TC, OC and EC strongly relays on the thermal procedures adopted in the various ovens of the analyzer. Nowadays, there are three main thermal protocols: the NIOSH (also called “Quartz”; Birch and Cary, 1996; Peterson and Richards, 2002), IMPROVE_A (Chow et al., 1993) and EUSAAR-2 (Cavalli et al., 2010). These protocols differ in the carrier gas composition, temperature steps and time stamps for EC and OC determination and optical correction. Here are reported the final conclusions of a recent overview on EC and OC measurements elaborated by Karanasiou et al. (2015). All thermal protocols are comparable for TC concentration, but significant discrepancies are observed concerning EC. The comparability of EC and OC depends on aerosol composition: a) samples influenced by biomass burning show higher discrepancies; b) presence of brow carbon amplifies the charring effects; c) positive sampling artifact due to the adsorption of gaseous organics onto the filter is likely to be significant at remote sites; d) carbonate carbon interference might be negligible for fine aerosol, but it can be significant for coarse OC or EC concentrations.

2.3.3 The EUSAAR-2 protocol

Within this work we have been using OC and EC data derived using the EUSAAR-2 protocol (Cavalli et al., 2010). The EUSAAR-2 was developed for the European regional background sites (EMEP network) with the aim to improve the accuracy of the discrimination between EC and OC. This was achieved implementing four different technical parameters. First, pyrolysis was reduced favoring the volatilization of OC. Negative and positive bias in EC determination, due to early evolution of light absorbing carbon during the and incomplete evolution of OC during the inert mode were minimized. Finally, the uncertainty due to the position of the OC/EC split point on the FID response profile by introducing multiple desorption steps in the oxidation-mode. The complete evolution of temperatures can be find in (Cavalli et al., 2010). However many improvements have been introduced, a certain variability of TC, OC and EC determined by different laboratories using the EUSAAR-2 protocol still exists. EC relative standard deviation between laboratories is of 20% for ambient samples (EUSAAR, 2010), which decreases to 17% for reference material samples (EUSAAR, 2011). The reproducibility relative standard deviation for EC/TC ratio is of 10-29% for ambient samples (ACTRIS, 2011). Discrepancies may be related to correction of the laser drift with temperature and/or to the inaccuracy of the real temperature experienced by the filter compared to the theory (Karanasiou et al., 2015). Due to such discrepancies, we applied harmonization coefficients (Cavalli et al., in preparation), which take into accounts the laboratory-specific errors, to calculate the most possible accurate EC mass concertation, see Section 3.2.3.4.

2.4 Laser induced incandescence

An absorbing particle, as black carbon, can be brought to incandescence under light irradiation. Depending on the composition and thus refractoriness, particles reach their or vaporization point at a temperature up to 4000 K. At this temperature, the absorbing particle acts like a black body emitting an incandescence thermal radiation. The single particle soot photometer (SP2) is based on this principle; the theory on which the instrument is based on is described in detail by Stephens et al. (2003); Moteki and Kondo (2007, 2010) and briefly summarized here. The time dependent intensity of the incandescence signal $I_{LII}(t)$ measured by the SP2 can be expressed as

$$I_{LII}(t) = \int_{\Delta\Omega} \int_{0}^{\infty} C_{emit}\,(v, m, \lambda, shape, \alpha, \beta, \gamma, \Omega, t)\; P_e(T(t), \lambda)\; \eta(\lambda)\; d\lambda d\Omega \tag{2.31}$$

where C_{emit} is the emission cross section of the thermal emission; η describes the transmissivity of the detectors; Ω is the direction of the radiation's propagation; υ is the particle volume; m is the complex refractive index; α, β, γ, are the Euler particle rotation angles of the particle and P_e represents the Plank function in unit of radiance. The latter describes energy of the electromagnetic radiation emitted by a black body as function of temperature and wavelength. According to Rytov's theorem (Rytov 1953), the emission cross section of a body is equal to its absorption cross section

$$C_{emit}(v, m, \lambda, shape, \alpha, \beta, \gamma, \Omega, t) = C_{ap}(v, m, \lambda, shape, \alpha, \beta, \gamma, -\Omega, t) \quad (2.32)$$

where (-Ω) indicates the opposite direction compared to the emitted thermal radiation. Then, the intensity of laser induced incandescence can be expressed as function of absorption efficiency (Q_{ap}) and mass equivalent diameter (D_m)

$$I_{LII}(t) = \frac{\pi}{4} D_m^2(t) \int_{\Delta\Omega} \int_0^{\infty} Q_{ap}(v, m, \lambda, shape, \alpha, \beta, \gamma, \Omega, t) P_e(T(t), \lambda) \eta(\lambda) d\lambda d\Omega \quad (2.33)$$

where the mass equivalent diameter is calculated from the mass of the particle considering the true particle density. As a result, the intensity of the light emitted is proportional to the volume of the BC core. Light scattering and laser induced incandescence are two physical phenomena used in the SP2 to detect and characterize the particles physical properties.

2.4.1 The single particle soot photometer

The SP2 is based on the laser induced incandescence; it implies the use of a high fluence laser. The SP2 is equipped with a continuous intra-cavity Nd-YAG laser with a wavelength of 1064 nm. The schematic of SP2 concept is shown in Figure 2.4. According to the soot terminology suggested by Petzold et al. (2013), the black carbon detected via laser induced incandesce will be called refractory black carbon (rBC).

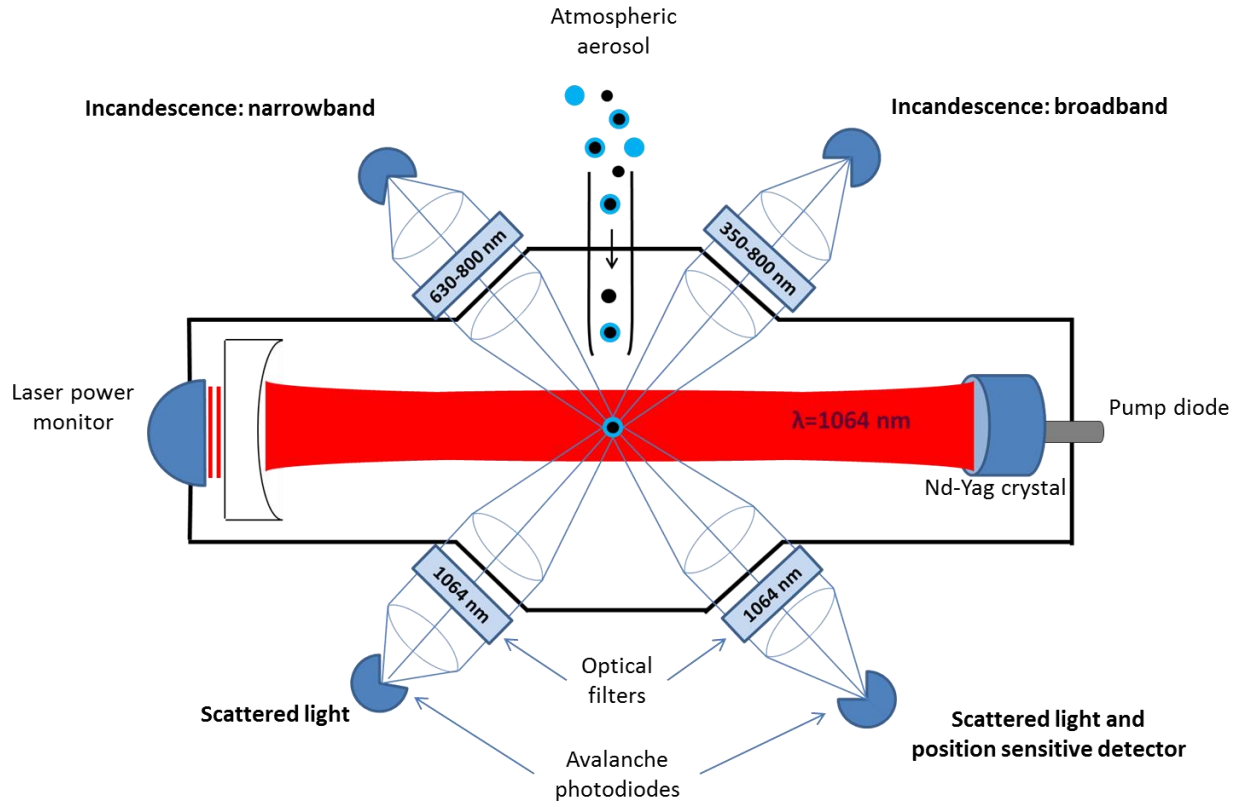

Figure 2.4. Schematic of the measurement chamber of the SP2.

2.4.1.1 BC mass determination

The intensity of the thermal radiation emitted at the rBC vaporization point is a linear function of the refractory volume of the particle. The refractoriness and light absorption characteristics are the properties ono which the SP2 detection is based on. Since rBc is the main atmospheric component remaining at temperature higher than 4000 K, the technique is selective for refractory black carbon and does not undergo major interferences by non-refractory absorbing materials. At particle incandescence, the emitted radiation is measured as function of time by two photomultiplier tubes. The two detectors have different bandpass with and are referred as “broadband” and “narrowband” detectors (Figure 2.4). The SP2 approach ensures 100% counting efficiency of the rBC particles above 0.3-1 fg of mass. The mass of every rBC particle is derived from the measured I_{LII} of signal, which is proportional to the height of the incandescence peak signal ($PkHt_{Inc}$). The relationship between $PkHt_{Inc}$ and particle mass is parametrized within the calibration procedure, performed measuring $PkHt_{Inc}$ when sampling pure rBC particles with a certain mobility diameter or mass (Figure 2.5). In case of mobility-diameter based calibration, the effective density of the calibration material used is needed to infer the rBC mass from the selected mobility diameter. The effective density of several common SP2 calibration materials was determined by Gysel et al. (2011). An alternative way of performing an incandescence calibration is to introduce particles with a known BC mass into the SP2.

In this case, the density of the calibration material is not needed. Both calibration methods were used throughout this work. During atmospheric measurements, the diameter of rBC particles is not directly measured, but derived from the particles mass using a material density of 1800 kg m^{-3}. Despite the advantages, the SP2 technique has one main disadvantage: the size range. Depending on theSP2 model the size detection range might vary. Considering the SP2s used here and belonging to four different institutes, the lower limit of detection of the different SP2s varied between 80 and 90 nm of mass equivalent diameter. The higher size limit of detection was more variable and dependent on the analogic amplification of the signal, making it ranging between 340 and 550 nm of mass equivalent diameter. The amplification of signal is chosen by the SP2 user and manually adjusted on each detector board. Usually this cut off leads to a total mass underestimation of 30-40% of the total ambient BC mass concentration. The missing mass is estimated from the lognormal fit, outside the boundary of range of detection, of the size distribution(Section 4;Schwarz et al., 2006; Kondo et al., 2011; Reddington et al., 2013).

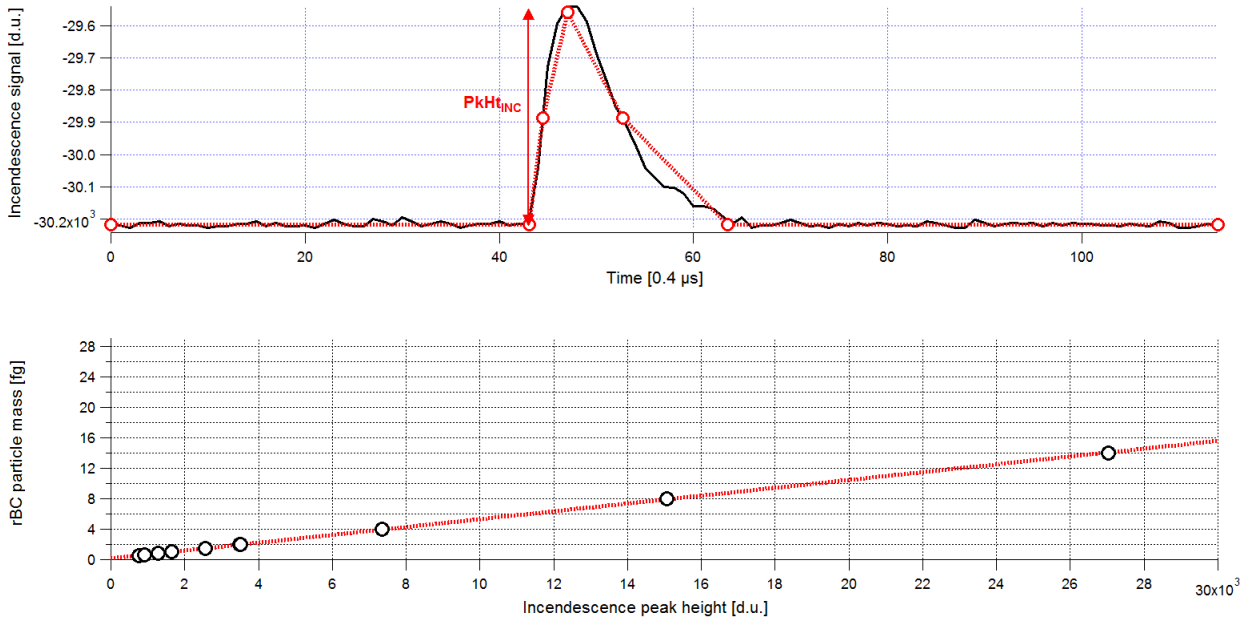

Figure 2.5. Top: incandescence raw signal of rBC particle (black line). Fitting curve (dashed red line) used to extrapolate the incandescence peak height. Bottom: calibration curve of the incandescence signal done using monodisperse fullerene soot.

2.4.1.2 Optical sizing of BC-free particles

With the SP2 is also possible to infer the optical diameter of BC-free particles from the measured differential scattering cross section of the single particle ($C_{sp\text{-}meas}(D_p\ ,\ RI)$). Assuming a spherical or a coated-sphere geometry and refractive index, Mie theory can be used to interpret the SP2 raw signal of the light scattering detectors. The time evolution of the diffused light by the particle moving through the laser beam is monitored by two avalanches photodiodes (Figure 2.4). The scattering

signal $S(t)$ is proportional to the incident laser intensity and to the scattering cross section and depends on the distribution of the laser intensity ($I_L(t)$), which is adjusted to be Gaussian (Figure 2.6). Due to the absence of light absorption, the scattering cross section of a rBC-free particle remains stable throughout the measurement time (Figure 2.6). As a consequence, the $S(t)$ is proportional only to the intensity of the laser light at which the particle is exposed and assumes a Gaussian shape peaking with an amplitude of $PkHt_{scatt}$ at the laser center (Figure 2.6).

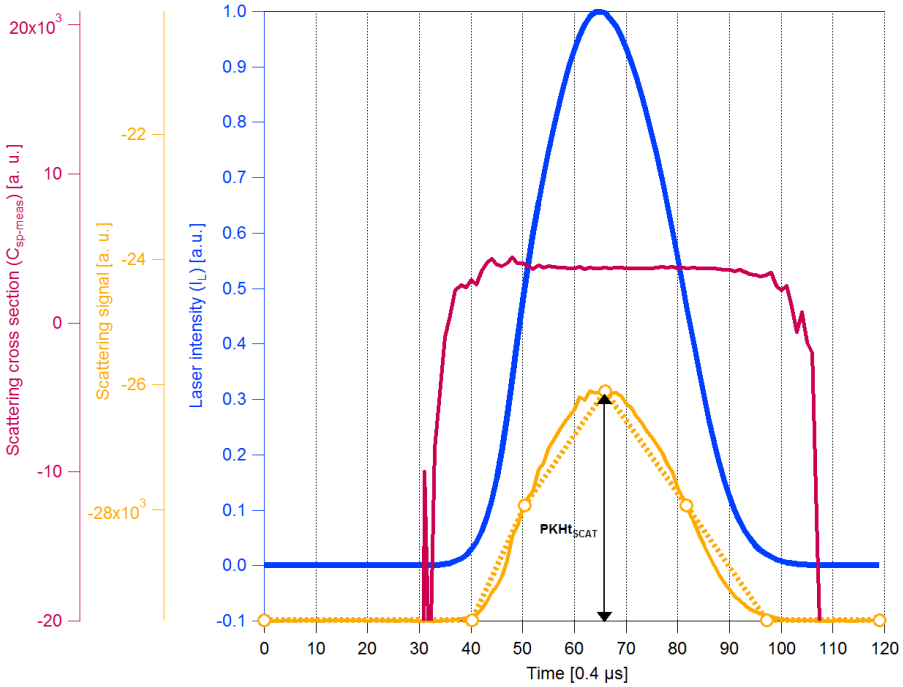

Figure 2.6. Example of scattering signal (orange line) and scattering cross section (red line) for a rBC-free particle. Dotted orange line represents the Gaussian fit applied to determine the scattering peak height for every particle. Blue line represents the distribution of laser beam intensity. All properties are expressed in arbitrary unit [a. u.].

The calibration of the scattering signal (i.e. the relationship between $PkHt_{scat}$ and particle's differential scattering cross section) is determined by measuring $PkHt_{scat}$ when sampling non-absorbing, spherical particles of a known diameter (D_p) and refractive index (RI) (e.g. RI=1.59 for polystyrene latex spheres, PSL). Mie theory and the homogeneous spherical particle model are then used in order to calculate the relationship between D_p and the corresponding differential scattering cross section ($C_{sp\text{-}Mie}(D_p; m)$). The scattering signal calibration factor CF_{scat} is then calculated, using the SP2 measurement of the integrated laser intensity ($I_{monitor}$ from the YAG monitor, Fig. 3.1) and the following equation:

$$CF_{scat} = \frac{PkHt_{scat}}{I_{monitor}\, C_{sp-Mie}(D_p, RI)} \tag{2.34}$$

The scattering signal calibration might be performed calculating the average of the scattering signal calibration factors measured for different particle diameters in order to gain in accuracy. Alternatively, the calibration factors might be calculated for a single particle diameter varying the

intensity of the laser beam ($I_{monitor}$). In this work both approaches have been used and the purely scattering (rBC-free) particles (as defined by the SP2) are assumed to be homogeneous spherical particles. The measured particle scattering cross section $C_{meas}(D_p;m)$ is then derived from the measurement of $PkHt_{scat}$, using the calibration factor and the following equation:

$$C_{sp-meas}(D_p, RI) = \frac{PkHt_{scat}}{I_{monitor}\, CF_{scat}} \tag{2.35}$$

The particle's optical diameter is then inferred from $C_{sp\text{-}meas}(Dp; RI)$, using Mie theory, and assuming a certain refractive index.

2.4.1.3 Optical sizing of BC-containing particles

Due to light absorption, the scattering cross section of an rBC-containing particle decreases during its path in the laser beam. This is due to the evaporation of non-rBC components (the coating) and the core vaporization at incandescence. As direct consequence, the maximum of the scattering signal does not occur in the middle of the laser beam as shown in Figure 2.6. Therefore, the scattering signal is still proportional to the original size of the particle only prior to light absorption by the rBC core and thermal transfer from the rBC core to the non-refractory coating. $PkHt_{scat}$ can be calculated by fitting the edge of the scattering signal (leading edge only fit, LEO) to a Gaussian function representing the laser intensity profile (Figure 2.7). This reconstructed signal represents the scattering signal that would have been measured if the particle had not evaporated. Its maximum represents $PkHt_{scat}$ as for the homogeneous spherical particle case and can be used to retrieve $C_{sp\text{-}meas}$ of the whole coated BC particle according to Equation 2.35.

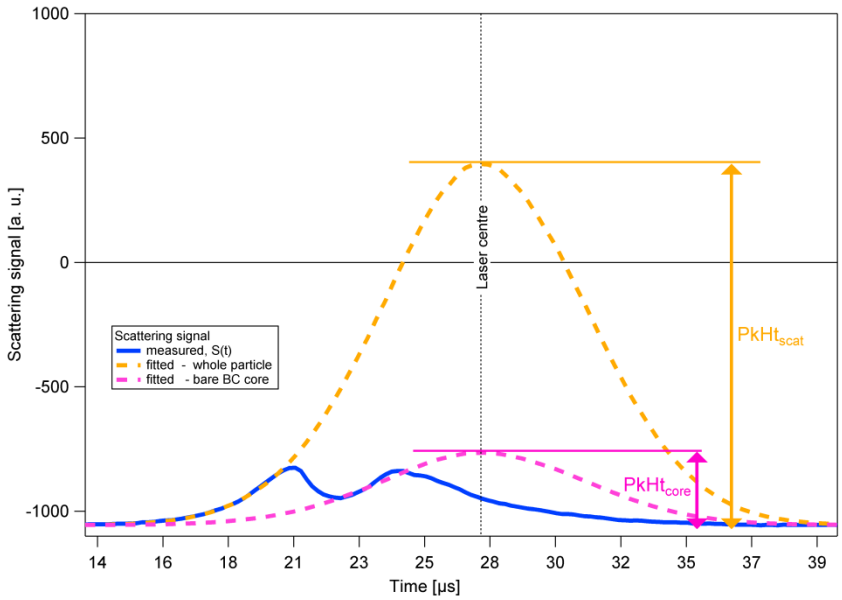

Figure 2.7. Example of reconstructed peak height for rBC-containing particle. Raw scattering signal in blue. Reconstructed scattering signal for the core-shell particle (PkHt$_{scat}$; dashed orange line) and the rBC core (PkHt$_{core}$; dashed pink line). The shape assumed for the Gaussian represent the shape of the laser and the maximum is kept at the centre of the laser beam while the Gaussian is scaled up and down until the signal is fitted up to the point of coating evaporation. All properties are expressed in arbitrary unit [a. u.]. Source: Laborde et al, (2012b))

The optical diameter of the rBC core can be calculated from the re constructed scattering signal, at the point in time when the BC core only remains but has the scattering signal which would have been measured if the bare rBC core was measured and if it was not evaporating. $PkHt_{core}$ is thus obtained from the maximum of the reconstructed signal (Figure 2.7, dashed pink line). $C_{sp\text{-}meas}$ is again calculated from the reconstructed $PkHt_{core}$ using Equation 2.35. The homogeneous sphere Mie model is then used to retrieve the optical diameter of the BC core Dc from it. The refractive index of the rBC core has also to be assumed. In terms of coating, this approach allows quantifying, indirectly, the thickness of the coating. Coating thickness is thus defined:

$$\boldsymbol{Coating\ thickness} = \frac{\boldsymbol{D_p - D_{core}}}{\boldsymbol{2}} \tag{2.36}$$

Where D_p and D_{core} are the diameter of the whole particle and the rBC-core calculated using the approach described before.

2.4.1.4 Unit-to-unit variability

During the SOOT11 campaign held at the AIDA chamber, 6 SP2s coming from different research institutes were compared (Laborde et al., 2012b). Number and mass size distribution agreed within

5% and 10% respectively. Larger discrepancy was observed for rBC cores lighter than 1fg. Discrepancies in rBC mass concentration are usually introduced by difference in accuracy of the mass calibration (Laborde et al., 2012b). The number size distribution of BC-free particles agreed within 15%. Furthermore the 6 instruments quantified coating thickness within 17%. The accuracy of the SP2's mass concentration measurement depends on the calibration material, thus a fullerene soot standard is recommended during calibration operations. Laborde et al. (2012b) showed that the SP2 provides accurate and reproducible data, but also that high data quality is only achieved if the SP2 is carefully tuned and calibrated.

2.5 BC measuring techniques: how do they compare?

The comparability of black carbon mass concentrations derived using different techniques has been widely investigated during the last decade. Due the fact that there is not yet a universally recognized technique to quantify the BC mass, is extremely important to understand how the different instruments compare and quantify the possible difference. In this section we summarize the results from the most recent laboratory and ambient intercomparison experiments.

Attenuation photometers: absorption coefficients

An intercomparison study of absorption coefficients determined by photometers as the Aethalometer, MAAP and PSAP during ambient and smog chamber experiments was conducted by Müller et al. (2011). After correction of instrumental artifacts like multiple scattering and loading effects for aethalometer (Weingartner et al., 2003) and PSAP (Bond et al., 1999), the comparability of absorption coefficients at 637 nm was calculated as the relative sensitivity of PSAP and Aethalometer results over the MAAP outputs. The MAAP was considered to be the reference instrument. PSAP and aethalometer agree with MAAP within 5% and 60% respectively. Aethalometer results might be implemented with more accurate correction of multiple scattering correction as suggested by Collaud Coen et al. (2010). Absorption coefficient measured with COSMOS and PSAP at a wavelength of 565 nm to agrees within 3% in urban locations (Miyazaki et al., 2008). A difference of 50% between COSMOS and aethalometer absorption coefficients was also observed (Miyazaki et al., 2008). Due to the fact that the aethalometer was not corrected for multiple scattering and loading effect, the COSMOS-aethalometer relative sensitivity reported there represents more a rough calibration factor C as in Weingartner et al. (2003).

Attenuation photometers: equivalent BC

Relative precision of attenuation photometers is also reported as function of equivalent BC mass concentration. Healy et al., (2012) found that Aethalometer eBC was underestimated compared to

eBC derived from MAAP. In this case MACs of 6.6 $m^2 g^{-1}$ at 637 and 5.08 $m^2 g^{-1}$ at 950 nm (calculated in situ) were used for MAAP and Aethalometer respectively. Discrepancies between the aethalometer and MAAP datasets are expected to be mostly due to inaccuracy in the corrections used to account for scattering effects (Petzold and Schönlinner, 2004). Kanaya et al. (2013) investigated the comparability of the COSMOS and MAAP in remote and urban locations. In both cases the correlation between the two techniques was high, but the eBC concentration derived with the MAAP was systematically overestimated by 60% and 80% in remote and urban location respectively. The author identified the cause in the conditions/protocols of the thermal optical BC determinations used for calibration of each optical instrument. The same author suggested that the manufacturer's MAC of MAAP should be increased.

Equivalent and refractory BC

The work of Slowik et al. (2007b) assessed the comparability of rBC derived from the SP2 and eBC calculated from the MAAP. eBC was calculated from MAAP using a MAC value of 6.6 $m^2 g^{-1}$at 637 nm. The study showed that for uncoated soot particles, the eBC mass measured by the MAAP was higher by ∼50% respect to the rBC mass detected using the SP2. A thick anthracene coating did not affect the readings provided by the SP2 instruments but increased the reading of the MAAP instrument by an additional ∼20%.

Elemental carbon and equivalent BC

Healy et al., (2012) compared the elemental carbon mass concentration measured with thermal-optical technique (Sunset EC/OC analyzer with NIOSH protocol) with equivalent black carbon concentration measured using filter based photometers like the Aethalometer and MAAP. Observed mass concentrations of EC and eBC were found to agree within 21%. Differences between MAAP eBC and thermal/optical EC mass concentrations may be partly due to the presence of light-absorbing brown carbon (Reisinger et al., 2008). Another possibility is that the NIOSH protocol may be inappropriate for the analysis of wood burning aerosols, leading to an underestimation of EC (Sciare et al., 2003, 2008). Kondo et al. (2011) compared EC and eBC mass concentration observed with laser induce incandesce technique (SP2) and filter based photometer (COSMOS) at six different locations of Asia. In that work a MAC of 5.4 $m^2 g^{-1}$ was used for COSMOS measurements. This intercomparison demonstrated that TOT and COSMOS agreed within less than 10%.

Elemental carbon and refractory black carbon

Comparability of EC and rBC mass concentration was investigated during winter in Paris by Laborde et al. (2013). rBC was determined via laser induced incandescence using the SP2 instrument. EC concentrations were measured with a thermal-optical Sunset OCEC analyzer (Bae et al., 2004)

applying the EUSAAR-2 protocol (Cavalli et al., 2010). The two instruments agreed within 5%. This indicates that the SP2 covers a relevant part of BC size distribution. Similar result was find by Kondo et al. (2011), which compared EC from thermal-optical transmittance technique (TOT; Birch and Cary 1996; Lim and Turpin 2002; Kondo et al. 2006) with rBC from the SP2. The intercomparison demonstrated that these two techniques agree within 10% in six different locations over Asia.

Overall comparability and recommendations

The laser induced incandescence technique avoids interferences by non-refractory coatings. Additionally the limited detection range does not seem to represent a consistent issue as revealed by the good agreement with EC measured by thermal-optical approach. EC measuring techniques show wide variability as function of the chosen thermal protocol and charring correction. Nevertheless, good inter-laboratory comparability of EC mass determined with the EUSAAR-2 protocol by different users is ensured. Discrepancies of absorption coefficients measured with different filter based absorption photometers might reach 60%. A proper correction procedure is essential to achieve a good instrumental precision. Comparability of eBC greatly depends on the assumed MAC used during the conversion from absorption coefficient to eBC mass concentration. In the COSMOS, the thermal treatment ensures volatilization of non-refractory matter reducing its direct absorption or absorption enhancement. As consequence the COSMOS is less affected by MAC variability compared to other attenuation photometers. Excluding COSMOS, in order to calculate an accurate eBC concentration using filter based photometers, MAC must be determined in situ. This calculation might be performed using reference techniques as laser induced incandescence or well calibrated thermal-optical technique. Despite the improvements in the relative precision, BC measuring techniques might differ with different degrees as function of chemical composition of the aerosol population.

3 A European aerosol phenomenology-5: climatology of black carbon optical properties at 9 regional background sites across Europe

M.Zanatta[1,2], F. Cavalli[3], M. Gysel[2], N. Bukowiecki[2], T. Müller[4], E. Weingartner[2,x], H. Areskoug[5], M. Fiebig[6], N. Mihalopoulos[7], G. Kouvarakis[7], D. Beddows[8], R.M. Harrison[8,9], J.P. Putaud[3], G. Spindler[4], A. Wiedensohler[4], A. Alastuey[10], M. Pandolfi[10], K. Sellegri[11], E. Swietlicki[12], U. Baltensperger[2] and P. Laj[1]

[1] *Univ. Grenoble Alpes/CNRS, Laboratoire de Glaciologie et Géophysique de l'Environnement, Grenoble, France*

[2] *Laboratory of Atmospheric Chemistry, Paul Scherrer Institute, Villigen, CH-5232, Switzerland*

[3] *European Commission, Joint Research Centre (JRC), Institute for Environment and Sustainability (IES), Air and Climate Unit, via E. Fermi 2749, 21027 Ispra VA, Italy*

[4] *Leibniz Institute for Tropospheric Research, Permoserstrasse 15, 04318 Leipzig, Germany*

[5] *Atmospheric Science Unit, Department of Environmental Science and Analytical Chemistry (ACES), Stockholm University, Svante Arrhenius väg 8, SE-11418 Stockholm, Sweden*

[6] *NILU, Norwegian Institute for Air Research, Kjeller, Norway*

[7] *Environmental Chemistry Processes Laboratory, Dept. of Chemistry, University of Crete, 71003 Heraklion Crete, Greece*

[8] *National Centre for Atmospheric Science, School of Geography, Earth and Environmental Sciences, University of*
Birmingham, B15 2TT, UK

[9] *Department of Environmental Sciences / Center of Excellence in Environmental Studies, King Abdulaziz University, PO Box 80203, Jeddah, 21589, Saudi Arabia*

[10] *Institute of Environmental Assessment and Water Research (IDAEA-CSIC), Barcelona, Spain*

[11] *Laboratoire de Meteorologie Physique, UMR 6016, CNRS/University of Clermont-Ferrand, Clermont-Ferrand, France*

[12] *Division of Nuclear Physics, Department of Physics, Lund University, Lund, Sweden*

[x] *now at Institute for Aerosol and Sensor Technology, University of Applied Sciences, Windisch, Switzerland*

Submitted at Atmospheric Environment

This work has been developed within the ACTRIS (**Aerosols, Clouds, and Trace gases Research InfraStructure**) European project and is developed in the working package 11 (Improving the accuracy of aerosol light absorption determinations) which aims, among other goals, to reduce uncertainty in the retrieval of the multiple wavelength optical properties of predominant aerosol light absorbers. Black carbon (BC) is widely investigated due to the positive radiative forcing caused by its absorbing behavior, which can be quantified as mass absorption cross section (MAC).The MAC is defined as absorption power for unit of mass and can be calculated from absorption coefficient and elemental carbon (EC) measurements. The MAC is used in radiative forcing calculation and equivalent BC ground measurements. Inaccuracy in MAC value might potentially lead to wrong radiative forcing estimation or to biased ambient monitoring. In the reviewed literature the MAC shows a large spread of values from 4 $m^2 g^{-1}$ to 23 $m^2 g^{-1}$ at a wavelength of 637 nm, which is the same wavelength adopted in the present study. This variability might be due to physical aerosol characteristics as the size, morphology and mixing or to instrumental errors. This works aims to assess the MAC variability induced only by atmospheric processes minimizing the systematic errors of measured absorption coefficient and BC concentration.

The MAC was calculated from absorption coefficients and elemental carbon mass concentrations measured at nine EUSAAR background supersites for a minimum period of one year. Absorption coefficients, derived from different photometer types were corrected for instrumental biases and harmonized on a reference technique following the recommendation of EUSAAR2007 workshop (Müller et al., 2011). EC mass concentration was mainly determined with the EUSAAR-2 protocol, inter-laboratory and inter-protocol discrepancies where assessed in the companion paper (Cavalli et al., in preparation) and rectified here. Finally the spatial and seasonal variability of European MAC at a wavelength of 637 nm was investigated.

A discrete spatial homogeneity of considered optical properties was observed, as a consequence, an overall MAC mean of 9.5 ± 1.9 $m^2 g^{-1}$ at 637 nm might be representative of BC at European background locations. The dominance of a seasonal MAC cycle, culminating in summer, suggested a change in mixing degree of BC with other species. The hypothesis is realistic and was confirmed by the mutual increase of MAC the relative mass fraction of non-absorbing matter (NAM) as sulfate, nitrate and organic matter. During summer the high NAM concentration and photochemistry promote internal mixing hennaing BC light absorption.

Abstract: A reliable assessment of the optical properties of atmospheric black carbon is of crucial importance for an accurate estimation of radiative forcing. In this study we investigated the spatio-temporal variability of the mass absorption cross-section (MAC) of atmospheric black carbon, defined as light absorption coefficient (σ_{ap}) divided by elemental carbon mass concentration (m_{EC}). σ_{ap} and m_{EC} have been monitored at supersites of the ACTRIS network for a minimum period of one year. The 9 rural background sites considered in this study cover southern Scandinavia, central Europe and the Mediterranean. σ_{ap} was determined using filter based absorption photometers and m_{EC} using a thermal-optical technique. Homogeneity of the data-set was ensured by harmonization of all involved methods and instruments during extensive intercomparison exercises at the European Center for Aerosol Calibration (ECAC). Annual mean values of σ_{ap} at a wavelength of 637 nm vary between 0.66–1.3 Mm^{-1} in southern Scandinavia, 3.7–11 Mm^{-1} in Central Europe and the British Isles, and 2.3–2.8 Mm^{-1} in the Mediterranean. Annual mean values of m_{EC} vary between 0.084–0.23 $\mu g\ m^{-3}$ in southern Scandinavia, 0.28–1.1 in Central Europe and the British Isles, and 0.22–0.26 in the Mediterranean. Both σ_{ap} and m_{EC} in southern Scandinavia and Central Europe have a distinct seasonality with maxima during the cold season and minima during summer, whereas at the Mediterranean sites an opposite trend was observed. Annual mean MAC values were quite similar across all sites and the seasonal variability was small at most sites such that a MAC value of 10.0 $m^2\ g^{-1}$ (geometric standard deviation = 1.33) at a wavelength of 637 nm can be considered to be representative of the mixed boundary layer at European background sites. This is a rather small spatial variability compared to the variability of values in previous literature, indicating that the harmonization efforts resulted in substantially increased precision of the reported MAC. However, absolute uncertainties of the reported MAC values remain as high as ± 30–70% due to the lack of appropriate reference method and calibration material.

The mass ratio between elemental carbon and non-light-absorbing matter was used as a proxy for the degree of internal mixing of the BC-containing particles, to assess the influence of mixing state on the MAC of BC. Indeed, the MAC was found to increase with increasing degree of internal mixing. This provides evidence that the lensing effect increases the MAC of atmospheric BC to some extent.

3.1 Introduction

Black carbon (BC) particulate matter, also commonly referred to as refractory carbon or elemental carbon, is emitted by incomplete combustion of fossil fuels and biomass (see Section 3.2.1 for details about the terminology for carbonacous combustion particles). BC represents a small fraction of the European atmospheric aerosol, typically contributing less than 10% to the total mass concentration of particles smaller than 2.5 µm and 10 µm in diameter (Putaud et al., 2004; Yttri et al., 2007). Despite being a minor mass fraction only, it has been argued that anthropogenic BC might cause the second largest radiative forcing after CO_2 (Jacobson, 2001; Bond et al., 2013). This value is, however, associated with a high uncertainty (90%), resulting in an RF_{BC} range between 0.17 and 2.1 W m^{-2} (Myhre et al., 2013). The calculation of RF_{BC} depends on the light absorption coefficient attributed to atmospheric particulate BC. The light absorption by BC is often inferred from measured or modeled BC mass concentrations using the mass absorption cross-section (MAC; see Equation 3.1 in Section 3.2.3.3). Thus, the estimated RF_{BC} is not only sensitive to the modeled BC mass concentration but also to the applied MAC value. Current state-of-the-art RF_{BC} estimates are based on a fixed MAC value without accounting for its spatio-temporal variability (Koch et al., 2009). However, the correct MAC value and its spatio-temporal variability remain poorly quantified, and thus could potentially lead to a considerable uncertainty in the RF_{BC} assessment (Schulz et al., 2006; Koch et al., 2009).

Besides radiative forcing assessment, the MAC value is also required to infer the equivalent black carbon (eBC) mass concentration from measurements of the light absorption coefficient. The eBC mass concentration is meant to be equal to the elemental carbon (EC) mass concentration as measured by thermal-optical methods (Petzold et al., 2013). However, this is only achieved under several conditions. First the light absorption coefficient is measured for a wavelength at which EC causes virtually all light absorption (red to near-infrared). Second, the light absorption coefficient is correctly measured, which is generally challenging and even more for filter-based methods (see Section 3.2.3.2). Third, the true MAC value of the sampled aerosol is applied for the conversion of the light absorption coefficient to eBC mass concentration. Commercial instruments typically use a predefined fixed MAC value. This is a potential source for differences between eBC and EC mass concentrations, given the facts that the MAC remains poorly constrained and that it may vary with the aerosol type.

In Table 3.1 we report MAC values from the literature, which range between 4.3 and 22.7 m^2 g^{-1} at a wavelength of 637 nm. Part of this variability may be attributed to variability of the microphysical properties of BC-containing particles due different sources (e.g. (Schwarz et al., 2008b; Martins et al., 1998) and/or differences in atmospheric aging processes during transport of BC to certain locations (Liousse et al., 1993a; Cozic et al., 2008a; Reche et al., 2011; Pandolfi et al., 2011 and 2014; Genberg et al., 2013; Laborde et al., 2013).

Table 3.1 Selected MAC values from literature. The 2nd and 3rd column list the MAC values and corresponding wavelength as reported in the original literature. The 4th column lists the MAC values adjusted to 637 nm assuming an absorption Ångstrom exponent of 1.

Location	MAC [$m^2 g^{-1}$]	Wavelength [nm]	MAC @ 637 nm [$m^2 g^{-1}$]	Reference
Remote areas	5	550	4.3	Liousse, Cachier & Jennings, 1993
Mediterranean	18		15.5	
Savannah	20		17.3	
Urban	12		10.4	
Biomass burning (Brazil)	12.1	550	10.5	Vanderlei Martins et al., 1998
High altitude winter	7.6	630	7.5	Cozic et al., 2008
High altitude summer	11.1		11	
Traffic	9.1	530	7.6	Schwarz et al., 2008
Biomass burning	13		10.8	
High altitude spring	10.2	630	10.1	Liu et al., 2010
Regional background	10.4	635	10.4	Pandolfi et al., 2011
Urban (Barcelona)			9.2	Reche et al., 2011
Traffic (Bern)			10.3	
Industrial (Huelva)			9.8	
Urban (Paris)	8.6	880	11.9	Laborde et al., 2013
Aspvreten	16.3	550	14.1	Genberg et al., 2013
Birkenes	25.9		22.4	
Harwell	9.14		7.9	
Melpitz	4.55		3.9	
Vavihill	26.2		22.7	
High altitude			10.9	Pandolfi et al., 2014

However, in this study we show that a substantial portion of this variability can also be attributed to experimental uncertainties, i.e. systematic biases of the methods applied to determine the MAC. Sources and atmospheric aging processes define the properties of BC-containing particles to which

the MAC is sensitive: index of refraction and material density of BC as well as particle size, shape and mixing with other particulate matter (Bond et al., 2013 and references therein). We can distinguish two different types of mixing: external mixture, where BC particles only exist in pure form, and internal mixture, where BC is mixed with other aerosol components in the same particle. Freshly emitted BC can be externally or internally mixed, depending on its source. Atmospheric aging processes such as condensation, cloud processing or coagulation additionally transform externally mixed BC to internally mixed BC. Most BC becomes mixed with other components such as inorganic salts and acids or organic matter within 1 to 5 days (Jacobson, 2001; Riemer et al., 2010; Fierce et al., 2015) while in polluted urban areas BC becomes internally mixed within 12 hours after emission (Moteki et al., 2007). In general, it is accepted that internal mixing with non-absorbing material induces an enhancement in the light absorption due to lensing effect (Schwarz et al., 2008a; Bond et al., 2013), even though this enhancement effect is still debated (Cappa et al., 2012).

In this work, we investigate the spatio-temporal variability of the MAC. For this purpose we use long-term data-sets from 9 supersites across Europe of the ACTRIS (Aerosols, Clouds, and Trace gases Research InfraStructure) research infrastructure, where more than 1 year of parallel light absorption coefficient and elemental carbon mass concentration measurements were available. A key feature of this data-set is its homogeneity, which is ensured with extensive instrument calibration and intercomparison exercises as part of the ACTRIS and ACTRIS-2 research infrastructure. Besides, this dataset provides evidence that the lensing effect increases the MAC of BC.

3.2 Method

3.2.1 Terminology

The terminology for describing various properties of carbonaceous particles emitted by incomplete combustion processes, referred to as soot particles, is ambiguous in the literature. Here we adopt the recent recommendations by Petzold et al. (2013). The term black carbon (BC) is used to refer, in a general sense, to the most refractory, insoluble and strongly light-absorbing component of combustion particles. BC is essentially elemental carbon (EC), i.e. almost pure carbon with a graphitic-like chemical microstructure. These features distinguish BC from organic carbon (OC), which is the other major component of carbonaceous combustion particles. The term BC-containing particle is used to refer to BC internally mixed with other particulate matter. More specific terms for BC are used whenever referring to BC properties in a quantitative manner. EC mass concentration (m_{EC}) is used for BC mass concentration measured by means of thermal-optical methods. Equivalent black carbon (eBC) is used whenever BC is indirectly quantified by inferring the eBC mass concentration (m_{eBC}) from light absorption coefficient (σ_{ap}) measurements. The attribute “equivalent” reflects the fact that the MAC value of the BC needs to be assumed for calculating m_{eBC} (this is readily seen by solving Equation (3.9 for m_{EC}, followed by substituting m_{eBC} for m_{EC}). Accordingly, m_{eBC} is only identical

with m_{EC}, if the MAC value assumed for calculating m_{eBC} from σ_{ap} is equal to the true MAC value of the BC in the aerosol under consideration, as already mentioned in Section 3.1.

3.2.2 The ACTRIS sites

The present work is based on data recorded at atmospheric research supersites of the ACTRIS (**A**erosols, **C**louds, and **T**race gases **R**esearch **I**nfra**S**tructure) network. All data presented here were downloaded from the EBAS database (http://ebas.nilu.no/), developed and operated by the Norwegian Institute for Air Research (NILU). In order to ensure statistical robustness and coverage of a full seasonal cycle for every site, we set a minimal requirement of at least one year of simultaneous absorption coefficient and EC mass concentration measurements. Nine supersites satisfied this criterion: Aspvreten (APT), Birkenes (BIR), Finokalia (FKL), Harwell (HRL), Ispra (IPR), Melpitz (MEL), Montseny (MSY), Puy de Dome (PUY) and Vavihill (VAV). Figure 3.1 shows the geographical location of the observations sites. They can be grouped by latitude in the three distinct regions: Scandinavia, Central Europe and British Isles, and Mediterranean. The main characteristics of each observation site including instrumentation relevant to this study are summarized in Table 3.2.

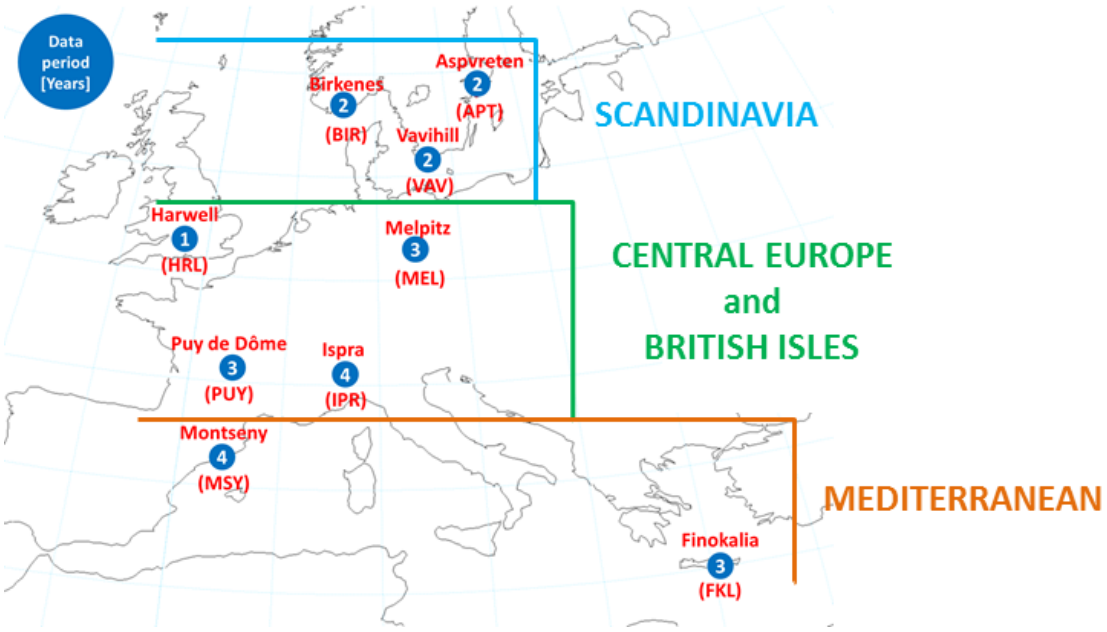

Figure 3.1. Location of sampling sites and duration of measurements included in this study.

Table 3.2. List of observatories included in this work and measurement description. Arranged alphabetically.

Site (Country)	Station code	Coordinates	Altitude [m asl]	Period	Thermal protocol for m_{EC} (collection time)	Instrument for σ_{ap} (wavelength)	Aerosol size fraction m_{EC}	Aerosol size fraction σ_{ap}	Region
Aspvreten (SE)	APT	58° 48' N, 17° 23'E	30	2010 2011	EUSAAR-2	PSAP-ITM (522nm)	PM10	Total	Scandinavia
Birkenes (NO)	BIR	58° 23' N, 8° 15' E	190	2010 2011	EUSAAR-2	PSAP-ITM (525nm)	PM10	PM10	Scandinavia
Finokalia (GR)	FKL	35° 20' N, 25° 40' E	250	2008 2010	EUSAAR-2 (24h)	Aethalometer AE21 (880nm)	PM10	Total	Mediterranean
Harwell (GB)	HRL	51° 34' N, 1° 19' W	60	2010	NIOSH-like[a] (24h)	Aethalometer AE22 (880nm)	PM10	Total	British Isles
Ispra (IT)	IPR	45° 49' N, 8° 38' E	209	2008 2011	EUSAAR-2 (24h)	MAAP (637nm)	PM2.5	Total	Continental Europe
Melpitz (DE)	MEL	51° 32' N, 12° 54' E	87	2008 2010	VDI-2465 (24h)	MAAP (637nm)	PM10	Total	Continental Europe
Montseny (ES)	MSY	41° 46' N, 2° 21' E	720	2008 2011	EUSAAR-2 (24h)	MAAP (637nm)	PM10	PM10	Mediterranean
Puy de Dôme (FR)	PUY	45° 46' N, 2° 57' E	1465	2008 2010	EUSAAR-2 (24h)	MAAP (637nm)	PM10	Total	Continental Europe
Vavihill (SE)	VAV	56° 01' N, 13° 09' E	172	2010 2011	EUSAAR-2	PSAP-ITM (520nm)	PM10	Total	Scandinavia

[a] NIOSH-like protocol alternatively named "QUARTZ" and described in (Yttri et al., 2009).

3.2.2.1 Scandinavia

The Aspvreten station (APT, Sweden, 58º 48'N, 17º 23'E, 30 m asl.) is operated by the Department of Environmental Science and Analytical Chemistry (ACES) of the Stockholm University. The station is located away from any local sources, placed in a boreal forest and is representative for the regional background. The Birkenes atmospheric research station (BIR, Norway, 58º 23'N, 8º 15'E, 190 m asl.) is run by the Norwegian Institute for Air Research (NILU), is located in the southern part of Norway, and is well suited to monitor long-range transported aerosol particles as it is far away from major anthropogenic sources. Vavihill (Sweden, VAV, 56º 01'N, 13º 09'E, 172 m asl.) is operated by Lund University. VAV is a background site with no local sources of pollution, situated in the southern-most part of Sweden.

3.2.2.2 Central Europe and British Isles

The Harwell site (HRL, England, 51º 34'N, 1º 19'W, 60 m asl.) is operated by the University of Birmingham, primarily on behalf of the Department for Environment, Food and Rural Affairs (DEFRA). HRL is a rural station representative of large-scale air masses affecting Southern England with the occasional influence of London emissions. The Ispra atmospheric research station (IPR, Italy, 45º 49'N, 8º 38'E, 209 m asl.) is run by the Institute for Environment and Sustainability of the EC Joint Research Centre. Ispra is representative of the regional background at the southern edge of the Alps affected by pollution from the Po Valley. The TROPOS atmospheric research station Melpitz, (MEL, Germany, 51º 32'N, 12º 54'E, 87 m asl.) is operated by the Leibniz Institute for Tropospheric Research and represents a rural polluted continental site in Eastern Germany. The Puy de Dôme station (PUY, France, 45º 46'N, 2º 57'E, 1465 m asl.) is run by the "Observatoire de Physique du Globe" (OPGC) and by the "Laboratoire de Météorologie Physique" (LaMP) of the National Center for Scientific Research (CNRS). Despite the proximity of the urban area of Clermont-Ferrand, the latter has very little influence on the aerosol observed at PUY (Henne et al., 2010). Measurements at PUY are representative of the regional atmospheric background aerosol composition on synoptic scale distances.

3.2.2.3 Mediterranean

The Finokalia station (FKL, Greece, 35º 20'N, 25º 40'E, 250m asl.) is run by the Environmental Chemical Processes Laboratory (ECPL) of the University of Crete. The FKL station is located in the Southeastern Mediterranean, far from any local source of pollution and the observations are representative of the aged regional background aerosol of the Eastern Mediterranean Basin with the frequent influence of dust (Sahara) and sea-salt (Mediterranean Sea). The station of Montseny (MSY, Spain, 41º 46'N, 2º 21'E, 720 m asl.) belongs to the Air Quality Network of the Government of Catalonia and is run by the Institute of Environmental Assessment and Water Research (IDAEA-CSIC). MSY is a middle altitude emplacement located in the Montseny Natural Park 40 km NNE of the Barcelona urban area and 25 km from the Mediterranean coast. Observations are representative of a regional background aerosol of the Western Mediterranean Basin with meteorology-driven urban, sea salt and dust (Sahara) influence.

3.2.3 Experimental methods

The work performed in the present study is based on experimental data acquired at different stations using a range of different instruments and measurement protocols. Interpretation of spatial differences, reflecting the influence of the local environment and typical transport pathways influencing each site, is only possible if the data-set is homogeneous across all involved sites. The

activities of the ACTRIS research infrastructure include considerable harmonization efforts such as extensive instrument intercomparison campaigns in order to minimize potential systematic differences between equal instrument types as well as between different instruments or protocols for measuring the same quantity. For this study, all σ_{ap} and m_{EC} measurements were harmonized to a common reference technique, as described in the following. This maximizes the homogeneity of the whole data-set, whereas uncertainties of the absolute values remain, due to the lack absolute standards (Baumgardner et al., 2012).

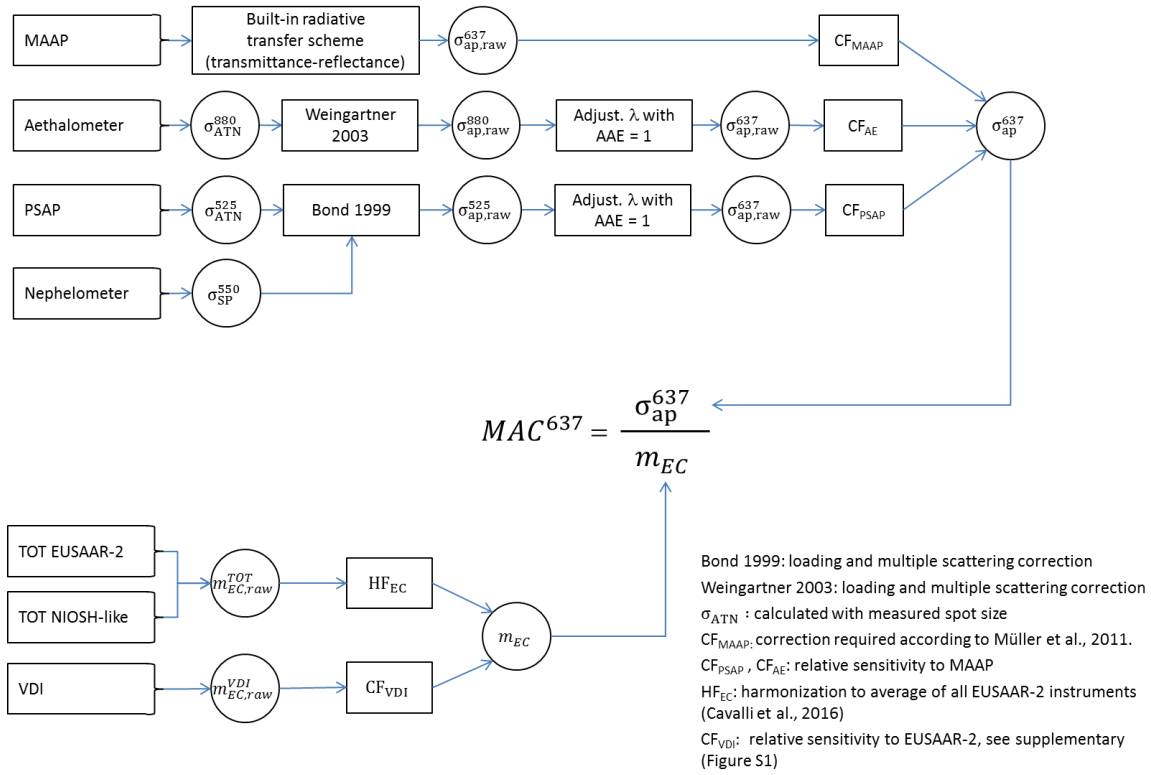

Figure 3.2. Flowsheet of how to obtain corrected and harmonized EC mass concentrations (mEC) and absorption coefficients (σ_{ap}^{637}) from the raw data delivered by different types of instruments and methods, which are then used to calculate the mass absorption cross-section values for a wavelength of 637 nm (MAC637).

3.2.3.1 Elemental carbon mass determination

A widespread approach to quantify OC and EC are thermal-optical techniques, which differentiate EC from OC through their thermal properties with optical correction for potential charring artefacts (Karanasiou et al., 2015). Most commonly applied temperature ramp protocols are NIOSH-5040 (Birch and Cary, 1996), QUARTZ (NIOSH-like; Yttri et al., 2009) IMPROVE (Chow et al., 2007), or EUSAAR-2 (Cavalli et al., 2010). Briefly, the aerosol is deposited on a quartz-fiber filter. The collected OC mass is then determined during a first desorption step in an inert atmosphere (He) at multiple medium-to-high temperatures starting at 140-310 °C and reaching up to 580-940 °C depending on the thermal protocol (NIOSH-5040, QUARTZ, IMPROVE-A or EUSAAR-2). The EC mass is then quantified during a

second desorption step under oxidizing conditions (He/O_2 mixture) at multiple higher temperatures starting at 500-580°C and reaching up to 840-890°C depending on the thermal protocol. Temperature steps and analysis time for the most common thermal protocols are summarized in Karanasiou et al. (2015). All desorbed carbonaceous compounds are oxidized to CO_2, which is measured via non-dispersive infrared detection (Chow et al., 1993) or by flame ionization detection after reduction to methane (Birch and Cary, 1996). Ideally, all OC should be completely desorbed during the first inert atmosphere step, while EC should only be burned off in the second oxidizing step. However, some OC may be pyrolized and converted to EC during the step, thereby systematically biasing the OC-EC discrimination (Huntzicker et al., 1982). Correction for this charring artefact is commonly done by estimating the contribution of the pyrolytic carbon to the carbon desorbed in the second step through continuous monitoring of the light transmittance through or light reflectance at the filter (Dod et al., 1978; Johnson and Huntzicker, 1979), which is referred to as thermal-optical transmittance (TOT) or thermal-optical reflectance (TOR) method, respectively. Previous inter-laboratory and inter-protocol comparison studies revealed a good agreement in the total carbon mass concentration, whereas substantial systematic differences are observed in discriminating between the OC and EC fractions between different temperature protocols, between TOT and TOR with equal temperature protocol as well as between individual instruments applying the same protocol (Chiappini et al., 2014; Cavalli et al., 2016).

In this study, we choose the EUSAAR-2 protocol with light transmission for charring correction (TOT), which has been selected as the standard method for the ACTRIS research infrastructure, as our basis for determining the EC mass concentrations, from which the MAC are calculated. Homogeneity of the EC data from sites that apply the EUSAAR-2 protocol is maximized by instrument specific harmonization factors to correct for systematic instrument-to-instrument variability. EC data from sites that apply a different protocol or approach are adjusted with correction factors, in order to make them equivalent to EUSAAR-2 based data.

A schematic of the data analysis and harmonization approach applied in this study is provided in Figure 3.2. Raw EC mass concentrations ($m_{\mathrm{EC,raw}}^{\mathrm{TOT}}$), which are already corrected for the charring artefact, were provided by the observatories. Final harmonized EC mass concentration (m_{EC}) were then obtained by applying instrument-specific harmonization factors ($\mathrm{HF}_{\mathrm{EC}}$):

$$\boldsymbol{m_{\mathrm{EC}} = \frac{m_{\mathrm{EC,raw}}^{\mathrm{TOT}}}{\mathrm{HF_{EC}}}} \tag{3.1}$$

The harmonization factors were determined by Cavalli et al. (2016) for all thermal-optical instruments applied at observatories of the ACTRIS research infrastructure as part of an intense intercomparison exercise. Identical samples, i.e. filter punches from the same filter, were analyzed by all instruments. This was done for a series of randomly chosen filters. The reference value, $m_{\mathrm{EC}}^{\mathrm{ref}}$, for the EC mass on each test filter was then defined to be the average of all raw EC mass values from those instruments that apply the EUSAAR-2 protocol. The harmonization factor for each instrument is then set equal to $m_{\mathrm{EC,raw}}^{\mathrm{TOT}}$ measured by this particular instrument divided by the reference value $m_{\mathrm{EC}}^{\mathrm{ref}}$ (after averaging both over all test filters). As a consequence, the final harmonized EC measurements, m_{EC}, become by

definition equal to the reference value, when again considering the average over all test filters. This harmonization procedure ensures the homogeneity of the EC mass concentration data-set from the different sites by minimizing potential differences arising from instrument to instrument variability as well as differences in the measurement protocol. The importance of the intercomparison and harmonization efforts is reflected in the fact that the harmonization factors, which are listed in Table 3.3**Erreur ! Source du renvoi introuvable.**, span a considerable range from 0.74 to 1.35 even for those seven sites were the identical EUSAAR-2 protocol is applied (Table 3.2).

At Harwell, the NIOSH-like protocol "QUARTZ" with light transmission for charring correction is applied (Yttri et al., 2009; Querol et al., 2013; we will refer to it as "NIOSH-like"). The temperature ramp of this thermal-optical protocol deviates slightly from that of the EUSAAR-2 protocol. Thus, the results of this instrument were not included in calculating $m_{\mathrm{EC}}^{\mathrm{ref}}$ of the inter-laboratory comparisons, whereas the harmonization factor was also determined against $m_{\mathrm{EC}}^{\mathrm{ref}}$ and applied in the same manner (Equation (3.1). Using this approach, the final harmonized EC mass from the NIOSH-like method become equivalent to EUSAAR-2 based EC mass.

The harmonization is somewhat more complex at Melpitz, where a modified VDI thermal method without optical charring correction was applied (Cachier et al., 1989). This protocol is known to have a considerable high bias in the EC mass concentration measurement, which also depends considerably on aerosol composition. Therefore, a full year comparison of EC measurements using both the VDI and the EUSAAR-2 protocols in parallel was performed at Melpitz in 2012. Figure S1 shows that the monthly mean ratio of the EC mass concentration measured by the two methods varies between 1.36 and 3.14 with a distinct seasonal pattern. We used the results of this comparison in 2012 to adjust the EC measurements, $m_{\mathrm{EC,raw}}^{\mathrm{VDI}}$, done at Melpitz from 2008 to 2010 in order to obtain EUSAAR-2 equivalent EC mass values. The adjustment of $m_{\mathrm{EC,raw}}^{\mathrm{VDI}}$ was done by correcting with the monthly mean $\mathrm{CF}_{\mathrm{VDI}}$ from the corresponding month of the year, which is taken from Figure S1. This approach accounts for the seasonal pattern of the VDI to EUSAAR-2 ratio as well as possible. No harmonization of the thermal-optical EC instrument, which was used to determine CF_{VDI} at Melpitz, against the EUSAAR-2 reference, was done, as the uncertainty associated with the correction factor CF_{VDI} is the dominating source of error. In the meantime the thermal-optical instrument of TROPOS used for Melpitz samples took part at European inter-comparison exercises in 2014 and 2015 successfully.

Table 3.3 Various harmonization and correction factors applied in the data analysis as described in Section 3.2.3. HF_{EC}, which was determined by Cavalli et al. (2016, in preparation), is the instrument specific harmonization factor to correct for systematic differences between the individual thermal-optical instruments employed at all sites. The range of values required to correct the thermal EC measurements at Melpitz is listed under CF_{VDI}[a]. CF_{MAAP} is the correction factor applied to the firmware output from the MAAP (Müller et al., 2011). D_{spot} is the measured spot diameter that was applied in the initial data analysis steps for the PSAP and aethalometer instruments. K_1 and K_2 are the coefficients that have been applied to the PSAP data following the Bond correction (Bond et al., 1999). CF_{PSAP} is a correction factor to harmonize PSAP results with MAAP measurements (from yet unpublished intercomparison workshop). f and C_{def} are the coefficients for loading and multi-scattering correction as applied using the approach by Weingartner et al. (2003). CF_{AE}[b] is a correction factor to harmonize the aethalometer results with MAAP measurements (Müller et al., 2011; WMO, 2016). α_{ap} is the absorption Ångström exponent applied to adjust the absorption coefficients determined by aethalometer and PSAP to the wavelength of the MAAP.

Site	HF_{EC}	CF_{VDI}[a]	CF_{MAAP}	K_1	K_2	CF_{PSAP}	D_{spot} [mm^2]	f	C_{def}[b]	CF_{AE}[b]	α_{ap}
Aspvreten	1.35	n.a.	n. a.	0.02	1.22	1.54	7.07[c]	n. a.	n. a.	n. a.	n.a.
Birkenes	1.02	n.a.	n. a.	0.02	1.22	1.94	11.3[c]	n. a.	n. a.	n. a.	n.a.
Finokalia	1.19	n.a.	n. a.	n. a.	n. a.	n. a.	42.6[c]	1.1	2.14	1.64	1.0
Harwell	1.45	n.a.	n. a.	n. a.	n. a.	n. a.	150[c]	1.1	2.14	1.64	1.0
Ispra	0.93	n.a.	0.952	n. a.	n. a.	n. a.	n. a.	n. a.	n. a.	n. a.	1.0
Melpitz	n.a.[a]	1.36-3.14[a]	0.952	n. a.	n. a.	n. a.	n. a.	n. a.	n. a.	n. a.	1.0
Montseny	0.97	n.a.	0.952	n. a.	n. a.	n. a.	n. a.	n. a.	n. a.	n. a.	1.0
Puy de Dome	1.23	n.a.	0.952	n. a.	n. a.	n. a.	n. a.	n. a.	n. a.	n. a.	1.0
Vavihill	0.74	n.a.	n. a.	0.02	1.22	2.2	7.30[d]	n. a.	n. a.	n. a.	1.0

[a]The thermal EC measurements made at Melpitz using the VDI method were adjusted to EC mass concentrations that are equivalent to values that would have been measured by a TOT-EUSAAR2 method. This was done by means of monthly mean corrections factors (Figure S1). No harmonization of the thermal-optical EC instrument, which was used to determine CF_{VDI} at Melpitz, against the EUSAAR-2 reference was done, as the uncertainty associated with the correction factor CF_{VDI} is the dominating source of uncertainty (see Section 3.2.3.4).
[b]Applying C_{def}=2.14 and CF_{AE}=1.64 for inferring the absorption coefficient from the attenuation coefficient measured by the aethalometer is equal to simply applying a C-value of 3.5 for the multi-scattering correction without any further corrections (except for the loading correction using the indicated f-value).
[c]Measured spot area and unit specific
[d]Spot area as defined in Krecl et al. (2007).

3.2.3.2 Absorption coefficient measurement and data analysis approach

The absorption coefficient was measured using one of the following three filter based absorption photometer types (see Table 3.2): the Multi Angle Absorption Photometer (MAAP, Thermo Fisher Scientific, Waltham, USA), the Aethalometer AE22 model (Magee Scientific, Berkeley, USA) or the custom made Particle Soot Absorption Photometer (PSAP-ITM). These are all filter-based methods, i.e. the aerosol sample is being continuously collected on the filter except during filter changes. The primary measurement is the rate of change of light transmittance through the filter per deposited

sample air volume unit, from which the attenuation coefficient is inferred (Weingartner et al., 2003). Quantitatively relating the absorption coefficient of an aerosol sample to its attenuation coefficient after deposition on the filter is mainly complicated by multiple scattering and "shadowing" effects (see e.g. Weingartner et al., 2003). First, the light attenuation coefficient of the particulate matter deposited on the filter is considerably larger than the corresponding absorption coefficient of the same amount of particulate matter in the form of an aerosol due to multiple scattering of light at the filter fibers. Second, the ratio of absorption coefficient to attenuation coefficient depends on the filter loading, as particles deposited deeper in the filter are shadowed by those deposited higher up in the filter. These two effects are accounted for with correction approaches. However, absorption coefficient measurements done with filter based methods always remain tainted with potentially substantial uncertainties. The MAAP, which has the most sophisticated measurement setup, has been shown to have the best accuracy (Petzold et al., 2005; Slowik et al., 2007; Moosmüller et al., 2009) among the instruments applied in the current study and it showed high agreement with an independent reference method which determines the absorption coefficient from the difference of light extinction minus scattering (Petzold et al., 2005). Therefore, we choose the absorption coefficients measured by the MAAP as a basis for calculating the MAC. Method specific correction factors are applied to the data from those sites operating a PSAP or an aethalometer to make them equivalent to MAAP based measurements and with that also as accurate as possible with available means. A schematic of the applied data analysis and correction procedures, which will be described in the following, is provided in Figure 3.2 and all relevant data analysis parameters and correction factors are listed in Table 3.3.

Petzold and Schönlinner (2004) provided a detailed description of the MAAP instrument and data analysis approach. Briefly, it measures light transmittance in orthogonal direction through the filter as well as back-reflectance at two different angles. The firmware includes a full data inversion, which is based on a radiative transfer model, to directly infer the absorption coefficient ($\sigma_{\mathrm{ap,raw}}^{637}$), whereby the reflectance signals provide the information required to account for the effects of multiple scattering and shadowing. Originally, the operating wavelength of the MAAP was thought to be 670 nm (Petzold et al., 2005), however, the true value was later shown to be 637±1 nm. As a consequence of this, the absorption coefficient ($\sigma_{\mathrm{ap,raw}}^{670}$) determined by the firmware of the MAAP needs to be increased by 5% assuming an Ångström exponent of 1 (Reno experiments; (Petzold et al., 2005)) to obtain the correct aerosol absorption coefficient ($\sigma_{\mathrm{ap}}^{637}$) at 637 nm (Müller et al., 2011):

$$\sigma_{\mathrm{ap}}^{637} = \frac{\sigma_{\mathrm{ap,raw}}^{670}}{\mathrm{CF_{MAAP}}} \qquad 3.2$$

We applied this correction with $\mathrm{CF_{MAAP}} = 0.952$ to the MAAP measurements used for this study, whereby the $\sigma_{\mathrm{ap,raw}}^{670}$ was first calculated by multiplying the BC mass concentration output of the MAAP with 6.6 $\mathrm{m^2 g^{-1}}$ (this is the MAC applied within the MAAP firmware to convert between measured absorption coefficient and reported BC mass concentration; Nordmann et al., 2013)).

The Aethalometer, model AE-22, measures the light transmission through the sample filter at 370 and 880 nm (Hansen et al., 1984). For the purpose of this study, we only used the 880 nm channel

because light absorption by atmospheric aerosols in the near-infrared wavelength range is fully dominated by black carbon, as opposed to the near ultraviolet range, where organic matter may contribute substantially (Kirchstetter et al., 2004). A multi-step data analysis and correction procedure was applied to obtain an absorption coefficient at 637 nm (Figure 3.2) that is equivalent to MAAP measurements. In a first step, the raw absorption coefficient at 880 nm ($\sigma_{\mathrm{ap,raw}}^{880}$) is derived from the attenuation coefficient at 880 nm (b_{ATN}^{880}) reported by the instrument using the approach from Weingartner et al. (2003):

$$\boldsymbol{\sigma_{\mathrm{ap,raw}}^{880} = \frac{b_{\mathrm{ATN}}^{880}}{C_{\mathrm{def}} R(\mathrm{ATN}, f)}} \tag{3.3}$$

where C_{def} is the factor to correct for multiple scattering effects and $R(\mathrm{ATN}, f)$, which depends on the filter loading, accounts for the shadowing effect. In the initial data analysis step to infer the raw absorption coefficient $\sigma_{\mathrm{ap,raw}}^{880}$ (Equation 3.4), we chose a "default" value of $C_{\mathrm{def}} = 2.14$ for the multi-scattering correction. The shadowing correction $R(\mathrm{ATN}, f)$ is of the form:

$$\boldsymbol{R(\mathrm{ATN}, f) = (1/f - 1) * [ln(\mathrm{ATN}) - ln(0.1)]/[ln(0.5) - ln(0.1)] + 1} \tag{3.4}$$

where ATN is the additional attenuation by adding particles to a blank filter. f is a parameter that mainly depends on the single scattering albedo of aerosol. Because no suitable simultaneous scattering coefficient measurements were available, we simply chose a fixed value of *f=1.1*, which is between typical values for aged BC (f=1.025) and freshly emitted BC (f=1.2) (Collaud Coen et al., 2010). In order to verify the reliability of the shadowing correction for the chosen *f* value, the inferred raw absorption coefficients ($\sigma_{\mathrm{ap,raw}}^{880}$) observed at the highest and lowest filter loadings, i.e. just before and after the filter change, respectively, were compared against each other. The fact that they differ as little as 0.18% and 0.28% for the Harwell and Finokalia data-sets, respectively, indicates that on average the shadowing effect is correctly accounted for.

In the next step, the raw absorption coefficient ($\sigma_{\mathrm{ap,raw}}^{880}$), which was inferred from measurements at 880 nm, is adjusted to a raw absorption coefficient ($\sigma_{\mathrm{ap,raw}}^{637}$) at the wavelength of the MAAP (637 nm). This is done with the common approach to assume a constant absorption Ångström exponent (AAE; e.g. Lack and Langridge, 2013 and reference therein):

$$\boldsymbol{\sigma_{\mathrm{ap}}^{\lambda_2} = \sigma_{\mathrm{ap}}^{\lambda_1} \left(\frac{\lambda_1}{\lambda_2}\right)^{\mathrm{AAE}}} \tag{3.5}$$

where λ_1 and λ_2 are the wavelengths 880 nm and 637 nm, respectively, and the AAE is assumed to be unity (AAE=1.0).

So far, the wavelength-adjusted absorption coefficient, $\sigma_{\mathrm{ap,raw}}^{637}$, was calculated with applying a legacy value of $C_{\mathrm{def}} = 2.14$ for the multi-scattering correction (Weingartner et al., 2003). However, Collaud Coen et al. (2010) found, by relating aethalometer measurements of the absorption coefficient to parallel MAAP measurements, that *C*-values in the range between 2.9 and 4.3 are more realistic for atmospheric aerosols. The latest recommendation, which is based on further yet unpublished intercomparison of parallel aethalometer and MAAP measurements of atmospheric aerosols (Müller at al., in preparation), is to apply a *C*-value 3.5 for atmospheric aerosols (WMO, 2016). In order to derive MAAP-equivalent and accurate absorption coefficients we had to apply another correction to the aethalometer data

$$\boldsymbol{\sigma_{ap}^{637} = \frac{\sigma_{ap,raw}^{637}}{\mathrm{CF_{AE}}}} \tag{3.6}$$

with $\mathrm{CF_{AE}}$=1.64. Note that the product of C_{def} (2.14) and $\mathrm{CF_{AE}}$ (1.64) equals 3.5. Thus, our two step correction approach, which was chosen for legacy reasons and also to show how different *C*-values and correction factors are related to each other, is identical to directly applying a *C*-value of 3.5 for the multiple-scattering correction in the Weingartner et al. (2003) approach. Applying a correction of $\mathrm{CF_{AE}} = 1.64$ is also in agreement with Müller et al. (2011), who reported a correction factor of $\mathrm{CF_{AE}} = 1.6$ for aethalometer data analyzed with the "default" *C*-value of $C_{\mathrm{def}} = 2.14$. No further efforts to minimize instrument-to-instrument variability were made, as the *C*-value is the dominant source of uncertainty (Section 3.2.3.4).

Custom made Particle Soot Absorption Photometers (PSAP-ITM) were installed at the Aspvreten, Birkenes, and Vavihill sites, operating at wavelengths of 522, 525, and 520 nm, respectively (Table 3.2). This instrument was developed by the Department of Applied Environmental Science at Stockholm University (ITM) and a full description of it is given in Krecl et al. (2007). It is similar to the commercial PSAP, which is described in detail in Bond et al. (1999). The latter study also provides a data correction approach, which is compatible with the data from the custom made PSAP-ITM. A first element of the Bond correction is to correct the instrument output for systematic deviations of the flow rate and spot size used in the firmware from their respective true values in order to obtain unbiased attenuation coefficients ($\sigma_{\mathrm{ATN}}^{525}$). We simply used the standard correction factors as they are always applied for these three instruments (Table 3.3). The second and main element of the Bond correction is to derive the raw absorption coefficient from the attenuation coefficient:

$$\boldsymbol{\sigma_{\mathrm{ap,raw}}^{525} = \frac{b_{\mathrm{ATN}}^{525} - K_1 \sigma_{\mathrm{sp}}}{K_2}} \tag{3.7}$$

where σ_{sp} denotes the scattering coefficient of the aerosol. The term $K_1\sigma_{\mathrm{sp}}$ accounts for misinterpretation of particle scattering as absorption and K_2 corrects for multiple scattering. We applied the Bond correction using the related correction coefficients $K_1 = 0.02$ and $K_2 = 1.22$, which are determined for the commercial PSAP but previously applied to PSAP-ITM data Müller et al. (2011),

and with using scattering coefficients simultaneously measured at these sites by nephelometers. In the next step, the raw absorption coefficient measured by the PSAP-ITM ($\sigma_{\mathrm{ap,raw}}^{525}$) at a wavelength of 525 nm (520 nm for Vavihill), was adjusted to the wavelength of the MAAP, which then provides the raw absorption coefficient at 637 nm ($\sigma_{\mathrm{ap,raw}}^{637}$). This was done in the same manner as for the aethalometer data, i.e. by using Equation 5 and assuming an absorption Ångström exponent of unity (AAE=1.0).

Recent intercomparison (unpublished) between MAAP and ITM-PSAP revealed that ($\sigma_{\mathrm{ap,raw}}^{637}$) measured by the PSAP-ITM from Aspreveten, Birkenes and Vavihill overestimated the $\sigma_{\mathrm{ap}}^{637}$ determined with MAAP. In order to derive MAAP-equivalent and accurate absorption coefficients we applied another correction to the PSAP-ITM data:

$$\boldsymbol{\sigma_{ap}^{637} = \frac{\sigma_{ap,raw}^{637}}{\mathrm{CF_{PSAP}}}} \tag{3.8}$$

with CF_{PSAP}=1.59 for the instrument operated at Aspvreten, CF_{PSAP} = 1.94 for the Birkenes instrument and CF_{PSAP}=2.2 for the Vavihill (Table 3.3). The reason for this discrepancy is yet unknown.

3.2.3.3 Mass absorption cross section (MAC)

The mass absorption cross section (MAC^{λ}; [m^2 g^{-1}]) of BC at a certain wavelength (λ) is defined as the ratio of the aerosol absorption coefficient ($\sigma_{\mathrm{ap}}^{\lambda}$; [$Mm^{-1}$]) at this wavelength to the mass concentration (m_{EC}; [µg m^{-3}]) of the BC:

$$\boldsymbol{\mathrm{MAC}^{\lambda} := \frac{\sigma_{\mathrm{ap}}^{\lambda}}{m_{\mathrm{EC}}}} \tag{3.9}$$

Note, this simplified definition is only valid for wavelengths at which the light absorption is dominated by black carbon. This is fulfilled at λ=637 nm, for which we report the MAC value of BC in this study, as already argued above. We used the absorption coefficients and EC mass concentrations including all adjustments and corrections as detailed in Sections 3.2.3.1 and 3.2.3.2, respectively, for calculating the MAC values. The filter samples for the EC analysis were collected over 24h at all Mediterranean, Central Europe and British Isles sites and, due to lower aerosol loadings, over 3 to 7 days at the Scandinavian sites. The measured absorption coefficients, which are available at higher time resolution (≤1h), were averaged over the intervals of the filter sampling, in order to obtain matching pairs of $\sigma_{\mathrm{ap}}^{637}$ and m_{EC}, before calculating the corresponding MAC values.

3.2.3.4 Uncertainty estimates

The uncertainty estimates for reported EC mass, light absorption coefficient, and MAC values are summarized in Table 3.4, Table 3.5 and Table 3.6, respectively. The harmonization procedure applied to EC measurements and described in Section 3.2.3 increases the reproducibility of the reported EUSAAR-2 equivalent EC mass concentrations and contributes to the spatial homogeneity of the data-set. The 1σ reproducibility of the harmonized EUSAAR-2 EC mass concentration measurements is estimated to be $\Delta m_{\mathrm{EC}}^{\mathrm{EUSAAR2}} \approx \pm 24\%$ for the sites adopting the EUSAAR-2 protocol (Table 3.4). The reproducibility is somewhat poorer for the EUSAAR-2 equivalent EC mass data from the Harwell site ($\Delta m_{\mathrm{EC}}^{\mathrm{NIOSH-like}} \approx \pm 52\%$), as the ratio of NIOSH-like to EUSAAR-2 derived EC mass concentrations is not constant for different aerosol types (Cavalli et al., 2016), as we assumed it for the harmonization approach. For Melpitz, using the modified thermal VDI protocol, the overall reproducibility is estimated to be $\Delta m_{\mathrm{EC}}^{\mathrm{VDI}} \approx \pm 55\%$, where the dominant uncertainty originates from the monthly mean correction factor ($\Delta \mathrm{CF}_{\mathrm{VDI}} \approx \pm 50\%$).

The accuracy of thermal-optical EC measurements always remains limited due to the lack of a reference method or suitable standards (Baumgardner et al., 2012). Here we simply define the EC mass from measurements by EUSAAR-2 instruments as the "true" value. Consequently, systematically different EC mass values would have been obtained if choosing a different protocol as reference. For example choosing NIOSH-5040 as reference method would provide EC mass values that are systematically lower by ~40% (Piazzalunga et al., 2011; Maenhaut and Claeys, 2012). In a similar manner using the IMPROVE-A protocol (with using light-transmission for charring correction) as EC mass reference, would have resulted in positive systematic biases of 10–20% (Piazzalunga et al., 2011; Wu et al., 2012).

The MAAP is expected to provide the absorption coefficient at 637 nm with an accuracy of $\Delta\sigma_{ap}^{MAAP} \approx \pm 15\%$ (Petzold et al., 2000; Müller et al., 2011), which directly applies to the reported absorption coefficients. The major uncertainty of the absorption coefficient measured by the aethalometer arises from the multi-scattering correction, since the *C*-value varies by about $\pm 25\%$ (1σ) for different aerosol types (WMO, 2016; Collaud Coen et al., 2010; Müller et al., 2011). Combined with unit-to-unit variability and accuracy of the MAAP, which served as a reference, this results in a 1σ accuracy of $\Delta\sigma_{ap}^{AE} \approx \pm 35\%$ for the corrected absorption coefficients from Aethalometers. The 1σ accuracy of corrected absorption coefficients from PSAP measurements is $\Delta\sigma_{ap}^{PSAP} \approx \pm 25\%$, where the major uncertainty arises from correcting the PSAP data to the MAAP reference.

The random errors of total absorption coefficients discussed in the previous paragraph are only valid if light absorption is fully dominated by BC. Additional errors occur if the ratio of light-absorbing organic matter to BC becomes high. These errors are systematic and therefore not included in the random errors provided above. Sandradewi et al., (2008) reported properties of ambient aerosol with a high fraction of organic matter from wood burning. In spite of this, the organic matter contributed less than 10% to total light absorption at a wavelength of 650 nm (Kirchstetter et al., 2004). We consider this as an upper limit for the potential light absorption by organic matter in aerosols at the

background sites such as those included in the present study (Table 3.5). The contribution to absorption by OC does not at all affect the reported absorption coefficients; it comes only into play when we assume that absorption by BC is equal to total absorption for calculating the MAC of BC. A second effect of interference from organic matter is that the true AAE becomes larger than unity as assumed for the wavelength adjustment of Aethalometer and PSAP-ITM data (see Section 3.2.3.2). Consequently, the true absorption coefficient at 637 nm will at most be 10% higher or 20% lower than the reported value if inferred from the Aethalometer measurements at 880 nm or the PSAP-ITM measurement at 525 nm (Table 3.5). Combining the two interference effects eventually provides true absorption coefficients from BC alone that are at most 0%, 10%, or 30% smaller than the reported total absorption coefficients from Aethalometer, MAAP, or PSAP-ITM measurements, respectively (Table 5). Note that there is no systematic error from organic matter interference left for the absorption coefficient at 637 nm by BC derived Aethalometer measurements at 880 nm, as interference from organic matter is negligible at this wavelength.

The uncertainty of the MAC values, listed in Table 3.6, is obtained by propagating the uncertainties of the EC mass concentration (Table 3.4) and the absorption coefficient (Table 3.5) through Equation 3.9. The smallest 1σ reproducibility of the MAC of BC is achieved at sites combining MAAP measurements with the EUSAAR-2 thermal-optical protocol and it is estimated to be $\Delta MAC \approx \pm 29\%$. The largest uncertainties were calculated for Melpitz (MAAP/VDI) $(\pm 57\%)$, and Harwell (Aethalometer/NIOSH-like), $(\pm 63\%)$. These uncertainty estimates are only valid if EUSAAR-2 is defined to be the reference method providing the true EC mass and if the total absorption at 637 nm is dominated by BC. MAC values would be approximately 40% larger if the NIOSH-5040 protocol had been used as reference method for EC mass instead of EUSAAR-2. Light-absorbing organic matter would not affect the MAC values for those sites that operated an Aethalometer. By contrast, the true MAC value of BC would at most be ~10% or ~30% smaller than reported for aerosols containing a large fraction of light-absorbing organic matter and sites that operated a MAAP or PSAP-ITM, respectively.

Table 3.4 Uncertainty estimates of harmonized EUSAAR-2 and EUSAAR-2 equivalent EC mass concentration.

Uncertainties of EC mass concentration (Δm_{EC}):			
	EUSAAR-2	NIOSH-like (Harwell)	VDI 2465 (Melpitz)
1σ reproducibility of the harmonized EUSAAR-2 or EUSAAR-2 equivalent EC mass. Valid if EUSAAR-2 is defined to be the reference method providing the true EC mass.	±24%	±52%	±55%
Approximate systematic decrease of m_{EC} if the NIOSH-5040 protocol would have been used as reference method instead of EUSAAR-2[a]	-~ 40%	-~ 40%	-~ 40%
Approximate systematic decrease of m_{EC} if the IMPROVE-A protocol would have been used as reference method instead of EUSAAR-2[a]	+ ~15%	+~15%	+~15%

[a]Estimated from Piazzalunga et al. (2011) and Maenhaut and Claeys (2012).
[b]Estimated from Piazzalunga et al. (2011) and Wu et al. 2012).

Table 3.5 Uncertainty estimates of corrected absorption coefficients for the wavelength 637 nm.

Uncertainties of absorption coefficient ($\Delta\sigma_{ap}^{637}$):			
	MAAP	Aethalometer	PSAP-ITM
1σ accuracy of reported total absorption coefficient σ_{ap}^{637}	±15%	±35%	±25%
Potential maximal interference in true total absorption coefficient from light-absorbing organic matter. The negative value indicates how much smaller the true absorption from BC alone would be relative to true total absorption.	-10%	-10%	-10%
Potential maximal systematic bias in reported total absorption coefficient due to assuming AAE=1 for the wavelength adjustment for aerosols types that contain light-absorbing organic matter. (positive value means that true total absorption would be higher than reported total absorption)	0%	+10%	-20%
Potential maximal systematic difference between reported total absorption coefficient and true absorption coefficient from BC alone at a wavelength of 637 nm for aerosols that contain light-absorbing organic matter (this is the sum of the above two lines). (negative value means that true absorption from BC alone is smaller than reported total absorption)	-10%	0%	-30%

Table 3.6 Uncertainty estimates of reported mass absorption cross-section values for a wavelength of 637 nm (ΔMAC^{637}) as obtained by propagating the uncertainties listed in Tables 3.7 and 3.5 through Equation (3.9.

Uncertainties of MAC (ΔMAC^{637}):					
	Instrument combination				
	EUSAAR-2 with MAAP	**EUSAAR-2 with Aethalometer**	**EUSAAR2 with PSAP**	**NIOSH-like with Aethalometer**	**VDI-2465 with MAAP**
Sites	Ispra Montseny Puy de Dôme	Finokalia	Aspvreten Birkenes Vavihill	Harwell	Melpitz
1σ reproducibility of MAC of BC at a wavelength of 637 nm based on harmonized and corrected absorption coefficient and EC mass values. Valid if EUSAAR-2 is defined to be the reference method providing the true EC mass and if total absorption at 637 is dominated by BC.	±29%	±43%	±35%	±63%	±57%
Potential maximal systematic difference between reported and true MAC at a wavelength of 637 nm for aerosols that contain light-absorbing organic matter. (Negative value means that the true MAC is smaller than the reported MAC.)	-10%	0%	-30%	0%	-10%
Approximate systematic increase of MAC if the NIOSH-5040 protocol would have been used as reference method for EC mass instead of EUSAAR-2. [a]	+ ~40%	+ ~40%	+ ~40%	+ ~40%	+ ~40%
Approximate systematic decrease of MAC if the IMPROVE-A protocol had been used as reference method for EC mass instead of EUSAAR-2. [b]	- ~15%	- ~15%	- ~15%	- ~15%	- ~15%

[a]Estimated from Piazzalunga et al. (2011) and Maenhaut and Claeys (2012).
[b]Estimated from Piazzalunga et al. (2011) and Wu et al. 2012).

3.3 Results and discussion

3.3.1 Spatial and seasonal variability of mEC and σap

Here, we focus on the spatial and seasonal variability of the EC mass concentrations and the absorption coefficients. The annual geometric mean EC mass concentrations differed by more than one order of magnitude between the Puy de Dôme mountain site (0.075 µg m^{-3}) and the polluted regional background site in Ispra (1.1 µg m^{-3}) (Figure 3.3a and Table 3.8). The Scandinavian background sites showed rather low EC burdens (0.084–0.23 µg m^{-3}). Medium EC concentrations were observed at the Mediterranean sites Finokalia and Montseny (0.22–0.26 µg m^{-3}) and at the slightly more polluted Continental and British sites Harwell and Melpitz (0.28–0.48 µg m^{-3}). The geometric standard deviations of the annual data-set of EC mass concentrations were between 1.47 and 1.88 for all sites (Table 3.8). Temporal variability of EC was lowest at the Scandinavian and Mediterranean sites and highest at the Continental as well as British Isles sites, which is mainly attributed to a more pronounced seasonal pattern for the latter (Figure 3.4).

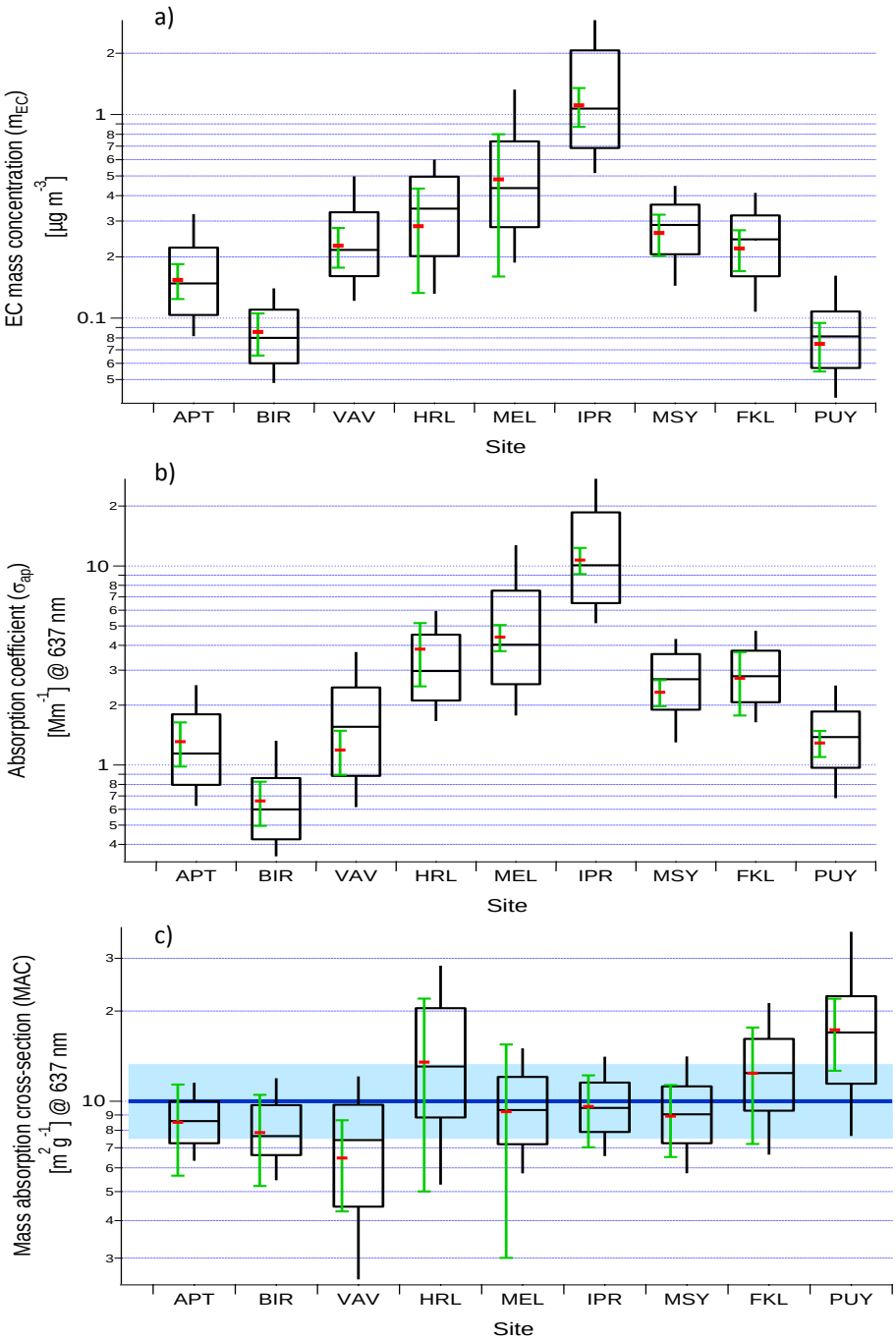

Figure 3.3 Box plots showing the 10th, 25th, median, 75th and 90th percentiles (black box and whiskers) as well as geometric mean values (red markers) of a) EUSAAR-2 EC mass concentration, b) absorption coefficient and c) mass absorption cross-section for all nine stations. These statistics are for data averaged over 24 hours at all sites, except for the Scandinavian sites (3-7 days). The green error bars indicate the 1σ uncertainties of the geometric mean value, which depend on the applied measurement technique. This uncertainty does not include potential systematic bias arising from e.g. light absorption by organics or from choosing a different thermal-optical protocol as reference method. The blue line and shading in panel c indicates the geometric mean ± geometric SD of the annual geometric mean MAC values from all sites.

The annual geometric mean values of the aerosol absorption coefficient at 637 nm range from 0.66 to 10.7 Mm^{-1} (Table 3.8). The spatial pattern was very similar to that of the EC mass concentration (Figure 3.3b). This is to be expected, if BC is the dominant light absorbing species at 637 nm as argued in Section 3.2.3.4, because the absorption coefficient is directly related to the EC mass concentration through the MAC value of BC (Equation 3.9). One minor difference is that the absorption coefficient was lowest at Birkenes instead of Puy de Dôme, which could reflect a systematic difference in the mean MAC at these two sites or it could simply be caused by experimental uncertainty. The temporal variability of the absorption coefficients was also very similar to that of EC (geom. SD between 1.45 and 1.93), except for Vavihill, where a substantially higher variability of the absorption coefficient (geom. SD 1.93) was observed (Table 3.8). However, the latter is most likely an artefact caused by very high instrumental noise, rather than reflecting true variability. These results for EC mass concentration and absorption coefficient show a clear spatial pattern with the highest values in Central Europe and distinctly lower values to the North and to the South. This is in agreement with previous studies by Yttri et al. (2007).

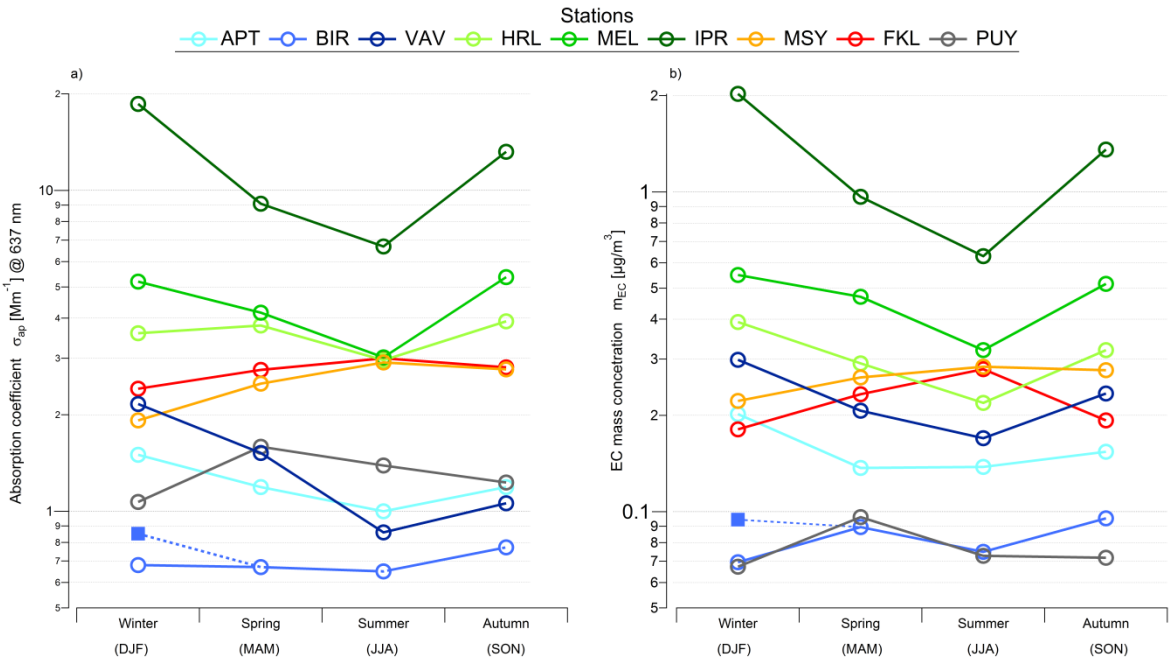

Figure 3.4 Seasonal trends for absorption coefficients (a) and EC mass concentration (b). Birkenes: two points for winter, square marker represent all winter points excluding December 2011.

The seasonal patterns of the absorption coefficient and EC mass concentration are plotted in Figure 3.4a and Figure 3.4b. The seasonal patterns of the two quantities are similar as they are linked to each other through the MAC of BC. Thus, we simply discuss the absorption coefficient in the following. The σ_{ap} values observed at the Scandinavian (ASP, BIR and VAV) and central European stations (HRL, IPR and MEL) followed the same pattern, with elevated values in winter/autumn compared to summer/spring. This is likely attributed to a lower polluted boundary layer (PBL) height

as well as to higher BC emissions during the heating season. A note is made for the wintertime values observed at Birkenes, as the site experienced unusual meteorological conditions in December 2011, which was exceptionally warm, with a surplus in the average temperature of 8.5°C and with several aerosol properties untypical for the winter season, which may be explained by reduced emissions from domestic heating and possibly more vertical mixing. Excluding this period from the winter data, i.e. just considering winter 2010 plus January and February 2011, results in considerably higher winter values for the absorption coefficient and EC (square symbols in Figure 3.4a and Figure 3.4b). An opposite seasonality compared to that in Scandinavia and Central Europe was observed at the Mediterranean sites Finokalia and Montseny, with σ_{ap} values being lowest in winter and highest in summer. At the slightly elevated Montseny site, this is explained by less favorable transport of aerosols to elevated areas during winter, contrasted by regional circulation enabling the accumulation and transport of pollutants from the urbanized coastline to Montseny during summer. The combined effects of rare precipitation, as well as intense agriculture and wild fire events during the warm season, explain the seasonality of σ_{ap} at Finokalia. The seasonal pattern was completely different at the Puy de Dôme mountain station, where σ_{ap} peaked in spring with gradually lower values in summer and autumn, and a minimum in winter. In winter, the Puy de Dôme site is frequently above the PBL, being affected by clean tropospheric air masses. In spring, vertical mixing becomes efficient enough such that the PBL reaches the site, while the wood combustion emissions from domestic heating are still high. The latter fades away in summer, thus explaining the spring maximum (Venzac et al., 2009).

3.3.2 Spatial variability of the MAC

The overall geometric mean MAC value observed at the 9 European background sites included in the present study was 10.0 $m^2 g^{-1}$ at 637 nm (Figure 3.4c). The annual geometric mean MAC values at individual stations varied between 7.5 and 13.3 $m^2 g^{-1}$ (geom. SD = 1.33; blue shading in Figure 3.3c), while the minimal and maximal observed values were 6.5 $m^2 g^{-1}$ and 17.3 $m^2 g^{-1}$ (Table 3.8). The differences between the sites (Table 3.8) are small in consideration of the experimental uncertainties, which are listed in Table 3.6 and indicated by the error bars in Figure 3.3c.

Table 3.8 Geometric mean and geometric standard deviation (in brackets) of (top panel) elemental carbon mass concentration (m_{EC}), (middle panel) absorption coefficient (σ_{ap}^{637}) and (bottom panel) mass absorption cross-section (MAC^{637}) for all nine stations. Data are averaged over 24 hours at all sites, except for the Scandinavian sites where single filter samples were collected over 3-7 days.

Elemental carbon mass concentration (m_{EC}) [µg m^{-3}]										
Site	Annual		Winter		Spring		Summer		Autumn	
APT	0.15	(1.65)	0.20	(1.68)	0.14	(1.63)	0.14	(1.56)	0.15	(1.51)
BIR	0.084	(1.48)	0.082	(1.66)	0.088	(1.33)	0.077	(1.42)	0.098	(1.48)
FKL	0.22	(1.59)	0.18	(1.65)	0.23	(1.51)	0.28	(1.50)	0.19	(1.55)
HRL	0.28	(1.76)	0.39	(1.59)	0.29	(1.79)	0.22	(1.55)	0.32	(1.77)
IPR	1.11	(1.88)	2.03	(1.61)	0.97	(1.63)	0.63	(1.30)	1.36	(1.76)
MEL	0.48	(1.69)	0.50	(1.71)	0.47	(1.64)	0.32	(1.41)	0.52	(1.68)
MSY	0.26	(1.47)	0.23	(1.48)	0.28	(1.54)	0.29	(1.40)	0.28	(1.43)
PUY	0.075	(1.52)	0.067	(1.55)	0.096	(1.60)	0.073	(1.36)	0.071	(1.35)
VAV	0.227	(1.65)	0.30	(1.69)	0.21	(1.46)	0.17	(1.44)	0.23	(2.01)

Absorption coefficient (σ_{ap}^{637}) [Mm^{-1}] @ 637 nm										
Site	Annual		Winter		Spring		Summer		Autumn	
APT	1.31	(1.65)	1.50	(1.68)	1.19	(1.65)	1.00	(1.58)	1.19	(1.58)
BIR	0.66	(1.63)	0.67	(1.86)	0.65	(1.52)	0.59	(1.41)	0.68	(1.87)
FKL	2.73	(1.45)	2.41	(1.77)	2.76	(1.30)	3.00	(1.39)	2.81	(1.53)
HRL	3.82	(1.56)	3.59	(1.53)	3.79	(1.43)	2.96	(1.43)	3.91	(1.52)
IPR	10.7	(1.84)	18.6	(1.72)	9.09	(1.63)	6.69	(1.40)	13.2	(1.70)
MEL	4.39	(1.73)	5.20	(1.78)	4.16	(1.63)	3.02	(1.39)	5.37	(1.76)
MSY	2.32	(1.53)	1.92	(1.63)	2.50	(1.52)	2.91	(1.41)	2.77	(1.44)
PUY	1.29	(1.86)	1.07	(1.69)	1.59	(1.66)	1.39	(1.49)	1.23	(1.65)
VAV	1.19	(1.93)	2.16	(1.92)	1.52	(1.79)	0.86	(1.51)	1.06	(1.50)

Mass absorption cross-section (MAC^{637}) [$m^2\ g^{-1}$] @ 637 nm										
Site	Annual		Winter		Spring		Summer		Autumn	
APT	8.51	(1.26)	8.38	(1.22)	9.10	(1.27)	8.41	(1.24)	8.17	(1.30)
BIR	7.86	(1.34)	8.09	(1.33)	7.59	(1.30)	8.12	(1.27)	7.71	(1.43)
FKL	12.4	(1.56)	15.1	(1.75)	11.1	(1.47)	10.9	(1.55)	15.1	(1.45)
HRL	13.5	(1.82)	8.87	(1.84)	14.9	(1.75)	15.9	(1.71)	15.1	(1.56)
IPR	9.61	(1.34)	9.31	(1.35)	9.03	(1.30)	10.9	(1.35)	9.34	(1.30)
MEL	9.23	(1.45)	8.22	(1.47)	8.74	(1.47)	9.5	(1.38)	11.3	(1.36)
MSY	8.92	(1.65)	8.29	(1.82)	8.97	(1.64)	9.73	(1.55)	8.73	(1.57)
PUY	17.3	(1.71)	13.4	(1.62)	16.5	(1.70)	19.9	(1.68)	19.8	(1.73)
VAV	6.47	(1.81)	7.04	(1.87)	7.23	(1.61)	4.85	(1.71)	4.20	(2.39)

The results from all stations but Puy de Dôme are in agreement with the overall mean of 10.0 $m^2\ g^{-1}$ and within the experimental uncertainty, which can thus be considered to be a representative MAC value of BC at 637 nm with respect to EC mass. It is important to emphasize that systematically higher MAC values would be obtained when using NIOSH-like protocols as a basis for the EC mass measurement instead of EUSAAR-2 (+ ~40%; Piazzalunga et al., 2011; Maenhaut and Claeys, 2012; see Table 5), whereas a ~15% difference compared to EUSAAR-2 can be expected when using the IMPROVE-A protocol (Karanasiou et al., 2015). Another potential source of systematic errors in the MAC value, which is not included in the error bars of Figure 3.3, is interferences in the light absorption measurement from e.g. light-absorbing organic matter. In Table 3.5, we provide an estimate of the maximum possible systematic bias, obtained by choosing the wavelength dependence of the light absorption coefficient of an ambient aerosol dominated by wood combustion emissions (Sandradewi et al., 2008) as a worst case scenario. No interference is expected for the aethalometer based measurements, as the actual measurement is done at 880 nm, where interference is negligible, and extrapolated to 637 nm using an AAE of unity, which is in the range of literature values reported for pure particles. For the sites operating a MAAP or PSAP-ITM, which measure at 637 or 525 nm, respectively, the interference can potentially cause a systematic bias of up to around +10% or +30% in the observed MAC of BC. The smallest MAC values were observed at the three Scandinavian sites. However, the difference from the grand average is within uncertainty, as pointed out above. Likewise, the higher MAC values observed at Harwell are not significantly different due to the additional uncertainties associated with using an aethalometer as well as adjusting EC mass values based on a NIOSH-like protocol to EUSAAR-2 equivalent values. Finokalia is a peculiar case, due to very frequent and strong dust influence, which might contribute to light absorption causing a positive bias. Otherwise, misinterpretation of carbon from carbonates as EC in the thermal-optical analysis would cause a negative bias, due to m_{EC} overestimation. Although the latter might be negligible for fine particulate matter (Querol et al., 2004), it might become severe in case of predominant coarse PM

fraction as in case of dust events (Karanasiou et al., 2015). The MAC values observed during very strong dust events were extremely low, which provides clear evidence of negative dust interference. A comparison of days with substantial dust influence (97 days in 2010) with dust-free days in 2010 indicates that the annual geometric mean MAC may have a low bias of ~15% due to dust interference. Accounting for this would move the MAC observed at Finokalia further away from the 10.0 $m^2 g^{-1}$ grand average, however, it would still not differ beyond uncertainty. The MAC values observed at the Puy de Dôme station seem significantly higher than the grand average. Part of this may possibly be explained by more aged and more internally mixed BC particles at this mountain site. However, there is some evidence that the low aerosol loadings frequently encountered at the Puy de Dôme station may have caused a low bias in the EC mass measurements and thus a high bias in the MAC values, which is not accounted for in our uncertainty analysis. Indeed, previous studies at the high-alpine site Jungfraujoch, Switzerland, reported values close to 10.0 $m^2 g^{-1}$ (Cozic et al., 2008; Liu et al., 2010).

Generally, the literature values for the MAC of BC listed in Table 3.1 are in the same ballpark as our grand average, though with considerably more variability than the spatial variability observed in our study. Genberg et al. (2013) also presented MAC values for the Melpitz, Aspvreten, Birkenes and Vavihill stations, which are also included in our study. Their MAC value reported for Melpitz is substantially lower than ours, which can be explained by the fact that they directly used the VDI-based EC mass concentrations, whereas we adjusted them to EUSAAR-2 equivalent values with the correction factors provided in Figure S1 and in Table 3.3. The MAC values reported by Genberg et al. (2013) for the Scandinavian sites are substantially higher than our results, which can be explained by the fact that we adjusted the PSAP-ITM based absorption coefficient measurements to MAAP equivalent values using the correction factors listed in Table 3.3.

In summary, the extensive intercomparison and harmonization efforts within the ACTRIS network made it possible to achieve a homogeneous long-term data-set from many background sites across Europe, which reveals only limited spatial variability of the mean MAC values. We recommend a MAC value of 10.0 $m^2 g^{-1}$ at 637 nm as best-estimate value for Europe, whenever a fixed MAC of BC is required for conversion of EUSAAR-2 based (or equivalent) EC mass concentrations to corresponding absorption coefficients, e.g. in model simulations, or for conversion from measured absorption coefficients to equivalent black carbon (eBC) mass concentrations. Potential deviations from the MAC independence of aerosol mixing state will be addressed in Section 3.3.4.

3.3.3 Temporal variability and seasonal cycles of the MAC

In the previous section we showed that the annual MAC-values exhibit little spatial variability across Europe. Here we investigate the temporal variability and seasonal patterns (and Table 3.8). The geometric standard deviation of all observed MAC values was not exceeding 1.34 for the three sites Aspvreten, Birkenes and Ispra. Such small variability is rather surprising, given the fact that a substantial fraction of it can be attributed to the random noise of single EC measurements, which have a repeatability that is hardly better than around ±10-20% (Cavalli et al., 2016). Thus, the true MAC value likely has little temporal variability at these sites, which also is consistent with little

seasonal variability; i.e. within the uncertainty. The observed MAC at Vavihill, the third Scandinavian background site, appeared much more variable in time. However, this is most likely an artifact from an uncommonly poor signal-to-noise ratio in the absorption coefficient measurements. In combination with poor counting statistics, it would be purely speculative to interpret the apparent seasonal pattern observed for this site in

Figure 3.5. The temporal variability observed at the Montseny site was in the medium range (geom. SD = 1.65) but without any significant seasonal pattern. Melpitz exhibited surprisingly small temporal variability, given the fact that the EC mass measurements were made with the VDI thermal protocol and adjusted to EUSAAR-2 equivalent EC mass values (see Section 2.3.1). The higher MAC observed in autumn is not significant, because the adjustment is tainted with considerable uncertainty and potential systematic seasonal bias (Figure S1 and Table 3.6). A mid-range temporal variability and higher values in autumn were observed at the Finokalia site. However, this may simply reflect differences between weak and strong dust interferences that affect the MAC values at this site (Section 3.3.2). The MAC values observed at the Harwell and Puy de Dôme site exhibited much higher temporal variability and apparent seasonal patterns. However, this is not statistically significant due to the relatively small number of samples and increased instrumental variability associated with using a different thermal-optical protocol (Harwell) and possible issues with very low aerosol concentrations (Puy de Dôme), respectively. In summary, the temporal variability of the observed MAC values was rather small, assuming a good repeatability of the measurements, whereas no statistically significant seasonal pattern could be observed for any of the sites.

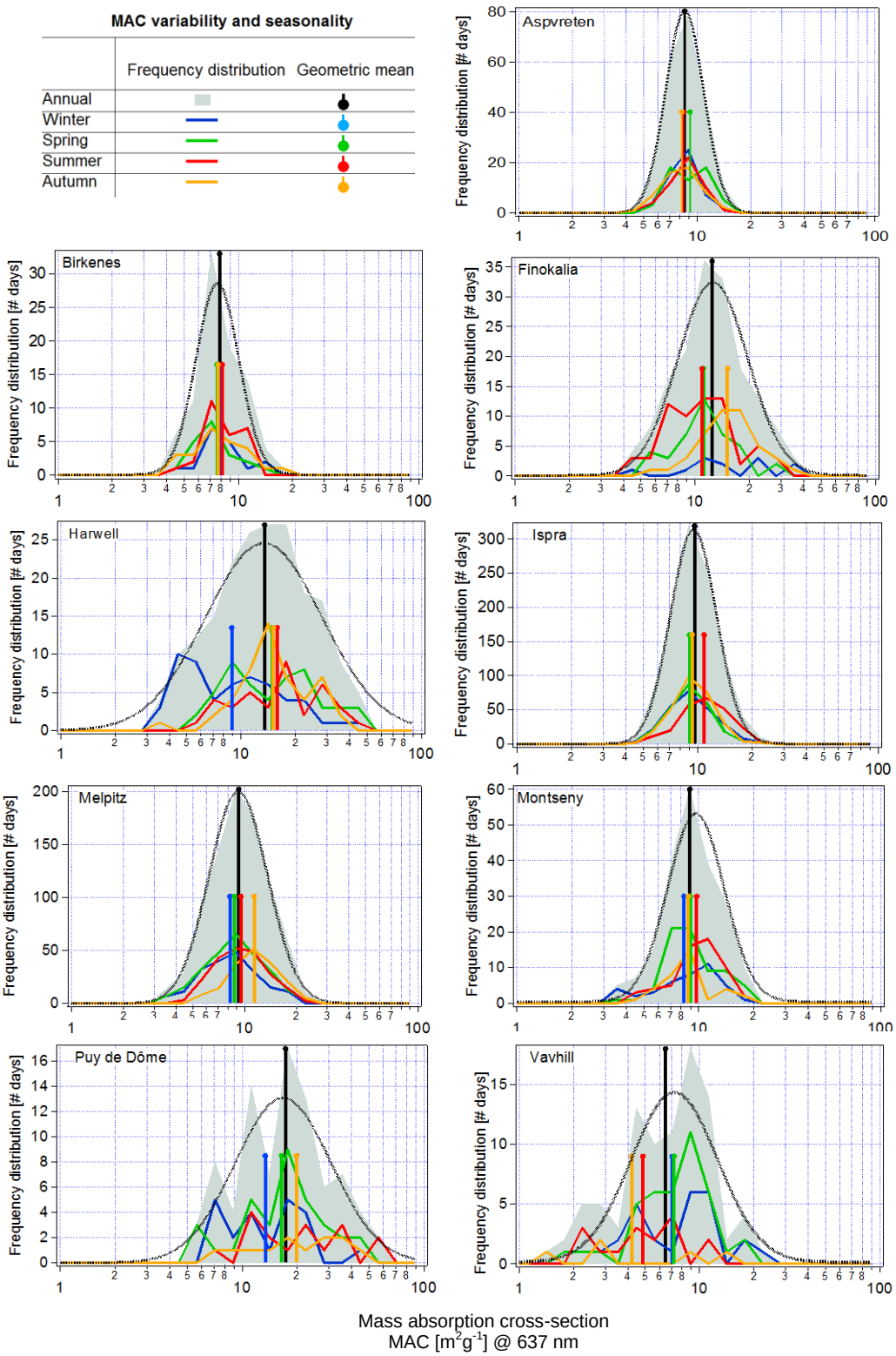

Figure 3.5 Frequency distribution of mass absorption cross-section (MAC) of black carbon for the whole multi-annual measurement period (grey surface) and corresponding geometric mean MAC (black sticks). Seasonal data are shown as coloured lines and sticks. Lognormal fitting of MAC values is shown as black dashed curves.

3.3.4 Dependence of MAC on aerosol mixing degree

Formation of a light-scattering coating around a BC core leads to enhanced light absorption, often referred to as the lensing effect. This was first theoretically predicted (e.g. Nessler et al., 2005; Bond and Bergstrom, 2006) and has later been confirmed in laboratory and field experiments (Bond et al., 2013 and references therein). Here we investigate whether evidence for light absorption enhancement by a light-scattering coating around the BC core is observed in the current data-sets. The available datasets do not allow quantifying the mixing state and coating thickness of BC-containing particles. Therefore, we use the mass ratio of non-absorbing matter (NAM) to EC as a proxy for the degree of internal mixing of BC. Some correlation between this proxy and the average coatings of the BC-containing particles can be expected for the following reasons: BC emitted from primary sources with a high emission ratio of NAM to EC typically has thicker coatings than BC emitted from sources with a low emission ratio of NAM to EC. Furthermore, secondary formation of NAM from gas phase precursors will also result in coating acquisition by BC particles through condensation (Oshima et al., 2009a, 2009b; Dahlkötter et al., 2014).

The NAM to EC mass ratio was calculated with the EC mass concentrations from the thermal-optical analyses and we defined NAM as the sum of particulate organic matter, nitrate and non-sea salt sulfate (nss-sulfate). The components included in NAM typically account for a major fraction of the submicron particulate matter and they are mainly of secondary origin, thus supporting the use of the NAM to EC ratio as a proxy for BC coating thickness (sea salt sulfate is not included in NAM as it is expected to be externally mixed to a large extent). The mass concentration of organic matter was inferred by multiplying the OC mass concentration obtained from the thermal-optical measurements with a factor of 1.6 (Turpin et al., 2000; Pio et al., 2007). Inorganic ions were measured by ion chromatography of water extracts from quartz filter samples. nss-sulfate is calculated as the difference between total measured sulfate mass and estimated sea salt sulfate mass, where the sea salt sulfate mass is set equal to one quarter of the total measured sodium mass (Pio et al., 2007). This approach might suffer from some bias due to the contribution of mineral dust to the sodium mass (Alastuey et al., 2016).

The chemical composition data required to calculate NAM as defined above are only available for the five stations Birkenes, Harwell, Ispra, Melpitz and Montseny. Annual mean mass concentrations of EC as well as nss-sulfate, nitrate and organic matter are listed in Table 3.9, while mass fractions of these components with respect to the sum of EC plus NAM are shown in Figure 3.6a. Except for the Harwell site, organic matter constitutes the largest fraction with 48% to 61%. EC is always a minor component (2-11%). Nitrate and nss-sulfate are also minor components at most sites. At Harwell, nitrate (44%) and nss-sulfate (29%) are the major components of the NAM, while organic matter represents 25%.

Table 3.9. Mass concentration of carbonaceous (OM and EC) and inorganic (non-sea salt sulfate and nitrate) particulate matter. Annual mean with SD in parentheses for 2010.

Mass concentration: geometric mean (geometric SD) [µg m^{-3}]								
	EC		OM		nss-Sulfate		Nitrate	
BIR	0.10	(1.71)	1.18	(1.66)	0.15	(2.68)	0.55	(2.27)
HRL	0.30	(2.34)	3.16	(1.71)	1.05	(2.39)	5.49	(12.0)
IPR	1.03	(2.35)	5.84	(3.12)	0.52	(3.43)	1.20	(6.74)
MEL	0.52	(2.54)	4.62	(2.02)	0.65	(2.36)	3.15	(4.97)
MSY	0.20	(1.88)	2.59	(1.52)	0.31	(2.79)	0.83	(2.19)

The observed dependence of the MAC on the BC mixing state proxy is shown in Figure 3.6b. The result for the Birkenes site (blue line with markers), where no dependence of the MAC on mixing state proxy is observed, is an unexplained exception. For the other 4 sites, a clear and consistent increase of the MAC of BC with increasing degree of internal mixing is observed from MAC values between 5.7 and 9.0 $m^2 g^{-1}$ at NAM/EC < 10 to values between 9.0 and 15.7 $m^2 g^{-1}$ at NAM/EC between 30 and 40. The grey shading in Figure 3.6b frames the approximate range of physically reasonable MAC values, which was obtained as follows. Concentric-spheres core-shell morphology was assumed for the BC core and the coating such that Mie theory could be applied. Three different BC core diameters of 100, 150 and 200 nm were used, which covers the typical range where BC mass size distributions peak when expressed as a function of BC core mass equivalent diameter (Schwarz et al., 2008b; Laborde et al., 2013). The index of refraction of the BC core was assumed to be 1.88+0.8i (Liu et al., 2015), which was already used during an European study and is in the range of expected values according to Bond and Bergstrom (2006). Three different indices of refraction (1.45 + 0i, 1.50 + 0i and 1.55 + 0i), which represent typical values of organic and inorganic species present in atmospheric aerosols, were used for the coating (e. g. Hess et al., 1998; Bond et al., 2006; Dinar et al., 2008; Moffet and Prather, 2009). The core-shell diameter ratio was either set to unity to obtain the minimal possible MAC of bare BC cores, or set to values >10 to obtain the maximal possible MAC in the range where the lensing effect is fully saturated, i.e. where a further coating thickness increase does not change the MAC any further (e.g. Nessler et al., 2005). The minimal and maximal MAC for a given set of parameters were calculated with all possible combinations of BC core diameter and coating index of refraction, and the average of it was chosen as approximation for the minimum (6.0 $m^2 g^{-1}$) and maximum (14.5 $m^2 g^{-1}$) possible MAC values at a wavelength of 637 nm. These estimates of the upper and lower limits for possible MAC values are consistent with previous literature. Most observations in Figure 3.6b fall into the physical boundaries, except for very high NAM to EC ratios. However, the latter data points are likely biased high due to a substantial and asymmetric contribution from outliers in the EC mass concentration and/or absorption coefficient data. The results shown in Figure 3.6b provide evidence that the lensing effect results in increased MAC values, as theoretically expected, and that variability of the degree of internal mixing of BC explains part of the temporal variability of the MAC values. However, the true magnitude of the lensing effect could possibly be smaller than implied by Figure 3.6b, as it cannot be excluded that experimental artefacts cause part of the correlation between MAC and NAM/EC.

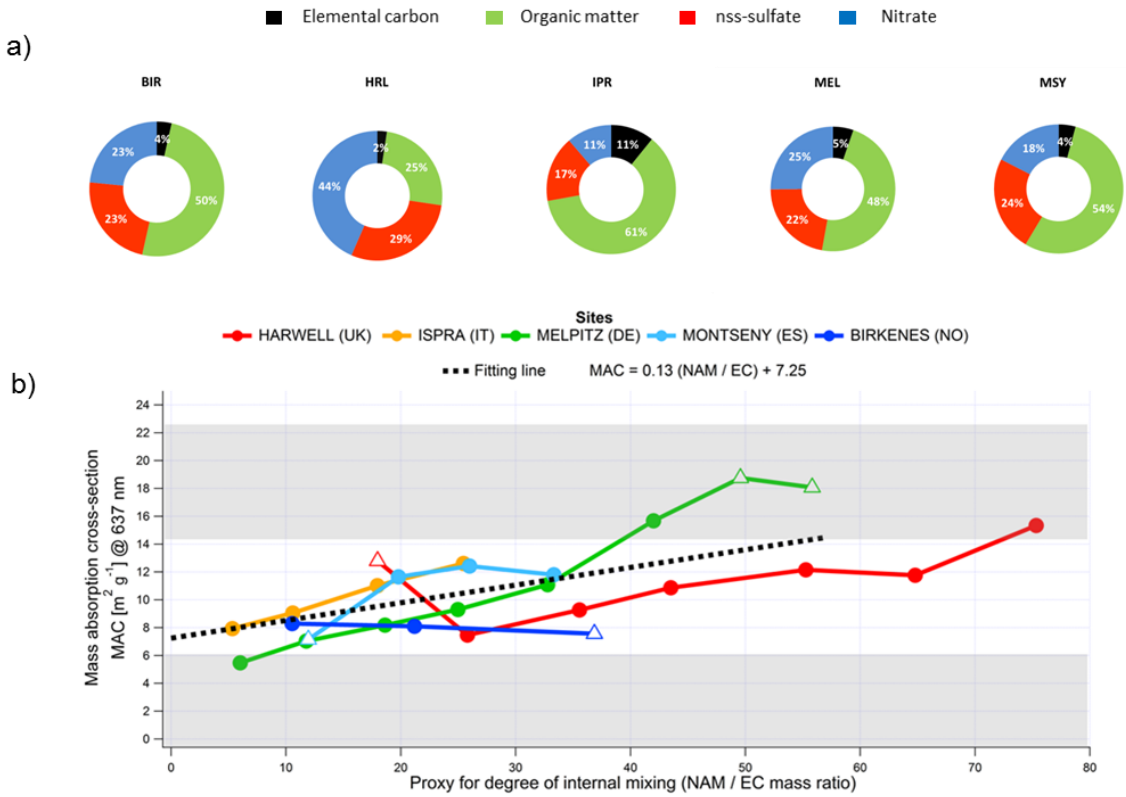

Figure 3.6 a) Annual mean mass fractions of major aerosol components (Organic matter, sulfate, nitrate and elemental carbon) used as input for the BC mixing state proxy. b) Dependence of the MAC on the proxy for the degree of internal mixing, defined as the mass ratio of non-absorbing matter (NAM) to elemental carbon (EC). Individual data points were grouped into bins with different NAM to EC mass ratios. The circular markers show the mean MAC value and the mean NAM to EC mass ratio of all data points falling into the corresponding bin. Averages based on 5-10 data points only are drawn as empty triangles instead of circles. The grey shading frames the approximate range of physically reasonable MAC values calculated using Mie theory. Experimental results outside this range are likely biased due to a substantial and asymmetric contribution from outliers in the EC mass concentration and/or absorption coefficient data.

The EC mass concentration appears as denominator in the equation to calculate both the MAC value and the NAM to EC ratio. Therefore, random noise in the EC mass measurement does also cause a positive correlation between MAC and NAM/EC. However, this effect caused – based on sensitivity analyzes – most likely only a minor fraction of the observed dependence of the MAC on NAM/EC.

Imperfect correction for multiple scattering within the filter matrix of the absorption instruments may potentially cause an apparent lensing effect as multiple scattering could be increased by deposition of light-scattering particulate matter. However, this is unlikely to cause an apparent absorption enhancement by a factor of ~2, in particular for the Melpitz, Ispra and Montseny sites, where a MAAP was used. We do not know whether the exceptional behavior observed for the Birkenes data in the bottom panel reflects a true difference in aerosol properties.

Interference from light-absorbing organic particulate matter would also cause an apparent lensing effect, however the estimated contribution to the total aerosol light absorption at wavelength larger than 637 nm has been shown to be less than 10% (Feng et al., 2013; Lack et al., 2012). Accordingly,

only a minor fraction of the MAC increase seen in the bottom panel of Figure 3.6b can potentially be caused by such interference.

So far we have argued that a substantial part of the observed MAC enhancement through internal mixing of BC with light-scattering particulate matter is likely reflecting a true lensing effect rather than just measurement artefacts and that it is essentially consistent with theoretical expectations. Several previous experimental investigations of the lensing effect using laboratory generated and ambient aerosols also reported substantial increase of light absorption by BC caused by coating acquisition, with maximal enhancement factors reaching up to ~2 (Schnaiter et al., 2005; Knox et al., 2009; Shiraiwa et al., 2010). By contrast, other studies on ambient aerosols report enhancement by as little as ~7% (Cappa et al., 2012; Lan et al., 2013). Our study provides another piece of evidence that the lensing effect does cause substantial MAC enhancement for internally mixed atmospheric BC particles.

3.4 Conclusion

In this study, we have presented the spatial and seasonal variability of the light absorption coefficient, the EC mass concentration and the corresponding BC mass absorption cross section (MAC) from long-term measurements at 9 rural background sites of the ACTRIS research infrastructure network across Europe. Homogeneity of data-sets was ensured by harmonization of all involved methods and instruments during extensive intercomparison exercises at the European Center for Aerosol Calibration.

The observed MAC values do not have distinct seasonal patterns at individual sites and annual values were equal within uncertainty across almost all sites. The geometric mean of the annual geometric means from each site is 10.0 $m^2 g^{-1}$ (geometric SD = 1.33 resulting in a range of 7.5 to 13.3 $m^2 g^{-1}$) at a wavelength of 637 nm. Consequently, we recommend this MAC value of BC, which is valid for EC mass defined through the EUSAAR-2 thermal-optical protocol, as best-estimate value for European background sites. However, absolute uncertainties of the reported MAC values remain as high as ± 30–70% due to the lack of appropriate reference methods. For example applying different thermal-optical protocols would potentially result in systematically different MAC values. This comprehensive data-set also provides evidence that part of the observed variability of the MAC value is likely caused by the lensing effect, i.e. that internal mixing of BC with other aerosol components enhances the light absorption by BC.

The observed absorption coefficients and EC mass concentrations exhibit distinct seasonal patterns. These patterns are almost equal for the absorption coefficient and EC at a given site, while they differ substantially between different sites. The former is a direct consequence of the fact that the MAC value exhibits only limited temporal variability without significant seasonal patterns.

Acknowledgments

ACTRIS project has received funding from the European Union's Horizon 2020 research and innovation programme under grant agreement No 654109. The research leading to these results has

received funding from the European Union Seventh Framework Programme (FP7/2007-2013) under grant agreement n° 262254. ACTRIS-2 is a European Project supported by the European Commission Horizon 2020 Research and Innovation Framework Programme (H2020-INFRAIA-2014-2015). This work was supported by grant from Labex OSUG@2020 (Investissements d'avenir – ANR10 LABX56) and by the ERC under grant 615922-BLACARAT.

Supplementary material

Comparison of parallel EC mass measurements using the VDI-2465 and EUSAAR-2 protocols at Melpitz

Figure S1 shows the monthly statistics of the ratio between EC mass concentrations measured in parallel with the VDI-2465 (thermal) and EUSAAR-2 (thermal-optical) methods at the Melpitz site in 2012. This ratio varies in time because it depends on the composition of the aerosol (Cavalli et al., 2016), but it exhibits a clear seasonal pattern due to the typical seasonal characteristics of aerosol composition at Melpitz. Therefore, the monthly median ratios are shown in Figure S1, which are defined to be the correction factor CF_{VDI} as a function of "month of year", form the basis to adjust VDI-2465 based EC mass measurements to EUSAAR-2 equivalent EC mass values, as detailed in Section 3.2.3.1.

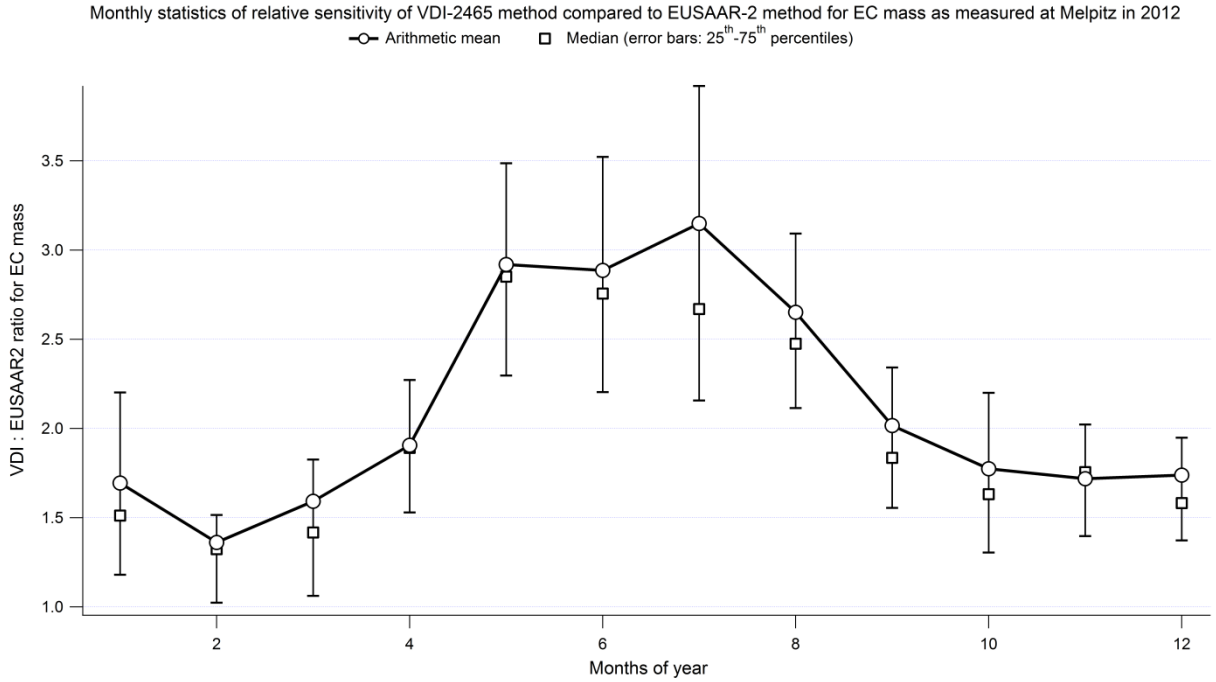

Figure S1: Seasonal pattern of the ratio between EC mass concentrations measured in parallel with the VDI-2465 (thermal) and EUSAAR-2 (thermal-optical) methods at the Melpitz site in 2012.

4 Mixing state and absorbing properties of black carbon during Arctic haze

M. Zanatta[1,2], P.Laj[1], M. Gysel[2], U. Baltensperger[2], S. Vratolis[3], K. Eleftheriadis[3], M. Irwin[4], Y. Kondo[4] and H. W. Jacobi[1]

[1]*Laboratoire de Glaciologie et Géophysique de l'Environnement, Université Grenoble Alpes/CNRS, Grenoble, France.*

[2]*Laboratory of Atmospheric Chemistry, Paul Scherrer Institute, Villigen PSI, Switzerland*

[3]*ERL, Demokritos National Center of Scientific Research, Institute of Nuclear Technology and Radiation Protection, Attiki, Greece*

[4]*Research Center for Advanced Science and Technology , University of Tokyo , Tokyo , Japan*

In preparation for Journal of Geophysical Research

This work is part of the CLIMSLIP (climate impact of short-lived pollutants and methane in the Arctic) project. Within other goals, the project aims to understand the role of black carbon (BC) as climate forcer in the Arctic. However the global radiative forcing of BC is positive, its amplitude is variable and depends on the geographic location, furthermore the effects of absorbing aerosols on the radiative budget are amplified in regions with low surface albedo as the Arctic (Zarzycki and Bond, 2010). While the increase of Arctic ocean temperature, 1.5°C in the last decade (AMAP, 2011), and the retreat of perennial ice, 9-14% over the period 2001-2011 (Vaughan et al., 2013) are considerable, the role of black carbon in these processes is not well understood yet. Beside BC-cloud interaction and albedo reduction of snow, BC may influence Arctic climate by aerosol-radiation interaction, directly warming the corresponding aerosol layer. Such warming depends on the total atmospheric burden of BC, but also on the efficiency of BC to absorb light, which might be enhanced by mixing of BC with other atmospheric non-absorbing materials (lensing effect). This process likely takes place in the Arctic due to long range transport, which promotes internal mixing and thus absorption enhancement. The mixing induced by long range transport has been observed and characterized in the Atlantic ocean (China et al., 2015) but never investigated in the Arctic. The objective of this work was to fill this knowledge gap on black carbon mixing and the effects on BC optical properties in Arctic region.

During field experiments conducted at the Zeppelin research station in Svalbard during the 2012 Arctic spring, we investigated the relative precision of different BC measuring techniques. A single particle soot photometer was then used to assess the coating of Arctic black carbon. This allowed quantifying the absorption enhancement induced by internal mixing via optical modelling. The optical assessment of aged black carbon in the arctic will be of major interest for future radiative forcing assessment.

Optical characterization of the total aerosol indicated that in 2012 no extreme smoke events took place and that the aerosol population was dominated by fine and non-absorbing particles. The single particle soot photometer (SP2) measurements showed a rBC mean mass concertation of 35 ng m^{-3}, while the mass was log-normally distributed around 240 nm of mass equivalent diameter. On average the number fraction of rBC-containing particles was less than 5%. rBC cores with a diameter between 170 nm and 280 nm were found to be covered by a layer of non-absorbing material having a median thickness of ~50 nm leading to a core-shell diameter ratio of 1.6. These numbers well represent aged BC, while observed mean diameter was unusually high compared to previous studies. Comparison of measured rBC and equivalent eBC concentration detected with the continuous soot monitoring system (COSMOS) showed good agreement (15%), suggesting that the two techniques are suitable for Arctic observations. Combining absorption coefficient observed with an aethalometer and rBC mass concentration from SP2, a mass absorption cross section (MAC) of 8.6 m^2 g^{-1} was found at a wavelength of 550 nm. Similar value (8.22 m^2 g^{-1} at 550 nm) was calculated using Mie theory and assuming a black carbon population homogeneously coated with a shell of 50 nm composed by organic matter and sulfate. The lensing effect triggered by the coating leads to 46% enhancement of MAC compared to a bare BC core. The MAC derived with Mie theory enabled to calculate absorption coefficient from rBC mass concentration detected with the SP2. Reliability of our approach was

ensured by a good agreement (18%) between observed and calculated absorption coefficients. Similar exercise performed using common MAC values adopted by radiative models suggested that wrong assumptions in BC optical properties might introduce discrepancies up to 80% Within this work we presented the major optical properties of the total aerosol in the Arctic, with particular emphasis on the dependency of BC absorption on internal mixing. These values, peculiar of the Arctic and poorly characterized in the past, will help to reduce the uncertainty of radiative estimations based on a priori assumptions.

Abstract: Aging promotes internal mixing of black carbon (BC), leading to absorption enhancement, which have never been investigated in the Arctic regions. Optical properties of refractory black carbon (rBC) and the influence of internal mixing were investigated at the Zeppelin Arctic station during field experiments conducted during the 2012 Arctic spring. Optical characterization of the total aerosol indicated that in 2012 no extreme smoke events took place and that the aerosol population was dominated by non-absorbing particles. The single particle soot photometer (SP2) measurements showed a rBC mean mass concertation of 35 ng m^{-3}, while the mass was log-normally distributed around 240 nm of mass equivalent diameter. On average the number fraction of rBC-containing particles was less than 5%. rBC cores were found to be covered by coating having a median thickness of ~50 nm leading to a core-shell diameter ratio of 1.6. Comparison of measured rBC and equivalent eBC concentration detected with the continuous soot monitoring system (COSMOS) showed good agreement (15%), suggesting that the two techniques are suitable for Arctic observations. Combining absorption coefficient observed with an aethalometer and rBC mass concentration from the SP2, a mass absorption cross-section (MAC) of 8.6 m^2 g^{-1} was found at a wavelength of 550 nm. Similar value (8.22 m^2 g^{-1} at 550 nm) was calculated using Mie theory and assuming a black carbon population homogeneously coated with a shell of 50 nm composed by organic matter and sulfate. The lensing effect triggered by the mixing leads to 46% enhancement of MAC compared to a bare BC core. Mie theory derived MAC enabled to calculate absorption coefficient from rBC mass concentration detected with the SP2. Reliability of our approach was ensured by a good agreement (18%) between observed and calculated absorption coefficients. Similar exercise performed using common MAC values adopted by radiative models suggested that wrong assumptions in BC optical properties might introduce discrepancies up to 80% compared to observed absorption coefficients in the Arctic. Moreover, the single scattering albedo of the total aerosol seems to be unaffected by changes in absorption of BC. Absorption enhancement, due to lensing effect, induces a decrease in total single scattering albedo f less than 1%, suggesting that the weight of BC to aerosol-radiation interaction might be negligible. Our work provides all the major optical properties of total aerosol and black carbon to minimize the uncertainty of radiative estimations based on a priori assumptions in Arctic region.

4.1 Introduction

Aerosol particles interact with solar radiation and clouds playing a relevant role in climate change, the latter is thought to be accentuated in polar regions like the Arctic (AMAP, 2015) where a consistent reduction of sea ice cover and amplification of near-surface air temperature is observed (Gillett et al., 2008; Screen and Simmonds, 2010). During late winter favorable transport pathways (Barrie, 1986) and scarce removal mechanisms (Shaw, 1995) lead to an enhancement of aerosol concentration, such well known event is defined as Arctic haze. The Arctic haze aerosol population is composed by sulfate, organic matter, ammonium, nitrate, mineral dust, and black carbon (BC) (Quinn et al., 2007). Among the other particles, BC is emitted by incomplete combustion of fossil fuels, biofuels and biomass, and due to its marked light absorption properties is responsible of a global positive radiative forcing (RF;

Bond et al., 2013). More specifically, BC may influence the arctic radiative budget by altering the radiative properties of clouds and snow, and absorbing the solar radiation in the atmosphere (AMAP, 2011). Despite the fact that Flanner (2013) demonstrated that the combination of these processes leads to a net warming of the Arctic surface, the variability of the net RF induced by BC in the Arctic is still consistent. In fact, BC climatic effect depends on its vertical distribution. High altitude BC would cool the Arctic surface, due to surface dimming and inefficient convection mixing (Shindell and Faluvegi, 2009; Flanner, 2013; Sand et al., 2013). On the other side, Flanner (2013) found that low-altitude BC (pressure > 430 hPa) causes strong surface warming by depositing energy near the surface, "burning off" low-level clouds, and decreasing the atmospheric stability. The sum of the above listed processes triggers the snow and ice albedo feedbacks, which amplifies surface warming. Nevertheless, all these effects are proportional to the atmospheric burden of BC, which have been observed to vary between 20-80 ng m^{-3} in late winter and early spring and less than 10 ng m^{-3} in summer at Alert (Canada), Barrow (Alaska), Pallas (Finland) and Zeppelin (Norway) sites (AMAP report, 2015). Similar trends are observed at Alert, Barrow and Zeppelin by Sharma et al. (2004, 2006) and at Zeppelin by Eleftheriadis et al. (2009). All the BC concentrations aforementioned refer to equivalent BC (eBC) that is converted from absorption coefficient using the mass absorption cross-section (MAC); the latter defines the absorption power of light in unit of mass. The MAC is also used in radiative forcing calculation to convert the BC atmospheric concentration into absorption coefficient. Due to long range transport, the BC observed in the Arctic is mainly aged and heavily processed. Thus a significant amount of internally mixed BC may be found (Yamanouchi et al., 2005), inducing a potential increase of absorbed light. In fact, the presence of a coating on a BC core causes the so-called "lensing effect", which leads to a MAC enhancement between 30-50 % (Bond et al., 2006a; Schwarz et al., 2008a). Adachi et al. (2010) showed that the presence of a coating on BC particles enhances the global radiative forcing of BC by ~70 %. Nevertheless, enhancement quantification is controversial (Lack et al., 2009) and affected by large variability associated to assumption of mixing geometry (Adachi et al. 2010), morphology (Scarnato et al., 2013), and accuracy in coating thickness quantification. At the current state of arts, the optical properties of arctic black carbon and its mixing state are poorly characterized. In order to decrease the uncertainty of RF and provide accurate BC concentrations in the Arctic regions, a proper quantification of BC absorbing properties as function of mixing is highly needed. Within this work we investigated the relative precision of different BC measuring techniques and calculated in situ MAC value for European Arctic. A single particle soot photometer was then used to assess BC mixing geometry and coating thickness. This allowed quantifying the absorption enhancement induced by internal mixing via optical modelling. Finally the impact of absorption enhancement on the single scattering albedo of the total aerosol is addressed.

4.2 Material and methods

4.2.1 Sampling site and meteorology

The CLIMSLIP (Climate impacts of short-lived pollutants in the Arctic) field experiments took place between the 22 March and 11 April 2012. The instrumentation was deployed at the Zeppelin station, (474 m asl; 78°54'N, 11°53'E), close to Ny-Ålesund (10m asl), Svalbard, Norway. The site is mainly influenced by free tropospheric air masses impacted by long-range transport from Europe and Russia, while local anthropogenic emissions rarely reaches the site (Beine et al., 1999). The campaign was characterized by anticyclonic conditions leading to the dominance of clear sky condition, only a few and weak snow precipitation events on 23/24 and 29/30 March were observed. The average temperature was below -10 °C, the relative humidity oscillated around 75 %, and pressure was constantly exceeding the 900 hPa. The wind direction was dominated by northerly winds with less frequent southerly inclusions, while no high wind speeds were observed (average wind speed ~3 ms^{-1}).

4.2.2 BC measuring techniques

4.2.2.1 The single particle soot photometer (SP2)

The single particle soot photometer (SP2, Droplet Measurement Technology, Boulder, CO) was used to observe concentration, size distribution and mixing state of refractory black carbon (rBC) at the Zeppelin site. The operation principles are given by Stephens et al., 2003; Schwarz et al., 2006; Moteki and Kondo (2010) and shortly summarized as following. The SP2 is based on the laser induced incandescence technique: the particles are heated to their vaporization point via irradiation using an intra-cavity Nd:YAG laser at 1064 nm of wavelength. The intensity of the thermal radiation emitted by rBC-containing particles at the boiling point is proportional to the rBC mass contained in the particle. The high temperature reached by the core induce the evaporation of all non-refractory material condensed on the rBC core, so that the quantification of the particle mass is unaffected by presence of non-refractory organic and inorganic compounds. From the incandescence thermal radiation, the user is able to retrieve the number and mass concentration of rBC, and the mass equivalent diameter (D_{MEV}), calculated from the particle mass assuming its spherical shape and a void-free density of 1800 kg m^{-3}. The technique allows 100 % detection efficiency of rBC particles between 80 nm and 550nm of D_{MEV}. The relatively narrow size detection range of the SP2 might lead to substantial underestimation of rBC mass concertation (Schwarz et al., 2006; Kondo et al., 2011; Reddington et al., 2013; Dahlkötter et al., 2014). The mass contribution of rBC cores having an estimated diameter between 10 and 80nm and between 550 and 1000 nm was extrapolated from the log-normal fit of the observed mass size distribution between 80 and 550 nm and quantified as 10 % of the total rBC mass (Figure 4.1). In the rest of the present work the rBC mass concentration will be permanently corrected accounting for this mass bias.

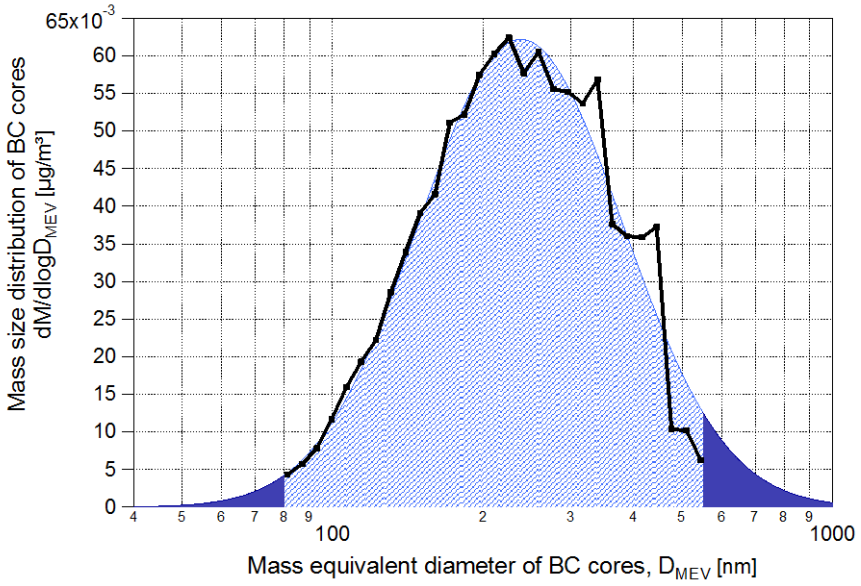

Figure 4.1 Mass size distribution of rBC cores and related log-normal mass size distribution fit. Dashed area: size detection range of SP2 between 80 and 550 nm. Solid area: size detection range extended from 40 to 1000 nm using the lognormal fit.

An avalanche photodiode (APD) was used to detect diffused light at 1064 nm, enabling us to observe the partial scattering cross-section, which is then converted in optical diameter assuming an index of refraction of 1.5. The optical size detection range of BC-free particles is between 150 nm and 500 nm. In order to investigate the internal mixing of rBC with other non-refractory materials we used the leading edge only (LEO) approach described by Gao et al. (2007). The method, implemented by (Laborde et al., 2012a), allows determining the time evolution of the scattering cross section of both refractory and non-refractory particles passing through the laser beam. The decrease of the scattering cross-section from the leading edge of the scattering signal until the beginning of incandescence allows estimating the thickness of coating shell. For pure rBC core and non-absorbing coating we used a refractive index of 2.26 + 1.26i and 1.50 + 0.00i respectively. This fully constrains the total particle size and coating thickness, defined as the difference between the radii of the total particle and the rBC core. All technical details, methods and uncertainties are given by (Gao et al., 2007; Laborde et al., 2012b; Dahlkötter et al., 2014) respectively.

With the SP2 was possible to partially investigate the geometry of the internally mixed rBC. Fragmentation of coated BC particles in laser beam might occur, involving the shattering of BC core from the non-absorbing coating (Sedlacek et al., 2012; Dahlkötter et al., 2014). The cause of this mechanism was attributed to the eccentric location of the BC core respect to the internally mixed cluster. Two possible mixing geometries of BC-containing particles might initiate this process: a “near surface” and “attached” configuration. The former implies that the BC component is embedded under the surface of the non-absorbing coating assuming non-concentric core shell geometry. Otherwise, the attached geometry describes the presence of a BC aggregate “attached” on the surface of a non-absorbing particle. BC particles having an attached geometry may be identified using the approach developed by Moteki et al. (2014). The algorithm is based on the variation of the time-dependent scattering cross section ($C_{sp}(t)$) in the laser beam and was already applied in urban

environment by the same author. Briefly, for a coated BC core, with a concentric geometry, the $C_{sp}(t)$ decreases to zero while entering the laser until complete evaporation of coating and vaporization of the core at the incandescence point. Considering the attached geometry, the thermic transfer from the core to the non-absorbing component is not efficient, thus before incandescence the size of the cluster stays constant, as well as the $C_{sp}(t)$. Sharp and consistent drop in $C_{sp}(t)$ between the beginning of measurements (edge of the laser beam) and at rising edge of incandescence indicates a consistent evaporation of coating, due to efficient thermic transfer induced by concentric geometry. Almost constant $C_{sp}(t)$ values between the aforementioned steps indicates no evaporation of non-absorbing matter, inefficient thermic transfer and thus and attached geometry. The same approach, with in situ specific operational parameters, was used here to discriminate BC-containing particles having an attached geometry.

The SP2 calibration for incandescence and scattering signals was performed in situ using size selected fullerene particulate (Alpha Aesar; #FS12S011) and spherical polystyrene latex size standards (Thermo Scientific, formerly Duke Scientific) respectively. A complete description of calibration set-up, standard materials and operative principles can be found in Moteki and Kondo (2010); Gysel et al. (2011); Baumgardner et al. (2012); Laborde et al. (2012a, 2012b).

4.2.2.2 The continuous soot monitoring system

The continuous soot monitoring system (COSMOS, Kanomax, Osaka, Japan) is a single wavelength photometer measuring the light attenuation through a collection filter (Miyazaki et al., 2008). The variation in attenuation derived with the COSMOS instrument is proportional to the accumulated absorbing-refractory material on the filter. Relatively volatile aerosols are removed by the heated inlet (400°C), so that the attenuation measurements are non-influenced by internal mixing or presence of absorbing-non-refractory material, which might lead to a possible absorption coefficient overestimation. Therefore, the mass absorption cross-section is only slightly influenced by mixing, leading to a low site specificity and spatial variability (Kondo et al., 2009). Deepness at which particles are imbedded in the filter might bias the measurements, correction for such effects, related to particles dimension, was developed by Nakayama et al. (2010) and applied in this work.

4.2.3 Additional dataset and optical modelling

Data from several instruments were used to infer optical properties of the total aerosol: a 7-wavelength aethalometer (Model A31, Magee Scientific Corporation, Berkeley, CA), a nephelometer (Model 3563, TSI Inc, St. Paul, MN) and a sun precision filter radiometer (PFR; WORCC, PMOD/WRC, Davos Dorf, CH-7260, Switzerland).

The nephelometer was used to observe scattering (σ_{sp}) and back scattering (σ_{bsp}) coefficients at three different wavelengths (450, 500, and 700 nm) in dry conditions (RH<20 %). A full characterization of

the nephelometer and correction procedure for truncation error applied in this work is given by Anderson and Ogren (1998) and Müller et al. (2009). Using the scattering and back scattering coefficients σ_{sp} and σ_{bsp} it was possible to derive the asymmetry parameter (*g*), which is of crucial importance for radiative transfer models. The asymmetry parameter describes the angular distribution of diffused light and discerns whether the particles scatter radiation preferentially to the front or back. Here is calculated applying the Henley-Greenstein approximation, which parametrizes *g* as a function of the backscattered fraction of light (Wiscombe and Grams, 1976). It was shown that this approximation is appropriate for a submicron aerosol population (Fiebig et al., 2005; Andrews et al., 2006).

The aethalometer was used to monitor the absorption coefficients (σ_{ap}) between 370 nm and 990 nm. This photometer measures light attenuation (*ATN*) through a filter, the observed change in attenuation (*ΔATN*) is directly proportional to the mass of absorbing material loaded over the time step (*Δt*), which is firstly estimated as attenuation coefficient (σ_{nt}) (Hansen et al., 1984)

$$\boldsymbol{\sigma_{ATN}(\lambda) \equiv \frac{A}{Q}\frac{\Delta ATN(\lambda)}{\Delta t}} \tag{4.1}$$

where *A* and *Q* represent the area of the collection spot on the filter and the sampling flow respectively. This technique suffers from instrumental artifacts as multiple scattering and loading effects. The latter is corrected following the Virkkula et al. (2007) algorithm, which assumes that the last σ_{ATN} values measured on the spot *i* and the first values measured on the next filter spot *i+1* should be equal. The σ_{ATN} measured on pristine filter spot is considered to do not suffer of loading artifacts and to be correct (σ_{ATN0}). The attenuation coefficient corrected for loading effect ($\sigma_{ATN,R\_corrected}$) is:

$$\boldsymbol{\sigma_{ATN,R_{corrected},n} = \frac{\sigma_{ATN,n}}{R} = (1 + k_i \cdot ATN) \cdot \sigma_{ATN,n}} \tag{4.2}$$

where *R* is the correction factor for loading effect and K_i parametrizes the variation of attenuation induced by loading effect, and is calculated as:

$$\boldsymbol{k_i = \frac{\sigma_{ATN0}(t_{i+1,first}) - \sigma_{ATN0}(t_{i,last})}{ATN(t_{i,last}) \cdot \sigma_{ATN0}(t_{i,last}) - ATN(t_{i+1,first}) \cdot \sigma_{ATN0}(t_{i+1,first})}} \tag{4.3}$$

where $t_{i,last}$ is the time of the last measurement on the filter spot *i* and t_{i+1},first is the time of the first measurement on the next filter spot *i+1*. A k_i value is therefore determined for each filter spot and applied to all *n* measurements on the *i*th filter spot. The multiple scattering artefact is corrected using a the approach developed by Weingartner et al. (2003). The related correction factor C_{Ref} is defined as

the relative sensitivity of attenuation coefficient, corrected for loading effect, over the absorption coefficient value observed by a reference technique (C_{Ref}). The C_{reve} used in the present work was at 3.5 (World Meteorological Organization and Global Atmospheric Watch; Zanatta et al., in preparation)

$$C_{Ref} = \frac{\sigma_{ATN,R_{corrected},n}(\lambda)}{\sigma_{ap,ref}(\lambda)} \tag{4.4}$$

Finally, the absorption coefficient is calculated as

$$\sigma_{ap}(\lambda) = \frac{\sigma_{ATN}(\lambda)}{R \cdot C_{Ref}} \tag{4.5}$$

Merging absorption and scattering coefficients we calculated the single scattering albedo (SSA) defined as:

$$SSA(\lambda) = \frac{\sigma_{sp}(\lambda)}{\sigma_{sp}(\lambda) + \sigma_{ap}(\lambda)} \tag{4.6}$$

The sun-radiometer installed at Ny-Ålesund was used for aerosol optical depth (AOD) observations at 368, 412, 500, and 862 nm. The AOD is used to assess the total aerosol loading over the vertical column. Indication on the particles size may be derived from the wavelength dependency of AOD. This dependency is parametrizes using the Ångström exponent of the AOD (α_{AOD}) defined as:

$$\alpha_{AOD} = -\frac{log(AOD^{\lambda 1}/AOD^{\lambda 2})}{log(\lambda_1/\lambda_2)} \tag{4.7}$$

Additional information on the aerosol size distribution was derived from the Ångström exponent difference (Deltaα). The latter was calculated as the difference between α_{AOD} at 412 and 675 nm and α_{AOD} at 675 and 862 nm following the scheme of Kaufman (1993). Negative Deltaα values indicate the dominance of particles in the fine mode. The light absorption strength of an aerosol may be expressed as the mass absorption cross-section (MAC), which is defined as the absorption coefficient normalized to the mass of the absorbing material. In our work we calculated the MAC of rBC (MAC_{rBC}) merging together σ_{ap} derived from aethalometer measurements and rBC mass concentration measured (m_{rBC}) using the SP2:

$$MAC_{rBC}(\lambda) = \frac{\sigma_{ap}(\lambda)}{m_{rBC}} \tag{4.8}$$

The list of instruments used in this work with measured and derived parameters is presented in Table 4.1.

The influence of a coating shell on the absorbing properties of BC was investigated using the "BHCOAT" code (Bohren and Huffman, 1998) which is based on Mie theory. The model assumes that the BC particles exist with spherical shape, and are enclosed by a concentric layer of non-absorbing material, such geometry is called "coated" or "encapsulated". The BHCOAT code needs specific inputs like the BC size distribution, the coating thickness, the refractive index (RI) of the absorbing core and non-absorbing coating, all of which are derived from the in-situ SP2 measurements. While RI values were taken by previous works, size distribution and coating thickness of rBC particles were observed with the SP2. In this way was possible to simulate the absorption enhancement by mixing representative of Arctic conditions. Absorption enhancement at a specified wavelength is defined as the ratio between the MAC of BC core having a certain size and coating thickness, and the MAC of the same core without coating.

Table 4.1 Instruments used in the present study.

Instrument	Parameter	Wavelength [nm]
Aethalometer	Absorption coefficient, eBC	370; 470; 520; 590; 660; 880; 990
Continuous soot measuring system (COSMOS)	eBC	565
Nephelometer	Scattering and backscattering coefficient	450; 500; 700
Single particle soot photometer	Mass concentration, size distribution and coating thickness of rBC	200-600
Sun-radiometer	AOD	368; 412; 500; 862

4.3 Arctic spring aerosol

4.3.1 Aerosol optical properties

Here we present an optical characterization of the total aerosol (Figure 4.2). The average AOD at 500 nm was 0.097 ± 0.022 with a maximum of 0.17. Such low values indicate a low aerosol burden, coherent with previous Arctic AOD values observations as observed by Yamanouchi et al (2005); Hoffmann et al. (2009). Nevertheless, the AOD observed in this work was considerably smaller compared to the intense smoke event recorded in 2006 by Treffeisen et al. (2007) at the Zeppelin station, where a 0.68 average AOD at 500nm was detected. As in Yamanouchi et al. (2005), Arctic haze conditions were identified here as function of AOD values at a wavelength of 550 nm: AOD>0.1 are considered to represent haze conditions while background conditions are identified by AOD<0.06. During the CLIMSLIP 2012 experiment 44% of AOD measurements were larger than 0.1, while 28% fell between 0.9 and 0.1. No AOD under 0.06 were observed, indicating that the measuring period was largely influenced by haze conditions. α_{AOD} average is quantified in 1.4 ± 0.22, which suggests the

presence of slightly larger particles compared to the smoke event of 2006, when a α_{AOD} of ~2 was observed (Treffeisen et al., 2007). Nevertheless, a consistent shift in size towards coarse mode is improbable as evidenced by dominant (90 % occurrence) negative Ångström exponent difference (Deltaα). However, the relative error of this property is higher than 50% for AOD≤0.1 (Gobbi et al., 2007), this result suggests that the aerosol population at the Zeppelin station during spring 2012 was dominated by the fine mode particles. Average scattering coefficient was 13.1 ± 5.72 Mm^{-1} at 550 nm. Previous Arctic hazes at Zeppelin station were characterize by average value of 9.8 Mm^{-1} (Yamanouchi et al., 2005). Calculated average *g* at 550 nm was 0.68 ± 0.018, exactly in the middle of *g* values for nuclei (0.637) and accumulation (0.745) modes calculated by Tomasi et al. (2015) during Arctic haze conditions. SSA_{550} average was quantified in 0.977 ± 0.00748 with maximum and minimum values at 0.96-0.99 respectively. Despite differences showed in aerosol loading and Ångström exponent, the single scattering albedo observed here and during the smoke event of 2006 by Lund Myhre et al. (2007) are surprisingly similar (SSA_{450}=0.98), suggesting not dissimilar particle composition but only different loads.

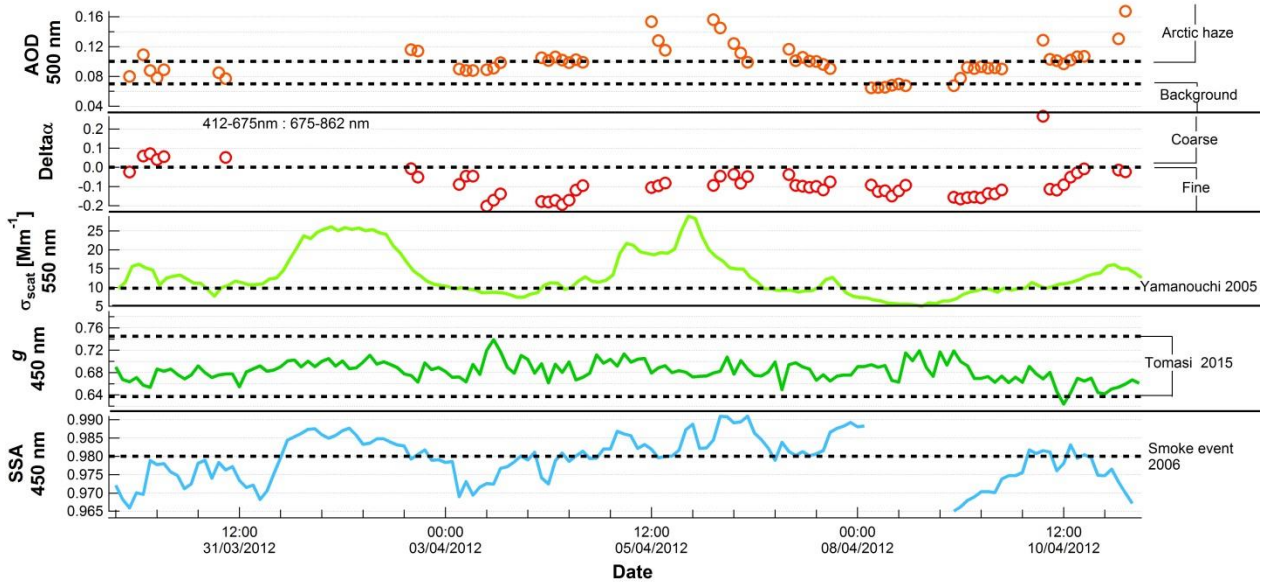

Figure 4.2 Time series of aerosol optical properties. In orange: Aerosol optical depth at 500 nm, AOD>1 Arctic haze conditions, AOD<0.7 background conditions. In red: difference of Ångström exponent from AOD at 675 and-862 nm and 412 and 675 nm, positive Deltaα: coarse mode, negative Deltaα: fine mode. In light green: scattering coefficient at 550 nm, σsp of 2000 Arctic haze at 9.8 Mm-1 from Yamanouchi et al., 2005. Dark green: asymmetry parameter at 450 nm, range of g observed by Tomasi et al. (2015). In blue: single scattering albedo at 450 nm, 2006 smoke event had a SSA of 0.98.

Aerosol optical properties observed during spring 2012 reflect previous measurements, indicating that 2012 spring was not influenced by intense smoke episodes. Despite low absolute AOD values, the measuring period was dominated by Arctic haze conditions with total aerosol size centered in the fine mode. Single scattering albedo suggests that absorbing aerosols were the minor components of the 2012 Arctic spring.

4.3.2 Arctic black carbon

4.3.2.1 Black carbon measuring instruments comparison

The parallel measurements at the Zeppelin station between the SP2, the COSMOS and the aethalometer were used to perform an inter-comparison during the period from 30 March until 12 April ensuring 254 hours of simultaneous measurements. Since the measurement periods of this intercomparison and the whole campaign were different, the absolute values of the quantified properties might differ.

Despite being a filter-based instrument, the design of the COSMOS instrument permits to obtain the eBC mass concentration (m_{eBC}) that is less influenced by mass absorption variability (Kondo et al., 2009). Thus, the relative sensitivity of COSMOS versus SP2 was directly calculated as the ratio between m_{eBC} and m_{rBC} (Figure 4.3a). COSMOS and SP2 showed a good correlation with a Pearson correlation coefficient of 0.89. The distribution of points in the scatter plot in Figure 4.3c was fitted with a least orthogonal linear fit forced through the origin, the calculated slope of the regression line indicates that eBC and rBC mass concertation agrees within 15 %.

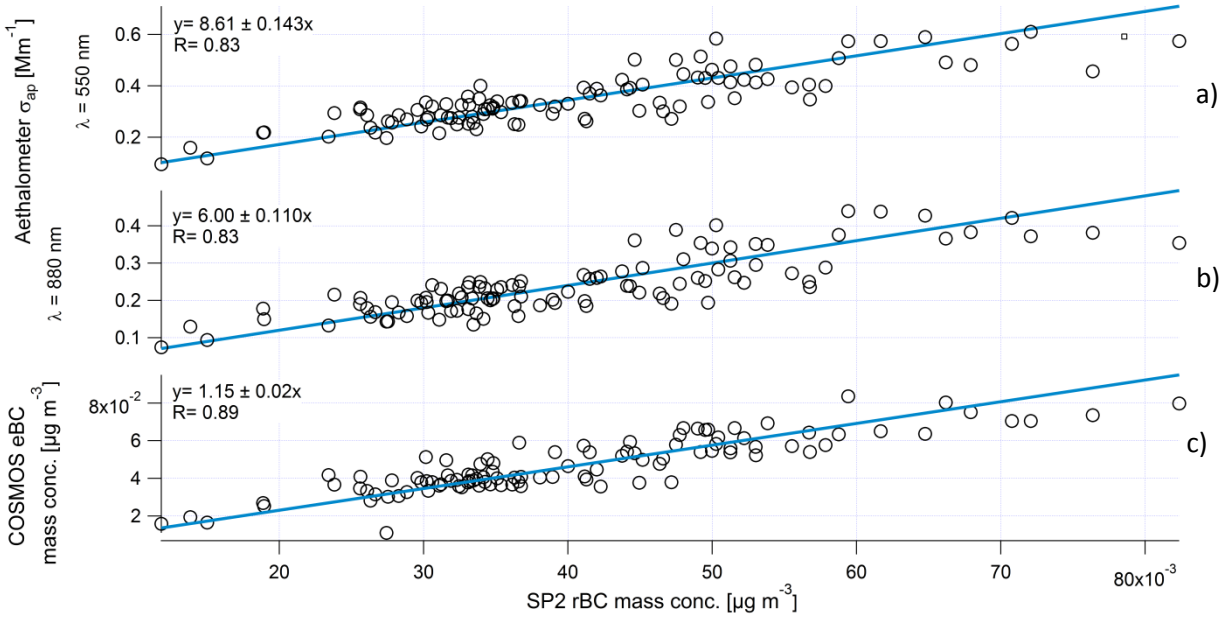

Figure 4.3 Scatter plots: a-b) absorption coefficient at 550 and 880 nm of wavelength (λ) measured with the aethalometer vs rBC mass concentration detected with the SP2;c) eBC mass concentration from COSMOS vs rBC mass concentration detected with the SP2. Least orthogonal linear fit drawn in blue.

A different approach was used in order to compare the aethalometer and SP2 observations. The aethalometer eBC mass concentration is extremely sensitive to the mass absorption cross section used during the conversion from the absorption coefficient. In order to not introduce an additional degree of uncertainty we directly compared the absorption coefficient derived by the aethalometer

at wavelengths of 550 and 880 nm with the rBC mass concentration detected by the SP2 (Figure 4.3a&b). In this case the relative sensitivity of the aethalometer compared to the SP2 represents the mass absorption cross-section of rBC (MAC_{rBC}). Aethalometer absorption coefficients and rBC mass concertation showed a Pearson correlation coefficient of 0.83. MAC_{rBC} is determined as the slope of linear regression of scatter plots showed in Figure 4.3 and quantified in 8.61 ± 0.143 $m^2 g^{-1}$ and 6.00 ± 0.143 $m^2 g^{-1}$ at wavelengths of 550 and 880 nm respectively. The MAC values derived here might be overestimated by at least a further 10-15%, due to the possible underestimation of rBC mass concertation discussed before. MAC in arctic locations was already investigated in previous works, calculated combining light absorption measured with an aethalometer (model AE-6) and elemental carbon (EC) mass concentration using thermal technique (Cachier et al., 1989) and quantified in 19 $m^2 g^{-1}$ and 29 $m^2 g^{-1}$ at a wavelength of 880 nm for winter/spring and for summer respectively (Sharma et al., 2004, 2006). It must be pointed out that the MAC presented by Sharma et al. (2004) was calculated from absorption coefficients uncorrected for loading and multiple scattering effects. Therefore it has to different contributions: one associated to direct absorption of imbedded BC and a second one related to the instrumental artifacts. Thus, the MAC presented there is not representative only of BC optical properties.

4.3.2.2 rBC concentration and size distribution

Figure 4.1 shows the mass size distribution of rBC cores; the diameter distribution peaked at 240 nm with a large fraction of the rBC mass between 200-300 nm of equivalent mass diameter. This value is higher compared to urban plumes, where mean rBC mass size distribution have been observed around 150 nm (Laborde et al., 2013), but closer to other SP2 Arctic studies which observed mean size diameter of 190 nm of mass equivalent diameter (Raatikainen et al., 2015b; Taketani et al., 2016). The shift of the rBC mean size is probably due to long range transport and accumulation, which promote particles coagulation (Shiraiwa et al., 2008 ; Tunved et al., 2013). On the other side, Moteki et al. (2012), showed that preferential wet removal of large particles might decrease the mean diameter of long range transported aerosols. The average observed rBC mass concentration was 35 ng m^{-3} ± 17 ng m^{-3} (average ± standard deviation) with one single event (6 hours average) showing concentration higher than 80 ng m^{-3}. Two studies recently investigated the BC presence in the Arctic. (Raatikainen et al., 2015b) found an average rBC concentration of 26 ng m^{-3} at the Pallas Global Atmosphere Watch (GAW) station (68°N, Finland) between December and January. Taketani et al. (2016) investigated the spatial variability of rBC at sea level altitude between the Northern-Pacific and Arctic oceans during September. At latitude higher than 75°N the rBC mass concentration was highly variable (0-60 ng m^{-3}), with an averaged quantified in 1 ± 1.2 ng m^{-3}. Our work and the work of (Raatikainen et al., 2015b) are in the same order of magnitude, the discrepancy is mostly caused by the different sampling period and by the intense stagnation event observed in 2012. Plausible reasons for the large discrepancy in rBC mass concertation between this work and Taketani et al. (2016) are unknown.

4.3.2.3 rBC mixing

As described in Section 4.2.2.1, it was possible to discriminate between two mixing geometries: coated and attached. We learned that the only 2% of rBC containing particles were present with the attached geometry. BC with the same mixing geometry was found to represent less 10% in urban environment (Moteki et al., 2014). Nevertheless, our result is in contrast with Taketani et al. (2016), who found a notable fraction (~20%) of attached and bare rBC-containing particles in the Arctic ocean (north of Barrow, Alaska). Due to the low BC concentration was not possible to investigate more in the details the time variability of attached rBC particles fraction, but its low number fraction and the low occurrence of fragmentation process (Sedlacek et al., 2012; Dahlkötter et al., 2014) supported the hypothesis that the core-shell is the dominant parametrized geometry after aging processes.

The rBC coating thickness investigation was restricted to rBC cores with a mass equivalent diameter between 160 nm and 280 nm. This size window comprised 29 % of all rBC particles and 42 % of the total rBC mass. As shown in the lower panel of Figure 4.4, the thickness of the non-absorbing shell was found to have an average value of (59 ± 40) nm. Although the size of the core diameter did not influence the mean and median coating thickness, a great variability in thickness was observed with values as high as 120 nm (90^{th} percentile respectively) and showed in Figure 4.4. The ratio between the core-shell particle diameter (D_{Shell}) and the core diameter (D_{Core}), called diameter ratio, was found to be 1.61 ± 0.69, 20% smaller compared to Finnish Arctic rBC (Raatikainen et al., 2015b).

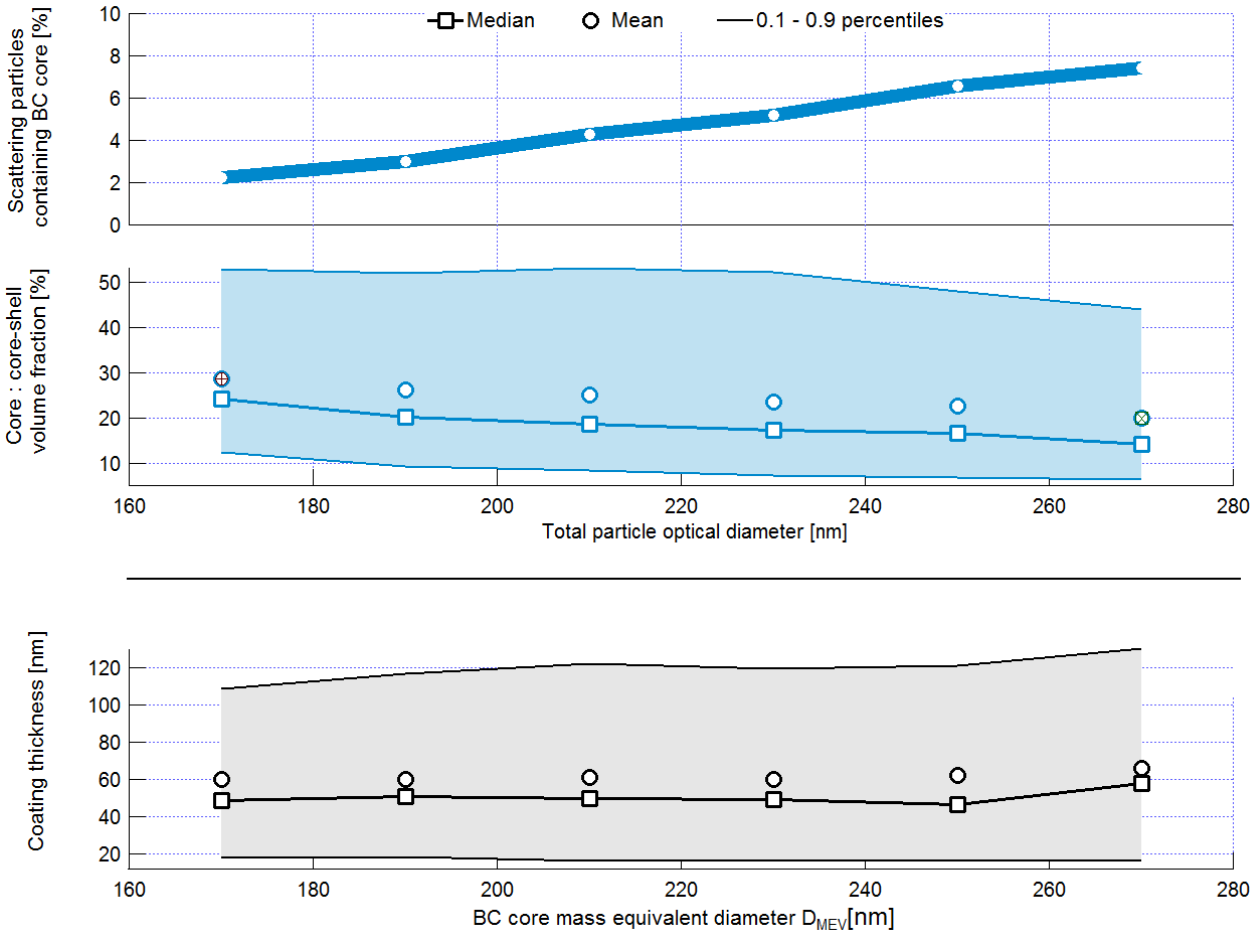

Figure 4.4 Top panel: fraction of particles internally mixed with BC over total particles. Middle panel: volume fraction of encapsulated particles composed by BC. Bottom panel: coating thickness of BC cores.

In the following part we restricted the investigation to rBC-containing particles having an optical diameter between 160-280 nm, without constraining the rBC core diameter. Within this optical size range we estimated the volume composition of rBC-containing particles, discriminating the rBC and non-rBC contributions. This approach gives directly usable information to simulate different volume mixing geometries as in Adachi et al. (2010). We found that rBC-containing particles are predominantly constituted in volume by non-rBC; the average rBC volume fraction was 24% ± 17% (mean ± standard deviation), on average only 10 % of the encapsulated particles showed a majoritarian rBC volume contribution, with maximum values around 75%.

Despite the major contribution in volume to rBC-containing particles, the non-absorbing matter constituting the coating was a minor fraction of the overall non-rBC aerosol volume, accounting for just the 4 %. Furthermore, if the majority of the rBC cores showed a coating thicker than 10 nm, the number of rBC-containing particles was tremendously low (<5%) compared to the total number. These last results, together with the high SSA, confirmed that absorbing matter is a minor component of the Arctic Aerosol

4.4 Coating effects on aerosol optical properties

4.4.1 Enhancement of black carbon mass absorption cross section

In this section we investigate the impact of internal mixing state on optical properties of rBC, a schematic view of our approach is shown in Figure 4.5. The mass absorption cross section of rBC-containing particles was calculated using Mie theory assuming a concentric core shell mixing geometry. Other necessary parameters as refractive indexes of core (RI_{Core}) and coating ($RI_{Coating}$) were taken from existing literature, while size of cores and coating thickens were taken from SP2 measurements (Figure 4.5). RI_{Core} increases with rBC density (Bond and Bergstrom, 2006), while $RI_{Coating}$ varies as a function of its chemical composition (Hess et al., 1998; Bond et al., 2006b; Moffet and Prather, 2009; Dinar et al., 2008a). Values of 1.95+0.79i at 550 nm were chosen as refractive index of the BC core (Bond and Bergstrom, 2006) while $1.55+e^{-6}i$ at 550 nm was used for the coating material (Bond et al., 2006a). This combination of RI_{core} and $RI_{coating}$ represents a compact BC core with low void fraction (high density), surrounded by processed organic and sulfate material. Different rBC-core diameters, D_{MEV} ranging between 160 and 280 nm, were assumed during this step of the calculation. For each core size we simulated twelve different cases corresponding to bare rBC and rBC coated with eleven different thicknesses of non-absorbing material. The thicknesses of the shell were directly taken from the SP2 measurements and were representative of 10^{th}, 20^{th}, 25^{th}, 30^{th}, 40^{th}, 50^{th}, 60^{th}, 70^{th}, 75^{th}, 80^{th}, 90^{th} percentiles of the SP2 coating thickness distribution for the given rBC core size. The MAC was then calculated from the simulated absorption cross section using the rBC particle mass calculated using a constant density of 1800 kg m^{-3} from its mass equivalent diameter and called as MAC_{Mie}. The density used here is representative of processed and relatively void free rBC particles (Moteki and Kondo, 2010).

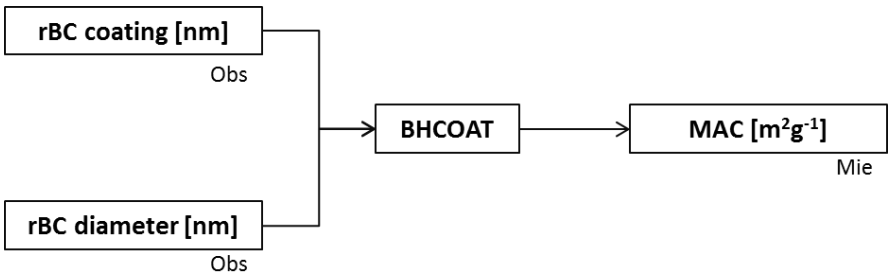

Figure 4.5 Schematic view of mass absorption cross section (MAC) calculation at 550 nm. "Obs" indicates observed properties; "Mie" corresponds to properties calculated using the BHCOAT code based on the Mie theory.

Assuming the refractive index of core and coating may introduce systematic error in the final MAC_{Mie}. Manifold refractive index values associated to black carbon aerosol and soot-like materials have been published in atmospheric and combustion research fields (Bond and Bergstrom, 2006; Koch et al., 2009). Furthermore, refractive indexes of non-absorbing and slightly-absorbing materials that may compose coating shells were also widely investigated (Hess et al., 1998; Bond et al., 2006a; Dinar et al., 2008a; Moffet and Prather, 2009). Sensitivity tests were performed in order to quantify the error

introduced by the variability of core and coating refractive indexes found in the literature during MAC_{Mie} calculations. Different MAC_{Mie} values were calculated for a bare rBC core (240 nm of diameter) varying only the RI_{Core} (see Table 4.2) and for the same core but coated with 47nm coating (representative of ambient measurements) assuming different $RI_{Coating}$ listed in Table 4.2. The MAC_{Mie} variability that is introduced by core and coating RI assumption was quantified in 7% and 2% respectively. The former represent the error in Mie estimations for uncoated rBC cores. For coated core, a value of 8% was estimated trough errors propagation approach.

Table 4.2 List of published refractive indexes for black carbon and non-absorbing coatings. Values used in this study underlined.

Core material		
RI (λ=550 nm)	Characteristic	Reference
1.68 + 0.56i	Diesel soot	Marley et al., 2001
1.75 + 0.44i	Soot	OPAC, Hess et al., 1998
1.75 + 0.63i	Function of the particle void fraction	Bond and Bergstrom, 2006
1.80 + 0.50i	Soot, ULAQ 99 model	Pitari et al., 1993, 2002
<u>1.95 + 0.79i</u>	Function of the particle void fraction	Bond and Bergstrom, 2006
2.00 + 1.00i	Carbon black	Janzen, 1979
2.07 + 0.60i	Soot,UMI model	Liu and Penner, 2002
Coating material		
RI (λ=550 nm)	Characteristic	Reference
1.43 + 0i	Sulfate OPAC	OPAC, Hess et al., 1998
1.49 + 0i	Organic matter	Moffet and Prather, 2009
1.52 + 0.002i	Ammonium sulfate	Dinar et al., 2008
1.55 + e-6i	Organic matter and sulfate mixture	Bond et al., 2006a
1.63 + 0.021i	Humic like proxy	Dinar et al., 2008

Figure 4.6 shows the relationship between the rBC mass absorption cross-section at a wavelength of 550 nm and the diameter ratio and is often used to describe the mixing degree regardless of absolute values of core diameter and coating thickness. The MAC_{Mie} enhancement was ranging between 15 and 99 % for thinly (D_{Shell}:D_{Core}<1.2) and thickly (D_{Shell}:D_{Core}>1.8) coated rBC cores respectively. The lensing effect induces a continuous increase of the MAC_{Mie} value, which reaches a plateau after a certain D_{Shell}:D_{Core} threshold, after that the lensing effect became negligible (Nessler et al., 2005; Bond et al., 2006; Cappa et al., 2012).

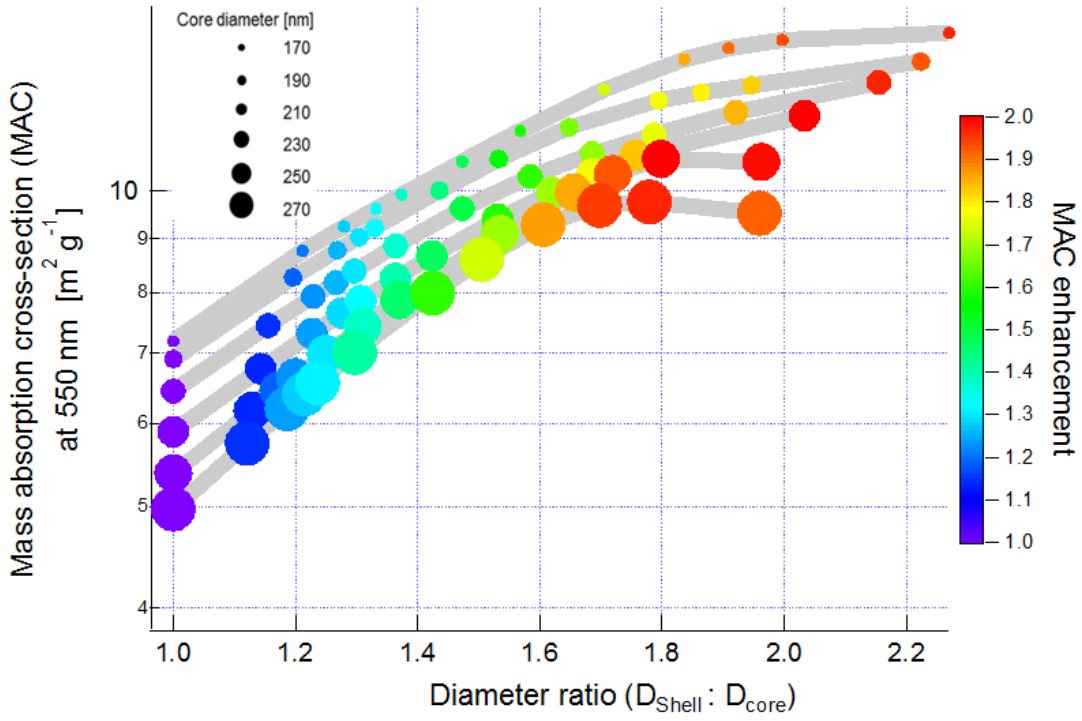

Figure 4.6 Mass absorption enhancemennt of rBC as a function of its mixing degree assuming a core-shell mixing geometry. MAC enhancement expressed as the MAC ratio of coated versus bare rBC. Assumed refractive index for rBC core: 1.95+0.79i. Assumed refractive index for non absorbing coating: 1.55 + e-6i.

In order to investigate the effective absorption enhancement of BC at Zeppelin station we run more specific simulations using inputs that are more representative of Arctic rBC in spring. We assumed a monodisperse rBC population having a mean size diameter of 240 nm D_{MEV}, that is the geometric mean of the rBC size distribution. Coating thicknesses used here were calculated for rBC core diameters ranging between 230 and 250 nm, MAC_{Mie} was extrapolated via BHCOAT code assuming as input the 10^{th}, 25^{th}, 50^{th}, 75^{th}, and 90^{th} percentile of coating thickness distribution and quantified in 16, 26, 47, 86, and 122 nm respectively. As most representative case of Arctic rBC we assumed the combination of 240 nm of core diameter and the median coating thickness of 47 nm. The resulting MAC_{Mie} value is 8.22 m^2 g^{-1} at 550 nm of wavelength. Thickening the coating causes an increase in MAC_{Mie} from 6.46 to 11.2 m^2 g^{-1} for the thinner (16 nm) and thicker (122 nm) coatings (Table 4.3). The MAC enhancement was quantified as the ratio in percentage between MACs of the coated and bare rBC and ranged between 15% and 99%. The median coating of 47 nm induced a MAC_{Mie} enhancement of 46 %. Compared to the median MAC_{Mie} calculated in this work, several MAC values used in radiative models (MAC_{RadMod}) do not reproduce the optical characteristics of aged black carbon, ranging between 16.2 and 2.3 m^2 g^{-1} at a wavelength of 550 nm. The former is meant to represent the worldwide spatial distribution of MAC values of internally mixed BC and used in the Aerosol, Transport, Radiation, General Circulation, Mesoscale, and Ocean Model (GATOR-GCMOM; Jacobson, 2012). The latter is used in the Spectral Radiation-Transport Model for Aerosol Species (SPRINTARS) model and chosen in order to represent black carbon internally mixed with organic carbon (Takemura et al., 2000, 2002, 2005). Several intermediate values are also available and resumed in Koch et al.

(2009). Such difference might lead to consistent discrepancy in absorption coefficient estimation, see section 4.4.2.

Table 4.3 Mixing state degree and relative optical properties of rBC and total aerosol.

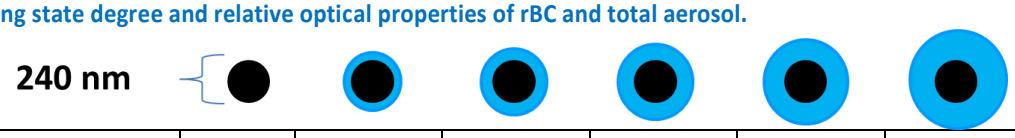

	Bare	Coating 10th percentile	Coating 25th percentile	Coating 50th percentile	Coating 75th percentile	Coating 90th percentile
Coating thickness [nm]	-	16	26	47	86	122
Core-to-shell diameter ratio	1.00	1.14	1.21	1.39	1.71	2.02
Mass absorption cross-section [m^2 g^{-1}]	5.62	6.46	6.96	8.22	10.45	11.18
MAC enhancement [%]	-	14.8	23.8	46.0	85.8	98.8
SSA	0.984	0.982	0.981	0.977	0.971	0.969
SSA reduction [%]	-	0.23	0.37	0.71	1.3	1.5

4.4.2 From particles to aerosol: estimated and observed optical properties

As following is described the approach adopted to calculate the absorption coefficient of the rBC aerosol and single scattering albedo of total aerosol using MAC_{Mie}, and aerosol particles properties observed with the SP2 and nephelometer. Sensitivity of absorption and single scattering albedo to different mixing degrees is also assessed. Absorption coefficient (σ_{apMer}) of rBC particles is estimated merging together the MAC_{Mie} and rBC mass concentration observed with the SP2 (Equation (4.9); Figure 4.7).

$$\sigma_{apMer}\ [Mm^{-1}] = MAC_{Mie}\ [m^2\ g^{-1}] * m_{rBC}\ [\mu g\ m^{-3}] \quad (4.9)$$

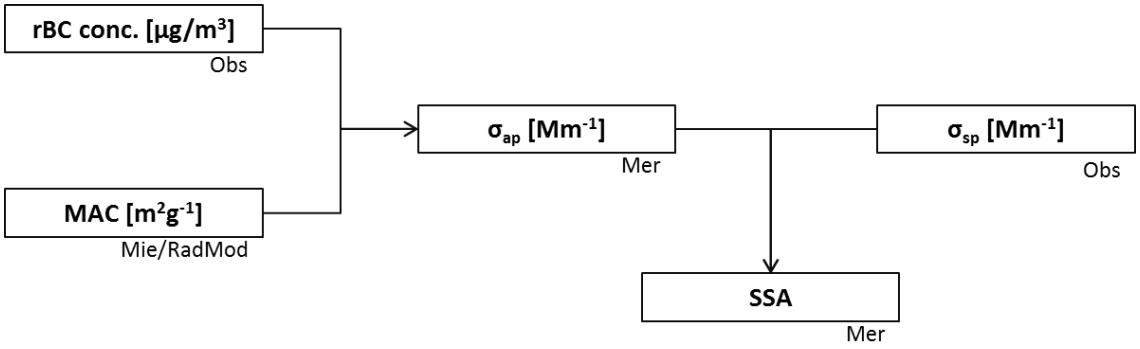

Figure 4.7 Schematic view of single scattering albedo (SSA) extrapolation at 550 nm. "Obs" indicates observed properties; "Mie" corresponds to properties calculated using the BHCOAT code based on the Mie theory; "RadMod" indicate MAC values often used in radiative models; "Mer" indicates aerosol properties calculated merging the Mie calculations and observed aerosol characteristics. rBC mass concentration observed with SP2, scattering coefficient (σ_{sp}) observed with a nephelometer. Additionally, absorption coefficient edited as σ_{ap}.

Combining the scattering coefficient obtained from nephelometer observations (σ_{spObs}) with merged absorption coefficient results in a final merged single scattering albedo (SSA_{Mer})

$$SSA_{Mer} = \frac{\sigma_{spObs}}{\sigma_{apMer} + \sigma_{spObs}} \tag{4.10}$$

where "Mer" designates properties quantified by merging Mie theory calculation with instrumentally observed properties, designated as "Obs" (Figure 4.7). At 550 nm the SSA_{Mer} are 0.982 ± 0.749, 0.977 ± 0.747 and 0.969 ± 0.739 (average ± standard deviation) considering 16, 47, and 122 nm of coating respectively. Enhancing the core shell ratio from 1 to 1.39 increased the MAC by 46 %, a similar assessment on SSA leads to a SSA decrease of 0.718 % (Table 4.3).

In order to verify the reliability of our approach, we compared the estimated optical properties with observed one at a wavelength of 550nm. The σ_{apMer} was compared with absorption coefficients observed with aethalometer instrument, while SSA_{Mer} was compared with SSA calculated from absorption and scattering coefficient observed with aethalometer and nephelometer respectively. Figure 4.8 shows the time series of absorption coefficients (top panel) and single scattering albedos (bottom panel).In both cases optical properties estimated assuming an uncoated rBC population does not agree with observations, while observation and coated particles simulations nicely agree (Figure 4.8 and Figure). Considering rBC particles coated with 47 nm (median value), observed and merged absorption coefficients showed an r^2 of 0.62 and agree within 18%. Differently, an uncoated rBC population does not reflect reality, underestimating the observed absorption coefficient by 45%. Differences between observations and calculation for SSA are smaller than 1% for both coated and bare rBC cores. Additional absorption coefficient and single scattering albedo were calculated following Equation 4.9 and Equation 4.10 using MAC_{RadMod}. Resulting range of σ_{RadMod} and SSA_{RadMod} is

plotted in Figure 4.8. Both σ_{RadMod} and SSA_{RadMod} do not well represent observation, with differences of 70-80% and 2% respectively.

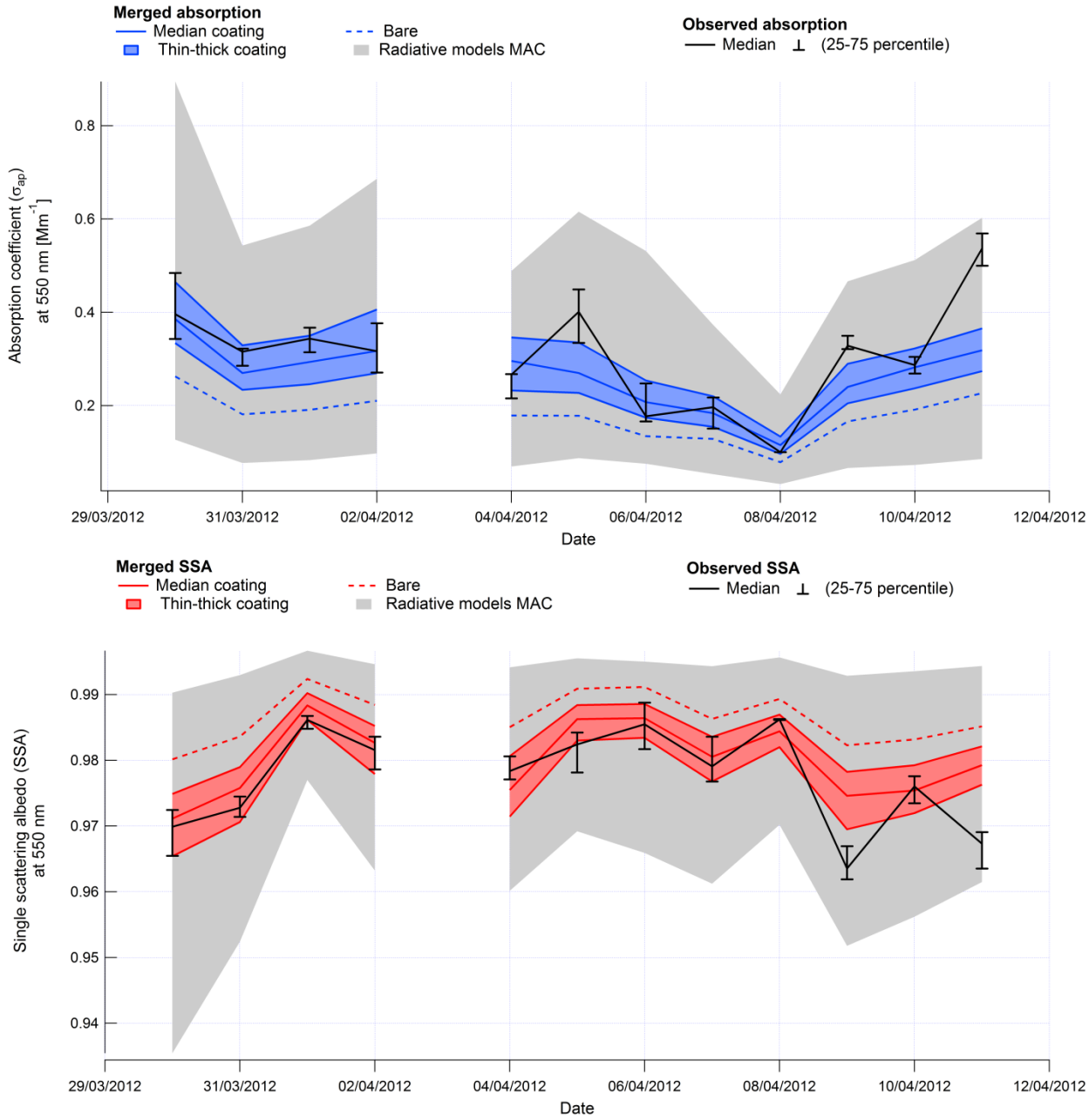

Figure 4.8 Time series of optical properties at a wavelength of 550 nm calculated with Mie theory (colour shadow), with MAC values used in radiative models (grey shadow) and observed (black line). Median, thin and thick coating: thickness of 47, 26 and 86 nm from ambient observations.

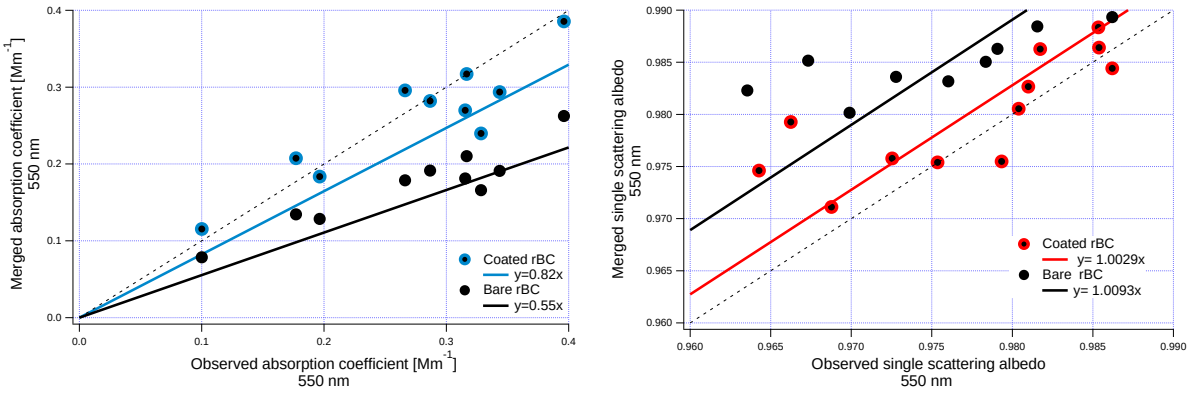

Figure 4.9 Scatter plot of merged versus observed optical properties. Solid lines: linear least squares fit forced through the origin.

4.5 Conclusion

To understand the transformation induced on black carbon optical properties after long range transport, intensive field experiment was conducted during arctic spring 2012 at the Zeppelin station (Svalbard, Norway). An optical characterization of the total aerosol was performed: small values of aerosol optical depth, negative values of Ångström exponent difference and high single scattering albedo indicated that in 2012 no extreme smoke events took place and that the aerosol population was dominated by fine and non-absorbing particles. The single particle soot photometer (SP2) was used to infer the major properties of refractory black carbon (rBC). Low concentration of 35 ng m^{-3} of rBC was found, with a mean mass equivalent diameter above 200 nm. The rBC concentrations detected with the continuous soot monitoring system and the single particle soot photometer were agreeing within 15%. Combining absorption coefficient observed with an Aethalometer and BC mass concentration from SP2, mass absorption cross section values of 6.0 m^2 g^{-1} and 8.6 m^2 g^{-1} were found at wavelengths of 550 and 880 nm respectively. Concerning mixing, BC with attached geometry represented a minor fraction (~2%) of BC-containing particles, while particles containing a rBC core where less than 5% of total particles. rBC core with a dimeter between 170 nm and 280 nm were covered by a layer of non-absorbing material having a median thickness of 50 nm (average diameter ratio = 1.61 ± 0.69) . From Mie calculation, such mixing would lead to an enhancement of absorption of 46% compared to a bare BC core. MAC of a medium coated particle was calculated with Mie theory in 8.21 m^2 g^{-1} at a wavelength of 550 nm. This is in high agreement (<5% difference) with calculated MAC from observations. We estimated that the discussed absorption enhancement would lead to a decrease of single scattering albedo of the total aerosol of less than 1%, suggesting that the BC particles have a minor weight on determining the optical properties of the total aerosol. With this work we provided some of the BC key properties (as mass concentration, diameter, coating thickness and mass absorption cross section) necessary to accurately simulate the impact of BC in the arctic and provided evidences that MAC values adopted in radiative models do not reflects the optical properties of aged Arctic BC.

Acknowledgments

This work was supported by IPEV, the “Agence Nationale de la Recherche” under the contract ANR 2011 Blanc SIMI 5-6 021 04, and a grant from Labex OSUG@2020 (Investissements d’avenir – ANR10 LABX56). We thank the AWI-PEV personnel for the logistic support. Thanks are also extended to the staff at the Norwegian Institute for Air Research (NILU).

5 Ice residual properties in mixed-phase clouds at the high Alpine Jungfraujoch site

P. Kupiszewski[1], M. Zanatta[1,2], S. Mertes[3] P. Vochezer[4], E. Hammer[1,*], G. Lloyd[5], I. Crawford[5], C. Linke[4], S. Schmidt[6], J. Schneider[6], M. Schnaiter[4], E.Weingartner[1,+], U. Baltensperger[1] and M. Gysel[1]

[1]*Laboratory of Atmospheric Chemistry, Paul Scherrer Institute, Villigen PSI, Switzerland*
[2]*Laboratoire de Glaciologie et Géophysique de l'Environnement, Université Grenoble Alpes/CNRS, Grenoble, France.*
[3]*Leibniz Institute for Tropospheric Research, Leipzig, Germany*
[4]*Institute for Meteorology and Climate Research, Karlsruhe Institute of Technology, Karlsruhe, Germany*
[5]*Centre for Atmospheric Science, SEAES, University of Manchester, Manchester, UK.*
[6]*Particle Chemistry Department, Max Planck Institute for Chemistry, Mainz, Germany*
[*]*now at: Grolimund + Partner AG - Environmental Engineering, Bern, Switzerland.*
[+]*now at: Institute for Aerosol and Sensor Technology, University of Applied Sciences, Windisch, Switzerland*

In preparation for Journal of Geophysical Research

In the conclusive part of the manuscript the role of different aerosols as ice nuclei (IN) in mixed phase clouds was investigated at the high elevation measuring site of Jungfraujoch (Switzerland) during the cloud and aerosol characterization experiment (CLACE) held in 2013. My work was focused to investigate the black carbon IN activity and its activation drivers. Since radiative properties and lifetime of liquid and glaciated clouds differs substantially, a better understanding of properties regulating the ice nucleating activity of different aerosols is needed. Despite the research in this field has been intensified, the role of BC as IN is still largely uncertain and source of intense debate. Laboratory and ambient experiments showed a wide spread of the ice nucleating activity of BC, contradicting results were found at the research station of Jungfraujoch (Cozic et al., 2008b); Kamphus et al., 2010; Chou et al., 2011). Furthermore, the effect of coatings on BC particles has been investigated during smog chamber experiments without reaching uniform conclusions (e. g. Möhler, 2007; Friedman et al., 2011), while the mixing-activation relationship was never assessed in ambient measurements.

In order to understand the feedbacks of BC particles on mixed phase clouds is necessary to quantify the quantity and to characterize the properties of ice activating BC. In this work small ice crystals were selected trough the ice selective counter-flow virtual impactor (Ice-CVI) developed by Mertes et al. (2007), while BC number concentration, size distribution and coating thickness were inferred with a single particle soot photometer (SP2). Thanks to a second SP2 sampling simultaneously the total aerosol, was possible to calculate the size dependent BC activated fraction as function of particle size. This setting ensures the selection of ice crystals and refractory BC (rBC) minimizing interferences introduced by non-ice particles and non-refractory material.

SP2 approach is considered to provide accurate quantification of rBC avoiding interference by other refractory material. For the first we observed interference apparently caused by metal containing matter as olivine or hematite. The time resolved shape of scattering and incandescence signals was used to filter all the incandescing signals attributed to refractory non BC material. Since the activated fraction is calculated merging together results from the two SP2, an intercomparison survey was conducted during the field experiment (see supplementary). The number concentration of rBC cores and rBC-free particles agreed within 10% while optical size distribution of rBC-containing particles and rBC-free particles agreed within 20%. Furthermore, difference in coating estimation was quantified in 10%. Finally, the two SP2s showed a unit to unit variability that will not introduce a consistent bias in the calculation of ice activated fraction (see supplementary). According to observation, rBC-containing particles were depleted in the ice residuals. The ice activated fraction of rBC-containing particles was approximately an order of magnitude lower than the ice activated fraction of rBC-free particles. Activation efficiency showed a size dependency, with larger rBC-containing particles activated more efficiently compared to smaller one. Activated rBC cores showed larger coating thickness (median = 53 nm) compared to total aerosol (median = 16 nm). Black carbon was found to not play a role in mixed phase clouds, thus RF due to BC mixed phase cloud is negligible. Despite the reasons remain unknown; coating thicknesses appeared to enhance the behavior of black carbon as ice nuclei.

Abstract: Ice residual particle and total aerosol properties were measured and compared during mixed-phase cloud (MPC) measurements at the high Alpine research station Jungfraujoch (3580 m asl in the Swiss Alps). Size distributions were obtained using optical particle size spectrometers and a scanning mobility particle sizer, while black carbon (BC) content and coating thickness of BC-containing particles were determined using a single-particle soot photometer. The ice activated fraction (IAF), derived from a comparison of ice residual and total size distributions, showed an enrichment of large particle in the ice residuals, with an increase in the activated fraction from the order of 10^{-4} to 10^{-3} for 100nm particles to 0.2 to 0.3 for 1 µm particles. Nonetheless, due to the high number fraction of sub-micrometer particles in the total aerosol size distribution, ice residual particle size distributions were dominated by the sub-micron aerosol fraction. A comparison of simultaneously measured number size distributions of BC-free and BC-containing ice residuals and total aerosols showed depletion of BC by number in the ice residuals, suggesting it does not play a significant role in ice nucleation in free tropospheric MPCs. The potential anthropogenic climate impact of BC via the glaciation effect in MPCs is therefore likely to be negligible. BC-containing ice residuals were larger than the BC-containing total aerosol, with an increasing IAF with size. Furthermore, BC-containing ice residuals were found to have a thicker coating than the BC-containing total aerosol, pointing to the importance of atmospheric aging for ice nucleation. It is not clear whether the coating influence on a particle's ice nucleating ability is due to an increase in its size or due to a change in its surface properties.

5.1 Introduction

At temperatures above -38 °C, i.e., above the limit below which homogeneous freezing of liquid droplets takes place, formation of ice in the atmosphere takes place on the surface of aerosol particles called ice nuclei (IN). These particles lower the Gibbs free energy barrier of nucleation and can thus trigger heterogeneous ice nucleation at lower supersaturations than would be required for homogeneous nucleation. IN particles are very few in number compared to the total aerosol. At -10 °C the concentration of IN is as much as seven to nine orders of magnitude lower than that of the total aerosol (Szyrmer and Zawadzki, 1997), while at 20 °C it is approximately five orders of magnitude lower (Pruppacher and Klett, 1997). Consequently, in the temperature range 0 to -38 °C the presence of IN, in combination with cloud dynamics, effectively regulates the phase of the clouds, which can be liquid, glaciated or mixed-phase, i.e., containing both supercooled liquid droplets and ice crystals. Formation of ice in the atmosphere affects cloud microphysical properties, which in turn influence radiative transfer and precipitation formation. In mixed-phase clouds (MPCs), under favorable thermodynamic conditions, rapid growth of ice crystals at the expense of liquid droplets can take place via the Wegener-Bergeron-Findeisen process (Korolev, 2007). A cloud containing relatively numerous, small liquid droplets can thus be transformed within minutes to a glaciated cloud with much fewer, but larger, ice crystals (Murray et al., 2012). This results in a strong decrease in the optical depth and albedo of the cloud (Sun and Shine, 1994) and can initiate precipitation (Chen and Lamb, 1999). Therefore, ice nucleation is of major importance for both the radiative properties of

clouds and the hydrological cycle of the Earth. Meanwhile, the properties of ice nuclei are still not well known with a paucity of field measurements focused on characterizing ice nucleating particles. While there has been a number of aircraft campaigns focused on sampling of ice crystals in cirrus clouds using the Counterflow Virtual Impactor (CVI) technique (e.g. Twohy and Poellot, 2005; Prenni et al., 2007; Cziczo et al., 2013), MPC measurements are particularly scarce. This is largely due to the difficulties involved in selectively extracting the relatively few ice crystals in such clouds, which contain also much more numerous supercooled liquid droplets of similar aerodynamic size, as well as interstitial aerosols. As ice nucleation in cirrus clouds takes place under different temperature and supersaturation conditions than in MPCs it is not possible to directly apply results from the former to the latter. Therefore, measurements of ice nucleating particles in mixed phase clouds are necessary to improve our understanding of the relevant ice nucleating processes. The Ice-CVI (Mertes et al., 2007) is an inlet which overcomes the aforementioned issues and selectively samples small (5-20 µm aerodynamic diameter) ice crystals, which are assumed to have grown primarily by water vapour diffusion. Consequently, the particles left after sublimation of these ice crystals, i.e., the ice residuals (IR), can be considered as the original IN. Following extraction and sublimation of the small ice crystals detailed measurements of the physical and chemical properties of the IR can be conducted, thus shedding light on the characteristics of ice nucleating particles. A characterization of IR in MPCs using the Ice-CVI during the CLACE-3 campaign at the Jungfraujoch showed that the likelihood of a particle acting as an IN increases with particle size (Mertes et al., 2007). Nonetheless, the IR were predominantly sub-micrometer particles, due to their sheer number as compared to super-micrometer particles. Previous studies at the Jungfraujoch have identified IR as predominantly containing mineral dust and organics (Cziczo et al., 2009a; Kamphus et al., 2010; Schmidt et al., 2015). Some studies have further identified lead as being strongly enriched in the IR (Cziczo et al., 2009b; Ebert et al., 2011). The role of black carbon (BC) is contentious, with varying results among different studies. (Cozic et al., 2008a) and Mertes et al. (2007) reported enrichment of BC in IR based on particle soot absorption photometer (PSAP) measurements, while Ebert et al. (2011) found enrichment of C-O-S particles (i.e., internal mixtures of organics, nitrates and sulfates, sometimes containing soot inclusions in sampled IR) using scanning electron microscopy and transmission electron microscopy. In contrast, based on single-particle mass spectrometer measurements (Kamphus et al., 2010; Schmidt et al., 2015) and multi-angle absorption photometer measurements (Chou et al., 2011), no proof for BC influence on ice nucleation in MPCs was found. This paper focuses on measurements of the physical properties and black carbon (BC) content of IR sampled using the Ice-CVI during the joint Cloud and Aerosol Characterization Experiment (CLACE) 2013 and Ice Nuclei Research Unit (INUIT) campaign at the high altitude research station Jungfraujoch in the winter (January-February) of 2013. Data from the Ice Selective Inlet, a second inlet for exclusive extraction of small ice crystals operated in the field for the first time during CLACE 2013, is not presented, due to the low transmission efficiency of ice crystals through the inlet, and the resulting poor counting statistics of IR. Based on an analysis of IR size distributions measured downstream of the Ice-CVI the size of particles predominantly acting as IN in MPCs is determined. Total aerosol and IR size distributions are compared, allowing for calculation of the ice activated fraction of particles as a function of size. Laser-induced incandescence is used to measure BC content in the IR and total aerosol on a single particle basis, providing a robust measurement for determining whether BC is

enriched in the IR. In combination with size distribution measurements of BC-containing particles in IR and in the total aerosol this allows for determination of whether BC is an atmospherically relevant IN. Finally, the coating thickness of BC-containing particles is measured, shedding light on the effect of coating of BC particles on their ice nucleating ability. The presented data set includes, to the best of our knowledge, the most extensive ground based measurements of the physical properties of IR in MPCs conducted to date, with a host of state-of-the-art aerosol probes including an Ultra-High Sensitivity Aerosol Spectrometer (UHSAS), scanning mobility particle sizers (SMPS), Grimm optical particle size spectrometers (OPSS), a waveband integrated bioaerosol sensor (WIBS3), a TSI optical particle sizer (OPS) and single-particle soot photometers (SP2) measuring ice residual size distributions in the range of 0.02-5 µm. Furthermore, the measurements of BC in IR at the Jungfraujoch are the first to be conducted with the SP2 instrument. While measurements of BC in IR and IN have been conducted previously using particle soot absorption photometers (Cozic et al., 2008a), a multi-angle absorption photometer (Chou et al., 2011) and single-particle mass spectrometers the SP2 data set is unique in providing detailed single-particle information, including core size and coating thickness, unavailable from any of the other aforementioned instruments. Furthermore, for sizes above its lower limit of detection the SP2 has unit detection efficiency for both BC-free and BC-containing particles, and therefore provides quantitative data which cannot be obtained using single-particle mass spectrometers.

5.2 Experimental: CLACE 2013 field campaign

The joint Cloud and Aerosol Characterization Experiment (CLACE) and Ice Nuclei Research Unit (INUIT) campaign were carried out in January-February 2013 at the Jungfraujoch site (3580m asl in the Swiss Alps) - a Global Atmosphere Watch (GAW) research station. The focus of the campaign was investigating the characteristics of ice nucleating particles (Boose et al., 2015; Kupiszewski et al., 2015; Schmidt et al., 2015; Worringen et al., 2015) and cloud microphysical properties (Lloyd et al., 2015; Vochezer et al., 2015). The Jungfraujoch is predominantly in the free troposphere during winter (over 60% of the time; Herrmann et al., 2015) and is frequently in cloud (around 40% of the time; Baltensperger et al., 1998). Consequently, the site is well suited to the objectives of the campaign, with aerosol measurements representative of the continental free tropospheric background (Nyeki et al., 1998) and frequent cloud occurrence.

5.2.1 Aerosol inlets: total inlet and Ice-CVI

A total aerosol inlet, mounted on the roof of the Sphinx laboratory, is operated year-round as part of the GAW monitoring program. All particles below 40 µm in diameter for wind speeds up to 20ms^{-1} are sampled by the inlet. The tubing is insulated and the inlet heated to 20 °C in order to dry the sampled hydrometeors and avoid transmission losses, and to prevent rime build-up on the inlet

(Weingartner et al., 1999). The Ice-CVI is an inlet system which employs a series of components to remove snow aggregates, supercooled liquid droplets and interstitial aerosol in mixed-phase clouds, thus extracting solely small ice crystals with aerodynamic diameters of 5-20 µm. During the CLACE 2013 campaign the Ice-CVI was set up adjacent to the total inlet, with the inlet of the Ice-CVI mounted _ 2m above the ground. The setup of the Ice-CVI is as follows: air is aspirated through an omni-directional, roofed inlet which limits the collection of hydrometeors larger than 50 µm. A virtual impactor subsequently removes particles above 20 µm. A two-stage pre-impactor removes the liquid droplets, which freeze onto the impaction plates at temperatures below 0 °C, while the ice crystals bounce off and stay in the sample flow. Finally, a counterflow virtual impactor (CVI) mounted within a wind tunnel is used to remove particles smaller than 5 µm. The ice crystals transmitted through the CVI are injected into dry, particle free air, thus ensuring sublimation of the ice crystals. A detailed characterization of the Ice-CVI based on modelling and measurements can be found in Mertes et al. (2007). At times, the Ice-CVI was operated in total aerosol inlet mode, by switching off the CVI counterflow. Those measurements from the UHSAS and TSI OPS probes (see Sect. 5.2.3.2 for instrument descriptions) which are referred to as “total inlet” measurements were obtained in this manner.

5.2.2 Cloud probes

5.2.2.1 Particulate Volume Monitor (PVM-100) and Cloud Droplet Probe (CDP)

Measurements of liquid water content (LWC) were carried out using a Cloud Droplet Probe (CDP, Droplet Measurement Technologies, USA; (Lance et al., 2010) and two Particulate Volume Monitors (PVM-100, Gerber Scientific Inc., USA; Gerber, 1991; Wendisch et al., 2002). The CDP is a single-particle instrument which provides a size distribution in the 2-50 µm diameter size range based on the intensity of scattered light at 4-12° in the forward direction from particles passing through a 658nm laser beam (Lance et al., 2010). LWC can subsequently be calculated from the measured size distributions. In contrast to the CDP, the PVMs measure light scattered by a particle ensemble. A 780nm laser illuminates particles passing between the transmitter and receiver arms of the instrument, which house the laser diode and receiver optics, respectively. The light scattered in the forward direction is collected by the receiver optics and transmitted through two spatial filters. One of the spatial filters weights the scattered light so that the output signal is proportional to the volume concentration of the particle ensemble, i.e., LWC in the case of a droplet ensemble. The second spatial filter weights the scattered light so that the output signal is proportional to the surface area concentration. In-cloud periods during CLACE 2013 were defined using a LWC threshold value of 0.02 gm−3 from 5 minute averages of the CDP and PVM-100 measurements (seeTable 5.1 for a list of all measured cloud events). It should be noted that the presence of ice will lead to LWC overestimation in both the CDP and PVM-100 measurements. As concentrations of small ice crystals are in general very low in MPCs as compared to the liquid droplet concentrations, and the CDP measured size range is constrained to 2-50 µm, the effect of ice presence on LWC inferred by the CDP should be minimal. The effect is likely larger for the PVM, as it does not have a size cut and larger ice particles will thus

also contribute to the PVM signal. As we are interested in LWC only as a determinant of cloud presence, overestimation of LWC due to additional light scattering from ice crystals is not considered to be an issue.

5.2.2.2 Small Ice Detector (SID-3)

The size, shape and phase of hydrometeors were measured using the Small Ice Detector (SID- 3; Kaye et al., 2008; Ulanowski et al., 2014), which acquires light scattering patterns from particles passing through a laser beam with a wavelength of 532nm. The particles are counted and sized based on the scattered light intensity. High resolution scattering patterns are recorded by an intensified CCD camera in the 6 - 26° forward direction. The camera exposure trigger threshold can be adjusted.

Table 5.1 Average temperature, wind speed, liquid water content and ice mass fraction during CLACE 2013 cloud events.

Cloud event	Cloud start time	Cloud end time	Cloud duration (HH:MM)	Temperature (ºC)	Wind speed (m/s)	CDP liquid water content (g/m3)	PVM liquid water content (g/m3)	Ice mass fraction
1	27.01.2013 15:30	28.01.2013 10:30	19:00	-12.2	8.2	0.22	-	0.17
2	29.01.2013 01:30	30.01.2013 00:05	22:35	-8	12.5	0.29	-	0.13
3	30.01.2013 16:00	31.01.2013 02:00	10:00	-8.4	16.7	0.35	-	0.31
4	31.01.2013 18:30	03.02.2013 11:00	64:30:00	-15.1	13.3	0.22	0.26	0.29
5	03.02.2013 21:45	04.02.2013 12:30	14:45	-14.4	15	0.38	0.51	0.31
6	04.02.2013 16:00	04.02.2013 21:30	05:30	-12	10.6	0.29	0.17	0.02
7	05.02.2013 07:30	05.02.2013 09:15	01:45	-14.7	11.9	0.03	0.07	0.09
8	05.02.2013 14:45	06.02.2013 05:25	14:40	-19.4	10.6	0.12	0.05	0.3
9	06.02.2013 08:05	08.02.2013 12:50	52:45:00	-23.2	8	0.3	-	0.18
10	08.02.2013 22:30	09.02.2013 19:00	20:30	-26.6	7.1	0.25	0.19	0.12
11	10.02.2013 16:00	10.02.2013 23:50	07:50	-16.1	9.6	0.07	0.38	0.13
12	11.02.2013 06:20	12.02.2013 06:30	24:10:00	-18.5	6.6	0.12	0.08	0.07
13	12.02.2013 12:00	13.02.2013 01:20	13:20	-19.4	7.3	0.36	-	0.09
14	14.02.2013 18:30	16.02.2013 02:05	31:35:00	-16.9	7.7	0.26	0.19	0.12
15	17.02.2013 13:00	17.02.2013 14:00	01:00	-17.1	0.8	-	0.02	0
16	17.02.2013 17:30	17.02.2013 19:15	01:45	-20.6	2.2	-	0.04	0
17	17.02.2013 21:45	18.02.2013 02:45	05:00	-21.1	8.2	-	0.04	0.01
18	19.02.2013 15:00	20.02.2013 19:05	28:05:00	-14.3	8.4	-	0.18	-
19	21.02.2013 11:15	21.02.2013 17:30	06:15	-18.8	4.9	-	0.03	-
20	21.02.2013 18:15	21.02.2013 19:30	01:15	-21.3	3.3	-	0.03	-
21	21.02.2013 20:30	21.02.2013 22:15	01:45	-22.3	5.2	-	0.06	-

Typically, the trigger threshold was set high enough to avoid acquisition of liquid droplet scattering patterns. However, this also prevents the acquisition of small (5-20 µm) ice crystal scattering patterns. During several periods only, the trigger threshold was lowered so that measurements of ice crystals in the 5-20 µm size range could be made. During CLACE 2013 the SID-3 was mounted on a rotating platform, which automatically adjusted to shifts in the wind direction. The high resolution scattering patterns obtained contain detailed information on the phase and habit of individual cloud particles. In order to distinguish the phase of the particles their azimuthal symmetry is analyzed. This is based on the fact that a spherical droplet generates an Airy pattern with perfect azimuthal symmetry, as opposed to ice crystal scattering patterns, which have lower azimuthal symmetry. Further details on the data retrieval procedure and associated uncertainties can be found in (Vochezer et al., 2015).

5.2.3 Aerosol concentration, size distribution and composition measurements

Aerosol concentration, size distribution and composition were measured downstream of the total inlet and the Ice-CVI by a host of instruments described below. The sampling positions of the instruments are given in Table 5.2 together with the size ranges measured. All size distributions measured downstream of the Ice-CVI were corrected for the enrichment of particles by the CVI component of the Ice-CVI (Mertes et al., 2007).

Table 5.2 CLACE 2013 aerosol instrumentation sampling downstream of the total inlet and the Ice-CVI. The asterisk refers to measurements of the total aerosol conducted using the Ice-CVI in total inlet mode, as described in Section 5.2.2.

Instrument	Total inlet	Ice-CVI	Measured property	Size Range [µm]
CPC model 3010	✓*	✓	concentration	>0.01
UHSAS	✓*	✓	optical size	0.06-1
SMPS TI	✓	×	electrical mobility size	0.016-0.53
SMPS Ice-CVI	×	✓	electrical mobility size	0.016-0.42
Grimm Sky-OPC 1.129	✓	✓	optical size	0.25-32
Grimm Dust Monitor 1.108	✓	×	optical size	0.3-20
TSI OPS model 3330	✓*	✓	optical size	0.3-10
WIBS3	✓	✓	optical size	0.8-20
SP2 TI	✓	×	optical size	0.17-0.44
SP2 Ice-CVI	×	✓	optical size	0.17-0.44
SP2 TI	✓	×	mass equivalent size	0.08-0.31
SP2 Ice-CVI	×	✓	mass equivalent size	0.08-0.31

5.2.3.1 Scanning Mobility Particle Sizers

For the size resolved measurement of aerosol particles two scanning mobility particle sizers (SMPS) were deployed, one downstream of the total inlet and one downstream of the Ice-CVI. Both SMPS systems were custom-built at PSI and their operation was verified in a study by Wiedensohler et al. (2012). The SMPS behind the total inlet consisted of a differential mobility analyzer (DMA; model 3071, TSI, USA) and a condensation particle counter (CPC; model 3776, TSI, USA); this SMPS system will be further on denoted by SMPS TI. The other system behind the Ice-CVI consisted of a TSI long type DMA (custom-built at PSI) and a CPC model 3022A (TSI, USA); the SMPS system behind the Ice-CVI will be further on denoted by SMPS Ice-CVI. Both DMAs were operated with a sheath air flow rate of 3 L min^{-1} and a sample air flow rate of 0.3 L min^{-1}. SMPS TI covered the mobility diameter range from 16 to 530nm while the SMPS Ice-CVI covered a larger mobility diameter range from 16 to 420nm. As the tubing connecting the SMPS Ice-CVI to the Ice-CVI was of considerable length (~2.5m tubing with an inner diameter of 0.004m), the SMPS Ice-CVI size distributions were corrected to account for tubing losses using the Particle Loss Calculator (von der Weiden et al., 2009). A particle density of 2 g cm^{-3} was used for the corrections, as assumed for IR density by (Cozic et al., 2008a).

5.2.3.2 Optical Particle Size Spectrometers (UHSAS, Grimm OPSSs, WIBS3 and TSI OPS)

The Ultra-High Sensitivity Aerosol Spectrometer (UHSAS; Cai et al., 2008), the Grimm Dust Monitor and Grimm Sky-OPC (Burkart et al., 2010) and TSI optical particle sizer (OPS) model 3330 all belong to the optical particle size spectrometer (OPSS) family of instruments, and operate on the same principle, whereby the intensity of light scattered by particles passing through a laser beam is measured and converted into an optical diameter (D_{opt}). The WIBS3 additionally measures ultraviolet laser-induced fluorescence, however, particle sizing in the instrument is conducted using the same method as standard OPSS instruments. As particle fluorescence measurements are not within the scope of this paper and only the particle sizing data is used, the WIBS3 is described alongside the other OPSS instruments. The Grimm Dust Monitor, Grimm Sky-OPC, WIBS3 and TSI OPS measure aerosol particles in the size ranges of 0.3-20 µm, 0.25-32 µm, 0.8-20 µm and 0.3-10 µm, respectively, while the UHSAS employs a high intensity intracavity laser to detect and size particles between 60 and 1000nm. Although size distributions are measured up to 32 µm, due to the cut-off of the CVI component of the Ice-CVI all size distributions are shown for sizes up to 5 µm; interstitial particles above this size can be transmitted through the CVI and cannot be distinguished from true ice residuals, thus leading to potential contamination of the signal. Particle counts measured by the Grimm Sky-OPC, which was set up a considerable distance from the Ice-CVI and total inlet (1.26m and 2.61m, respectively) were corrected for tubing losses, as done for the SMPS. The reduction in counting efficiency of the WIBS3 towards its lower detection limit (Gabey et al., 2011) was used to correct the WIBS3 size distributions. All the OPSSs used were calibrated using polystyrene latex spheres with a refractive index (RI) of 1.59. As the RI of the aerosol is not known we are not able to correct the measured optical sizes for the true RI and thus there is some error in the size distributions shown. In order to get an approximate idea of the magnitude of the error in the sub-micrometer size range, we have calculated the change in optical diameter for the UHSAS instrument assuming an RI of 1.5. The change in optical diameter assuming an RI of 1.59 versus an RI of 1.5 is 5-19 %, with higher values towards the upper range of the UHSAS. In the super-micrometer size range additional uncertainties from the ambiguity in sizing due to the non-monotonic relationship between particle size and the intensity of scattered light, as well as from the influence of the imaginary part on the derived size become increasingly important.

5.2.3.3 Singe Particle Soot Photometers

Concentration, size distribution and mixing state of refractory black carbon (rBC) were monitored using single-particle soot photometers (SP2) manufactured by Droplet Measurement Technologies (Boulder, CO, USA). Two 4-channel SP2s were deployed during the campaign; one sampled the total aerosol, while the second measured the IR downstream of the Ice-CVI inlet. A comprehensive description of the SP2 operation principles is given by Stephens et al. (2003); Schwarz et al. (2006); Moteki and Kondo, (2007). In brief, absorbing refractory particles passing through a 1064nm high-fluence Nd:YAG laser beam are brought to their boiling point. The peak of the thermal radiation emitted by the incandescent BC core is proportional to the single particle mass of rBC. This

dependency was calibrated during multiple calibrations using size selected fullerene soot (Alpha Aesar; #FS12S011) according to Baumgardner et al. (2012);(Gysel et al., 2011; Laborde et al., 2012b; Moteki et al., 2012). rBC mass of a single particle is converted to a rBC mass equivalent diameter (D_{MEV}) using a void-free BC material density of 1800 kgm^{-3} (Moteki et al., 2010). Detection of diffused light at 1064nm enables optical sizing of the sampled aerosol. The peak of the scattering signal is converted into the partial scattering cross section using a calibration coefficient defined during in-situ calibrations carried out with spherical polystyrene latex size standards (Thermo Scientific, formerly Duke Scientific). The optical size is then calculated from the calibrated partial scattering cross section using Mie theory and assuming the particles are spherical. A refractive index of 1.59 was used for the calibration, while 1.50 was assumed for measurements of the total aerosol and IR. The SP2 design ensures 100% detection efficiency for particles above the lower size limit of detection, which corresponds to a D_{MEV} = 80nm for rBC cores and D_{opt} = 150nm for BC-free particles. As the SP2 is a quantitative, single-particle based instrument, there is no number or mass concentration lower limit of detection, making it well suited to IR measurements. The leading edge only (LEO) method introduced by Gao et al. (2007) and slightly adapted by (Laborde et al., 2012a) was applied for the optical sizing of the BC-containing particles in order to avoid interference from particle evaporation within the laser beam. The partial scattering cross section derived from the LEO-fit was converted to an optical diameter using Mie theory and assuming a concentric spheres core-shell structure. The rBC core is assumed to have an index of refraction of 2.26 + 1.26*i* (Moteki et al., 2010), while the coating index of refraction is assumed to be 1.50, for consistency with the standard optical sizing. This fully constrains the total particle size and coating thickness, defined as the difference between the radii of the total particle and the rBC core. In this work the coating thickness is derived for rBC cores having a D_{MEV} between 170 and 220nm. The reduced size range ensures the best counting statistic for our operating conditions. Additionally, using the LEO approach, the optical sizing range was extended up to 440nm.

5.3 Results and discussion

In the following section a comparison of ice residuals and concentration of small ice crystals is presented, based on a case study period. Size distributions from simultaneous total inlet aerosol measurements are analyzed in order to assess the instrument inter-comparability and the magnitude of the differences in size distributions arising from using different instruments. Subsequently, size distributions of the aerosol measured downstream of the total inlet and the Ice-CVI as well as the particle ice activated fraction is shown, shedding light on the absolute and relative number contribution of the total aerosol to IR as a function of size. An analysis of BC content and the coating thickness of BC-containing particles in the total aerosol and in IR follows, clarifying the role of BC for ice nucleation in ambient MPCs, and the influence of coating on its ice nucleating ability.

5.3.1 Comparison of ice residual and small ice crystal concentrations

An important step in verifying the operation of the Ice-CVI is a comparison of the IR and small ice crystal concentrations. The period 22:00 LT (local time), 8 February 2013 to 07:00 LT, 9 February 2013 presented an opportunity for such a comparison between the Ice- CVI and the SID-3. During this period the SID-3 was operated such that it detected ice particles in a size range of 5-20 µm (i.e., the size range of ice crystals extracted by the Ice-CVI; see Section 5.2.2.2 for details on the SID-3 settings). Concurrently, IR concentrations were recorded by the CPC operated downstream of the Ice-CVI.

Figure 5.1 shows an overview of air temperature and wind speed measured by MeteoSwiss (panel a), cloud particle size distributions (panel b), the size-resolved ice number fraction (panel c) and small ice crystal and droplet integrated number concentrations (panel d) during the case study period. Air temperature was stable over the period, with values between -26.5 and −25.5 °C, while wind speed was 5-7ms^{-1} over the first half of the period, increasing to approximately 8-10ms−1 during the second half. As seen in panels b and d, shortly after 23:00 LT a cloud lasting throughout the night is formed, initially containing only droplets and glaciating over the course of the night with increasingly high ice number fractions (panel c).

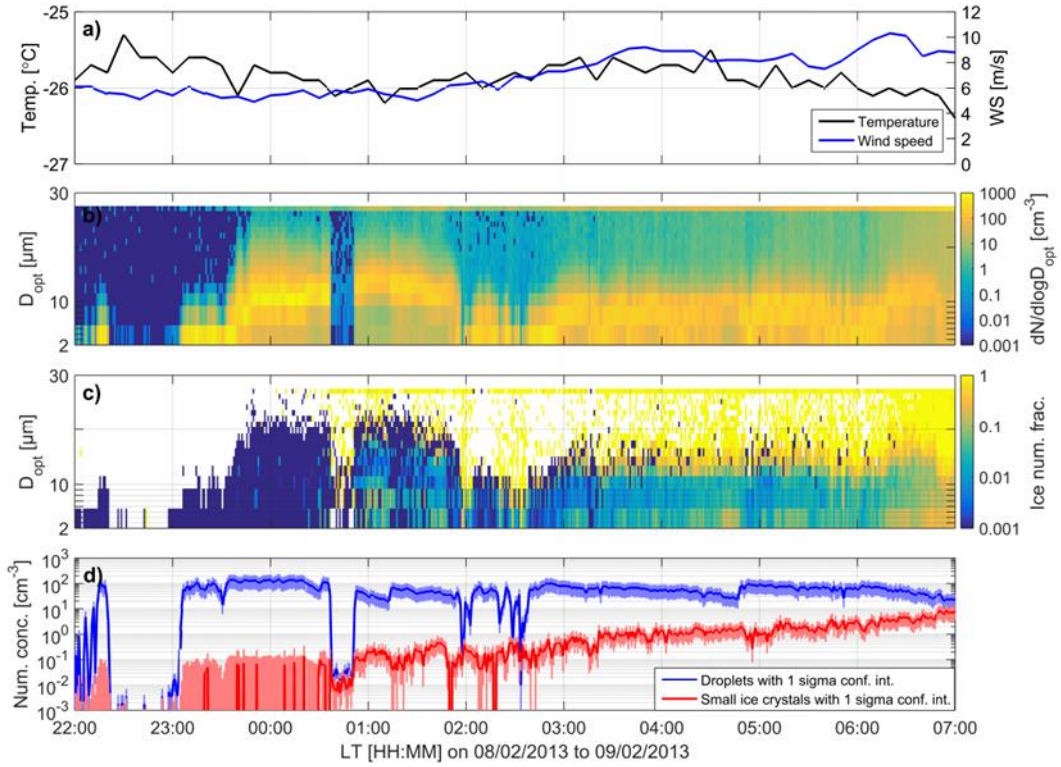

Figure 5.1 Measurements of air temperature, wind speed and cloud particles during CLACE 2013, 22:00 LT, 8 February 2013 to 07:00 LT, 9 February 2013. Panel (a) shows the air temperature (black trace) and wind speed (blue trace measured by MeteoSwiss, panel (b) shows the size distribution of cloud particles, panel (c) shows the size-resolved ice number fraction and panel (d) shows the integrated number concentrations of droplets and small ice crystals obtained from SID-3 measurements.

The increase in ice number fraction is visible particularly at sizes above 10-15 µm, where ice becomes dominant in the number fraction; at smaller sizes droplet number fractions remain substantial, although decreasing during the presented period. The time series of small ice crystal and IR concentrations (Figure 5.2) shows that initially more IR than small ice crystals are detected, but in general the two measurements tracked each other quite well, with the strong increase in concentrations after 03:00 LT clearly visible in both instruments and an r^2 of 0.65. It should be noted that perfect agreement between the two instruments cannot be expected, as the optical diameter size range measured by the SID-3 is not directly comparable with the aerodynamic diameter size range sampled by the Ice-CVI. Based on the case study comparison of small ice crystal and IR concentrations we qualitatively confirm that the Ice-CVI is selectively sampling and extracting small ice crystals.

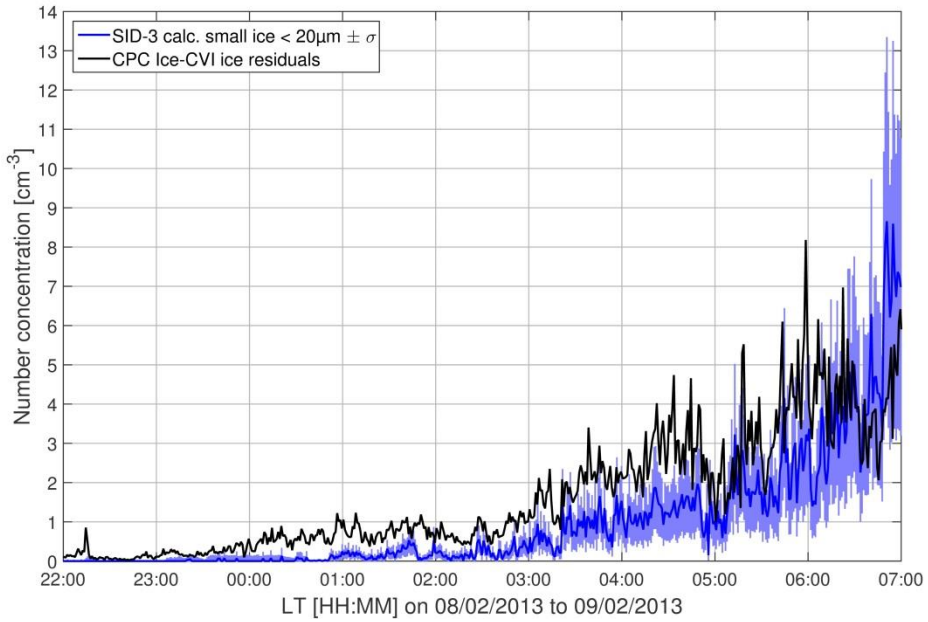

Figure 5.2 Time series of small (D_{opt} < 20 µm) ice crystal concentrations measured by the SID- 3 and ice residual concentrations measured by the Ice-CVI CPC during CLACE 2013, 22:00 LT, 8 February 2013 to 07:00 LT, 9 February 2013.

5.3.2 Assessment of aerosol instrument inter-comparability

In order to establish how well the aerosol instruments compare between one another and the magnitude of uncertainties in the size distributions, we compare averaged size distributions of the total aerosol and of IR from the different instruments for simultaneous measurement periods. Figure 5.3 shows 6 such periods for the total aerosol measurements and shows 5 of such periods for the Ice-CVI; the size distributions from a given measurement period are denoted by a common color. As shown by the simultaneous measurements, there is very good agreement between instruments for sizes up to a few hundred nanometers. However, at larger sizes the measured size distributions from

the optical particle size spectrometers (UHSAS, WIBS3, Grimm OPSSs and TSI OPS) frequently differ by several factors, and sometimes as much as an order of magnitude, as is the case, for example, for total inlet event (TIE) 5 (cyan traces in Figure 5.3) and Ice-CVI cloud event (CE) 1b (red traces in Figure 5.4).

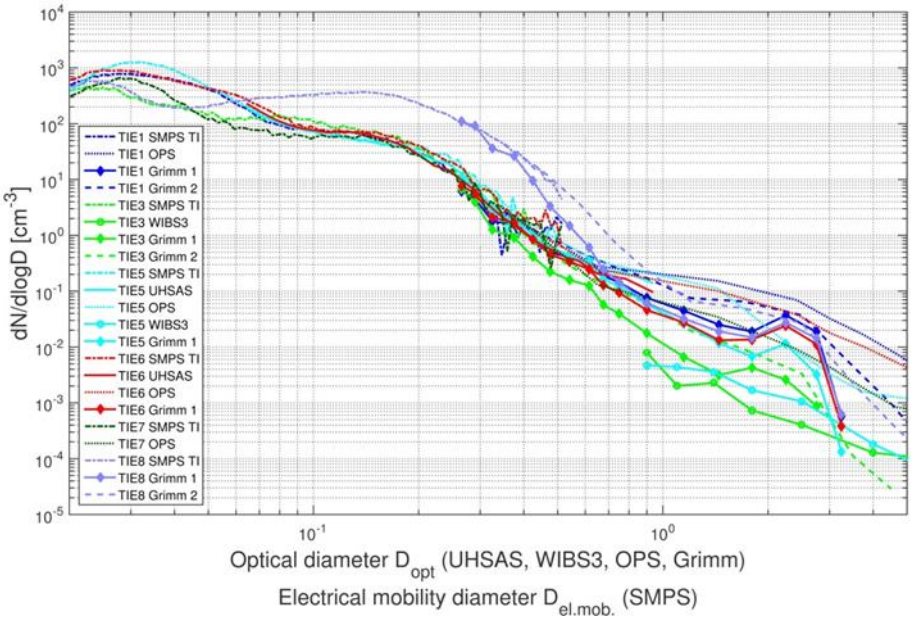

Figure 5.3 Measurements of total aerosol size distributions during multiple CLACE 2013 total inlet measurement periods. Simultaneous measurements by different instrument during the same event are denoted by a common trace color.

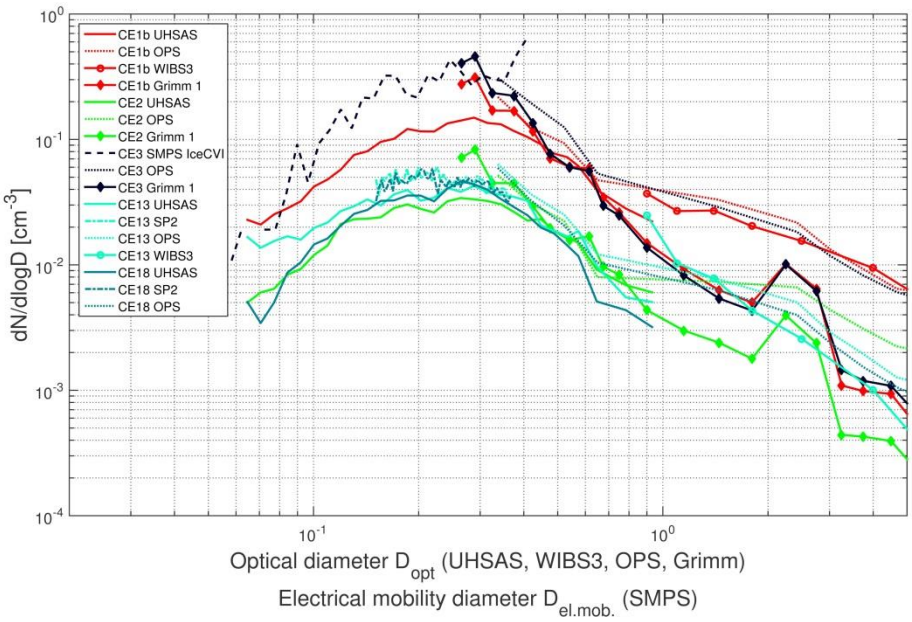

Figure 5.4 Measurements of ice residual size distributions during multiple CLACE 2013 cloud events. Simultaneous measurements by different instrument during the same cloud event are denoted by a common trace colour.

The differences in the size distributions are systematically biased, with the instruments in order of highest to lowest counts at a given size generally ordered as follows: TSI OPS, Grimm Dust Monitor (denoted as Grimm 2), Grimm Sky-OPC (denoted as Grimm 1) and WIBS3. While we have corrected the measurements for tubing losses and differences in counting efficiency where significant, as described in the respective instrument sections, the corrections are insufficient to account for all inconsistencies. Differences in calibration and sizing of the instruments may be one of the principal reasons for the disagreement; such differences will lead to the size distributions being shifted in the horizontal with respect to one another. A further reason for the discrepancies are the different sizing ambiguities arising from Mie wiggles depending on the properties of the given instrument, as well as differences between the true Mie oscillations and those assumed by the respective instruments. While the sizing uncertainties for larger particles are considerable, the resulting differences are not critical for two reasons: Firstly, the majority of IR are found in the sub-micrometer size range, and thus are affected by these uncertainties to a much smaller degree. Secondly, the calculated ice activated fractions are based on size distribution ratios between comparable instruments, which means only the horizontal sizing shifts remain a concern.

5.3.3 Ice residual size distributions

A total of 15 CLACE 2013 cloud events were selected for the analysis of IR size distributions during CLACE 2013. The variability in size distributions between cloud events can be seen in Figure 5.5, which shows the UHSAS cloud event mean size distributions for 12 of the events, during which the UHSAS

was in operation. The size distributions are very similar in shape from cloud to cloud, but differ greatly in concentration, spanning two orders of magnitude. The 25th and 75th percentiles of the 10 minute measurements for a given CE, plotted here for CE2, shows that variability in the number concentrations of small ice crystals within a single cloud is considerable. High temporal variability of cloud microphysical properties was also observed in the ice mass fractions (IMF) derived from measurements of LWC and IWC (ice water content) during CLACE 2013 (Lloyd et al., 2015). However, a direct comparison with their findings is not possible for several reasons: Firstly, as opposed to the absolute measure of IR concentrations, IMF is a relative measure which depends not only on IWC in the cloud, but also on the LWC. Secondly, the IMF is mass based, while the IR concentration is number based. Finally, due to resolution-based instrument limitations in distinguishing between ice and liquid particles, the IMF presented by Lloyd et al. (2015) are based on measurements of larger ice crystals only, which are above the upper cut-off of the Ice-CVI.

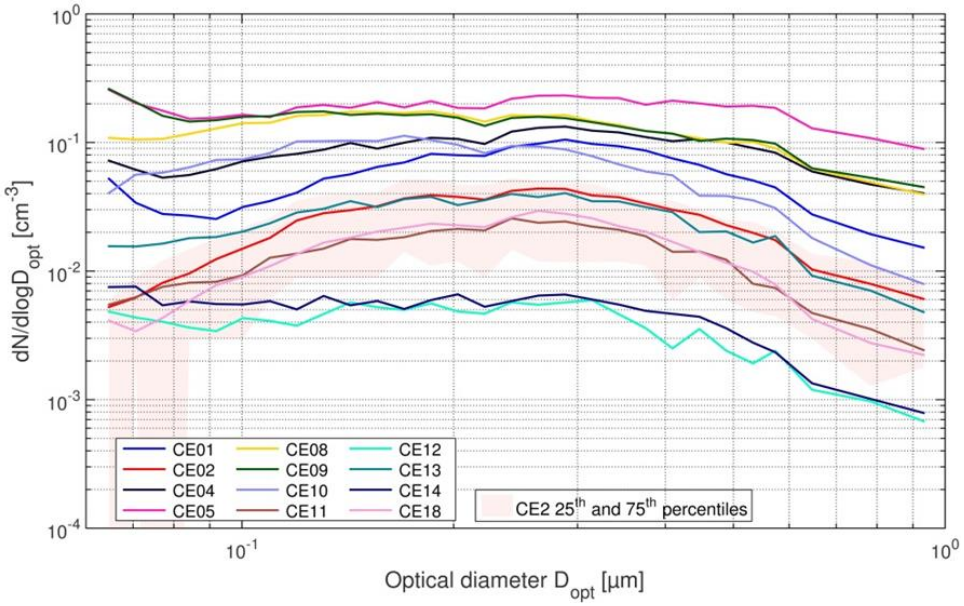

Figure 5.5 Cloudeventaveraged ice residualsizedistributionsmeasuredbytheUHSASduring CLACE 2013

A compilation of campaign averages and medians of the size distributions measured by seven aerosol sizing instruments downstream of the total inlet and the Ice-CVI are shown in Figure 5.6 . The total aerosol size distributions show high concentrations of aerosols below 0.15 µm, subsequently decreasing sharply with increasing size. Concentrations at a size D_{opt} =1 µm are approximately 3-4 orders of magnitude lower than at D_{opt} = 0.1 µm (see the UHSAS size distribution which spans the optical diameter size range of 0.06-1 µm). Meanwhile, the IR size distributions are much flatter with a mode at 0.3 µm and decreasing only gradually with increasing particle size. As opposed to the total aerosol measurements, the UHSAS size distributions at D_{opt} = 0.1 µm and D_{opt} = 1 µm show concentrations on the same order of magnitude. In order to quantify the contribution of particles in a given size range to the IR population, as compared to the total aerosol population, we calculate the number fractions of particles in the size ranges of 0.1-0.5 µm, 0.5-1 µm and 1-5 µm relative to the total number in the 0.1-5 µm size range. The combined UHSAS median size distribution between 0.1

and 0.6 µm and the OPS median size distribution above 0.6 µm are used to calculate the integrated number concentrations for the given size ranges. For the total aerosol the respective number fractions are 0.991, 0.006 and 0.003, while for the IR there is a clear shift to larger sizes with number fractions of 0.76, 0.13 and 0.11, respectively. It should be noted that some instruments measured exclusively from either the total inlet or the Ice-CVI, while others were switched between the two inlets (see Table 5.2 for details). This means that the data coverage of each instrument is different. The non-simultaneous sampling times thus introduce an additional uncertainty in the comparison of size distributions from different instruments. The non-simultaneous sampling periods are, to a large extent, the reason for the difference in the SMPS and UHSAS IR size distributions; a comparison of simultaneous measurements (not shown) gives considerably better agreement.

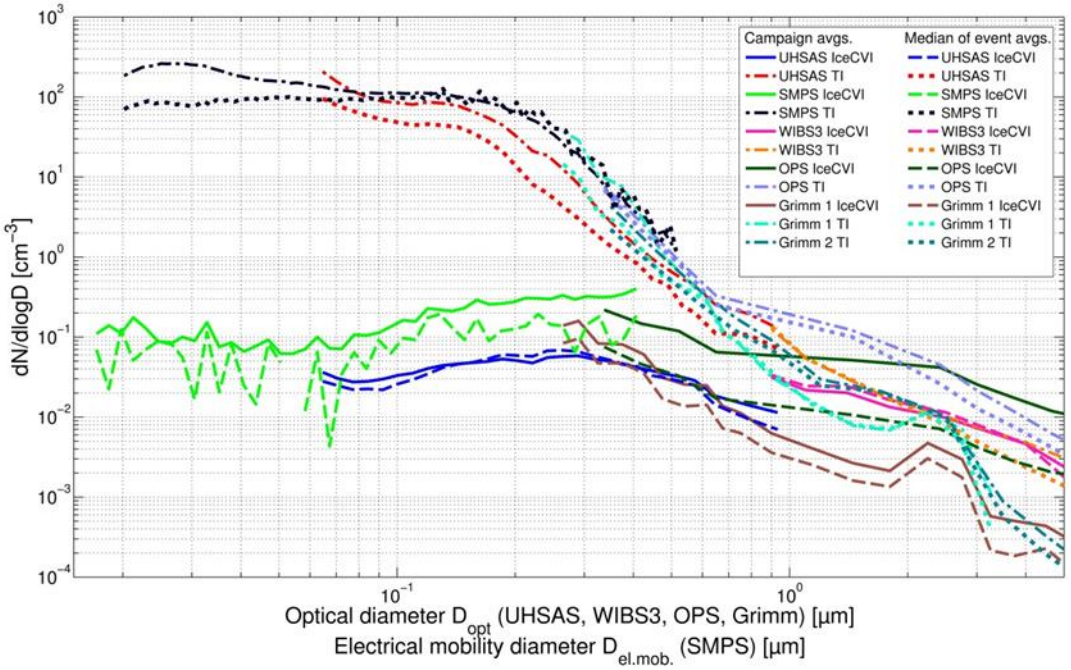

Figure 5.6 Average and median size distributions of ice residuals and total aerosol measured during CLACE 2013.

5.3.3.1 Activated number fraction

The campaign average size distributions presented in were used to calculate the ice activated fraction (IAF) as a function of size, shown in Figure 5.5. As discussed in Section 5.2.3 , these size distributions are based on non- or only partially simultaneous measurements.

The differences between the IAF for a given particle size measured by different instruments are thus affected by the variable sampling periods. Nonetheless, the IAF show a consistent trend, increasing from approximately 10^{-4} to 10^{-3} for 100nm particles to values around 0.2 to 0.3 for 1 µm particles. We hypothesize that this increase can be explained by a combination of two effects: Firstly, by an increase in the number of active surface sites with particle size. This is supported by the findings of Archuleta et al. (2005) who found that ice nucleation onset took place at lower relative humidities for

larger particles based on continuous flow diffusion chamber (CFDC) measurements of mineral dust surrogates, as well as by Hung et al. (2003), who found that larger hematite cores induced freezing of aqueous ammonium sulfate at lower ice supersaturations than smaller hematite cores. Secondly, the increase in IAF with size could be due to an increase in the fraction of particles which are good IN, most notably mineral dust, in the total aerosol as a function of size. The IAF trend observed in this study is similar to the results reported by Mertes et al., (2007) during previous Ice-CVI measurements at the Jungfraujoch, although the absolute IAF values are generally several factors higher in this study. However, it should be noted that the results from Mertes et al., (2007) are based on a single cloud event of 10 hour duration, as compared to several weeks of data presented in this paper and, thus differences in the absolute values should not be overstated. In order to provide a means for predicting the number of small (5-20 µm) ice crystals formed, a logistic function has been fitted to the measurement-derived IAF traces:

$$IAF_{fit} = 3.0 \cdot 10^{-4} \frac{0.59997}{1 + D_p^{-3.3}} \quad (5.1)$$

where *Dp* is the particle diameter in µm. The fit is shown in Figure 5.7 as the blue trace with the shaded area giving the IAF values in the range of *IAF*fit/5 and *IAF*fit ·5, constrained at the upper end by an IAF of 1. Based on Equation (5.1) and a total aerosol size distribution, the number of ice crystals formed as a result of heterogeneous freezing can thus be estimated. It is important to note that this fit is applicable only for conditions similar to those experienced during the measurements of IAF in this study (a median cloud temperature *T*med = −18.1 °C with a first quartile of *T*Q1 = −21.3 °C and a third quartile of *T*Q3 = −13.1 °C). In order to put the *IAF*fit into the context of previous work, we calculate the predicted number of small ice crystals using the average total aerosol size distribution weighted with Equation (5.1), and compare this with the IN concentration predicted based on the parametrization put forward by DeMott et al. (2010), henceforth referred to as D2010. For the total aerosol size distribution the combined UHSAS median size distribution between 0.1 and 0.6 µm and the OPS median size distribution above 0.6 µm are used. The lower size limit of 0.1 µm is set as ice nuclei are generally considered to be larger than 0.1 µm (Pruppacher and Klett, 1997) and, as discussed by Mertes et al. (2007), it is possible that small IR sampled downstream of the Ice-CVI are a measurement artifact. The number of small ice crystals thus predicted is 29 L^{-1}. Meanwhile, using D2010 with the median cloud temperature *T*med and the number concentration of total aerosol larger than 0.5 µm *N*>0.5, we obtain ice nuclei concentrations of 0.32 L^{-1}, while IN concentrations of 0.46 L^{-1} and 0.15 L^{-1} are obtained when using *T*Q1 and *T*Q3, respectively. The small ice crystal concentrations using Equation (5.1) are thus approximately two orders of magnitude higher than those calculated using D2010. This is broadly similar to the findings of Lloyd et al. (2015) who compared ice crystal concentrations measured using a Two-Dimensional Stereoscopic (2D-S) probe during CLACE 2013 with the IN concentration calculated from the D2010 parametrization and found the former to be 2-3 orders of magnitude higher than the latter. It should be noted that the 2D-S ice crystal concentrations used by Lloyd et al. (2015) were measured in the size range of approximately 60-1280 µm and *N*>0.5 was obtained from measurements at an upwind measurement site and thus their results are not directly comparable with those presented in this work. The reason for the large

difference in the IN concentrations predicted by D2010 on the one hand andthe small ice crystal concentrations predicted in this work or the ice crystal concentrations measured by Lloyd et al. (2015) on the other hand is not clear. Lloyd et al. (2015) suggest surface sources, such as break-up of frost crystals and blowing snow are responsible for the difference. However, as shown in this work and in previous studies (e.g. Kamphus et al., 2010; Mertes et al., 2007; Schmidt et al., 2015), the IR extracted from small ice crystals have physical and chemical properties different to those of the total aerosol, often with enrichment of particle types which, based on theory and laboratory experiments, would be expected to preferentially act as IN, e.g. larger particles and mineral dust. This would suggest that the IR contribute to the ice nucleation process, which one would not necessarily expect if the IR are predominantly extracted from ice crystals with a surface source. Nonetheless, it is clear that further work is needed to close the gap between measurements of ice crystals, IR and IN in MPCs.

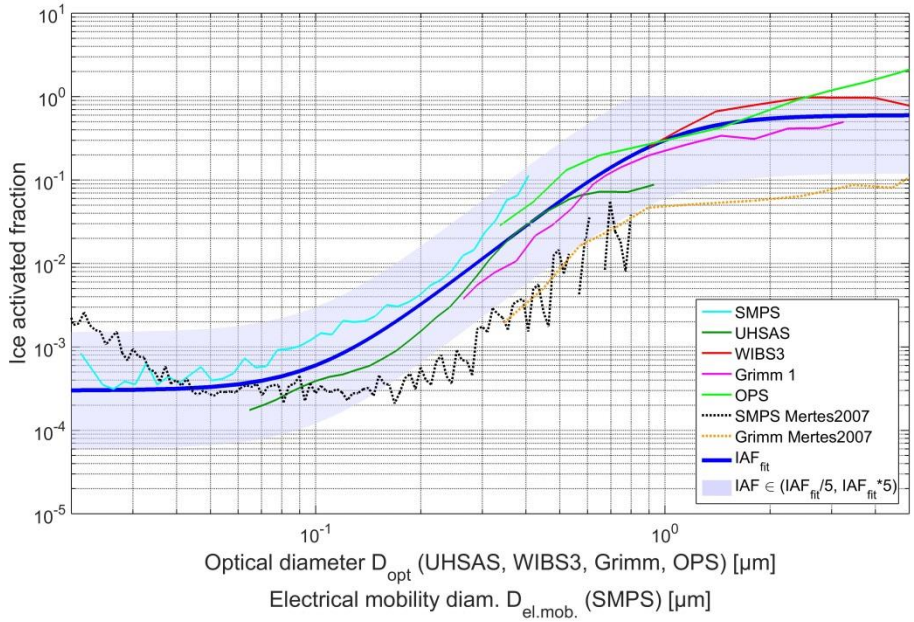

Figure 5.7 Ice activated fractions (campaign averages) during CLACE 2013

5.3.3.2 BC activation into ice

The IAF was also calculated for the subset of measurements obtained using the SP2 instruments. In this case, the IAF is calculated based on periods with simultaneous measurements of the total and Ice-CVI SP2 only. As this is a considerably smaller subset than all data included in Figure 5.7, the results are shown in a separate figure (IAF as a function of optical diameter is shown in Figure 5.8). In order to verify the SP2-based results (the sum of BC-free and BC-containing particles measured by the SP2 is given by the cyan trace in Figure 5.8), the measurements were compared with the IAF derived from the SMPS for the same period (red trace in Figure 5.8), and showed good agreement. The IAF obtained from the SP2 instruments was calculated separately for BC-free particles (green trace in Figure 5.8) and for incandescing BC-containing particles (black trace in Figure 5.8). While both traces

show an increase in the IAF with increasing particle size, the IAF for BC-containing particles is an order of mag- nitude lower than the IAF for BC-free particles, for a given size.

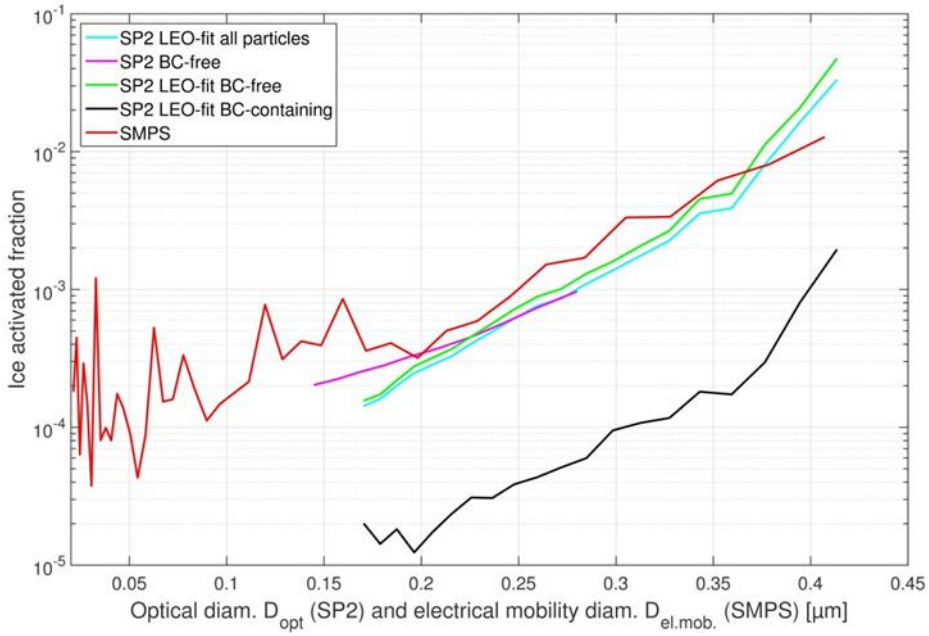

Figure 5.8 Ice activated fractions for BC-free versus BC-containing particles as a function of optical diameter D_{opt} during CLACE 2013

The IAF was also calculated for BC-containing particles as a function of the D_{MEV} of the rBC core (total aerosol and ice residual size distributions of the rBC core are shown in the upper panel of Figure 5.9, with the resulting IAF displayed in the lower panel of Figure 5.9). An increase in the IAF from $2 \cdot 10^{-5}$ for an rBC core with D_{MEV} = 0.08 µm to 5 10^{-4} for an rBC core with D_{MEV} = 0.29 µm is observed. The total aerosol BC number size distribution peaks below a BC core diameter of 100nm and decreases with size, reaching a value one order of magnitude lower for a core size D_{MEV} = 200nm and two orders of magnitude lower for a core size D_{MEV} = 290nm. Consequently, the number weighted mean activation ratio of BC-containing particles is below 10^{-4}, implying that, on average, BC is a very poor IN in the probed MPC conditions. Furthermore, BC-containing particles are depleted in the IR, with a number fraction of 1% in the IR population as compared to 11% in the total aerosol, based on SP2 measurements in the optical size range of 170 and 440nm. Therefore, BC is not considered to play a significant role in nucleating ice at the Jungfraujoch. This result is in agreement with the study of Kamphus et al. (2010), who found no enrichment of BC in IR measured downstream of the Ice-CVI with an Aerosol Time-of-Flight Mass Spectrometer, and the study of Chou et al. (2011), who did not find any correlation between concentrations of ice nucleating particles and BC mass (both studies were performed at the Jungfraujoch site).

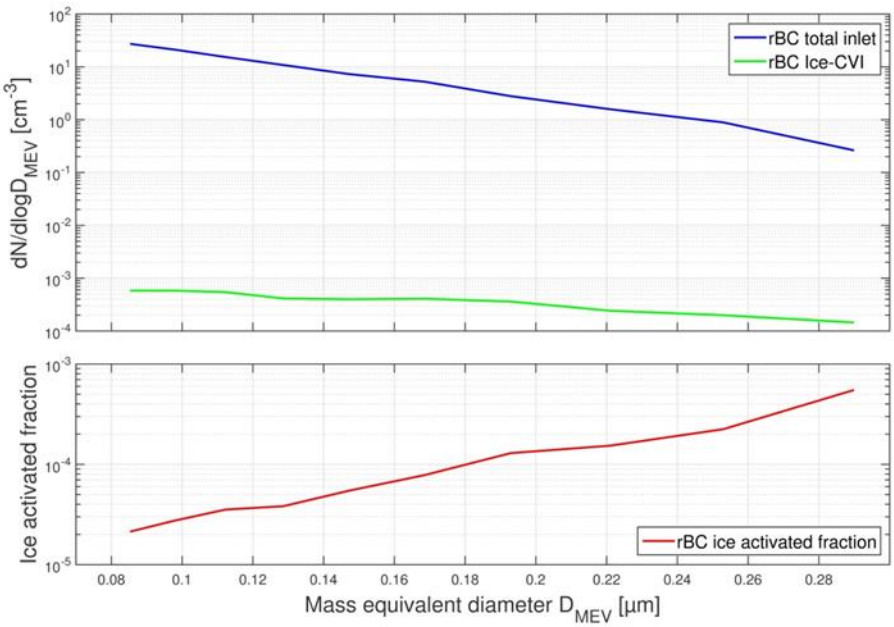

Figure 5.9 Size distributions of rBC cores and ice activated fractions for BC-containing particles as a function of rBC mass equivalent diameter D_{MEV} during CLACE 2013.

However, it is in contrast with the finding of (Cozic et al., 2008a), who found a higher BC mass fraction in Ice-CVI IR than in the total aerosol, based on measurements with two PSAPs, SMPS and Grimm OPSS. In order to understand the difference in the results obtained by Cozic et al. (2008a) and those presented in this paper, it is necessary to consider the characteristics and limitations of the instruments used, and the data processing procedure followed, in the two respective studies. The PSAP used by (Cozic et al., 2008a) is a filter-based technique, which provides a measure of the attenuation coefficient. This can be converted into an absorption coefficient as described by Bond et al. (1999) and, assuming a mass absorption cross-section (MAC), the equivalent black carbon (eBC) mass concentration can be derived. However, the PSAP measurements are prone to artifacts due to cross-sensitivity of the PSAP to other absorbing aerosols, such as mineral dust, as well as to scattering by sampled particles. Cozic et al. (2008a) attempted to correct the absorption downstream of the Ice-CVI for potential interference from mineral dust absorption in the following manner: the ice residual size distribution based on SMPS and Grimm measurements (size range of 17nm to 20 µm) was converted into a maximum mineral dust mass concentration, assuming a density of 2.5 g cm^{-3}. The absorption coefficient for mineral dust was subsequently derived using a MAC of 0.04 m^2 g^{-1}. The upper limit of mineral dust contribution to the absorption obtained from the PSAP was obtained based on the ratio of the mineral dust absorption coefficient to the absorption coefficient measured by the PSAP, and was found to be 15% on average. The BC mass fraction was derived from the ratio of the eBC mass measured by the PSAP to the mass of the sub-micrometer total aerosol, which was calculated using the particle volume measured by the SMPS (size range of 17 nm to 900 nm). It should be noted that the potential contribution of mineral dust to the absorption measured by the PSAP is uncertain may have been underestimated by Cozic et al. (2008a). As shown in this work there are large uncertainties in the size distributions derived by OPSS instruments at larger sizes, with the Grimm size distributions generally considerably lower than the TSI OPS size distributions (see Section

5.3.3). Under-counting of the Grimm OPSS and/or losses of large particles in the tubing between the Ice-CVI and the Grimm OPSS would have resulted in a low-bias in the assumed mineral dust mass concentration and, therefore, an underestimation of the contribution of mineral dust to the absorption derived from the PSAP. The SP2 is a single-particle instrument, as opposed to the filter-based PSAP, and does not suffer from the potential artifacts introduced into the PSAP data processing by interference from non-BC absorbing particles, which, additionally, are likely to differ in contribution between the total inlet and Ice-CVI. In order to establish whether data obtained from the PSAP could be affected by such artifacts downstream of the Ice-CVI, we have calculated and compared the MAC values downstream of the Ice-CVI and total inlet, based on the absorption coefficient derived from the PSAP and the BC mass concentration derived from the SP2, for the respective inlets. Non-simultaneous time periods are used for the Ice-CVI and total inlet as only one PSAP, switched between the Ice-CVI and total inlet, was operated. The PSAP absorption measurements were corrected following Bond et al. (1999). Scattering coefficient measurements were not available and thus, as in Cozic et al. (2008a), no correction for scattering was applied. The calculated MAC values were 14 $m^2\ g^{-1}$ downstream of the total inlet and 1000 $m^2\ g^{-1}$ downstream of the Ice-CVI. This enormous difference highlights that the PSAP absorption measurements downstream of the Ice-CVI are strongly affected by the presence of non-BC absorbing aerosol, such as mineral dust or metallic particles. It should be noted that the BC mass concentration measured by the SP2 will be biased low for the IR as compared to the total aerosol. As the detection range of the SP2 is limited to 80 − 310nm and the mode of the mass size distribution of BC-containing particles is shifted to a larger size for ice residuals (D_{MEV} = 290 nm, or potentially larger, as this the uppermost size bin of the SP2) than for the total aerosol D_{MEV} = 170nm, a larger fraction of the BC mass in IR than in the total aerosol is above the detection limit of the SP2. Nonetheless, while this bias contributes to the difference in MAC values between the Ice-CVI and total aerosol measurements, the contribution of non-BC absorbing aerosol is most likely dominant. The discussion of potential biases when comparing mass-based measurements for assessing ice nucleating activity of particles highlights that number-based measurements should be favored. Furthermore, it should be noted that BC mass and BC number are not perfectly correlated and, as it is the number of ice nucleating particles which is of importance, the latter should be favored when analyzing the contribution of BC to ice nucleation. As such, we consider the SP2 to be a more robust measurement technique for determining the BC content in IR. Furthermore the normalization of BC mass by the mass of the sub-micrometer total aerosol done by Cozic et al. (2008a) in order to obtain a BC mass fraction introduces a further uncertainty in the interpretation of their results, as the mass of the IR will vary strongly depending on dust particle activation during a given sampling event. Consequently, we consider the IAF derived from number concentrations to be a more reliable method for establishing the importance of BC for ice nucleation.

5.3.4 Black carbon coating thickness

The coating thickness of total aerosol and IR BC-containing particles with a D_{MEV} core size of 170 to 220nm was determined using the SP2, as described in Section 5.2.3.3. A comparison of the frequency of occurrence of a given coating thickness as a function of size is shown in Figure 5.10, with a distinct difference in the coating behavior for the total aerosol and the ice residuals. While BC found in the total aerosol was only moderately coated, with a median value of 16nm, the BC found in IR had a much thicker coating (median= 53nm) and had a much broader frequency of occurrence distribution, with coatings up to 200nm thick. Based on our findings, coating of the rBC core increases the ice nucleating ability of a particle. However, it is unclear whether this is due to an increase in the size of the particle (as described in the previous section, the likelihood of a particle acting as an ice nuclei increases with its size), or due to a change in its surface properties. Previous studies of the influence of coating on ice nucleation by BC particles have resulted in a broad range of findings concerning the direction of the coating effect: Möhler et al. (2005) found that sulfuric acid decreased the ice nucleation activity of soot in the temperature range of −88 °C to −43 °C. DeMott et al. (1999), on the contrary, identified multi-layer sulfuric acid coatings as enhancing ice nucleation as compared to uncoated soot at temperatures below −53 °C. Meanwhile, organic coating and exposure to ozone, as in the case of uncoated soot, did not lead to heterogeneous ice nucleation above the experimental detection limit at −20 °C and −30 °C in a study by Friedman et al. (2011). Similarly, Chou et al. (2013) did not identify photochemical aging of combustion aerosol in a smog chamber as having a noticeable effect on its ice nucleating ability, except for an experiment during which a thicker organic coating was created, resulting in larger particles. Considering our current understanding of the influence of coating on ice nucleation, it cannot be stated with certainty whether the increase in particle size, or the change in hydrophilicity, in the functional groups at the particle surface or in the shape of the particle was the dominating factor in increasing the ice nucleating ability of the sampled particles.

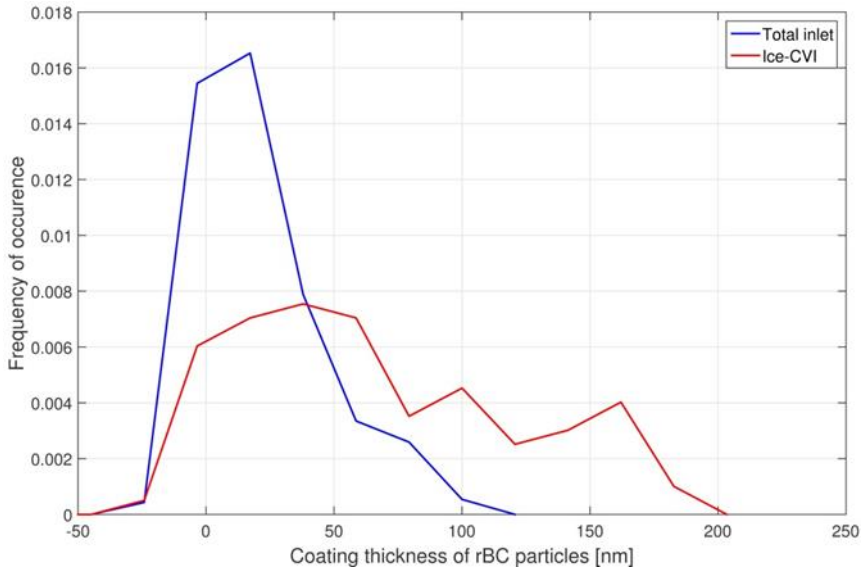

Figure 5.10 Coating thickness of BC-containing particles with a core size in the range of 170 to 220 nm measured during simultaneous sampling downstream of the total inlet and the Ice-CVI using SP2.

5.4 Conclusions

Size distributions, black carbon content and coating thickness of BC-containing particles were measured for total aerosol and IR particles in MPCs at the Jungfraujoch. IR are found to be enriched in larger particles, with an increase in the IAF with particle size; IAFs were on the order of 10^{-4} to 10^{-3} for 100nm and 0.2 to 0.3 for for 1 µm particles. Nonetheless, size distributions show that sub-micrometer particles dominate the IR population by number, due to their sheer number relative to super-micrometer particles in the total aerosol. As in the case of the overall IR population, the IAF of BC-containing particles increases with size. BC-containing particles were depleted in IR, with an IAF for a given particle size approximately 1 order of magnitude lower than that of BC-free particles and a number-weighted mean IAF of BC-containing particles below 10^{-4}. This finding provides strong evidence that a potential anthropogenic climate impact of BC via the glaciation effect in MPCs (Lohmann, 2002) is likely to be negligible. An analysis of the coating thickness of BC-containing particles showed hat in the total aerosol they are moderately coated, while in the ice residuals the coating is significantly thicker. It is not clear whether the coating influence on ice nucleation is mainly via an increase in the particle size, or via a change in the particle surface properties.

Acknowledgements

This project is funded by the Swiss National Science Foundation (grant 135356), the DFG priority program HALO (SPP 1294, grant ME 3534/1-2), the DFG research unit INUIT (grant STR453/7-1), the DFG (grant SCHN 1140/2-1), MeteoSwiss (GAW-CH program), the European Research Council (grant 615922-BLACARAT) and the ACTRIS program (European Union Seventh Framework Program (FP7/2007-2013), grant 262254) and the BACCHUS project (European Union Seventh Framework Program (FP7/2007-2013), grant 603445). We thank the International Foundation High Altitude Research Stations Jungfraujoch and Gornergrat (HFSJG) for the opportunity to perform experiments on the Jungfraujoch. We also thank MeteoSwiss for providing the meteorological data.

Supplementary

a) SP2 comparison

In order to perform proper measurements, the relative precision of the two different SP2s have been tested. The SP2 permanently linked to the total inlet was deployed by the Atmospheric Aerosol Research division of the Karlsruher Institute of Technology ($SP2_{KIT}$). Otherwise, a second SP2, belonging to the Laboratory of Atmospheric Chemistry of the Paul Scherrer Institute ($SP2_{PSI}$), was running at the ice-CVI inlet. The intercomparison has been conducted the 8th, 9th and 13th of February 2013 at the total inlet, this ensures high counts and robust statistic. Both SP2s were equipped with four detection channels, two of them dedicated to incandescence radiation and two for scattered light. Despite being the same version, the two SP2s had different size ranges. In this part of the work, as elsewhere, particles showing an incandescence signal are called "rBC-containing particles" while particles not showing an incandescence signal are addressed as "rBC-free particles". The size range of $SP2_{PSI}$ was reduced to match with $SP2_{KIT}$. Final size range for optical sizing of rBC-free particles was between 150 and 290 nm; detection of rBC cores was done within 80 and 340 nm of mass equivalent diameter. Comparison of rBC cores number concentrations and rBC-free particles is showed in Figure 5.11. The number concentration of rBC cores and rBC-free particles agreed within 10%, with correlation coefficients of 0.85 and 0.92 respectively.

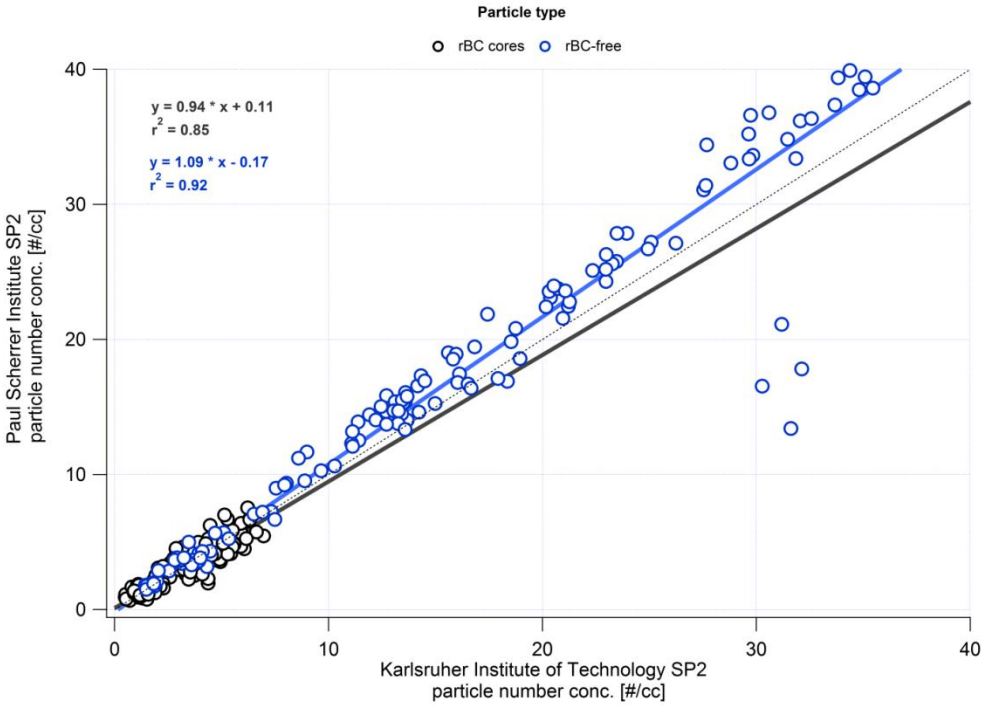

Figure 5.11. Scatter plot of rBC-cores and rBC-free particles mass concertation detected. Each point represents 30 min average. Linear fit calculated using the least orthogonal distance approach.

Detection efficiency of the SP2 for rBC-cores and rBC-free particles has been assessed as function of particles size (Figure 5.12). rBC core size distributions agree within 7%, while rBC-free particles size

distributions agreed within 10%. Similar variability has been found in previous SP2 intercomparison by (Laborde et al., 2012b) and quantified at 7% and 15% for rBC cores and rBC-free particles respectively.

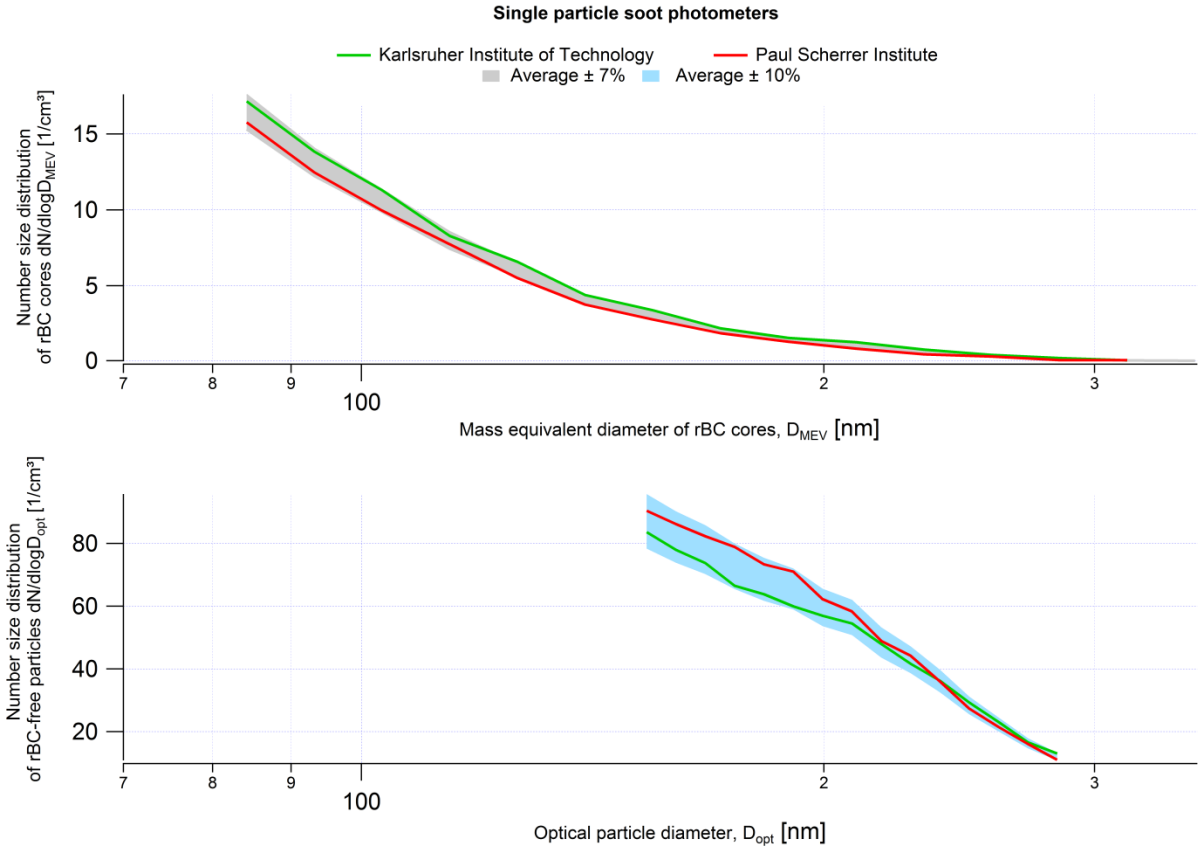

Figure 5.12. Comparison of particle number distribution of ambient air in the low free troposphere. Top panel: Number size distribution of rBC cores detected via laser induced incandescence. Bottom panel: number size distribution of rBC-free particles detected via optical approach. Refractive index for non-refractory material: 1.50

Relative precision of LEO-fit sizing was tested in a similar manner (Figure 5.13). The detection range of the LEO-fit approach ranged between 170 and 440 nm of optical diameter. The two rBC-free particle distributions agreed nicely along all the detection range, with less than 10% difference. rBC-containing particle distributions are in good agreement under the 250nm (less than 10% difference). Discrepancies between 10 and 25% are observed after 300 nm.

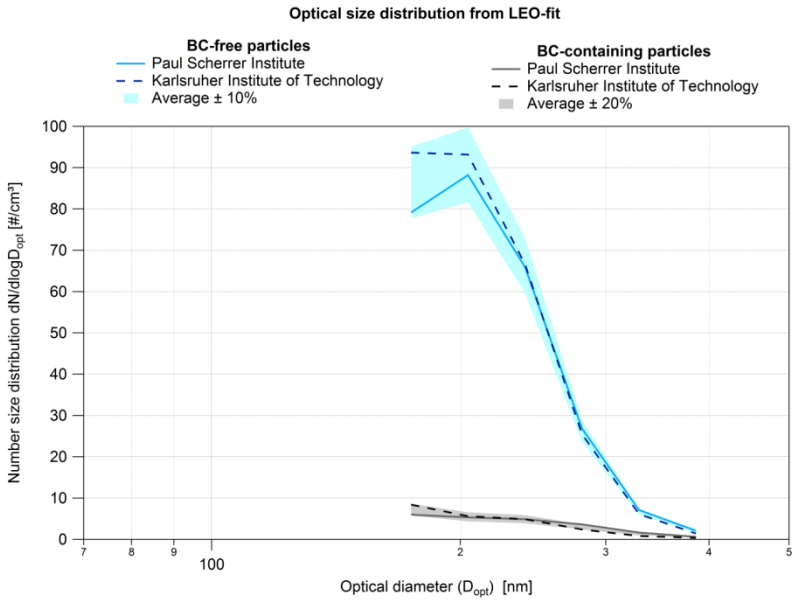

Figure 5.13. Comparison of rBC-free and rBC-containing particles number distribution. Size distribution derived from leading edge only (LEO) fit. Refractive index for non-refractory material: 1.50. Refractory index for rBC cores: 2.26 + 1.26i.

In previous intercomparison study, coating thickness derived from six different SP2s was found to agree within 17% (Laborde et al., 2012b). In this thesis the coating thickness derived for rBC cores having a mass equivalent diameter between 170 and 220 nm agreed within 10% (Figure 5.14). The median coating thickness was quantified in 14 nm and 16 nm for the $SP2_{PSI}$ and the $SP2_{KIT}$ respectively. In general, discrepancies bigger than 20% were not observed indicating that calibration and tuning of the optical system were properly done on both instruments and ensured high relative precision between the two instruments.

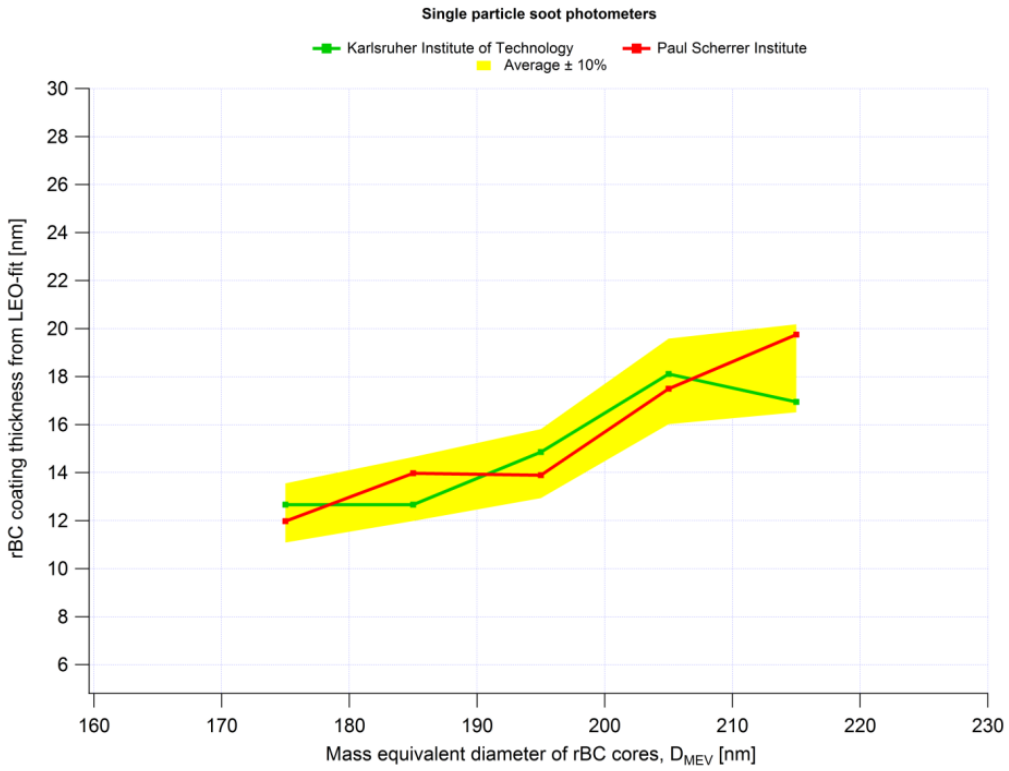

Figure 5.14. Comparison of coating thickness derived for rBC particles with different diameters.

b) Refractory non-BC matter

According to the manufacturer and previous works, interference induced by non-refractory coating and other refractory materials was never observed during rBC observatioons using the SP2. In this section we show evidences that during CLACE campaign 2013 the SP2 suffered from interferences caused by the presence of refractory materials other than rBC, most probably metal containing particles as mineral dust. During the rest of the section this incandescing particles, showing different behavior than rBC will be called refractory non-BC (r-nBC) particles. In Figure 5.15. are showed the incandescence and scattering signals for refractory particles having a mass equivalent diameter of 140-160 nm. Large rBC-containing particles show intense scattering signal (S_{scat}), for larger particles the scattering detector saturates avoiding the optical sizing. Thickly coated rBC cores can show a saturates scattering signal (Figure 5.15.b), but usually, the time duration of saturation does not exceed the half of acquisition time. Else, the r-nBC particles showed longer saturated scattering signal suggesting an extremely large incandescing particle (Figure 5.15.c). For comparison, a typical signal of a coated rBC-core is showed in Figure 5.15.a.

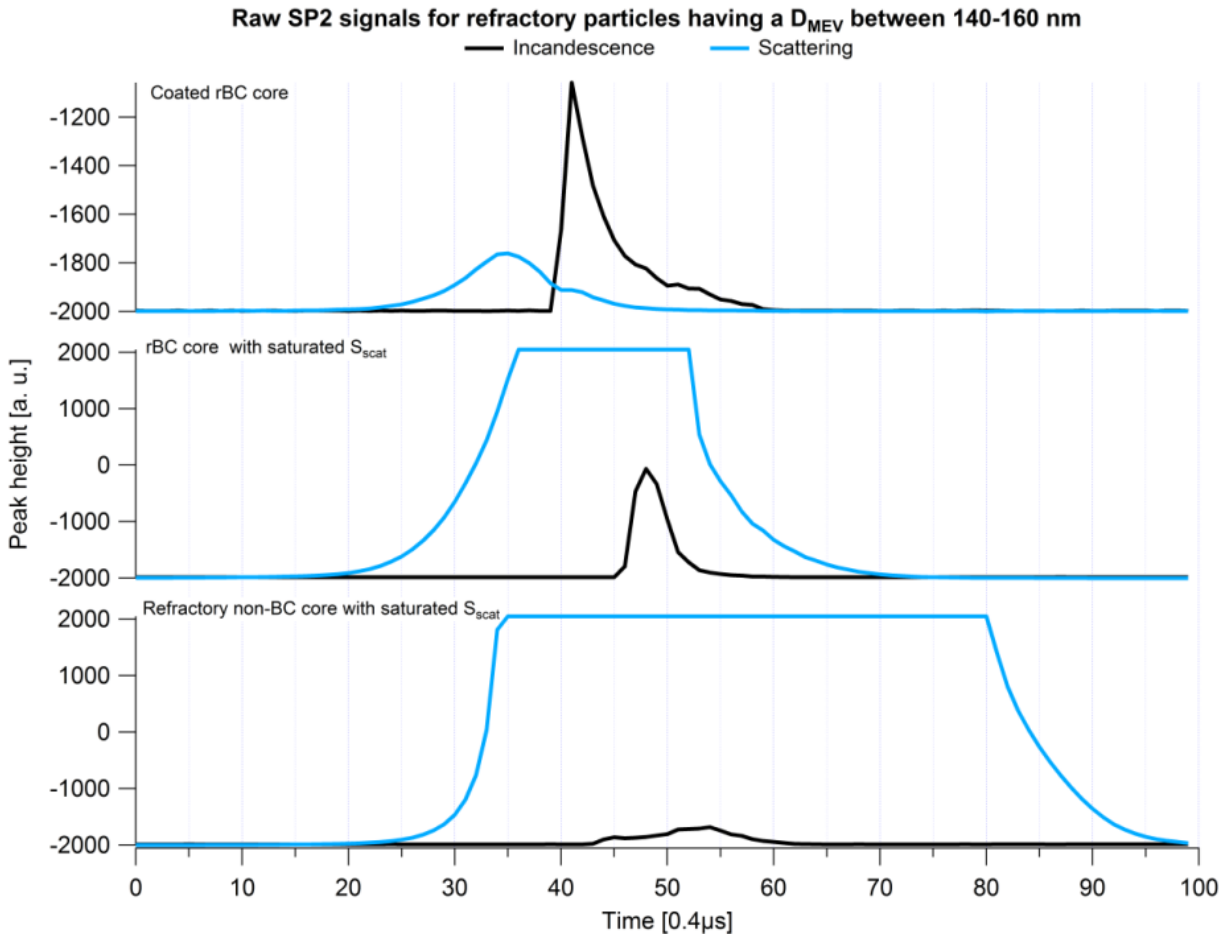

Figure 5.15. Scattering and incandescence raw signals for a coated rBC core (top), a rBC core with saturated scattering signal (middle) and an incandescing particle with super-micron diameter (bottom). All the particle kinds have the same mass equivalent diameter (140-160 nm).

Differences in the time evolution of incandescence signal were observed between rBC-containing particles without saturated scattering signal and r-nBC (incandescence signal plus saturated scattering). rBC cores usually show a sharp rise of incandescence, whit a short delay between start on incandescence and peak position (Figure 5.16). Incandesce ignition and decay are slower for r-nBC particles, leading to a time prolonged emission of incandescence radiation. This different incandescing behavior suggests that particle composition between these two cases might differ.

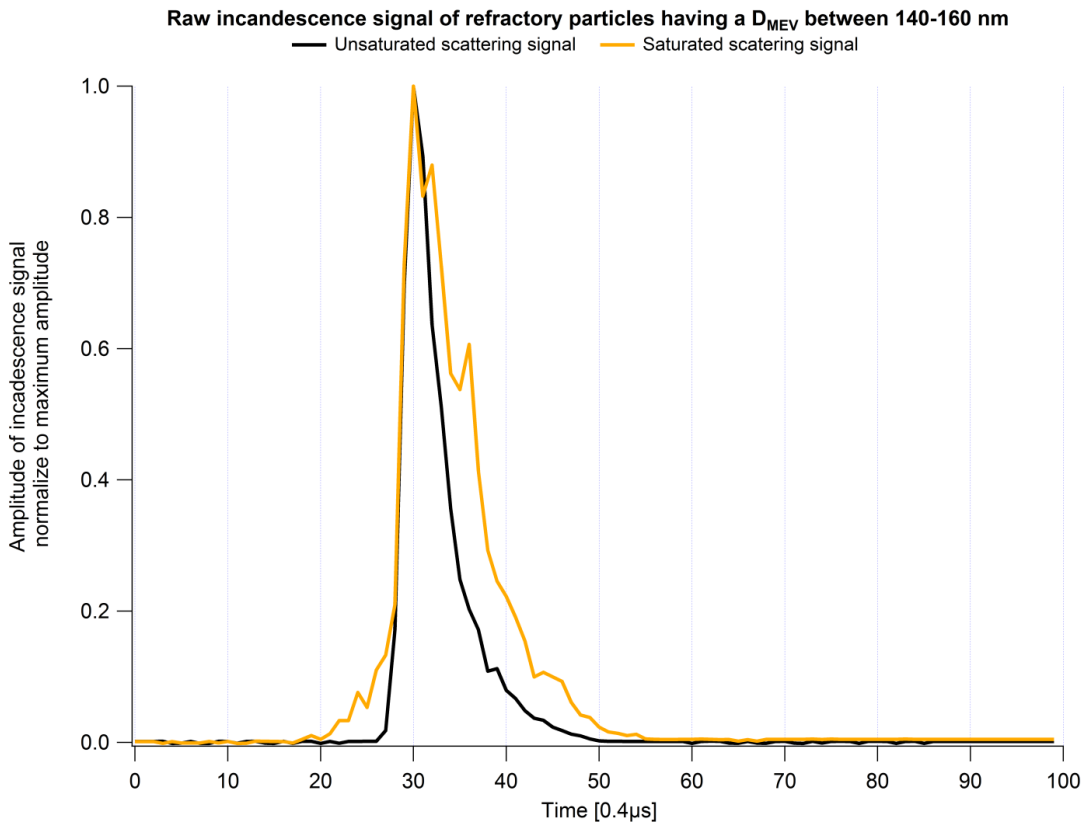

Figure 5.16 Shape of incandescence signals of refractory particles having the same mass equivalent diameter (140-160 nm with saturated or unsaturated scattering signal.

The emission spectrum of a particle is function of its chemical composition, which define also the vaporization temperature. The color ratio is usually defined as the ratio of emitted light at two different wavelengths and gives indications on the vaporization temperature and might be used to differentiate between different types of incandescing materials. The ratio of incandescence peak heights detected by the broadband and narrowband detector (Figure 2.4) is used, here to discriminate the rBC-containing particles from the n-rBC particles. rBC particles showed a different color ratio values compared to the n-rBC particles, suggesting that rBC and r-nBC particles have a different emissivity spectrum, vaporization temperature and thus chemical composition.

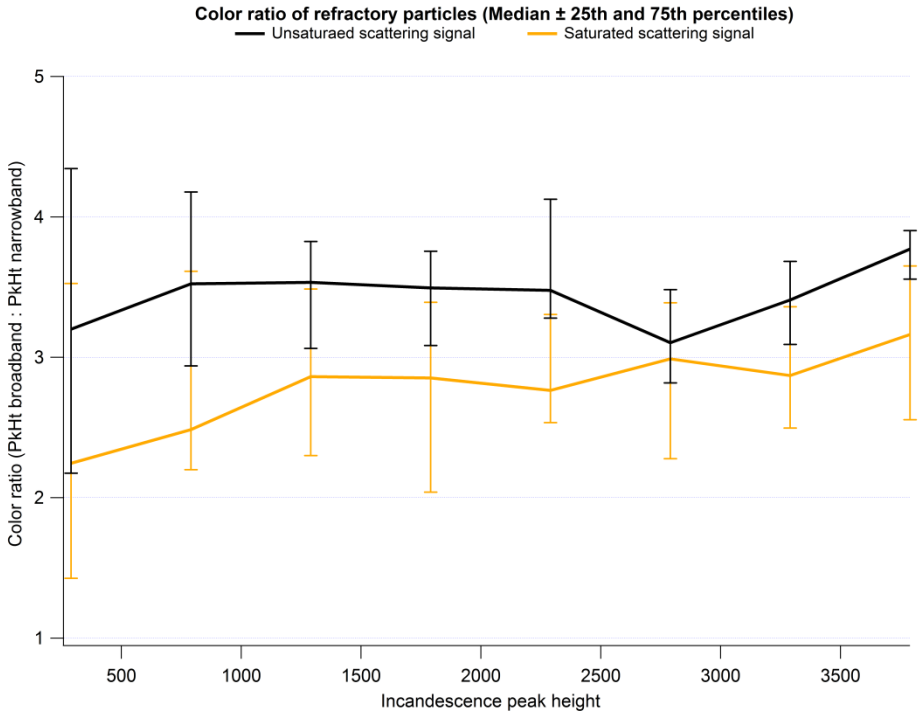

Figure 5.17 Color ratio as function of incandescence peak height, proportional to mass equivalent diameter. Color ratio calculated as the emitted radiation between a wavelength range of 350-800 nm (broadband) and 600-800nm (narrowband).

Resuming, a consistent fraction of incandescing particles showed a saturated scattering signal, the duration of the saturation was unusually long and rarely observed in past field experiments. The duration of saturation suggested super-micron diameters. The time resolved shape of incandescence signal differed consistently between refractory particles with and without saturation of scattering signal. Different color ratio means that emissivity, vaporization temperature and composition are not equal. These observations lead to the preliminary conclusion that we observed two different refractory and absorbing types of particulate matter. Additionally, the refractory non-BC particles were enriched in the ice residuals compared to the rBC cores (Figure 5.18). The r-nBC particles would have large diameter, strong light absorption in the near infrared spectrum, stronger incandescence emissivity in the red part of the visible spectrum and discrete refractoriness properties. Iron reach minerals as olivine (Fe^{2+}; Fe_2SiO_4) and hematite (Fe^{3+}; Fe_2O_3) have similar characteristics: intense light absorption bands between 800 nm and 1100 nm a and strong emissivity in the red part of visible spectrum (Vander Wal et al., 1999). Additionally, mineral dust is recognized to be a strong ice nucleus being enriched in the ice residuals (Hoose and Möhler, 2012), as observed here. However we are not able to prove it, all our findings suggest that the SP2 is sensitive to the presence of refractory non-BC particles as iron rich mineral dust.

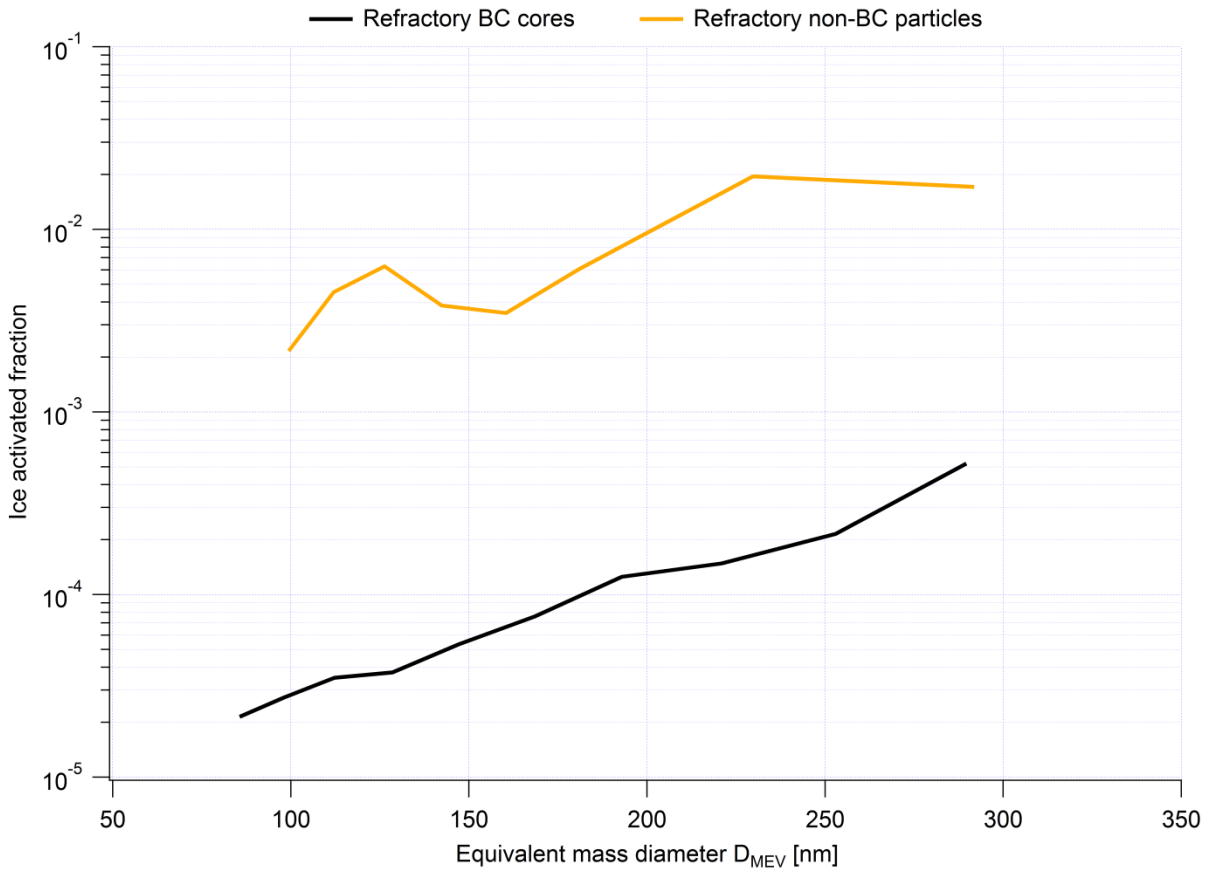

Figure 5.18 Ice activation of refractory BC cores and refractory non-BC cores.

In this section of the thesis, all the incandescing particles showing saturation of scattering signal at the incandescence point have been filtered and called r-nBC particles. This is a preliminary filtering method that needs further implementation based on laboratory experiments, but allowed to remove all the possible interferences.

6 Conclusion and outlook

Black carbon (BC) has a great impact on earth's climate due to its light absorption behavior. However, the lack of a deep knowledge in behavior of atmospheric BC leads to a large uncertainty in the estimation of its global radiative forcing. The motivation of this thesis was to investigate the BC-radiation and BC-cloud interactions as function of mixing with other atmospheric matter aiming to provide fresh and accurate BC properties for future radiative forcing estimation.

The estimation of radiative forcing due to BC-radiation interaction is based not only on the amount of BC atmospheric burden but also on its optical properties. The mass absorption cross-section (MAC) of BC is used to infer radiative forcing from BC atmospheric burden. At the actual state of the art, radiative models use constant global MAC to calculate radiative forcing, regardless of spatial and seasonal variability of black carbon optical properties. Additionally, MAC values found in the literature are highly heterogeneous, with a factor of four between the minimum and maximum values. We investigated MAC spatial and seasonal variability over Europe. MAC was calculated from absorption coefficients (σ_{ap}) and elemental carbon mass concentrations (m_{EC}) observed at nine background ACTRIS supersites spread from the Mediterranean to Scandinavia. Both σ_{ap} and m_{EC} data were corrected for potential instrumental artifacts and then harmonized on a reference technique. A strong spatial variability of absolute MAC values was not observed between the different stations. Statistical analysis revealed a discrete homogeneity of considered optical properties; as a consequence, an overall MAC mean of 10 $m^2 g^{-1}$ ± 2.5 $m^2 g^{-1}$ at 637 nm might be representative of BC at European background locations. However every station showed a MAC variability, a statistical significant and common seasonal trend was not observed. The spatial homogeneity suggested that BC undergoes similar processing in Europe, while the seasonal variability indicates a consistent change of optical properties from the cold to the warm season, probably induced by aging and internal mixing. Due to this seasonal cycle, we investigated the dependence of MAC as function of presence of non-absorbing matter (NAM) in the visible spectrum. The latter was assumed to be composed by organic matter, sulfate and nitrate particulate. The mass ratio of NAM over EC might be interpreted as a proxy for the degree of internal mixing. MAC at five stations was found to increase with the relative presence of NAM. Despite all assumptions, this positive relationship confirms results from previous work suggesting an increase of absorption due to internal mixing. Compared to previous studies investigating MAC, we elaborated a highly homogeneous dataset, which ensured reducing the instrumental artifacts leading to narrow MAC uncertainty. These findings suggest that the assumption of a constant and globally averaged mass absorption cross section does not reflect reality introducing an unpredicted error in radiative forcing calculation.

Once emitted, the black carbon particles might be transported on intercontinental scale. According to previous studies, morphology and mixing evolve during transport leading to a consistent change in optical properties of BC. To understand the transformation induced on black carbon after long range transport, intensive field experiment was conducted during arctic spring in Svalbard, Norway. An optical characterization of the total aerosol was performed: small values of aerosol optical depth, negative values of Ångström exponent difference and high single scattering albedo indicated that in

2012 no extreme smoke events took place and that the aerosol population was dominated by fine and non-absorbing particles. The single particle soot photometer (SP2) was used to infer the major properties of refractory black carbon (rBC). Low concentration around 30 ng m^{-3} of rBC was found, with a mean mass equivalent diameter above 200 nm. rBC concentration detected with the continuous soot monitoring system and the single particle soot photometer was ageing within 15%. Combining absorption coefficient observed with an Aethalometer and BC mass concentration from SP2, a mass absorption cross section of 6.0 m^2 g^{-1} was found at a wavelength of 880 nm. Concerning mixing, BC with attached geometry represented a minor fraction of BC-containing particles. rBC cores with a dimeter between 170 nm and 280 nm were covered by a layer of non-absorbing material having a median thickness of 50 nm. From Mie calculation, such mixing would lead to an enhancement of absorption of 46% compared to a bare BC core. However was not possible to calculate the influence of coating of radiative forcing in the arctic, we estimated that the discussed absorption enhancement would lead to a net decrease of single scattering albedo of the total aerosol of less than 1%. Considering the high albedo of arctic region this might induce a consistent increase of radiative forcing. Despite this is only a speculation, with this work we provided some of the BC key properties (as mass concentration, diameter, coating thickness and mass absorption cross section) to accurately simulate the impact of BC in the arctic.

BC can also interact with clouds, inducing the so called aerosol-cloud radiative forcing. As explained in Section 1.4.2, high uncertainty and contradicting results have been found in the past literature concerning the role of black carbon as ice nucleus. For the first time we investigated the presence of refractory black carbon in ice residuals (IR) of mixed phase clouds using the laser induced technique combined with an Ice-CVI inlet. rBC detection was performed with two SP2s, operating simultaneously, one linked to a total inlet and the other sampling only the ice residuals. During data analysis became clear that the SP2 was undergoing some extra counts. Behavior of incandesce signals and saturation of scattering detector suggested that we were dealing with unusual incandescing particles with a super-micron diameter. However our hypothesis must be confirmed by laboratory experiments, false positive cunts may be caused by incandescing metal-containing particles as iron rich mineral dust. The extra counts attributed to dust were successfully filtered during data analysis. The observation revealed that the number size distribution in the ice residuals was dominated by sub-micrometric particles, and that rBC-containing particles were depleted in the IR. The number of rBC-containing particles in ice residuals was very low (1% of IR in the size range detected by the SP2, as compared to 11% in the total aerosol). The ice activated fraction of rBC-containing particles was approximately an order of magnitude lower than the ice activated fraction of BC-free particles. Based on these findings, we conclude that rBC does not significantly contribute to ice nucleation in free tropospheric mixed-phase clouds. Consequently, a potential anthropogenic climate impact of rBC via the glaciation effect in mixed phase clouds is likely to be negligible. As regards the coating thickness of rBC-containing particles, the total aerosol was only moderately coated (median= 16nm), in contrast to the ice residuals which had thicker coatings (median= 53 nm), with a broad distribution of frequency of occurrence as a function of coating thickness and coatings up to as much as 200nm thick. The influence of a coating on a particle's ice nucleating ability could be either via an increase in particle size or via change in the particle's surface properties. However the cause cannot be

determined based on this study, the finding that ice residuals have much thicker coatings than the total aerosol highlights the importance of atmospheric aging processes for ice nucleation.

Along this project we understood how optical properties and ice activation behavior of black carbon particles might depend on the internal mixing with other non-absorbing or non-refractory components. The SP2 has been revealed to be a powerful tool to investigate refractory black carbon characterizing including mixing state. Further and more accurate laboratory experiments and analysis must be conducted in the future to confirm and understand the sensitivity of the instrument to other refractory material as mineral dust. Radiative forcing simulations are encouraged to finally understand the influence of black carbon mixing on the arctic warming. Considering the acquired experience in treating absorption data coming from absorption photometers, and despite the several instrumental intercomparisons a universally recognized methodology for absorption coefficient observation is definitely needed.

List of Figures

List of tables

References

Ackerman, T. P. and Toon, O. B.: Absorption of visible radiation in atmosphere containing mixtures of absorbing and nonabsorbing particles, Appl. Opt., 20(20), 3661, doi:10.1364/AO.20.003661, 1981.

Adachi, K. and Buseck, P. R.: Internally mixed soot, sulfates, and organic matter in aerosol particles from Mexico City, Atmos Chem Phys, 8(21), 6469–6481, doi:10.5194/acp-8-6469-2008, 2008.

Adachi, K., Chung, S. H. and Buseck, P. R.: Shapes of soot aerosol particles and implications for their effects on climate, J. Geophys. Res. Atmospheres, 115(D15), D15206, doi:10.1029/2009JD012868, 2010.

AMAP: The Impact of Black Carbon on Arctic Climate (2011). By: P.K. Quinn, A. Stohl, A. Arneth,T. Berntsen, J. F. Burkhart, J. Christensen, M. Flanner, K. Kupiainen, H. Lihavainen, M. Shepherd, V. Shevchenko,H. Skov, and V. Vestreng. AMAP Technical Report No. 4 (2011). Arctic Monitoring and Assessment Programme (AMAP), Oslo. 72 pp., [online] Available from: http://www.amap.no/documents/doc/the-impact-of-black-carbon-on-arctic-climate/746 (Accessed 7 January 2016), 2011.

AMAP: AMAP Assessment 2015: Black carbon and ozone as Arctic climate forcers. Arctic Monitoring and Assessment Programme (AMAP), Oslo, Norway. vii + 116 pp., [online] Available from: http://www.amap.no/documents/doc/amap-assessment-2015-black-carbon-and-ozone-as-arctic-climate-forcers/1299 (Accessed 7 January 2016), 2015.

Anderson, T. L. and Ogren, J. A.: Determining Aerosol Radiative Properties Using the TSI 3563 Integrating Nephelometer, Aerosol Sci. Technol., 29(1), 57–69, doi:10.1080/02786829808965551, 1998.

Andrews, E., Sheridan, P. J., Fiebig, M., McComiskey, A., Ogren, J. A., Arnott, P., Covert, D., Elleman, R., Gasparini, R., Collins, D., Jonsson, H., Schmid, B. and Wang, J.: Comparison of methods for deriving aerosol asymmetry parameter, J. Geophys. Res. Atmospheres, 111(D5), D05S04, doi:10.1029/2004JD005734, 2006.

Anon: AEO2012 Early Release Overview - 0484(2014).pdf, [online] Available from: http://www.eia.gov/forecasts/ieo/pdf/0484(2014).pdf (Accessed 9 November 2015a), n.d.

Anon: Fifth Assessment Report - Climate Change 2013, [online] Available from: http://www.ipcc.ch/report/ar5/wg1/ (Accessed 4 August 2015b), n.d.

Anon: World Population Prospects - Population Division - United Nations, [online] Available from: http://esa.un.org/unpd/wpp/DVD/ (Accessed 9 November 2015c), n.d.

Archuleta, C. M., DeMott, P. J. and Kreidenweis, S. M.: Ice nucleation by surrogates for atmospheric mineral dust and mineral dust/sulfate particles at cirrus temperatures, Atmos Chem Phys, 5(10), 2617–2634, doi:10.5194/acp-5-2617-2005, 2005.

Asmi, A., Wiedensohler, A., Laj, P., Fjaeraa, A.-M., Sellegri, K., Birmili, W., Weingartner, E., Baltensperger, U., Zdimal, V., Zikova, N., Putaud, J.-P., Marinoni, A., Tunved, P., Hansson, H.-C., Fiebig,

M., Kivekäs, N., Lihavainen, H., Asmi, E., Ulevicius, V., Aalto, P. P., Swietlicki, E., Kristensson, A., Mihalopoulos, N., Kalivitis, N., Kalapov, I., Kiss, G., de Leeuw, G., Henzing, B., Harrison, R. M., Beddows, D., O'Dowd, C., Jennings, S. G., Flentje, H., Weinhold, K., Meinhardt, F., Ries, L. and Kulmala, M.: Number size distributions and seasonality of submicron particles in Europe 2008–2009, Atmos Chem Phys, 11(11), 5505–5538, doi:10.5194/acp-11-5505-2011, 2011.

Babu, S. S., Moorthy, K. K., Manchanda, R. K., Sinha, P. R., Satheesh, S. K., Vajja, D. P., Srinivasan, S. and Kumar, V. H. A.: Free tropospheric black carbon aerosol measurements using high altitude balloon: Do BC layers build "their own homes" up in the atmosphere?, Geophys. Res. Lett., 38(8), L08803, doi:10.1029/2011GL046654, 2011.

Bae, M.-S., Schauer, J. J., DeMinter, J. T., Turner, J. R., Smith, D. and Cary, R. A.: Validation of a semi-continuous instrument for elemental carbon and organic carbon using a thermal-optical method, Atmos. Environ., 38(18), 2885–2893, doi:10.1016/j.atmosenv.2004.02.027, 2004.

Baltensperger, U., Schwikowski, M., Jost, D. T., Nyeki, S., H.W Gäggeler and Poulida, O.: Scavenging of atmospheric constituents in mixed phase clouds at the high-alpine site jungfraujoch part I: Basic concept and aerosol scavenging by clouds, Atmos Env., 32(23), 3975 – 3983, doi:10.1016/S1352-2310(98)00051-X, 1998.

Barrie, L. A.: Arctic air pollution: An overview of current knowledge, Atmospheric Environ. 1967, 20(4), 643–663, doi:10.1016/0004-6981(86)90180-0, 1986.

Baumgardner, D., Popovicheva, O., Allan, J., Bernardoni, V., Cao, J., Cavalli, F., Cozic, J., Diapouli, E., Eleftheriadis, K., Genberg, P. J., Gonzalez, C., Gysel, M., John, A., Kirchstetter, T. W., Kuhlbusch, T. A. J., Laborde, M., Lack, D., Müller, T., Niessner, R., Petzold, A., Piazzalunga, A., Putaud, J. P., Schwarz, J., Sheridan, P., Subramanian, R., Swietlicki, E., Valli, G., Vecchi, R. and Viana, M.: Soot reference materials for instrument calibration and intercomparisons: a workshop summary with recommendations, Atmospheric Meas. Tech., 5(8), 1869–1887, doi:10.5194/amt-5-1869-2012, 2012.

Beine, H. J., Dahlback, A. and Ørbæk, J. B.: Measurements of J(NO2) at Ny-Ålesund, Svalbard, J. Geophys. Res. Atmospheres, 104(D13), 16009–16019, doi:10.1029/1999JD900237, 1999.

Berna, F., Goldberg, P., Horwitz, L. K., Brink, J., Holt, S., Bamford, M. and Chazan, M.: Microstratigraphic evidence of in situ fire in the Acheulean strata of Wonderwerk Cave, Northern Cape province, South Africa, Proc. Natl. Acad. Sci., 109(20), E1215–E1220, doi:10.1073/pnas.1117620109, 2012.

Birch, M. E. and Cary, R. A.: Elemental Carbon-Based Method for Monitoring Occupational Exposures to Particulate Diesel Exhaust, Aerosol Sci. Technol., 25(3), 221–241, doi:10.1080/02786829608965393, 1996.

Bird, M. I.: Fire, prehistoric humanity, and the environment, Interdiscip. Sci. Rev., 20(2), 141–154, doi:10.1179/isr.1995.20.2.141, 1995.

Bird, M. I. and Cali, J. A.: A million-year record of fire in sub-Saharan Africa, Nature, 394(6695), 767–769, doi:10.1038/29507, 1998.

Bohren, C. F. and Huffman, D. R.: Appendix B: Coated Sphere, in Absorption and Scattering of Light by Small Particles, pp. 483–489, Wiley-VCH Verlag GmbH. [online] Available from: http://onlinelibrary.wiley.com/doi/10.1002/9783527618156.app3/summary (Accessed 23 March 2015), 1998.

Bond, T. C. and Bergstrom, R. W.: Light Absorption by Carbonaceous Particles: An Investigative Review, Aerosol Sci. Technol., 40(1), 27–67, doi:10.1080/02786820500421521, 2006.

Bond, T. C., Anderson, T. L. and Campbell, D.: Calibration and Intercomparison of Filter-Based Measurements of Visible Light Absorption by Aerosols, Aerosol Sci. Technol., 30(6), 582–600, doi:10.1080/027868299304435, 1999.

Bond, T. C., Habib, G. and Bergstrom, R. W.: Limitations in the enhancement of visible light absorption due to mixing state, J. Geophys. Res. Atmospheres, 111(D20), D20211, doi:10.1029/2006JD007315, 2006a.

Bond, T. C., Habib, G. and Bergstrom, R. W.: Limitations in the enhancement of visible light absorption due to mixing state, J. Geophys. Res. Atmospheres, 111(D20), D20211, doi:10.1029/2006JD007315, 2006b.

Bond, T. C., Bhardwaj, E., Dong, R., Jogani, R., Jung, S., Roden, C., Streets, D. G. and Trautmann, N. M.: Historical emissions of black and organic carbon aerosol from energy-related combustion, 1850–2000, Glob. Biogeochem. Cycles, 21(2), GB2018, doi:10.1029/2006GB002840, 2007.

Bond, T. C., Doherty, S. J., Fahey, D. W., Forster, P. M., Berntsen, T., DeAngelo, B. J., Flanner, M. G., Ghan, S., Kärcher, B., Koch, D., Kinne, S., Kondo, Y., Quinn, P. K., Sarofim, M. C., Schultz, M. G., Schulz, M., Venkataraman, C., Zhang, H., Zhang, S., Bellouin, N., Guttikunda, S. K., Hopke, P. K., Jacobson, M. Z., Kaiser, J. W., Klimont, Z., Lohmann, U., Schwarz, J. P., Shindell, D., Storelvmo, T., Warren, S. G. and Zender, C. S.: Bounding the role of black carbon in the climate system: A scientific assessment, J. Geophys. Res. Atmospheres, 118(11), 5380–5552, doi:10.1002/jgrd.50171, 2013.

Boose, Y., Kohn, M., Kanji, Z. A., Sierau, B., Lohmann, U., Zipori, A., Crawford, I., Lloyd, G., Bukowiecki, N., Herrmann, E., Kupiszewski, P. and Steinbacher, M.: Three-year ice nucleating particle climatology in the free troposphere during winter, Submitt. J Atmos Sci, 2015.

Boucher, D. Randall, P. Artaxo, C. Bretherton, G. Feingold, P. Forster, V.-M. Kerminen, Y. Kondo, H. Liao, U. and Lohmann, P. Rasch, S.K. Satheesh, S. Sherwood, B. Stevens and X.Y. Zhang: IPCC, 2013: Clouds and Aerosols. In: Climate Change 2013: The Physical Science Basis. Contribution of Working Group I to the Fifth Assessment Report of the Intergovernmental Panel on Climate Change, edited by Stocker, T.F., Cambridge University Press, Cambridge, United Kingdom and New York, NY, USA, 571–657, 2013.

Bourgeois, Q. and Bey, I.: Pollution transport efficiency toward the Arctic: Sensitivity to aerosol scavenging and source regions, J. Geophys. Res. Atmospheres, 116(D8), D08213, doi:10.1029/2010JD015096, 2011.

Bowman, D. M. J. S., Balch, J., Artaxo, P., Bond, W. J., Cochrane, M. A., D'Antonio, C. M., DeFries, R., Johnston, F. H., Keeley, J. E., Krawchuk, M. A., Kull, C. A., Mack, M., Moritz, M. A., Pyne, S., Roos, C. I.,

Scott, A. C., Sodhi, N. S. and Swetnam, T. W.: The human dimension of fire regimes on Earth, J. Biogeogr., 38(12), 2223–2236, doi:10.1111/j.1365-2699.2011.02595.x, 2011.

Brown, K. S., Marean, C. W., Herries, A. I. R., Jacobs, Z., Tribolo, C., Braun, D., Roberts, D. L., Meyer, M. C. and Bernatchez, J.: Fire As an Engineering Tool of Early Modern Humans, Science, 325(5942), 859–862, doi:10.1126/science.1175028, 2009.

Burkart, J., Steiner, G., Reischl, G., Moshammer, H., Neuberger, M. and Hitzenberger, R.: Characterizing the performance of two optical particle counters (Grimm OPC1.108 and OPC1.109) under urban aerosol conditions, J Aerosol Sci, 41(10), 953 – 962, doi:10.1016/j.jaerosci.2010.07.007, 2010.

Cachier, H., Bremond, M.-P. and Buat-Ménard, P.: Determination of atmospheric soot carbon with a simple thermal method, Tellus B, 41B(3), 379–390, doi:10.1111/j.1600-0889.1989.tb00316.x, 1989.

Cai, Y., Montague, D. C., Mooiweer-Bryan, W. and Deshler, T.: Performance characteristics of the ultra high sensitivity aerosol spectrometer for particles between 55 and 800 nm: Laboratory and field studies, J Aerosol Sci, 39(9), 759 – 769, doi:10.1016/j.jaerosci.2008.04.007, 2008.

Cappa, C. D., Onasch, T. B., Massoli, P., Worsnop, D. R., Bates, T. S., Cross, E. S., Davidovits, P., Hakala, J., Hayden, K. L., Jobson, B. T., Kolesar, K. R., Lack, D. A., Lerner, B. M., Li, S.-M., Mellon, D., Nuaaman, I., Olfert, J. S., Petäjä, T., Quinn, P. K., Song, C., Subramanian, R., Williams, E. J. and Zaveri, R. A.: Radiative Absorption Enhancements Due to the Mixing State of Atmospheric Black Carbon, Science, 337(6098), 1078–1081, doi:10.1126/science.1223447, 2012.

Cavalli, F., Viana, M., Yttri, K. E., Genberg, J. and Putaud, J.-P.: Toward a standardised thermal-optical protocol for measuring atmospheric organic and elemental carbon: the EUSAAR protocol, Atmos Meas Tech, 3(1), 79–89, doi:10.5194/amt-3-79-2010, 2010.

Cavalli, F., Putaud, J. P. and ACTRIS station leaders: A European aerosol phenomenology -4: carbonaceous aerosol sampling artifacts, analytical discrepancies, and harmonised concentrations at 10 regional background sites across Europe, , in preparation, 2016.

Chen, J.-P. and Lamb, D.: Simulation of cloud microphysical and chemical processes using a multicomponent framework. Part II: microphysical evolution of a wintertime orographic cloud, J Atmos Sci, 56(14), 2293–2312, doi:10.1175/1520-0469(1999)056<2293:SOCMAC>2.0.CO;2, 1999.

Cherian, R., Quaas, J., Salzmann, M. and Wild, M.: Pollution trends over Europe constrain global aerosol forcing as simulated by climate models, Geophys. Res. Lett., 41(6), 2176–2181, doi:10.1002/2013GL058715, 2014.

Chiacchio, M., Ewen, T., Wild, M., Chin, M. and Diehl, T.: Decadal variability of aerosol optical depth in Europe and its relationship to the temporal shift of the North Atlantic Oscillation in the realm of dimming and brightening, J. Geophys. Res. Atmospheres, 116(D2), D02108, doi:10.1029/2010JD014471, 2011.

Chiappini, L., Verlhac, S., Aujay, R., Maenhaut, W., Putaud, J. P., Sciare, J., Jaffrezo, J. L., Liousse, C., Galy-Lacaux, C., Alleman, L. Y., Panteliadis, P., Leoz, E. and Favez, O.: Clues for a standardised thermal-

optical protocol for the assessment of organic and elemental carbon within ambient air particulate matter, Atmos Meas Tech, 7(6), 1649–1661, doi:10.5194/amt-7-1649-2014, 2014.

China, S., Scarnato, B., Owen, R. C., Zhang, B., Ampadu, M. T., Kumar, S., Dzepina, K., Dziobak, M. P., Fialho, P., Perlinger, J. A., Hueber, J., Helmig, D., Mazzoleni, L. R. and Mazzoleni, C.: Morphology and mixing state of aged soot particles at a remote marine free troposphere site: Implications for optical properties, Geophys. Res. Lett., 42(4), 2014GL062404, doi:10.1002/2014GL062404, 2015.

Chou, C., Stetzer, O., Weingartner, E., Jurányi, Z., Kanji, Z. A. and Lohmann, U.: Ice nuclei properties within a Saharan dust event at the Jungfraujoch in the Swiss Alps, Atmos Chem Phys, 11(10), 4725–4738, doi:10.5194/acp-11-4725-2011, 2011.

Chou, C., Kanji, Z. A., Stetzer, O., Tritscher, T., Chirico, R., Heringa, M. F., Weingartner, E., Prévôt, A. S. H., Baltensperger, U. and Lohmann, U.: Effect of photochemical ageing on the ice nucleation properties of diesel and wood burning particles, Atmos Chem Phys, 13(2), 761–772, doi:10.5194/acp-13-761-2013, 2013.

Chow, J. C., Watson, J. G., Pritchett, L. C., Pierson, W. R., Frazier, C. A. and Purcell, R. G.: The dri thermal/optical reflectance carbon analysis system: description, evaluation and applications in U.S. Air quality studies, Atmospheric Environ. Part Gen. Top., 27(8), 1185–1201, doi:10.1016/0960-1686(93)90245-T, 1993.

Chow, J. C., Watson, J. G., Chen, L.-W. A., Chang, M. C. O., Robinson, N. F., Trimble, D. and Kohl, S.: The IMPROVE_A Temperature Protocol for Thermal/Optical Carbon Analysis: Maintaining Consistency with a Long-Term Database, J. Air Waste Manag. Assoc., 57(9), 1014–1023, doi:10.3155/1047-3289.57.9.1014, 2007.

Clarke, A. D. and Noone, K. J.: Soot in the Arctic snowpack: a cause for perturbations in radiative transfer, Atmospheric Environ. 1967, 19(12), 2045–2053, doi:http://dx.doi.org/10.1016/0004-6981(85)90113-1, 1985.

Collaud Coen, M., Weingartner, E., Apituley, A., Ceburnis, D., Fierz-Schmidhauser, R., Flentje, H., Henzing, J. S., Jennings, S. G., Moerman, M., Petzold, A., Schmid, O. and Baltensperger, U.: Minimizing light absorption measurement artifacts of the Aethalometer: evaluation of five correction algorithms, Atmos Meas Tech, 3(2), 457–474, doi:10.5194/amt-3-457-2010, 2010.

Cozic, J., Verheggen, B., Mertes, S., Connolly, P., Bower, K., Petzold, A., Baltensperger, U. and Weingartner, E.: Scavenging of black carbon in mixed phase clouds at the high alpine site Jungfraujoch, Atmos Chem Phys, 7(7), 1797–1807, doi:10.5194/acp-7-1797-2007, 2007.

Cozic, J., Mertes, S., Verheggen, B., Cziczo, D. J., Gallavardin, S. J., Walter, S., Baltensperger, U. and Weingartner, E.: Black carbon enrichment in atmospheric ice particle residuals observed in lower tropospheric mixed phase clouds, J. Geophys. Res. Atmospheres, 113(D15), D15209, doi:10.1029/2007JD009266, 2008a.

Cozic, J., Verheggen, B., Weingartner, E., Crosier, J., Bower, K. N., Flynn, M., Coe, H., Henning, S., Steinbacher, M., Henne, S., Collaud Coen, M., Petzold, A. and Baltensperger, U.: Chemical composition of free tropospheric aerosol for PM1 and coarse mode at the high alpine site Jungfraujoch, Atmos Chem Phys, 8(2), 407–423, doi:10.5194/acp-8-407-2008, 2008b.

Cziczo, D. J., Murphy, D. M., Hudson, P. K. and Thomson, D. S.: Single particle measurements of the chemical composition of cirrus ice residue during CRYSTAL-FACE, J. Geophys. Res. Atmospheres, 109(D4), D04201, doi:10.1029/2003JD004032, 2004.

Cziczo, D. J., Froyd, K. D., Gallavardin, S. J., Moehler, O., Benz, S., Harald Saathoff and Murphy, D. M.: Deactivation of ice nuclei due to atmospherically relevant surface coatings, Environ. Res. Lett., 4(4), 044013, doi:10.1088/1748-9326/4/4/044013, 2009a.

Cziczo, D. J., Stetzer, O., Worringen, A., Ebert, M., Weinbruch, S., Kamphus, M., Gallavardin, S. J., Curtius, J., Borrmann, S., Froyd, K. D., Mertes, S., Möhler, O. and Lohmann, U.: Inadvertent climate modification due to anthropogenic lead, Nat Geosci, 2(5), 333–336, doi:10.1038/ngeo499, 2009b.

Cziczo, D. J., Froyd, K. D., Hoose, C., Jensen, E. J., Diao, M., Zondlo, M. A., Smith, J. B., Twohy, C. H. and Murphy, D. M.: Clarifying the dominant sources and mechanisms of cirrus cloud formation, Science, 340(6138), 1320–1324, doi:10.1126/science.1234145, 2013.

Dahlkötter, F., Gysel, M., Sauer, D., Minikin, A., Baumann, R., Seifert, P., Ansmann, A., Fromm, M., Voigt, C. and Weinzierl, B.: The Pagami Creek smoke plume after long-range transport to the upper troposphere over Europe – aerosol properties and black carbon mixing state, Atmos Chem Phys, 14(12), 6111–6137, doi:10.5194/acp-14-6111-2014, 2014.

DeMott, P. J., Chen, Y., Kreidenweis, S. M., Rogers, D. C. and Sherman, D. E.: Ice formation by black carbon particles, Geophys Res Lett, 26(16), 2429–2432, doi:10.1029/1999GL900580, 1999.

DeMott, P. J., Prenni, A. J., Liu, X., Kreidenweis, S. M., Petters, M. D., Twohy, C. H., Richardson, M. S., Eidhammer, T. and Rogers, D. C.: Predicting global atmospheric ice nuclei distributions and their impacts on climate, Proc. Natl. Acad. Sci., 107(25), 11217–11222, doi:10.1073/pnas.0910818107, 2010.

Dinar, E., Riziq, A. A., Spindler, C., Erlick, C., Kiss, G. and Rudich, Y.: The complex refractive index of atmospheric and model humic-like substances (HULIS) retrieved by a cavity ring down aerosol spectrometer (CRD-AS), Faraday Discuss., 137, 279–295; discussion 297–318, 2008a.

Dinar, E., Riziq, A. A., Spindler, C., Erlick, C., Kiss, G. and Rudich, Y.: The complex refractive index of atmospheric and model humic-like substances (HULIS) retrieved by a cavity ring down aerosol spectrometer (CRD-AS), Faraday Discuss., 137, 279–295; discussion 297–318, 2008b.

Doherty, S. J., Warren, S. G., Grenfell, T. C., Clarke, A. D. and Brandt, R. E.: Light-absorbing impurities in Arctic snow , Atmos Chem Phys, 10(23), 34, doi:10.5194/acp-10-11647-2010, 2010.

Dusek, U., Reischl, G. P. and Hitzenberger, R.: CCN Activation of Pure and Coated Carbon Black Particles, Environ. Sci. Technol., 40(4), 1223–1230, doi:10.1021/es0503478, 2006.

Ebert, M., Worringen, A., Benker, N., Mertes, S., Weingartner, E. and Weinbruch, S.: Chemical composition and mixing-state of ice residuals sampled within mixed phase clouds, Atmos Chem Phys, 11(6), 2805–2816, doi:10.5194/acp-11-2805-2011, 2011.

Eleftheriadis, K., Vratolis, S. and Nyeki, S.: Aerosol black carbon in the European Arctic: Measurements at Zeppelin station, Ny-Ålesund, Svalbard from 1998–2007, Geophys. Res. Lett., 36(2), L02809, doi:10.1029/2008GL035741, 2009.

Feichter, J., Sausen, R., Graßl, H. and Fiebig, M.: Comment on "Control of fossil-fuel particulate black carbon and organic matter, possibly the most effective method of slowing global warming" by M. Z. Jacobson, J. Geophys. Res. Atmospheres, 108(D24), 4767, doi:10.1029/2002JD003223, 2003.

Feng, Y., Ramanathan, V. and Kotamarthi, V. R.: Brown carbon: a significant atmospheric absorber of solar radiation?, Atmos Chem Phys, 13(17), 8607–8621, doi:10.5194/acp-13-8607-2013, 2013.

Fiebig, M., Stein, C., Schröder, F., Feldpausch, P. and Petzold, A.: Inversion of data containing information on the aerosol particle size distribution using multiple instruments, J. Aerosol Sci., 36(11), 1353–1372, doi:10.1016/j.jaerosci.2005.01.004, 2005.

Fierce, L., Riemer, N. and Bond, T. C.: Explaining variance in black carbon's aging timescale, Atmos Chem Phys, 15(6), 3173–3191, doi:10.5194/acp-15-3173-2015, 2015.

Flanner, M. G.: Arctic climate sensitivity to local black carbon, J. Geophys. Res. Atmospheres, 118(4), 1840–1851, doi:10.1002/jgrd.50176, 2013.

Flanner, M. G., Zender, C. S., Randerson, J. T. and Rasch, P. J.: Present-day climate forcing and response from black carbon in snow, J. Geophys. Res.-Atmospheres, 112(D11), doi:Artn D11202Doi 10.1029/2006jd008003, 2007a.

Flanner, M. G., Zender, C. S., Randerson, J. T. and Rasch, P. J.: Present-day climate forcing and response from black carbon in snow, J. Geophys. Res. Atmospheres, 112(D11), D11202, doi:10.1029/2006JD008003, 2007b.

Flanner, M. G., Zender, C. S., Hess, P. G., Mahowald, N. M., Painter, T. H., Ramanathan, V. and Rasch, P. J.: Springtime warming and reduced snow cover from carbonaceous particles, Atmos Chem Phys, 9(7), 2481–2497, doi:10.5194/acp-9-2481-2009, 2009.

Freney, E. J., Sellegri, K., Canonaco, F., Boulon, J., Hervo, M., Weigel, R., Pichon, J. M., Colomb, A., Prévôt, A. S. H. and Laj, P.: Seasonal variations in aerosol particle composition at the puy-de-Dôme research station in France, Atmos Chem Phys, 11(24), 13047–13059, doi:10.5194/acp-11-13047-2011, 2011.

Friedman, B., Kulkarni, G., Beránek, J., Zelenyuk, A., Thornton, J. A. and Cziczo, D. J.: Ice nucleation and droplet formation by bare and coated soot particles, J. Geophys. Res. Atmospheres, 116(D17), D17203, doi:10.1029/2011JD015999, 2011.

Fuller, K. A., Malm, W. C. and Kreidenweis, S. M.: Effects of mixing on extinction by carbonaceous particles, J. Geophys. Res. Atmospheres, 104(D13), 15941–15954, doi:10.1029/1998JD100069, 1999.

Gabey, A. M., Stanley, W. R., Gallagher, M. W. and Kaye, P. H.: The fluorescence properties of aerosol larger than $0.8 \mathrm\m um$ in urban and tropical rainforest locations, Atmos Chem Phys, 11(11), 5491–5504, doi:10.5194/acp-11-5491-2011, 2011.

Gao, R. S., Schwarz, J. P., Kelly, K. K., Fahey, D. W., Watts, L. A., Thompson, T. L., Spackman, J. R., Slowik, J. G., Cross, E. S., Han, J.-H., Davidovits, P., Onasch, T. B. and Worsnop, D. R.: A Novel Method for Estimating Light-Scattering Properties of Soot Aerosols Using a Modified Single-Particle Soot Photometer, Aerosol Sci. Technol., 41(2), 125–135, doi:10.1080/02786820601118398, 2007.

Genberg, J., Denier van der Gon, H. A. C., Simpson, D., Swietlicki, E., Ceburnis, D., Fiebig, M., Hansson, H. C., Harrison, R. M., Jennings, S. G., Saarikoski, S., Spindler, G., Visschedijk, A. J. H., Wiedensohler, A., Yttri, K. E. and Bergström, R.: Light-absorbing carbon in Europe – measurement and modelling, with a focus on residential wood combustion emissions, Atmos Chem Phys, 13(17), 8719–8738, doi:10.5194/acp-13-8719-2013, 2013.

Gerber, H.: Direct measurement of suspended particulate volume concentration and far-infrared extinction coefficient with a laser-diffraction instrument, Appl Opt, 30(33), 4824–4831, doi:10.1364/AO.30.004824, 1991.

Gillett, N. P., Stone, D. A., Stott, P. A., Nozawa, T., Karpechko, A. Y., Hegerl, G. C., Wehner, M. F. and Jones, P. D.: Attribution of polar warming to human influence, Nat. Geosci., 1(11), 750–754, doi:10.1038/ngeo338, 2008.

Ginot, P., Dumont, M., Lim, S., Patris, N., Taupin, J.-D., Wagnon, P., Gilbert, A., Arnaud, Y., Marinoni, A., Bonasoni, P. and Laj, P.: A 10 yr record of black carbon and dust from Mera Peak ice core (Nepal): variability and potential impact on Himalayan glacier melting, Cryosphere Discuss., 7(6), 6001–6042, doi:10.5194/tcd-7-6001-2013, 2013.

Ginot, P., Dumont, M., Lim, S., Patris, N., Taupin, J.-D., Wagnon, P., Gilbert, A., Arnaud, Y., Marinoni, A., Bonasoni, P. and Laj, P.: A 10 year record of black carbon and dust from a Mera Peak ice core (Nepal): variability and potential impact on melting of Himalayan glaciers, The Cryosphere, 8(4), 1479–1496, doi:10.5194/tc-8-1479-2014, 2014.

Gobbi, G. P., Kaufman, Y. J., Koren, I. and Eck, T. F.: Classification of aerosol properties derived from AERONET direct sun data, Atmos Chem Phys, 7(2), 453–458, doi:10.5194/acp-7-453-2007, 2007.

Gysel, M., Laborde, M., Olfert, J. S., Subramanian, R. and Gröhn, A. J.: Effective density of Aquadag and fullerene soot black carbon reference materials used for SP2 calibration, Atmos Meas Tech Discuss, 4(4), 4937–4955, doi:10.5194/amtd-4-4937-2011, 2011.

Hansen, A. D. A., Rosen, H. and Novakov, T.: The aethalometer — An instrument for the real-time measurement of optical absorption by aerosol particles, Sci. Total Environ., 36, 191–196, doi:10.1016/0048-9697(84)90265-1, 1984.

Hansen, J. and Nazarenko, L.: Soot climate forcing via snow and ice albedos, Proc. Natl. Acad. Sci. U. S. A., 101(2), 423–428, doi:DOI 10.1073/pnas.2237157100, 2004.

Hansen, J., Nazarenko, L., Ruedy, R., Sato, M., Willis, J., Genio, A. D., Koch, D., Lacis, A., Lo, K., Menon, S., Novakov, T., Perlwitz, J., Russell, G., Schmidt, G. A. and Tausnev, N.: Earth's Energy Imbalance: Confirmation and Implications, Science, 308(5727), 1431–1435, doi:10.1126/science.1110252, 2005.

Hara, K., Yamagata, S., Yamanouchi, T., Sato, K., Herber, A., Iwasaka, Y., Nagatani, M. and Nakata, H.: Mixing states of individual aerosol particles in spring Arctic troposphere during ASTAR 2000 campaign, J. Geophys. Res. Atmospheres, 108(D7), 4209, doi:10.1029/2002JD002513, 2003.

Hartmann, D.L, A.M.G. Klein Tank, M. Rusticucci, L.V. Alexander, S. Brönnimann, Y. Charabi, F.J. Dentener, E.J., Dlugokencky, D.R. Easterling, A. Kaplan, B.J. Soden, P.W. Thorne, M. Wild and P.M. Zhai and R. Kwok: IPCC, 2013: Observations: Cryosphere. In: Climate Change 2013: The Physical Science Basis. Contribution of Working Group I to the Fifth Assessment Report of the Intergovernmental Panel on Climate Change, edited by T. F. Stocker, Cambridge University Press, Cambridge, United Kingdom and New York, NY, USA, 159–254, 2013.

Healy, R. M., Sciare, J., Poulain, L., Kamili, K., Merkel, M., Müller, T., Wiedensohler, A., Eckhardt, S., Stohl, A., Sarda-Estève, R., McGillicuddy, E., O'Connor, I. P., Sodeau, J. R. and Wenger, J. C.: Sources and mixing state of size-resolved elemental carbon particles in a European megacity: Paris, Atmos Chem Phys, 12(4), 1681–1700, doi:10.5194/acp-12-1681-2012, 2012.

Henne, S., Brunner, D., Folini, D., Solberg, S., Klausen, J. and Buchmann, B.: Assessment of parameters describing representativeness of air quality in-situ measurement sites, Atmos Chem Phys, 10(8), 3561–3581, doi:10.5194/acp-10-3561-2010, 2010.

Herrmann, E., Weingartner, E., Henne, S., Vuilleumier, L., Bukowiecki, N., Steinbacher, M., Conen, F., Collaud Coen, M., Hammer, E., Jurányi, Z., Baltensperger, U. and Gysel, M.: Analysis of long-term aerosol size distribution data from Jungfraujoch with emphasis on free tropospheric conditions, cloud influence, and air mass transport, J. Geophys. Res. Atmospheres, 120(18), 2015JD023660, doi:10.1002/2015JD023660, 2015.

Hess, M., Koepke, P. and Schult, I.: Optical Properties of Aerosols and Clouds: The Software Package OPAC, Bull. Am. Meteorol. Soc., 79(5), 831–844, doi:10.1175/1520-0477(1998)079<0831:OPOAAC>2.0.CO;2, 1998.

Hoffer, A., Gelencsér, A., Guyon, P., Kiss, G., Schmid, O., Frank, G. P., Artaxo, P. and Andreae, M. O.: Optical properties of humic-like substances (HULIS) in biomass-burning aerosols, Atmos Chem Phys, 6(11), 3563–3570, doi:10.5194/acp-6-3563-2006, 2006.

Hoffmann, A., Ritter, C., Stock, M., Shiobara, M., Lampert, A., Maturilli, M., Orgis, T., Neuber, R. and Herber, A.: Ground-based lidar measurements from Ny-Ålesund during ASTAR 2007, Atmos Chem Phys, 9(22), 9059–9081, doi:10.5194/acp-9-9059-2009, 2009.

Hoose, C. and Möhler, O.: Heterogeneous ice nucleation on atmospheric aerosols: a review of results from laboratory experiments, Atmos Chem Phys, 12(20), 9817–9854, doi:10.5194/acp-12-9817-2012, 2012.

Hung, H.-M., Malinowski, A. and Martin, S. T.: Kinetics of heterogeneous ice nucleation on the surfaces of mineral dust cores inserted into aqueous ammonium sulfate particles, J Phys Chem A, 107(9), 1296–1306, doi:10.1021/jp021593y, 2003.

Huntzicker, J. J., Johnson, R. L., Shah, J. J. and Cary, R. A.: Analysis of Organic and Elemental Carbon in Ambient Aerosols by a Thermal-Optical Method, in Particulate Carbon, edited by G. T. Wolff and R. L. Klimisch, pp. 79–88, Springer US. [online] Available from:

http://link.springer.com/chapter/10.1007/978-1-4684-4154-3_6 (Accessed 23 November 2015), 1982.

IPCC: IPCC, 2013, Cambridge University Press, Cambridge, United Kingdom and New York, NY, USA, 2013.

Jacobson, M. Z.: Strong radiative heating due to the mixing state of black carbon in atmospheric aerosols, Nature, 409(6821), 695–697, 2001.

Jacobson, M. Z.: Investigating cloud absorption effects: Global absorption properties of black carbon, tar balls, and soil dust in clouds and aerosols, J. Geophys. Res. Atmospheres, 117(D6), D06205, doi:10.1029/2011JD017218, 2012.

Janzen, J.: The refractive index of colloidal carbon, J. Colloid Interface Sci., 69(3), 436–447, doi:10.1016/0021-9797(79)90133-4, 1979.

John Webb, M. D.: Fire and Stone, Science, 325(5942), 820–1, doi:10.1126/science.1178014, 2009.

Kamphus, M., Ettner-Mahl, M., Klimach, T., Drewnick, F., Keller, L., Cziczo, D. J., Mertes, S., Borrmann, S. and Curtius, J.: Chemical composition of ambient aerosol, ice residues and cloud droplet residues in mixed-phase clouds: single particle analysis during the Cloud and Aerosol Characterization Experiment (CLACE 6), Atmos Chem Phys, 10(16), 8077–8095, doi:10.5194/acp-10-8077-2010, 2010.

Kanaya, Y., Taketani, F., Komazaki, Y., Liu, X., Kondo, Y., Sahu, L. K., Irie, H. and Takashima, H.: Comparison of Black Carbon Mass Concentrations Observed by Multi-Angle Absorption Photometer (MAAP) and Continuous Soot-Monitoring System (COSMOS) on Fukue Island and in Tokyo, Japan, Aerosol Sci. Technol., 47(1), 1–10, doi:10.1080/02786826.2012.716551, 2013.

Karanasiou, A., Minguillón, M. C., Viana, M., Alastuey, A., Putaud, J.-P., Maenhaut, W., Panteliadis, P., Močnik, G., Favez, O. and Kuhlbusch, T. A. J.: Thermal-optical analysis for the measurement of elemental carbon (EC) and organic carbon (OC) in ambient air a literature review, Atmos Meas Tech Discuss, 8(9), 9649–9712, doi:10.5194/amtd-8-9649-2015, 2015.

Kaufman, Y. J.: Aerosol optical thickness and atmospheric path radiance, J. Geophys. Res. Atmospheres, 98(D2), 2677–2692, doi:10.1029/92JD02427, 1993.

Kaye, P. H., Hirst, E., Greenaway, R. S., Ulanowski, Z., Hesse, E., DeMott, P. J., Saunders, C. and Connolly, P.: Classifying atmospheric ice crystals by spatial light scattering, Opt Lett, 33(13), 1545–1547, doi:10.1364/OL.33.001545, 2008.

Kirchstetter, T. W., Novakov, T. and Hobbs, P. V.: Evidence that the spectral dependence of light absorption by aerosols is affected by organic carbon, J. Geophys. Res. Atmospheres, 109(D21), D21208, doi:10.1029/2004JD004999, 2004.

Knox, A., Evans, G. J., Brook, J. R., Yao, X., Jeong, C.-H., Godri, K. J., Sabaliauskas, K. and Slowik, J. G.: Mass Absorption Cross-Section of Ambient Black Carbon Aerosol in Relation to Chemical Age, Aerosol Sci. Technol., 43(6), 522–532, doi:10.1080/02786820902777207, 2009.

Koch, D., Schulz, M., Kinne, S., McNaughton, C., Spackman, J. R., Balkanski, Y., Bauer, S., Berntsen, T., Bond, T. C., Boucher, O., Chin, M., Clarke, A., De Luca, N., Dentener, F., Diehl, T., Dubovik, O., Easter, R., Fahey, D. W., Feichter, J., Fillmore, D., Freitag, S., Ghan, S., Ginoux, P., Gong, S., Horowitz, L., Iversen, T., Kirkevåg, A., Klimont, Z., Kondo, Y., Krol, M., Liu, X., Miller, R., Montanaro, V., Moteki, N., Myhre, G., Penner, J. E., Perlwitz, J., Pitari, G., Reddy, S., Sahu, L., Sakamoto, H., Schuster, G., Schwarz, J. P., Seland, Ø., Stier, P., Takegawa, N., Takemura, T., Textor, C., van Aardenne, J. A. and Zhao, Y.: Evaluation of black carbon estimations in global aerosol models, Atmos Chem Phys, 9(22), 9001–9026, doi:10.5194/acp-9-9001-2009, 2009.

Kondo, Y., Sahu, L., Kuwata, M., Miyazaki, Y., Takegawa, N., Moteki, N., Imaru, J., Han, S., Nakayama, T., Oanh, N. T. K., Hu, M., Kim, Y. J. and Kita, K.: Stabilization of the Mass Absorption Cross Section of Black Carbon for Filter-Based Absorption Photometry by the use of a Heated Inlet, Aerosol Sci. Technol., 43(8), 741–756, doi:10.1080/02786820902889879, 2009.

Kondo, Y., Sahu, L., Moteki, N., Khan, F., Takegawa, N., Liu, X., Koike, M. and Miyakawa, T.: Consistency and Traceability of Black Carbon Measurements Made by Laser-Induced Incandescence, Thermal-Optical Transmittance, and Filter-Based Photo-Absorption Techniques, Aerosol Sci. Technol., 45(2), 295–312, doi:10.1080/02786826.2010.533215, 2011.

Koren, I., Kaufman, Y. J., Remer, L. A. and Martins, J. V.: Measurement of the Effect of Amazon Smoke on Inhibition of Cloud Formation, Science, 303(5662), 1342–1345, doi:10.1126/science.1089424, 2004.

Korolev, A.: Limitations of the Wegener–Bergeron–Findeisen mechanism in the evolution of mixed–phase clouds, J Atmos Sci, 64(9), 3372–3375, doi:10.1175/JAS4035.1, 2007.

Krecl, P., Ström, J. and Johansson, C.: Carbon content of atmospheric aerosols in a residential area during the wood combustion season in Sweden, Atmos. Environ., 41(33), 6974–6985, doi:10.1016/j.atmosenv.2007.06.025, 2007.

Kupiszewski, P., Weingartner, E., Vochezer, P., Schnaiter, M., Bigi, A., Gysel, M., Rosati, B., Toprak, E., Mertes, S. and Baltensperger, U.: The Ice Selective Inlet: a novel technique for exclusive extraction of pristine ice crystals in mixed-phase clouds, Atmos Meas Tech, 8(8), 3087–3106, doi:10.5194/amt-8-3087-2015, 2015.

Kuwata, M., Kondo, Y. and Takegawa, N.: Critical condensed mass for activation of black carbon as cloud condensation nuclei in Tokyo, J. Geophys. Res. Atmospheres, 114(D20), D20202, doi:10.1029/2009JD012086, 2009.

Laborde, M., Mertes, P., Zieger, P., Dommen, J., Baltensperger, U. and Gysel, M.: Sensitivity of the Single Particle Soot Photometer to different black carbon types, Atmos Meas Tech, 5(5), 1031–1043, doi:10.5194/amt-5-1031-2012, 2012a.

Laborde, M., Schnaiter, M., Linke, C., Saathoff, H., Naumann, K.-H., Möhler, O., Berlenz, S., Wagner, U., Taylor, J. W., Liu, D., Flynn, M., Allan, J. D., Coe, H., Heimerl, K., Dahlkötter, F., Weinzierl, B., Wollny, A. G., Zanatta, M., Cozic, J., Laj, P., Hitzenberger, R., Schwarz, J. P. and Gysel, M.: Single Particle Soot Photometer intercomparison at the AIDA chamber, Atmos Meas Tech, 5(12), 3077–3097, doi:10.5194/amt-5-3077-2012, 2012b.

Laborde, M., Crippa, M., Tritscher, T., Jurányi, Z., Decarlo, P. F., Temime-Roussel, B., Marchand, N., Eckhardt, S., Stohl, A., Baltensperger, U., Prévôt, A. S. H., Weingartner, E. and Gysel, M.: Black carbon physical properties and mixing state in the European megacity Paris, Atmos Chem Phys, 13(11), 5831–5856, doi:10.5194/acp-13-5831-2013, 2013.

Lack, D. A. and Cappa, C. D.: Impact of brown and clear carbon on light absorption enhancement, single scatter albedo and absorption wavelength dependence of black carbon, Atmospheric Chem. Phys., 10, 4207–4220, 2010.

Lack, D. A. and Langridge, J. M.: On the attribution of black and brown carbon light absorption using the Ångström exponent, Atmos Chem Phys, 13(20), 10535–10543, doi:10.5194/acp-13-10535-2013, 2013.

Lack, D. A., Cappa, C. D., Cross, E. S., Massoli, P., Ahern, A. T., Davidovits, P. and Onasch, T. B.: Absorption Enhancement of Coated Absorbing Aerosols: Validation of the Photo-Acoustic Technique for Measuring the Enhancement, Aerosol Sci. Technol., 43(10), 1006–1012, doi:10.1080/02786820903117932, 2009.

Lack, D. A., Langridge, J. M., Bahreini, R., Cappa, C. D., Middlebrook, A. M. and Schwarz, J. P.: Brown carbon and internal mixing in biomass burning particles, Proc. Natl. Acad. Sci., 109(37), 14802–14807, doi:10.1073/pnas.1206575109, 2012.

Lamarque, J.-F., Bond, T. C., Eyring, V., Granier, C., Heil, A., Klimont, Z., Lee, D., Liousse, C., Mieville, A., Owen, B., Schultz, M. G., Shindell, D., Smith, S. J., Stehfest, E., Van Aardenne, J., Cooper, O. R., Kainuma, M., Mahowald, N., McConnell, J. R., Naik, V., Riahi, K. and van Vuuren, D. P.: Historical (1850–2000) gridded anthropogenic and biomass burning emissions of reactive gases and aerosols: methodology and application, Atmos Chem Phys, 10(15), 7017–7039, doi:10.5194/acp-10-7017-2010, 2010.

Lance, S., Brock, C. A., Rogers, D. and Gordon, J. A.: Water droplet calibration of the Cloud Droplet Probe (CDP) and in-flight performance in liquid, ice and mixed-phase clouds during ARCPAC, Atmos Meas Tech, 3(6), 1683–1706, doi:10.5194/amt-3-1683-2010, 2010.

Lan, Z.-J., Huang, X.-F., Yu, K.-Y., Sun, T.-L., Zeng, L.-W. and Hu, M.: Light absorption of black carbon aerosol and its enhancement by mixing state in an urban atmosphere in South China, Atmos. Environ., 69, 118–123, doi:10.1016/j.atmosenv.2012.12.009, 2013.

Lanz, V. A., Prévôt, A. S. H., Alfarra, M. R., Weimer, S., Mohr, C., DeCarlo, P. F., Gianini, M. F. D., Hueglin, C., Schneider, J., Favez, O., D'Anna, B., George, C. and Baltensperger, U.: Characterization of aerosol chemical composition with aerosol mass spectrometry in Central Europe: an overview, Atmos Chem Phys, 10(21), 10453–10471, doi:10.5194/acp-10-10453-2010, 2010.

Lavanchy, V. M. H., Gäggeler, H. W., Nyeki, S. and Baltensperger, U.: Elemental carbon (EC) and black carbon (BC) measurements with a thermal method and an aethalometer at the high-alpine research station Jungfraujoch, Atmos. Environ., 33(17), 2759–2769, doi:10.1016/S1352-2310(98)00328-8, 1999.

Liousse, C., Cachier, H. and Jennings, S. G.: Optical and thermal measurements of black carbon aerosol content in different environments: Variation of the specific attenuation cross-section, sigma (σ), Atmospheric Environ. Part Gen. Top., 27(8), 1203–1211, doi:10.1016/0960-1686(93)90246-U, 1993a.

Liousse, C., Cachier, H. and Jennings, S. G.: Optical and thermal measurements of black carbon aerosol content in different environments: Variation of the specific attenuation cross-section, sigma (σ), Atmospheric Environ. Part Gen. Top., 27(8), 1203–1211, doi:10.1016/0960-1686(93)90246-U, 1993b.

Liu, D., Flynn, M., Gysel, M., Targino, A., Crawford, I., Bower, K., Choularton, T., Jurányi, Z., Steinbacher, M., Hüglin, C., Curtius, J., Kampus, M., Petzold, A., Weingartner, E., Baltensperger, U. and Coe, H.: Single particle characterization of black carbon aerosols at a tropospheric alpine site in Switzerland, Atmos Chem Phys, 10(15), 7389–7407, doi:10.5194/acp-10-7389-2010, 2010.

Liu, L., Mishchenko, M. I. and Patrick Arnott, W.: A study of radiative properties of fractal soot aggregates using the superposition T-matrix method, J. Quant. Spectrosc. Radiat. Transf., 109(15), 2656–2663, doi:10.1016/j.jqsrt.2008.05.001, 2008.

Liu, S., Aiken, A. C., Gorkowski, K., Dubey, M. K., Cappa, C. D., Williams, L. R., Herndon, S. C., Massoli, P., Fortner, E. C., Chhabra, P. S., Brooks, W. A., Onasch, T. B., Jayne, J. T., Worsnop, D. R., China, S., Sharma, N., Mazzoleni, C., Xu, L., Ng, N. L., Liu, D., Allan, J. D., Lee, J. D., Fleming, Z. L., Mohr, C., Zotter, P., Szidat, S. and Prévôt, A. S. H.: Enhanced light absorption by mixed source black and brown carbon particles in UK winter, Nat. Commun., 6, 8435, doi:10.1038/ncomms9435, 2015.

Liu, X. and Penner, J. E.: Effect of Mount Pinatubo H2SO4/H2O aerosol on ice nucleation in the upper troposphere using a global chemistry and transport model, J. Geophys. Res. Atmospheres, 107(D12), AAC 2–1, doi:10.1029/2001JD000455, 2002.

Lloyd, G., Choularton, T. W., Bower, K. N., Gallagher, M. W., Connolly, P. J., Flynn, M., Farrington, R., Crosier, J., Schlenczek, O., Fugal, J. and Henneberger, J.: The origins of ice crystals measured in mixed phase clouds at High-Alpine site Jungfraujoch, Atmos Chem Phys Discuss, 15(13), 18181–18224, doi:10.5194/acpd-15-18181-2015, 2015.

Lohmann, U.: A glaciation indirect aerosol effect caused by soot aerosols, Geophys Res Lett, 29, 4(4), 11–1–11–4, doi:10.1029/2001GL014357, 2002.

Lukács, H., Gelencsér, A., Hammer, S., Puxbaum, H., Pio, C., Legrand, M., Kasper-Giebl, A., Handler, M., Limbeck, A., Simpson, D. and Preunkert, S.: Seasonal trends and possible sources of brown carbon based on 2-year aerosol measurements at six sites in Europe, J. Geophys. Res. Atmospheres, 112(D23), D23S18, doi:10.1029/2006JD008151, 2007.

Lund Myhre, C., Toledano, C., Myhre, G., Stebel, K., Yttri, K. E., Aaltonen, V., Johnsrud, M., Frioud, M., Cachorro, V., de Frutos, A., Lihavainen, H., Campbell, J. R., Chaikovsky, A. P., Shiobara, M., Welton, E. J. and Tørseth, K.: Regional aerosol optical properties and radiative impact of the extreme smoke event in the European Arctic in spring 2006, Atmos Chem Phys, 7(22), 5899–5915, doi:10.5194/acp-7-5899-2007, 2007.

Maenhaut, W. and Claeys, M.: EC=OC Analyses 2010–2011, Final report, Study for the Vlaamse Milieumaatschappij (VMM), afdeling Meetnetten en Onderzoek. Order number: LUC/2010/EC/OC, 25 July 2011, Flemish Environment Agency, 2012.

Marley, N. A., Gaffney, J. S., Baird, J. C., Blazer, C. A., Drayton, P. J. and Frederick, J. E.: An Empirical Method for the Determination of the Complex Refractive Index of Size-Fractionated Atmospheric Aerosols for Radiative Transfer Calculations, Aerosol Sci. Technol., 34(6), 535–549, doi:10.1080/02786820118599, 2001.

Massoli, P., Onasch, T. B., Cappa, C. D., Nuamaan, I., Hakala, J., Hayden, K., Li, S.-M., Sueper, D. T., Bates, T. S., Quinn, P. K., Jayne, J. T. and Worsnop, D. R.: Characterization of black carbon-containing particles from soot particle aerosol mass spectrometer measurements on the R/V Atlantis during CalNex 2010, J. Geophys. Res. Atmospheres, 120(6), 2014JD022834, doi:10.1002/2014JD022834, 2015.

McConnell, J. R., Edwards, R., Kok, G. L., Flanner, M. G., Zender, C. S., Saltzman, E. S., Banta, J. R., Pasteris, D. R., Carter, M. M. and Kahl, J. D. W.: 20th-Century Industrial Black Carbon Emissions Altered Arctic Climate Forcing, Science, 317(5843), 1381–1384, doi:10.1126/science.1144856, 2007.

McMeeking, G. R., Hamburger, T., Liu, D., Flynn, M., Morgan, W. T., Northway, M., Highwood, E. J., Krejci, R., Allan, J. D., Minikin, A. and Coe, H.: Black carbon measurements in the boundary layer over western and northern Europe, Atmos Chem Phys, 10(19), 9393–9414, doi:10.5194/acp-10-9393-2010, 2010.

Mertes, S., Verheggen, B., Walter, S., Connolly, P., Ebert, M., Schneider, J., Bower, K. N., Cozic, J., Weinbruch, S., Baltensperger, U. and Weingartner, E.: Counterflow Virtual Impactor Based Collection of Small Ice Particles in Mixed-Phase Clouds for the Physico-Chemical Characterization of Tropospheric Ice Nuclei: Sampler Description and First Case Study, Aerosol Sci. Technol., 41(9), 848–864, doi:10.1080/02786820701501881, 2007.

Ming, J., Cachier, H., Xiao, C., Qin, D., Kang, S., Hou, S. and Xu, J.: Black carbon record based on a shallow Himalayan ice core and its climatic implications, Atmos Chem Phys, 8(5), 1343–1352, doi:10.5194/acp-8-1343-2008, 2008.

Mishchenko, M. I., Travis, L. D. and Macke, A.: Scattering of light by polydisperse, randomly oriented, finite circular cylinders, Appl. Opt., 35(24), 4927, doi:10.1364/AO.35.004927, 1996.

Miyazaki, Y., Kondo, Y., Sahu, L. K., Imaru, J., Fukushima, N. and Kano, M.: Performance of a newly designed continuous soot monitoring system (COSMOS), J. Environ. Monit. JEM, 10(10), 1195–1201, 2008.

Moffet, R. C. and Prather, K. A.: In-situ measurements of the mixing state and optical properties of soot with implications for radiative forcing estimates, Proc. Natl. Acad. Sci., 106(29), 11872–11877, doi:10.1073/pnas.0900040106, 2009.

Möhler, O.: Heterogeneous Ice Nucleation on Soot Particles, in Nucleation and Atmospheric Aerosols, edited by C. D. O'Dowd and P. E. Wagner, pp. 445–449, Springer Netherlands. [online] Available from: http://link.springer.com/chapter/10.1007/978-1-4020-6475-3_89 (Accessed 19 November 2015), 2007.

Möhler, O., Büttner, S., Linke, C., Schnaiter, M., Saathoff, H., Stetzer, O., Wagner, R., Krämer, M., Mangold, A., Ebert, V. and Schurath, U.: Effect of sulfuric acid coating on heterogeneous ice

nucleation by soot aerosol particles, J Geophys Res Atmos, 110, D11210(D11), doi:10.1029/2004JD005169, 2005.

Moosmüller, H., Chakrabarty, R. K. and Arnott, W. P.: Aerosol light absorption and its measurement: A review, J. Quant. Spectrosc. Radiat. Transf., 110(11), 844–878, doi:10.1016/j.jqsrt.2009.02.035, 2009.

Moteki, N. and Kondo, Y.: Effects of Mixing State on Black Carbon Measurements by Laser-Induced Incandescence, Aerosol Sci. Technol., 41(4), 398–417, 2007.

Moteki, N. and Kondo, Y.: Dependence of Laser-Induced Incandescence on Physical Properties of Black Carbon Aerosols: Measurements and Theoretical Interpretation, Aerosol Sci. Technol., 44(8), 663–675, doi:10.1080/02786826.2010.484450, 2010.

Moteki, N., Kondo, Y., Miyazaki, Y., Takegawa, N., Komazaki, Y., Kurata, G., Shirai, T., Blake, D. R., Miyakawa, T. and Koike, M.: Evolution of mixing state of black carbon particles: Aircraft measurements over the western Pacific in March 2004, Geophys. Res. Lett., 34(11), L11803, doi:10.1029/2006GL028943, 2007.

Moteki, N., Kondo, Y. and Nakamura, S.: Method to measure refractive indices of small nonspherical particles: Application to black carbon particles, J. Aerosol Sci., 41(5), 513–521, doi:10.1016/j.jaerosci.2010.02.013, 2010.

Moteki, N., Kondo, Y., Oshima, N., Takegawa, N., Koike, M., Kita, K., Matsui, H. and Kajino, M.: Size dependence of wet removal of black carbon aerosols during transport from the boundary layer to the free troposphere, Geophys. Res. Lett., 39(13), L13802, doi:10.1029/2012GL052034, 2012.

Moteki, N., Kondo, Y. and Adachi, K.: Identification by single-particle soot photometer of black carbon particles attached to other particles: Laboratory experiments and ground observations in Tokyo, J. Geophys. Res. Atmospheres, 119(2), 2013JD020655, doi:10.1002/2013JD020655, 2014.

Müller, T., Nowak, A., Wiedensohler, A., Sheridan, P., Laborde, M., Covert, D. S., Marinoni, A., Imre, K., Henzing, B., Roger, J.-C., dos Santos, S. M., Wilhelm, R., Wang, Y.-Q. and de Leeuw, G.: Angular Illumination and Truncation of Three Different Integrating Nephelometers: Implications for Empirical, Size-Based Corrections, Aerosol Sci. Technol., 43(6), 581–586, doi:10.1080/02786820902798484, 2009.

Müller, T., Henzing, J. S., de Leeuw, G., Wiedensohler, A., Alastuey, A., Angelov, H., Bizjak, M., Collaud Coen, M., Engström, J. E., Gruening, C., Hillamo, R., Hoffer, A., Imre, K., Ivanow, P., Jennings, G., Sun, J. Y., Kalivitis, N., Karlsson, H., Komppula, M., Laj, P., Li, S.-M., Lunder, C., Marinoni, A., Martins dos Santos, S., Moerman, M., Nowak, A., Ogren, J. A., Petzold, A., Pichon, J. M., Rodriquez, S., Sharma, S., Sheridan, P. J., Teinilä, K., Tuch, T., Viana, M., Virkkula, A., Weingartner, E., Wilhelm, R. and Wang, Y. Q.: Characterization and intercomparison of aerosol absorption photometers: result of two intercomparison workshops, Atmos Meas Tech, 4(2), 245–268, doi:10.5194/amt-4-245-2011, 2011.

Murray, B. J., O'Sullivan, D., Atkinson, J. D. and Webb, M. E.: Ice nucleation by particles immersed in supercooled cloud droplets, Chem Soc Rev, 41(19), 6519–6554, doi:10.1039/C2CS35200A, 2012.

Myhre, G., D. Shindell, F.-M. Bréon, W. Collins, J. Fuglestvedt, J. Huang, D. Koch, J.-F. Lamarque, D. Lee, B. Mendoza, and T. Nakajima, A. Robock, G. Stephens, T. Takemura and H. Zhang: IPCC, 2013:

Anthropogenic and Natural Radiative Forcing. In: Climate Change 2013: The Physical Science Basis. Contribution of Working Group I to the Fifth Assessment Report of the Intergovernmental Panel on Climate Change, edited by T. F. Stocker, Cambridge University Press, Cambridge, United Kingdom and New York, NY, USA, 659–740, 2013.

Myhre, G., Samset, B. H., Schulz, M., Balkanski, Y., Bauer, S., Berntsen, T. K., Bian, H., Bellouin, N., Chin, M., Diehl, T., Easter, R. C., Feichter, J., Ghan, S. J., Hauglustaine, D., Iversen, T., Kinne, S., Kirkevåg, A., Lamarque, J.-F., Lin, G., Liu, X., Lund, M. T., Luo, G., Ma, X., van Noije, T., Penner, J. E., Rasch, P. J., Ruiz, A., Seland, ø., Skeie, R. B., Stier, P., Takemura, T., Tsigaridis, K., Wang, P., Wang, Z., Xu, L., Yu, H., Yu, F., Yoon, J.-H., Zhang, K., Zhang, H. and Zhou, C.: Radiative forcing of the direct aerosol effect from AeroCom Phase II simulations, Atmospheric Chem. Phys., 13(4), 1853–1877, doi:10.5194/acp-13-1853-2013, 2013.

Nakayama, T., Kondo, Y., Moteki, N., Sahu, L. K., Kinase, T., Kita, K. and Matsumi, Y.: Size-dependent correction factors for absorption measurements using filter-based photometers: PSAP and COSMOS, J. Aerosol Sci., 41(4), 333–343, doi:10.1016/j.jaerosci.2010.01.004, 2010.

Nessler, R., Weingartner, E. and Baltensperger, U.: Effect of humidity on aerosol light absorption and its implications for extinction and the single scattering albedo illustrated for a site in the lower free troposphere, J. Aerosol Sci., 36(8), 958–972, doi:10.1016/j.jaerosci.2004.11.012, 2005.

Nyeki, S., Baltensperger, U., Colbeck, I., Jost, D. T., Weingartner, E. and Gäggeler, H. W.: The Jungfraujoch high-alpine research station (3454 m) as a background clean continental site for the measurement of aerosol parameters, J Geophys Res Atmos, 103(D6), 6097–6107, doi:10.1029/97JD03123, 1998.

Ogren, J. A.: Comment on "Calibration and Intercomparison of Filter-Based Measurements of Visible Light Absorption by Aerosols," Aerosol Sci. Technol., 44(8), 589–591, doi:10.1080/02786826.2010.482111, 2010.

Ogren, J. A. and Charlson, R. J.: Elemental carbon in the atmosphere: cycle and lifetime, Tellus B, 35B(4), 241–254, doi:10.1111/j.1600-0889.1983.tb00027.x, 1983.

Okada, K., Ikegami, M., Zaizen, Y., Tsutsumi, Y., Makino, Y., Jensen, J. B. and Gras, J. L.: Soot particles in the free troposphere over Australia, Atmos. Environ., 39(28), 5079–5089, doi:10.1016/j.atmosenv.2005.05.015, 2005.

Onasch, T. B., Trimborn, A., Fortner, E. C., Jayne, J. T., Kok, G. L., Williams, L. R., Davidovits, P. and Worsnop, D. R.: Soot Particle Aerosol Mass Spectrometer: Development, Validation, and Initial Application, Aerosol Sci. Technol., 46(7), 804–817, doi:10.1080/02786826.2012.663948, 2012.

Oshima, N. and Koike, M.: Development of a parameterization of black carbon aging for use in general circulation models, Geosci Model Dev, 6(2), 263–282, doi:10.5194/gmd-6-263-2013, 2013.

Oshima, N., Koike, M., Zhang, Y. and Kondo, Y.: Aging of black carbon in outflow from anthropogenic sources using a mixing state resolved model: 2. Aerosol optical properties and cloud condensation nuclei activities, J. Geophys. Res. Atmospheres, 114(D18), D18202, doi:10.1029/2008JD011681, 2009a.

Oshima, N., Koike, M., Zhang, Y., Kondo, Y., Moteki, N., Takegawa, N. and Miyazaki, Y.: Aging of black carbon in outflow from anthropogenic sources using a mixing state resolved model: Model development and evaluation, J. Geophys. Res. Atmospheres, 114(D6), D06210, doi:10.1029/2008JD010680, 2009b.

Painter, T. H., Flanner, M. G., Kaser, G., Marzeion, B., VanCuren, R. a. and Abdalati, W.: End of the Little Ice Age in the Alps forced by industrial black carbon, Proc. Natl. Acad. Sci., 1–6, doi:10.1073/pnas.1302570110, 2013.

Pandolfi, M., Cusack, M., Alastuey, A. and Querol, X.: Variability of aerosol optical properties in the Western Mediterranean Basin, Atmos Chem Phys, 11(15), 8189–8203, doi:10.5194/acp-11-8189-2011, 2011.

Pandolfi, M., Ripoll, A., Querol, X. and Alastuey, A.: Climatology of aerosol optical properties and black carbon mass absorption cross section at a remote high-altitude site in the western Mediterranean Basin, Atmos Chem Phys, 14(12), 6443–6460, doi:10.5194/acp-14-6443-2014, 2014.

Panteliadis, P., Hafkenscheid, T., Cary, B., Diapouli, E., Fischer, A., Favez, O., Quincey, P., Viana, M., Hitzenberger, R., Vecchi, R., Saraga, D., Sciare, J., Jaffrezo, J. L., John, A., Schwarz, J., Giannoni, M., Novak, J., Karanasiou, A., Fermo, P. and Maenhaut, W.: ECOC comparison exercise with identical thermal protocols after temperature offset correction – instrument diagnostics by in-depth evaluation of operational parameters, Atmos Meas Tech, 8(2), 779–792, doi:10.5194/amt-8-779-2015, 2015.

Petzold, A. and Niessner, R.: Photoacoustic soot sensor for in-situ black carbon monitoring, Appl. Phys. B, 63(2), 191–197, doi:10.1007/BF01095272, 1996.

Petzold, A. and Schönlinner, M.: Multi-angle absorption photometry—a new method for the measurement of aerosol light absorption and atmospheric black carbon, J. Aerosol Sci., 35(4), 421–441, doi:10.1016/j.jaerosci.2003.09.005, 2004.

Petzold, A., Schloesser, H., Sheridan, P. J., Arnott, W. P., Ogren, J. A. and Virkkula, A.: Evaluation of Multiangle Absorption Photometry for Measuring Aerosol Light Absorption, Aerosol Sci. Technol., 39(1), 40–51, doi:10.1080/027868290901945, 2005a.

Petzold, A., Schloesser, H., Sheridan, P. J., Arnott, W. P., Ogren, J. A. and Virkkula, A.: Evaluation of Multiangle Absorption Photometry for Measuring Aerosol Light Absorption, Aerosol Sci. Technol., 39(1), 40–51, doi:10.1080/027868290901945, 2005b.

Petzold, A., Ogren, J. A., Fiebig, M., Laj, P., Li, S.-M., Baltensperger, U., Holzer-Popp, T., Kinne, S., Pappalardo, G., Sugimoto, N., Wehrli, C., Wiedensohler, A. and Zhang, X.-Y.: Recommendations for reporting “black carbon” measurements, Atmos Chem Phys, 13(16), 8365–8379, doi:10.5194/acp-13-8365-2013, 2013a.

Petzold, A., Ogren, J. A., Fiebig, M., Laj, P., Li, S.-M., Baltensperger, U., Holzer-Popp, T., Kinne, S., Pappalardo, G., Sugimoto, N., Wehrli, C., Wiedensohler, A. and Zhang, X.-Y.: Recommendations for reporting “black carbon” measurements, Atmos Chem Phys, 13(16), 8365–8379, doi:10.5194/acp-13-8365-2013, 2013b.

Piazzalunga, A., Belis, C., Bernardoni, V., Cazzuli, O., Fermo, P., Valli, G. and Vecchi, R.: Estimates of wood burning contribution to PM by the macro-tracer method using tailored emission factors, Atmos. Environ., 45(37), 6642–6649, doi:10.1016/j.atmosenv.2011.09.008, 2011.

Pio, C. A., Legrand, M., Oliveira, T., Afonso, J., Santos, C., Caseiro, A., Fialho, P., Barata, F., Puxbaum, H., Sanchez-Ochoa, A., Kasper-Giebl, A., Gelencsér, A., Preunkert, S. and Schock, M.: Climatology of aerosol composition (organic versus inorganic) at nonurban sites on a west-east transect across Europe, J. Geophys. Res. Atmospheres, 112(D23), D23S02, doi:10.1029/2006JD008038, 2007.

Pitari, G., Rizi, V., Ricciardulli, L. and Visconti, G.: High-speed civil transport impact: Role of sulfate, nitric acid trihydrate, and ice aerosols studied with a two-dimensional model including aerosol physics, J. Geophys. Res. Atmospheres, 98(D12), 23141–23164, doi:10.1029/93JD02600, 1993.

Pitari, G., Mancini, E., Rizi, V. and Shindell, D. T.: Impact of Future Climate and Emission Changes on Stratospheric Aerosols and Ozone, J. Atmospheric Sci., 59(3), 414–440, doi:10.1175/1520-0469(2002)059<0414:IOFCAE>2.0.CO;2, 2002.

Prenni, A. J., DeMott, P. J., Twohy, C., Poellot, M. R., Kreidenweis, S. M., Rogers, D. C., Brooks, S. D., Richardson, M. S. and Heymsfield, A. J.: Examinations of ice formation processes in Florida cumuli using ice nuclei measurements of anvil ice crystal particle residues, J Geophys Res Atmos, 112, D10221(D10), doi:10.1029/2006JD007549, 2007.

Pruppacher, H. R. and Klett, J. D.: Microphysics of Clouds and Precipitation, 2nd ed., Kluwer Academic Publishers, Dordrecht, The Netherlands., 1997.

Putaud, J.-P., Raes, F., Van Dingenen, R., Brüggemann, E., Facchini, M.-C., Decesari, S., Fuzzi, S., Gehrig, R., Hüglin, C., Laj, P., Lorbeer, G., Maenhaut, W., Mihalopoulos, N., Müller, K., Querol, X., Rodriguez, S., Schneider, J., Spindler, G., Brink, H. ten, Tørseth, K. and Wiedensohler, A.: A European aerosol phenomenology—2: chemical characteristics of particulate matter at kerbside, urban, rural and background sites in Europe, Atmos. Environ., 38(16), 2579–2595, doi:10.1016/j.atmosenv.2004.01.041, 2004.

Querol, X., Alastuey, A., Ruiz, C. R., Artiñano, B., Hansson, H. C., Harrison, R. M., Buringh, E., ten Brink, H. M., Lutz, M., Bruckmann, P., Straehl, P. and Schneider, J.: Speciation and origin of PM10 and PM2.5 in selected European cities, Atmos. Environ., 38(38), 6547–6555, doi:10.1016/j.atmosenv.2004.08.037, 2004.

Querol, X., Alastuey, A., Viana, M., Moreno, T., Reche, C., Minguillón, M. C., Ripoll, A., Pandolfi, M., Amato, F., Karanasiou, A., Pérez, N., Pey, J., Cusack, M., Vázquez, R., Plana, F., Dall'Osto, M., de la Rosa, J., Sánchez de la Campa, A., Fernández-Camacho, R., Rodríguez, S., Pio, C., Alados-Arboledas, L., Titos, G., Artíñano, B., Salvador, P., García Dos Santos, S. and Fernández Patier, R.: Variability of carbonaceous aerosols in remote, rural, urban and industrial environments in Spain: implications for air quality policy, Atmos Chem Phys, 13(13), 6185–6206, doi:10.5194/acp-13-6185-2013, 2013.

Quinn, P. K., Shaw, G., Andrews, E., Dutton, E. G., Ruoho-Airola, T. and Gong, S. L.: Arctic haze: current trends and knowledge gaps, Tellus B, 59(1), 99–114, doi:10.1111/j.1600-0889.2006.00238.x, 2007.

Raatikainen, T., Brus, D., Hyvärinen, A.-P., Svensson, J., Asmi, E. and Lihavainen, H.: Black carbon concentrations and mixing state in the Finnish Arctic, Atmos Chem Phys Discuss, 15(11), 15621–15654, doi:10.5194/acpd-15-15621-2015, 2015a.

Raatikainen, T., Brus, D., Hyvärinen, A.-P., Svensson, J., Asmi, E. and Lihavainen, H.: Black carbon concentrations and mixing state in the Finnish Arctic, Atmos Chem Phys, 15(17), 10057–10070, doi:10.5194/acp-15-10057-2015, 2015b.

Ramanathan, V., Cess, R. D., Harrison, E. F., Minnis, P., Barkstrom, B. R., Ahmad, E. and Hartmann, D.: Cloud-Radiative Forcing and Climate: Results from the Earth Radiation Budget Experiment, Science, 243(4887), 57–63, doi:10.1126/science.243.4887.57, 1989.

Ramanathan, V., Ramana, M. V., Roberts, G., Kim, D., Corrigan, C., Chung, C. and Winker, D.: Warming trends in Asia amplified by brown cloud solar absorption, Nature, 448(7153), 575–578, doi:10.1038/nature06019, 2007.

Reche, C., Querol, X., Alastuey, A., Viana, M., Pey, J., Moreno, T., Rodríguez, S., González, Y., Fernández-Camacho, R., de la Rosa, J., Dall'Osto, M., Prévôt, A. S. H., Hueglin, C., Harrison, R. M. and Quincey, P.: New considerations for PM, Black Carbon and particle number concentration for air quality monitoring across different European cities, Atmos Chem Phys, 11(13), 6207–6227, doi:10.5194/acp-11-6207-2011, 2011.

Reddington, C. L., McMeeking, G., Mann, G. W., Coe, H., Frontoso, M. G., Liu, D., Flynn, M., Spracklen, D. V. and Carslaw, K. S.: The mass and number size distributions of black carbon aerosol over Europe, Atmos Chem Phys, 13(9), 4917–4939, doi:10.5194/acp-13-4917-2013, 2013.

Rhein, S.R. Rintoul, S. Aoki, E. Campos, D. Chambers, R.A. Feely, S. Gulev, G.C. Johnson, S.A. Josey, A. Kostianoy, C. Mauritzen, D. Roemmich, L.D. Talley and F. Wang and J.C. Cosimo: IPCC, 2013: Observations: Cryosphere. In: Climate Change 2013: The Physical Science Basis. Contribution of Working Group I to the Fifth Assessment Report of the Intergovernmental Panel on Climate Change, edited by T. F. Stocker, Cambridge University Press, Cambridge, United Kingdom and New York, NY, USA, 255–315, 2013.

Riemer, N., West, M., Zaveri, R. and Easter, R.: Estimating black carbon aging time-scales with a particle-resolved aerosol model, J. Aerosol Sci., 41(1), 143–158, doi:10.1016/j.jaerosci.2009.08.009, 2010.

Ripoll, A., Pey, J., Minguillón, M. C., Pérez, N., Pandolfi, M., Querol, X. and Alastuey, A.: Three years of aerosol mass, black carbon and particle number concentrations at Montsec (southern Pyrenees, 1570 m a.s.l.), Atmos Chem Phys, 14(8), 4279–4295, doi:10.5194/acp-14-4279-2014, 2014.

Roebroeks, W. and Villa, P.: On the earliest evidence for habitual use of fire in Europe, Proc. Natl. Acad. Sci. U. S. A., 108(13), 5209–5214, doi:10.1073/pnas.1018116108, 2011.

Ruckstuhl, C. and Norris, J. R.: How do aerosol histories affect solar "dimming" and "brightening" over Europe?: IPCC-AR4 models versus observations, J. Geophys. Res. Atmospheres, 114(D10), D00D04, doi:10.1029/2008JD011066, 2009.

Sand, M., Berntsen, T. K., Kay, J. E., Lamarque, J. F., Seland, Ø. and Kirkevåg, A.: The Arctic response to remote and local forcing of black carbon, Atmos Chem Phys, 13(1), 211–224, doi:10.5194/acp-13-211-2013, 2013.

Sandradewi, J., Prévôt, A. S. H., Szidat, S., Perron, N., Alfarra, M. R., Lanz, V. A., Weingartner, E. and Baltensperger, U.: Using aerosol light absorption measurements for the quantitative determination of wood burning and traffic emission contributions to particulate matter, Environ. Sci. Technol., 42(9), 3316–3323, 2008.

Santer, B. D., Taylor, K. E., Wigley, T. M. L., Penner, J. E., Jones, P. D. and Cubasch, U.: Towards the detection and attribution of an anthropogenic effect on climate, Clim. Dyn., 12(2), 77–100, doi:10.1007/BF00223722, 1995.

Scarnato, B. V., Vahidinia, S., Richard, D. T. and Kirchstetter, T. W.: Effects of internal mixing and aggregate morphology on optical properties of black carbon using a discrete dipole approximation model, Atmos Chem Phys, 13(10), 5089–5101, doi:10.5194/acp-13-5089-2013, 2013.

Schmid, H., Laskus, L., Jürgen Abraham, H., Baltensperger, U., Lavanchy, V., Bizjak, M., Burba, P., Cachier, H., Crow, D., Chow, J., Gnauk, T., Even, A., ten Brink, H. M., Giesen, K.-P., Hitzenberger, R., Hueglin, C., Maenhaut, W., Pio, C., Carvalho, A., Putaud, J.-P., Toom-Sauntry, D. and Puxbaum, H.: Results of the “carbon conference” international aerosol carbon round robin test stage I, Atmos. Environ., 35(12), 2111–2121, doi:10.1016/S1352-2310(00)00493-3, 2001.

Schmidt, S., Schneider, J., Klimach, T., Mertes, S., Schenk, L. P., Curtius, J., Kupiszewski, P., Hammer, E., Vochezer, P., Lloyd, G., Ebert, M., Kandler, K., Weinbruch, S. and Borrmann, S.: In-situ single submicron particle composition analysis of ice residuals from mountain-top mixed-phase clouds in Central Europe, Atmos Chem Phys Discuss, 15(4), 4677–4724, doi:10.5194/acpd-15-4677-2015, 2015.

Schnaiter, M., Horvath, H., Möhler, O., Naumann, K.-H., Saathoff, H. and Schöck, O. W.: UV-VIS-NIR spectral optical properties of soot and soot-containing aerosols, J. Aerosol Sci., 34(10), 1421–1444, doi:10.1016/S0021-8502(03)00361-6, 2003.

Schnaiter, M., Linke, C., Möhler, O., Naumann, K.-H., Saathoff, H., Wagner, R., Schurath, U. and Wehner, B.: Absorption amplification of black carbon internally mixed with secondary organic aerosol, J. Geophys. Res. Atmospheres, 110(D19), D19204, doi:10.1029/2005JD006046, 2005.

Schulz, M., Textor, C., Kinne, S., Balkanski, Y., Bauer, S., Berntsen, T., Berglen, T., Boucher, O., Dentener, F., Guibert, S., Isaksen, I. S. A., Iversen, T., Koch, D., Kirkevåg, A., Liu, X., Montanaro, V., Myhre, G., Penner, J. E., Pitari, G., Reddy, S., Seland, Ø., Stier, P. and Takemura, T.: Radiative forcing by aerosols as derived from the AeroCom present-day and pre-industrial simulations, Atmos Chem Phys, 6(12), 5225–5246, doi:10.5194/acp-6-5225-2006, 2006.

Schwarz, J. P., Gao, R. S., Fahey, D. W., Thomson, D. S., Watts, L. A., Wilson, J. C., Reeves, J. M., Darbeheshti, M., Baumgardner, D. G., Kok, G. L., Chung, S. H., Schulz, M., Hendricks, J., Lauer, A., Kärcher, B., Slowik, J. G., Rosenlof, K. H., Thompson, T. L., Langford, A. O., Loewenstein, M. and Aikin, K. C.: Single-particle measurements of midlatitude black carbon and light-scattering aerosols from the boundary layer to the lower stratosphere, J. Geophys. Res. Atmospheres, 111(D16), D16207, doi:10.1029/2006JD007076, 2006.

Schwarz, J. P., Spackman, J. R., Fahey, D. W., Gao, R. S., Lohmann, U., Stier, P., Watts, L. A., Thomson, D. S., Lack, D. A., Pfister, L., Mahoney, M. J., Baumgardner, D., Wilson, J. C. and Reeves, J. M.: Coatings and their enhancement of black carbon light absorption in the tropical atmosphere, J. Geophys. Res. Atmospheres, 113(D3), D03203, doi:10.1029/2007JD009042, 2008a.

Schwarz, J. P., Gao, R. S., Spackman, J. R., Watts, L. A., Thomson, D. S., Fahey, D. W., Ryerson, T. B., Peischl, J., Holloway, J. S., Trainer, M., Frost, G. J., Baynard, T., Lack, D. A., de Gouw, J. A., Warneke, C. and Del Negro, L. A.: Measurement of the mixing state, mass, and optical size of individual black carbon particles in urban and biomass burning emissions, Geophys. Res. Lett., 35(13), L13810, doi:10.1029/2008GL033968, 2008b.

Screen, J. A. and Simmonds, I.: The central role of diminishing sea ice in recent Arctic temperature amplification, Nature, 464(7293), 1334–1337, doi:10.1038/nature09051, 2010.

Sedlacek, A. J., Lewis, E. R., Kleinman, L., Xu, J. and Zhang, Q.: Determination of and evidence for non-core-shell structure of particles containing black carbon using the Single-Particle Soot Photometer (SP2), Geophys. Res. Lett., 39(6), L06802, doi:10.1029/2012GL050905, 2012.

Sharma, S., Lavoué, D., Cachier, H., Barrie, L. A. and Gong, S. L.: Long-term trends of the black carbon concentrations in the Canadian Arctic, J. Geophys. Res. Atmospheres, 109(D15), D15203, doi:10.1029/2003JD004331, 2004.

Sharma, S., Andrews, E., Barrie, L. A., Ogren, J. A. and Lavoué, D.: Variations and sources of the equivalent black carbon in the high Arctic revealed by long-term observations at Alert and Barrow: 1989–2003, J. Geophys. Res. Atmospheres, 111(D14), D14208, doi:10.1029/2005JD006581, 2006.

Shaw, G. E.: The Arctic Haze Phenomenon, Bull. Am. Meteorol. Soc., 76(12), 2403–2413, doi:10.1175/1520-0477(1995)076<2403:TAHP>2.0.CO;2, 1995.

Shindell, D. and Faluvegi, G.: Climate response to regional radiative forcing during the twentieth century, Nat. Geosci., 2(4), 294–300, doi:10.1038/ngeo473, 2009.

Shiraiwa, M., Kondo, Y., Moteki, N., Takegawa, N., Sahu, L. K., Takami, A., Hatakeyama, S., Yonemura, S. and Blake, D. R.: Radiative impact of mixing state of black carbon aerosol in Asian outflow, J. Geophys. Res. Atmospheres, 113(D24), D24210, doi:10.1029/2008JD010546, 2008.

Shiraiwa, M., Kondo, Y., Iwamoto, T. and Kita, K.: Amplification of Light Absorption of Black Carbon by Organic Coating, Aerosol Sci. Technol., 44(1), 46–54, doi:10.1080/02786820903357686, 2010.

Slowik, J. G., Cross, E. S., Han, J.-H., Davidovits, P., Onasch, T. B., Jayne, J. T., Williams, L. R., Canagaratna, M. R., Worsnop, D. R., Chakrabarty, R. K., Moosmüller, H., Arnott, W. P., Schwarz, J. P., Gao, R.-S., Fahey, D. W., Kok, G. L. and Petzold, A.: An Inter-Comparison of Instruments Measuring Black Carbon Content of Soot Particles, Aerosol Sci. Technol., 41(3), 295–314, doi:10.1080/02786820701197078, 2007a.

Slowik, J. G., Cross, E. S., Han, J.-H., Davidovits, P., Onasch, T. B., Jayne, J. T., Williams, L. R., Canagaratna, M. R., Worsnop, D. R., Chakrabarty, R. K., Moosmüller, H., Arnott, W. P., Schwarz, J. P., Gao, R.-S., Fahey, D. W., Kok, G. L. and Petzold, A.: An Inter-Comparison of Instruments Measuring

Black Carbon Content of Soot Particles, Aerosol Sci. Technol., 41(3), 295–314, doi:10.1080/02786820701197078, 2007b.

Smith, S. J. and Bond, T. C.: Two hundred fifty years of aerosols and climate: the end of the age of aerosols, Atmos Chem Phys, 14(2), 537–549, doi:10.5194/acp-14-537-2014, 2014.

Spindler, G., Müller, K. and Herrmann, H.: Main particulate matter components in Saxony (Germany), Environ. Sci. Pollut. Res., 6(2), 89–94, doi:10.1007/BF02987559, 1999.

Stephens, M., Turner, N. and Sandberg, J.: Particle identification by laser-induced incandescence in a solid-state laser cavity, Appl. Opt., 42(19), 3726–3736, doi:10.1364/AO.42.003726, 2003.

Sun, Z. and Shine, K. P.: Studies of the radiative properties of ice and mixed-phase clouds, Q. J. R. Meteorol. Soc., 120(515), 111–137, doi:10.1002/qj.49712051508, 1994a.

Sun, Z. and Shine, K. P.: Studies of the radiative properties of ice and mixed-phase clouds, Quart J Roy Meteor Soc, 120(515), 111–137, doi:10.1002/qj.49712051508, 1994b.

Szyrmer, W. and Zawadzki, I.: Biogenic and anthropogenic sources of ice-forming nuclei: A Review., Bull Amer Meteor Soc, 78, 209–209, doi:10.1175/1520-0477(1997)078<0209:BAASOI>2.0.CO;2, 1997.

Takemura, T., Okamoto, H., Maruyama, Y., Numaguti, A., Higurashi, A. and Nakajima, T.: Global three-dimensional simulation of aerosol optical thickness distribution of various origins, J. Geophys. Res. Atmospheres, 105(D14), 17853–17873, doi:10.1029/2000JD900265, 2000.

Takemura, T., Nakajima, T., Dubovik, O., Holben, B. N. and Kinne, S.: Single-Scattering Albedo and Radiative Forcing of Various Aerosol Species with a Global Three-Dimensional Model, J. Clim., 15(4), 333–352, doi:10.1175/1520-0442(2002)015<0333:SSAARF>2.0.CO;2, 2002.

Takemura, T., Nozawa, T., Emori, S., Nakajima, T. Y. and Nakajima, T.: Simulation of climate response to aerosol direct and indirect effects with aerosol transport-radiation model, J. Geophys. Res. Atmospheres, 110(D2), D02202, doi:10.1029/2004JD005029, 2005.

Taketani, F., Miyakawa, T., Takashima, H., Komazaki, Y., Kanaya, Y., Taketani, F., Miyakawa, T., Inoue, J., Kanaya, Y., Takashima, H., Pan, X. and Inoue, J.: Ship-borne observations of atmospheric black carbon aerosol particles over the Arctic Ocean, Bering Sea, and North Pacific Ocean during September 2014, J. Geophys. Res. Atmospheres, 2015JD023648, doi:10.1002/2015JD023648, 2016.

Tomasi, C., Kokhanovsky, A. A., Lupi, A., Ritter, C., Smirnov, A., O'Neill, N. T., Stone, R. S., Holben, B. N., Nyeki, S., Wehrli, C., Stohl, A., Mazzola, M., Lanconelli, C., Vitale, V., Stebel, K., Aaltonen, V., de Leeuw, G., Rodriguez, E., Herber, A. B., Radionov, V. F., Zielinski, T., Petelski, T., Sakerin, S. M., Kabanov, D. M., Xue, Y., Mei, L., Istomina, L., Wagener, R., McArthur, B., Sobolewski, P. S., Kivi, R., Courcoux, Y., Larouche, P., Broccardo, S. and Piketh, S. J.: Aerosol remote sensing in polar regions, Earth-Sci. Rev., 140, 108–157, doi:10.1016/j.earscirev.2014.11.001, 2015.

Tørseth, K., Aas, W., Breivik, K., Fjæraa, A. M., Fiebig, M., Hjellbrekke, A. G., Lund Myhre, C., Solberg, S. and Yttri, K. E.: Introduction to the European Monitoring and Evaluation Programme (EMEP) and observed atmospheric composition change during 1972–2009, Atmos Chem Phys, 12(12), 5447–5481, doi:10.5194/acp-12-5447-2012, 2012.

Tosca, M. G., Diner, D. J., Garay, M. J. and Kalashnikova, O. V.: Human-caused fires limit convection in tropical Africa: First temporal observations and attribution, Geophys. Res. Lett., 42(15), 2015GL065063, doi:10.1002/2015GL065063, 2015.

Treffeisen, R., Tunved, P., Ström, J., Herber, A., Bareiss, J., Helbig, A., Stone, R. S., Hoyningen-Huene, W., Krejci, R., Stohl, A. and Neuber, R.: Arctic smoke – aerosol characteristics during a record smoke event in the European Arctic and its radiative impact, Atmos Chem Phys, 7(11), 3035–3053, doi:10.5194/acp-7-3035-2007, 2007.

Tunved, P., Ström, J. and Krejci, R.: Arctic aerosol life cycle: linking aerosol size distributions observed between 2000 and 2010 with air mass transport and precipitation at Zeppelin station, Ny-Ålesund, Svalbard, Atmos Chem Phys, 13(7), 3643–3660, doi:10.5194/acp-13-3643-2013, 2013.

Turnock, S. T., Spracklen, D. V., Carslaw, K. S., Mann, G. W., Woodhouse, M. T., Forster, P. M., Haywood, J., Johnson, C. E., Dalvi, M., Bellouin, N. and Sanchez-Lorenzo, A.: Modelled and observed changes in aerosols and surface solar radiation over Europe between 1960 and 2009, Atmos Chem Phys Discuss, 15(9), 13457–13513, doi:10.5194/acpd-15-13457-2015, 2015.

Turpin, B. J., Saxena, P. and Andrews, E.: Measuring and simulating particulate organics in the atmosphere: problems and prospects, Atmos. Environ., 34(18), 2983–3013, doi:10.1016/S1352-2310(99)00501-4, 2000.

Twohy, C. H. and Poellot, M. R.: Chemical characteristics of ice residual nuclei in anvil cirrus clouds: evidence for homogeneous and heterogeneous ice formation, Atmos Chem Phys, 5(8), 2289–2297, doi:10.5194/acp-5-2289-2005, 2005.

Ulanowski, Z., Kaye, P. H., Hirst, E., Greenaway, R. S., Cotton, R. J., Hesse, E. and Collier, C. T.: Incidence of rough and irregular atmospheric ice particles from Small Ice Detector 3 measurements, Atmos Chem Phys, 14(3), 1649–1662, doi:10.5194/acp-14-1649-2014, 2014.

Utry, N., Ajtai, T., Filep, Á., Dániel Pintér, M., Hoffer, A., Bozoki, Z. and Szabó, G.: Mass specific optical absorption coefficient of HULIS aerosol measured by a four-wavelength photoacoustic spectrometer at NIR, VIS and UV wavelengths, Atmos. Environ., 69, 321–324, doi:10.1016/j.atmosenv.2013.01.003, 2013.

Utry, N., Ajtai, T., Pintér, M., Tombácz, E., Illés, E., Bozóki, Z. and Szabó, G.: Mass specific optical absorption coefficients of mineral dust components measured by a multi wavelength photoacoustic spectrometer, Atmos Meas Tech Discuss, 7(9), 9025–9046, doi:10.5194/amtd-7-9025-2014, 2014.

Vander Wal, R. L., Ticich, T. M. and West, J. R.: Laser-induced incandescence applied to metal nanostructures, Appl. Opt., 38(27), 5867, doi:10.1364/AO.38.005867, 1999.

Van Dingenen, R., Raes, F., Putaud, J.-P., Baltensperger, U., Charron, A., Facchini, M.-C., Decesari, S., Fuzzi, S., Gehrig, R., Hansson, H.-C., Harrison, R. M., Hüglin, C., Jones, A. M., Laj, P., Lorbeer, G., Maenhaut, W., Palmgren, F., Querol, X., Rodriguez, S., Schneider, J., Brink, H. ten, Tunved, P., Tørseth, K., Wehner, B., Weingartner, E., Wiedensohler, A. and Wåhlin, P.: A European aerosol phenomenology—1: physical characteristics of particulate matter at kerbside, urban, rural and background sites in Europe, Atmos. Environ., 38(16), 2561–2577, doi:10.1016/j.atmosenv.2004.01.040, 2004.

Vaughan D. G., J.C. Cosimo, I. Allison, J. Carrasco, G. Kaser, R. Kwok, P. Mote, F. Paul, J. Ren, E. Rignot, O. Solomina, K. Steffen and T. Zhang: IPCC, 2013: Observations: Cryosphere. In: Climate Change 2013: The Physical Science Basis. Contribution of Working Group I to the Fifth Assessment Report of the Intergovernmental Panel on Climate Change, edited by T. F. Stocker, Cambridge University Press, Cambridge, United Kingdom and New York, NY, USA, 317–382, 2013.

Vautard, R., Yiou, P. and van Oldenborgh, G. J.: Decline of fog, mist and haze in Europe over the past 30 years, Nat. Geosci., 2(2), 115–119, doi:10.1038/ngeo414, 2009.

Venzac, H., Sellegri, K., Villani, P., Picard, D. and Laj, P.: Seasonal variation of aerosol size distributions in the free troposphere and residual layer at the puy de Dôme station, France, Atmos Chem Phys, 9(4), 1465–1478, doi:10.5194/acp-9-1465-2009, 2009.

Vestreng, V., Myhre, G., Fagerli, H., Reis, S. and Tarrasón, L.: Twenty-five years of continuous sulphur dioxide emission reduction in Europe, Atmos Chem Phys, 7(13), 3663–3681, doi:10.5194/acp-7-3663-2007, 2007.

Virkkula, A., Mäkelä, T., Hillamo, R., Yli-Tuomi, T., Hirsikko, A., Hämeri, K. and Koponen, I. K.: A Simple Procedure for Correcting Loading Effects of Aethalometer Data, J. Air Waste Manag. Assoc., 57(10), 1214–1222, doi:10.3155/1047-3289.57.10.1214, 2007.

Vochezer, P., Järvinen, E., Wagner, R., Kupiszewski, P., Leisner, T. and Schnaiter, M.: In situ characterization of mixed phase clouds using the Small Ice Detector and the Particle Phase Discriminator, Atmos Meas Tech Discuss, 8(6), 6511–6558, doi:10.5194/amtd-8-6511-2015, 2015.

Warren, S. G.: Impurities in Snow - Effects on Albedo and Snowmelt Review, Ann. Glaciol., 5, 177–179, 1984.

von der Weiden, S.-L., Drewnick, F. and Borrmann, S.: Particle Loss Calculator – a new software tool for the assessment of the performance of aerosol inlet systems, Atmos Meas Tech, 2(2), 479–494, doi:10.5194/amt-2-479-2009, 2009.

Weiner, S., Xu, Q., Goldberg, P., Liu, J. and Bar-Yosef, O.: Evidence for the Use of Fire at Zhoukoudian, China, Science, 281(5374), 251–253, doi:10.1126/science.281.5374.251, 1998.

Weingartner, E., Burtscher, H. and Baltensperger, U.: Hygroscopic properties of carbon and diesel soot particles, Atmos. Environ., 31(15), 2311–2327, doi:10.1016/S1352-2310(97)00023-X, 1997.

Weingartner, E., Saathoff, H., Schnaiter, M., Streit, N., Bitnar, B. and Baltensperger, U.: Absorption of light by soot particles: determination of the absorption coefficient by means of aethalometers, J. Aerosol Sci., 34(10), 1445–1463, doi:10.1016/S0021-8502(03)00359-8, 2003.

Wendisch, M., Garrett, T. J. and Strapp, J. W.: Wind tunnel tests of the airborne PVM-100A response to large droplets, J Atmos Ocean. Tech, 19(10), 1577–1584, doi:10.1175/1520-0426(2002)019<1577:WTTOTA>2.0.CO;2, 2002.

Wiedensohler, A., Birmili, W., Nowak, A., Sonntag, A., Weinhold, K., Merkel, M., Wehner, B., Tuch, T., Pfeifer, S., Fiebig, M., Fjäraa, A. M., Asmi, E., Sellegri, K., Depuy, R., Venzac, H., Villani, P., Laj, P., Aalto, P., Ogren, J. A., Swietlicki, E., Williams, P., Roldin, P., Quincey, P., Hüglin, C., Fierz-Schmidhauser, R.,

Gysel, M., Weingartner, E., Riccobono, F., Santos, S., Grüning, C., Faloon, K., Beddows, D., Harrison, R., Monahan, C., Jennings, S. G., O'Dowd, C. D., Marinoni, A., Horn, H.-G., Keck, L., Jiang, J., Scheckman, J., McMurry, P. H., Deng, Z., Zhao, C. S., Moerman, M., Henzing, B., de Leeuw, G., Löschau, G. and Bastian, S.: Mobility particle size spectrometers: harmonization of technical standards and data structure to facilitate high quality long-term observations of atmospheric particle number size distributions, Atmos Meas Tech, 5(3), 657–685, doi:10.5194/amt-5-657-2012, 2012.

Wiscombe, W. J. and Grams, G. W.: The Backscattered Fraction in two-stream Approximations, J. Atmospheric Sci., 33(12), 2440–2451, doi:10.1175/1520-0469(1976)033<2440:TBFITS>2.0.CO;2, 1976.

WMO: AEROSOL MEASUREMENT PROCEDURES GUIDELINES AND RECOMMENDATIONS, SECOND EDITION, 2016.

Worringen, A., Kandler, K., Benker, N., Dirsch, T., Mertes, S., Schenk, L., Kästner, U., Frank, F., Nillius, B., Bundke, U., Rose, D., Curtius, J., Kupiszewski, P., Weingartner, E., Vochezer, P., Schneider, J., Schmidt, S., Weinbruch, S. and Ebert, M.: Single-particle characterization of ice-nucleating particles and ice particle residuals sampled by three different techniques, Atmos Chem Phys, 15(8), 4161–4178, doi:10.5194/acp-15-4161-2015, 2015.

Xu, B., Cao, J., Hansen, J., Yao, T., Joswia, D. R., Wang, N., Wu, G., Wang, M., Zhao, H., Yang, W., Liu, X. and He, J.: Black soot and the survival of Tibetan glaciers, Proc. Natl. Acad. Sci., 106(52), 22114–22118, doi:10.1073/pnas.0910444106, 2009a.

Xu, B., Cao, J., Hansen, J., Yao, T., Joswia, D. R., Wang, N., Wu, G., Wang, M., Zhao, H., Yang, W., Liu, X. and He, J.: Black soot and the survival of Tibetan glaciers, Proc. Natl. Acad. Sci., doi:10.1073/pnas.0910444106, 2009b.

Yamanouchi, T., Treffeisen, R., Herber, A., Shiobara, M., Yamagata, S., Hara, K., Sato, K., Yabuki, M., Tomikawa, Y., Rinke, A., Neuber, R., Schumachter, R., Kriews, M., Ström, J., Schrems, O. and Gernandt, H.: Arctic Study of Tropospheric Aerosol and Radiation (ASTAR) 2000: Arctic haze case study, Tellus B, 57(2), 141–152, doi:10.1111/j.1600-0889.2005.00140.x, 2005.

Yasunari, T. J., Bonasoni, P., Laj, P., Fujita, K., Vuillermoz, E., Marinoni, A., Cristofanelli, P., Duchi, R., Tartari, G. and Lau, K.-M.: Estimated impact of black carbon deposition during pre-monsoon season from Nepal Climate Observatory – Pyramid data and snow albedo changes over Himalayan glaciers, Atmos Chem Phys, 10(14), 6603–6615, doi:10.5194/acp-10-6603-2010, 2010.

Yttri, K. E., Aas, W., Bjerke, A., Cape, J. N., Cavalli, F., Ceburnis, D., Dye, C., Emblico, L., Facchini, M. C., Forster, C., Hanssen, J. E., Hansson, H. C., Jennings, S. G., Maenhaut, W., Putaud, J. P. and Tørseth, K.: Elemental and organic carbon in PM10: a one year measurement campaign within the European Monitoring and Evaluation Programme EMEP, Atmos Chem Phys, 7(22), 5711–5725, doi:10.5194/acp-7-5711-2007, 2007.

Yttri, K. E., Dye, C., Braathen, O.-A., Simpson, D. and Steinnes, E.: Carbonaceous aerosols in Norwegian urban areas, Atmos Chem Phys, 9(6), 2007–2020, doi:10.5194/acp-9-2007-2009, 2009.

Yttri, K. E., Simpson, D., Nøjgaard, J. K., Kristensen, K., Genberg, J., Stenström, K., Swietlicki, E., Hillamo, R., Aurela, M., Bauer, H., Offenberg, J. H., Jaoui, M., Dye, C., Eckhardt, S., Burkhart, J. F., Stohl, A. and Glasius, M.: Source apportionment of the summer time carbonaceous aerosol at Nordic

rural background sites, Atmos Chem Phys, 11(24), 13339–13357, doi:10.5194/acp-11-13339-2011, 2011.

Zarzycki, C. M. and Bond, T. C.: How much can the vertical distribution of black carbon affect its global direct radiative forcing?, Geophys. Res. Lett., 37(20), L20807, doi:10.1029/2010GL044555, 2010.

Zotter, P., Ciobanu, V. G., Zhang, Y. L., El-Haddad, I., Macchia, M., Daellenbach, K. R., Salazar, G. A., Huang, R.-J., Wacker, L., Hueglin, C., Piazzalunga, A., Fermo, P., Schwikowski, M., Baltensperger, U., Szidat, S. and Prévôt, A. S. H.: Radiocarbon analysis of elemental and organic carbon in Switzerland during winter-smog episodes from 2008 to 2012 – Part 1: Source apportionment and spatial variability, Atmos Chem Phys, 14(24), 13551–13570, doi:10.5194/acp-14-13551-2014, 2014.